First-principles investigations of solid solution strengthening in Al alloys

Von der Fakultät für Georessourcen und Materialtechnik

der Rheinisch-Westfälischen Technischen Hochschule Aachen

zur Erlangung des akademischen Grades eines

Doktors der Ingenieurwissenschaften

genehmigte Dissertation

vorgelegt von **M.Sc.**

Duancheng Ma
aus Liaoning/China

Berichte aus der Materialwissenschaft

Duancheng Ma

**First-principles investigations of
solid solution strengthening in Al alloys**

Shaker Verlag
Aachen 2012

Acknowledgments

The completion of this dissertation would not be not possible without any of the following individuals:

Foremost, I would like to express my sincere gratitude to **Prof. Dierk Raabe** for his continuous support, guidance and encouragement for this work, also for his visionary perspectives and immense knowledge.

My appreciation is to **Dr. Martin Friák**, **Prof. Jörg Neugebauer** and **Dr. Johann von Pezold** for their insightful comments and suggestions.

I also would like to thank the other colleagues who ever participated the discussion during the inter-department meetings: **Dr. Tilmann Hickel**, **Dr. Blazej Grabowski**, **Dr. Philip Eisenlohr**, **Dr. Stefanie Sandlöbes**, **Dr. Franz Roters**, **Dr. William Counts**, **Dr. Liverios Lymperakis**, and **Dr. Mira Todorova**.

My appreciation is also to **Dr. Alexey Dick** for doing a excellent job as a queuing system administrator, and our brilliant administrators, **Achim Kuhl** and **Berthold Beckschäfer** for helping me with various software and hardware installations. I would like to thank **Dr. Alexander Auer** for his mini lecture given in our institute which enlightened me of the basics of first-principles calculations. My gratitude is also to our librarians, **Christa Regner** and **Petra Siegmund**, for doing their jobs in a fast and reliable fashion.

Last but not least, I would like to appreciate the other current or former colleagues, and visiting scientists with whom I had fruitful scientific discussions in various areas (in alphabetical order):

Current colleagues:

Ugur Aydin, Kemal Davut, Martin Diehl, Nahid-Nora Elhami, Pavlína Elstnerová, Dr. Helge Fabritius, Albert Glensk, Dr. Ivan Gutierrez, Dr. Masood Hafez Haghighat, Nima Hamidi Sibani, Dr. Clara Herrera Pulgarin, Tom Jäpel, Dr. Anahita Khorashadizadeh, Helene Knoll, Christoph Kords, Dr. Aleksander Kostka, Dr. Yujiao Li, Bing Liu, Dr. Tao Liu, Julio Millán, Dr. Roman Nazarov, Dr. Dirk Ponge, Konda Gokuldoss Pradeep, Farangis Ram, David Steinmetz, Dr. Cem Tasan, Natalie Tillack, Dr. Alexander Udyansky, Ute Witt, Xia Wu, Lei Yuan, Dr. Stefan Zaefferer, Dr. Claudio Zambaldi, and **Dr. Lifang Zhu**.

Former colleagues:

Dr. Alankar Alankar, Dr. Keerthika Balasundaram, Dr. Marion Calcagnotto, Prof. Yanping Cao, Dr. Eralp Demir, Dr. Olga Dmitrieva, Luc Hantcherli, Dong He, Olga Kim, Dr.

Contents

Part I

Introduction, Motivation, and Fundamentals

Chapter 1

Introduction

1.1 Bridging quantum mechanics and materials science and engineering

Exciting progress has been made in applying quantum mechanics in materials science (Hafner, 2000). Especially in recent years, first-principles calculations has gone beyond the ground-state to finite temperatures (Wang et al., 2004; Grabowski et al., 2007; Körmann et al., 2008; Grabowski et al., 2009; Shang et al., 2010b). A large number of materials properties are accessible by first-principles by now, some of which are listed in Table 1.1.

One of the purposes of using first-principles is to determine the materials properties. In designing functional materials, the structure or/and the composition can be even tailored to fulfill the target properties (Ceder et al., 1998; Franceschetti and Zunger, 1999; Dudiy and Zunger, 2006; Piquini et al., 2008; van de Walle, 2008).

For the structural materials, the full-scale calculation is not feasible, because the related phenomena are usually too complex and the current computational power is limited. In practice, only a few decisive materials properties are calculated, and used as the input parameters in a multi-scale modeling scheme (McDowell and Olson, 2008; Kuehmann and Olson, 2009).

Apart from that, first-principles also help understand various mechanisms from the electronic origin. As discovered by Hume-Rothery, simple rules can be derived in predicting the formation of intermetallics. Also as pointed by Eberhart (Eberhart and Clougherty, 2004), the electron density should give some correlations with some mechanical properties, just like the correlation between the electron density and the chemical reactions (Woodward and Hoffmann, 1969). However, this aspect is still inadequately studied.

Table 1.1: Some of the materials properties which can be investigated by first-principles

Property	Relevance in materials science	Reference
phase diagram	structure, constituent phase	Wolverton et al. (2002); Liu (2009)
theoretical strength	upper bound of the materials strength	Friák et al. (2001, 2003) Ogata et al. (2009)
elastic modulus	elastic property, dislocation etc.	Zhao et al. (2007) Page and Saxe (2001, 2002)
interface grain boundary	recrystallization, grain growth, cohesion	Mishin et al. (2010)
twinning	plastic deformation	Ogata et al. (2005) Kibey et al. (2007a,b)
stacking fault	twinning, dislocation	Kibey et al. (2006) Brandl et al. (2007)
diffusion	homogenization, phase transformation	Van der Ven et al. (2010)
dislocations	mechanical property, CRSS	Woodward (2005) Tarrat et al. (2009) Matsubara et al. (2010)

1.2 Motivation

Sir Alan Cottrell:

Simplification is an art rather like that of the cartoonist who captures the key features of a familiar face in a few deft strokes to make it instantly recognizable.

If one wants to study the solid solution strengthening by first-principles, technically, the dislocations and the solid solutions should be explicitly depicted by first-principles. These two aspects, however, are great challenges in the current first-principles calculations. Special treatments are proposed to overcome the difficulties (Table 1.2). Even with these special treatments, however, the calculations could be still lengthy[1].

Table 1.2: The difficulties in describing the dislocation and the solid solution by first-principles and the special treatments to overcome the difficulties.

	Difficulty by first-principles	Special treatment	Reference
Dislocation	geometric incompatibility of a single dislocation and the periodic boundary condition	dislocation dipole PN+γ-surface[a] FB-DFT[b]	Woodward (2005)
Solid solution	randomness of the solute atoms	CPA[c] CE[d] SQS[e]	Gyorffy (1972) Sanchez (2010) Zunger et al. (1990)

[a] PN+γ-surface: Peierls-Nabarro model+γ-surface.
[b] FB-DFT: flexible boundary-DFT.
[c] CPA: coherent potential approximation.
[d] CE: cluster expansion.
[e] SQS: special quasi-random structure.

In this thesis, the direct solid solution strengthening calculation are simplified as following:

- *Key features of the solid solution strengthening*: volume and modulus mismatch. These key features have been recognized by the linear elasticity theory (Cottrell, 1948; Fleischer, 1961, 1963). Very recently, confirmed by direct DFT calculations (Yasi et al., 2010), the volume mismatch takes the dominant contribution to the solid solution strengthening. Therefore, the direct calculation can be simplified to the calculation of the lattice parameters and the elastic modulus.

- *Dilute solid solution by the ordered supercells (OSC)*: in the dilute solid solutions, the effect of the randomness of the solute atoms should be significantly reduced or can be

---

[1]Fairly speaking, CPA in Table 1.2 is not as computationally expensive as the others, but the atomic relaxation is not included in CPA. As to be shown in Section 7.2, the atomic relaxation indeed has effect on the perturbation by the solute atoms. The other effects of the atomic relaxation are still unknown.

ignored. It has been shown that the total energy or the formation enthalpy calculated by the OSC are in satisfactory agreement with CPA, CE or SQS (Abrikosov et al. (1998); Ghosh et al. (2008) and Table 4.4). The elastic properties predicted by using OSC are also in reasonable agreement with the experiments (Ganeshan et al., 2009; Kim et al., 2009; Wang and Wang, 2009; Counts et al., 2009).

Besides predicting of the solid solution strengthening, some basic phenomena, such as the perturbation by the solute elements, are needed to be investigated in order to gain further insight into the electronic origin of the strengthening.

In this thesis, seven Al binary solid solutions were investigated (Al-X, X=Ca, Sr, Ir, Cu, Mg, Li and Zn). The lattice parameters and elastic properties of these binary solid solutions were calculated by using OSC approximation. These calculated properties were inserted into the elastic models to determine the strengthening parameters of the solute elements.

1.3   Outlines of each chapter

This thesis is divided into three parts:

Part I is the introductory material to the subject and the methods used in this thesis.

Part II presents the results of this thesis and the corresponding discussions.

Part III is the appendix which includes the technical details. This part serves as the support for the accuracy of the results presented in **Part II**.

The outlines of each chapter are as following:

Part I Introduction, Motivation, and Fundamentals

- **Chapter 2 Fundamentals of solid solution strengthening**. A brief survey on the subject of solid solution strengthening. The survey is focused on the experimental and theoretical aspects of the strengthening phenomenon. Other phenomena, such as the strain ageing, the copper-brass texture, the over-shooting, and etc., are disregarded.

- **Chapter 3 Theoretical methods used in this thesis**. Brief introductions to all the theoretical methods used in this thesis, including DFT (density functional theory), EOS (equation of state), the elastic modulus, Bader analysis, and Ashby's materials property and design chart.

Part II Results and Discussion

- **Chapter 4 Equation of states of studied Al binary solid solutions**. The calculated lattice parameters, bulk modulus, and enthalpies of the studied Al binary solid solutions are presented.

- **Chapter 5 Elastic properties of studied Al binary solid solutions**. The calculated elastic properties, including the elastic constants and the homogenized elastic modulus, of the studied Al binary solid solutions are presented.

- **Chapter 6 Strengthening parameters of studied Al solid solutions**. The solid solution strengthening parameters are calculated by using the results in Chapter 4 and 5, and compared with what is observed in experiments and another direct DFT study. The limitation and applicability of the simplification in this thesis is discussed. A trend of the solid solution strengthening effects is found on the periodic table. The correlation between the solubility enthalpies and the strengthening parameters is also found.

- **Chapter 7 Perturbation caused by solute atoms in studied Al binary solid solutions**. The perturbation of the solute atoms in Al is investigated through the average electron density change of each Al atoms. The perturbation is correlated with the strengthening effect and the supercell size dependence.

- **Chapter 8 DFT guided Ashby's materials property and design charts of studied Al binary solid solutions**. The properties from DFT in this thesis enter Ashby's materials property and design charts. The performance of the studied Al binary solid solutions revealed by those charts reasonably coincides with their current applications.

- **Chapter 9 Summary and outlook**. This thesis is summarized. And the possible further work is suggested.

Part III Appendix: Technical details

- **Appendix A Convergence test**. A routine of ensuring the parameters for DFT calculations are the converged ones.

- **Appendix B Numerical tests of Equation of State**. Numerical tests on the Equation of States (EOS) models. The tests include the amount of volume change, the number of data points and etc..

- **Appendix C Calculating elastic constants from energy-strain curves**. Numerical tests on the calculation of the elastic constants from the energy-strain curves. The tests include the order of the fitting function, the amount of the applied strain and etc..

- **Appendix D Calculation setup**. Calculation setup based on the tests in Appendix A, B, and C.

Chapter 2

Fundamentals of solid solution strengthening

2.1 Experimental observation of solid solution strengthening

The term "solid solution strengthening" is used throughout this thesis instead of "solid solution hardening", because "hardening" is sometimes related to the knowledge of the whole flow stress curve in which the strain hardening comes into play. In this thesis, it is only focused on the change in the critical resolved shear stress (CRSS) or the yield stress. The interplay of the solid solution strengthening and the strain hardening can be referred to the reviews of Kocks (1979, 1985).

2.1.1 fcc solid solutions

A typical temperature dependence of the CRSS of fcc solid solutions is shown in Figure 2.1 (Caillard and Martin, 2003). Table 2.1 lists the fcc solid solutions which have similar temperature dependence. This dependence seems to apply to all the fcc solid solutions. The important feature is except at elevated temperatures (temperature regime 4 in Figure 2.1) the strengthening phenomenon always prevails.
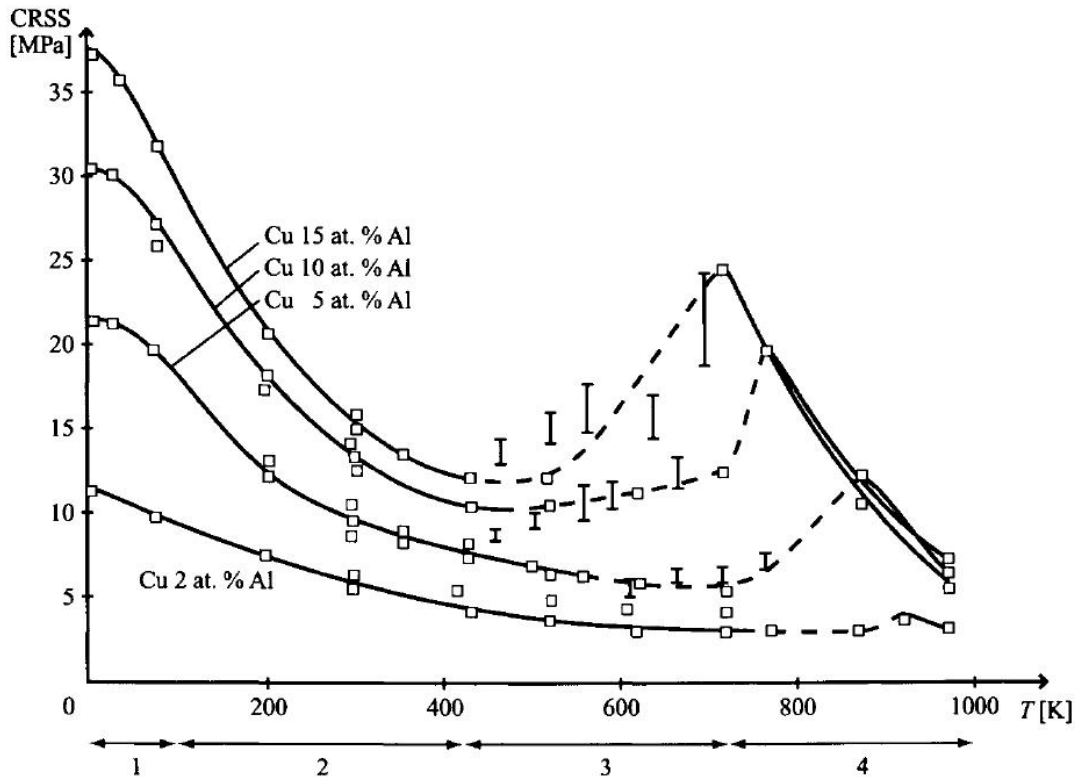
Figure 2.1: Temperature dependence of the critical resolved shear stress (CRSS) of Cu-Al solid solutions (Caillard and Martin, 2003). 4 temperature regimes: (1) underdamping; (2) overdamping; (3) dynamic strain ageing and Portevin-LeChatelier effect; (4) dislocation dragged by the solute atmosphere.

Table 2.1: fcc solid solutions with similar temperature dependence of CRSS or yield stress as in Figure 2.1

Alloy	Reference	Alloy	Reference
fcc substitutional solid solutions			
Cu-Ge	Haasen and King (1960)	Cu-Ga	Haasen and King (1960)
	Kostorz and Haasen (1969)		Kostorz and Haasen (1969)
	Gastberger et al. (1974a)		Gastberger et al. (1974a)
	Monchoux and Neuhäuser (1987)	Cu-Sn	Vöhringer and Macherauch (1967)
Cu-As	Gastberger et al. (1974b)	Cu-In	
Cu-Mn	Nagata and Yoshida (1972)	Cu-Zn	Mitchell and Thornton (1963)
	Wille et al. (1982)		Ghauri et al. (1986)
	Wille et al. (1987)		Köster and Speidel (1965)
	Butt et al. (1990)	Cu-Ni-Zn	Köster and Speidel (1965)
	Kalk and Schwink (1995)	Cu-Fe	Wendt and Wagner (1982)
	Shevakin and Tsypin (1997)		
Ag-Al	Hendrickson and Fine (1961)	Ag-Zn	Tardiff and Hendrickson (1964)
	Butt et al. (1983)		Butt et al. (1983)
Au-Ag	Kloske and Fine (1969)	Au-Zn	Jax et al. (1970)
		Au-In	
Ni-Cr	Akhtar and Teghtsoonian (1971)		
	Roth et al. (1997)		
fcc interstitial solid solutions			
Ni-C	Nakada and Keh (1971)	Th-C	Peterson and Skaggs (1968)
		Th-N	Peterson and Mclachlan (1975)

2.1.2 bcc solid solutions

Figure 2.2 shows the change in the yield stress of various Fe-base alloys. The remarkable phenomenon is that below a certain temperature (~250 K), most of the alloy additions lower the yield stress, and above this temperature, the strengthening effect can be observed. Some elements, such as Cr and Co, however, do not cause any softening (up to 6 at. %) (Leslie, 1972). The softening behavior is observed in many bcc substitutional and interstitial solid solutions alloys (Pink and Arsenault, 1980). It is believed that the softening effect at low temperature is because of the promotion of the kink-pair formation and migration by the solute atoms.

This aspect has been studied by first-principles calculations (Trinkle and Woodward, 2005; Medvedeva et al., 2005, 2007).
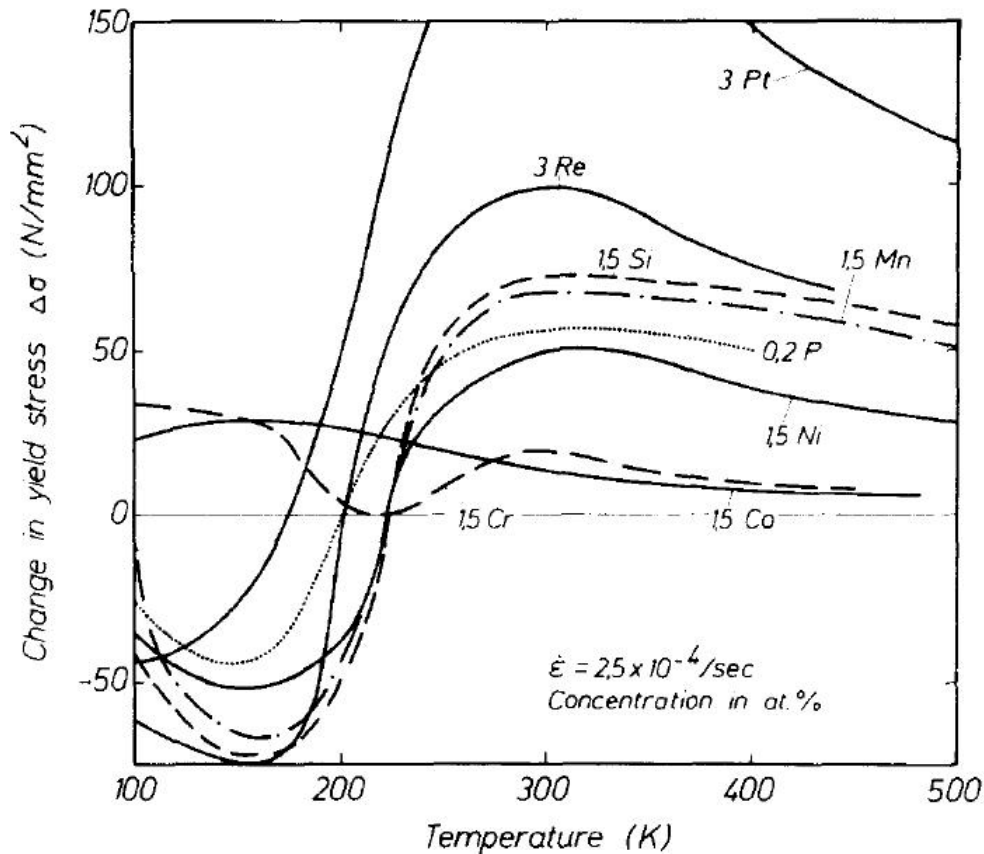
Figure 2.2: Temperature dependence of the change in yield stress of Fe-base alloys (Pink and Arsenault, 1980).

2.1.3 hcp solid solutions

The effect of the solute elements on the strength of hcp metals is even more complex. Taking Mg solid solutions as an example, the strengthening effect is always observed on the basal slip (Akhtar and Teghtsoonian, 1972). Also the temperature dependence of CRSS is the same to fcc solid solutions. However, the softening effect occurs on prismatic and pyramidal plane. An example is shown in Figure 2.3. In Figure 2.3, Li only causes strengthening on basal plane. On prismatic and pyramidal plane, the softening phenomenon can be observed even up to relatively high temperature (~450K on prismatic and >300K on pyramidal). This softening effect is very important for the ductility of Mg alloys, because it provides additional deformation modes (Agnew et al., 2001).
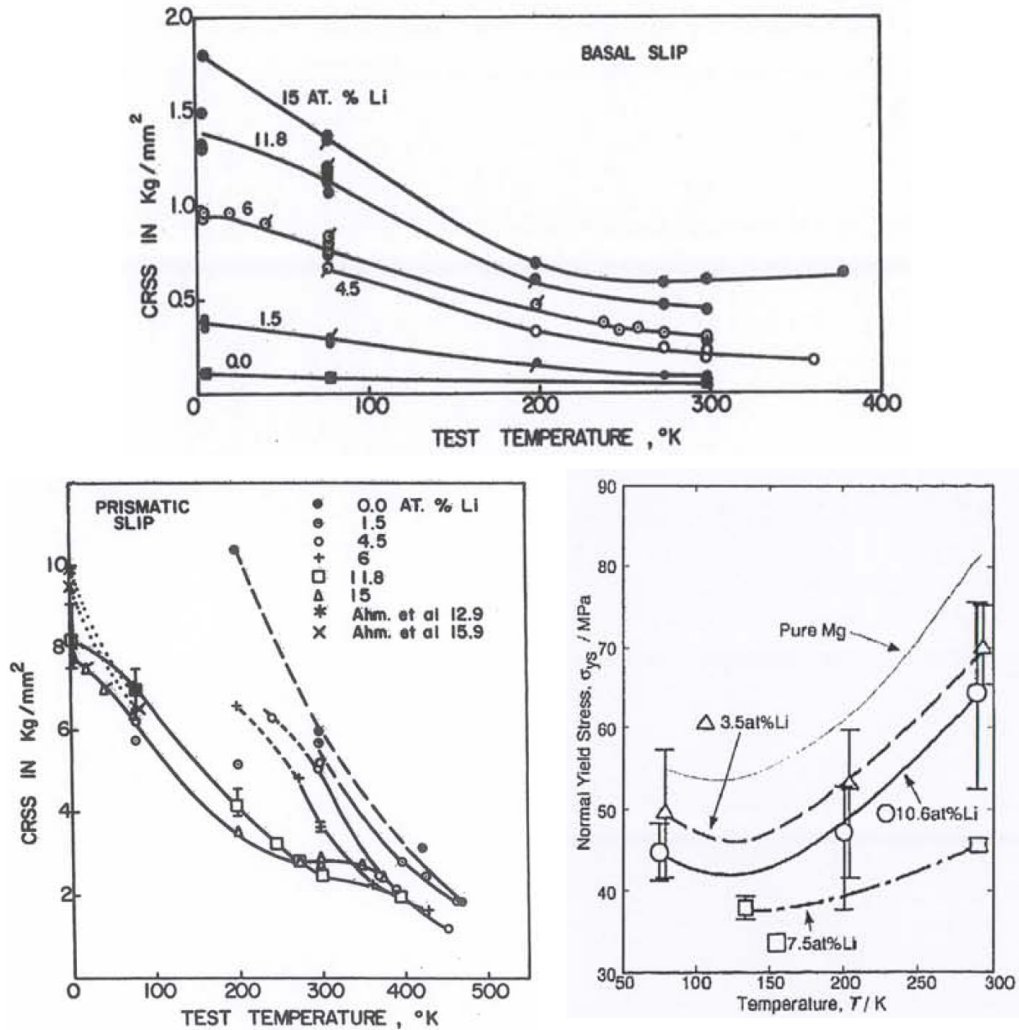
Figure 2.3: Temperature dependence of CRSS or yield stress of Mg-Li on basal (top), prismatic (bottom left) (Urakami et al., 1970), and pyramidal plane (bottom right) (Ando and Tonda, 2000).

2.2 Theoretical models of solid solution strengthening

There are four elementary interactions between the solute atoms and the dislocations : (1) the elastic effect; (2) the chemical effect; (3) the electrostatic effect; (4) the short range ordering. The detailed description and derivation of those elementary interactions can be found in the reviews of Fiore and Bauer (1968); Bullough and Newman (1970); Haasen (1979, 1996); Suzuki (1979), and Mohri and Suzuki (1999).

2.2.1 Elastic effect

Based on the continuum linear elasticity theory, there are three measures of the strengthening effect:

1. The volume change or lattice distortion: δ_b (Mott and Nabarro, 1940; Cottrell, 1948).
   In substitutional fcc and bcc solid solutions, the solute atom can be considered as a dilatation center in a continuum matrix. The elastic energy caused by this spherical distortion in a stress field of a dislocation is:

$$\Delta E^p = p \Delta V \tag{2.1}$$

$$p = -\frac{1}{3}(\sigma_{xx}^{dis} + \sigma_{yy}^{dis} + \sigma_{zz}^{dis}) \tag{2.2}$$

$$\Delta V = 4\pi\delta_b r_0^3 \tag{2.3}$$

$$\delta_b = \frac{1}{a_0}\frac{\delta a}{\delta c} \tag{2.4}$$

The general expression of such an interaction is:

$$\Delta E^p = V_0 \epsilon_{ij}^{sol} \sigma_{ij}^{dis} \tag{2.5}$$

where ϵ_{ij}^{sol} is the strain field caused by the solute atom. This interaction energy is usually termed as par-elastic or the first-order elastic effect.

2. Elastic dipole or the strength of the defect: P_{ij} (Eshelby, 1956; Bacon et al., 1980; Vannarat et al., 2001).
   Equation (2.5) can be rewritten as:

$$\Delta E^p = V_0 \sigma_{ij}^{sol} \epsilon_{ij}^{dis} \tag{2.6}$$

where σ_{ij}^{sol} is the stress field caused by the solute atom, and ϵ_{ij}^{dis} is the strain field caused by the dislocation. The elastic dipole P_{ij} is:

$$P_{ij} = \sigma_{ij}^{sol} V \tag{2.7}$$

In practical first-principles or atomistic calculations, the elastic dipole is evaluated in the following way (Clouet et al., 2008; Hanlumyuang et al., 2010): (1) put a single defect into a simulation box; (2) deactivate the external relaxation and activate the internal relaxation; (3) the stress developed in the supercell enters Equation (2.7) together with the volume of the simulation box. In the substitutional solid solutions of fcc and bcc metals, the stress evaluated by the aforementioned procedure should be the hydrostatic pressure. Thus, the stress in Equation (2.7) can be replaced by the pressure formulated by a certain model of equation of state (see Section 3.2):

$$P = p_{\left(B_0, B_0', V_{0,alloy}, V\right)} V \tag{2.8}$$

3. Empirical measure of the volume change and the modulus change: ϵ_L (Fleischer, 1961, 1963).

   Additional to the contribution from the lattice distortion, there should be another contribution from the local modulus change around the solute atom (Fleischer, 1961, 1963). This contribution is termed as di-elastic or the second-order elastic effect. The strengthening is characterized by a single parameter (Labusch, 1970):

$$\epsilon_L = (\alpha^2 \delta_b^2 + \eta_G^2)^{1/2} \tag{2.9}$$

$$\eta_G = \frac{1}{G_0} \frac{\delta G}{\delta c} \tag{2.10}$$

   where α=16 for the edge dislocation and 3 for the screw dislocation. There are other expressions different from Equation (2.9) (Fleischer, 1963; Labusch, 1970; Gypen and Deruyttere, 1981) and Equation (2.10) (Fleischer, 1963; Saxl, 1964; Takeuchi, 1968; Gypen and Deruyttere, 1981). The strengthening effect evaluated by different expressions turns out to be the same (Kratochvíl and Neradová, 1971; Mishima et al., 1986).

The above measures are derived from the continuum linear elasticity theory. It is sometimes questionable for the application of this theory in describing the dislocations in a discrete media. In general, there are three problems:

1. Stress singularity at the dislocation core region.

   The problem is widely recognized. The atomistic simulations, however, indicates that if only the positions where the atoms actually sit are considered, this problem can be solved naturally (Clouet, 2006; Clouet et al., 2008; Liu et al., 2008). In order to eliminate the singularity, Cai et al proposed an idea in the form of a spreading function characterized by a single parameter a (Cai et al., 2006). The parameter a can be calibrated by fitting the stress data from the atomistic simulations. Another method is to use non-local elasticity theory (Eringen, 2002). To be precise, the stress singularity at the dislocation core only

exists in the Volterra dislocation, but it doesn't exist in the Peierls-Nabarro dislocation (Peierls, 1940; Nabarro, 1947; Schoeck, 2005).

2. Dislocation dissociation.

   If the dissociation of the dislocation is not considered, there is a great discrepancy in the solute-dislocation binding energy between the prediction of the elasticity theory and atomistic simulation (Olmsted et al., 2006). On the other hand, if the dissociation is considered, a much better agreement can be achieved (Clouet, 2006; Liu et al., 2008). Even though, the stress field or the binding energy in the stacking fault ribbon treated by the elasticity theory is not physically justified, because in the region, the crystal symmetry is changed, consequently so is the atomic potential.

3. Nonlinear effects.

   The binding energy on the compressed and expanded sides of an edge dislocation is asymmetric, namely the maximum binding energies on the compressed and expanded sides are different shown by atomistic simulations (Yasi et al., 2010; Leyson et al., 2010; Clouet, 2006). In linear elasticity description, they are symmetric. This discrepancy might be caused by the absent consideration of the non-linear effect in the linear elasticity. The non-linear effects consist of two aspects: the volume dependence (Takeuchi, 1968; Birch, 1947) and the higher order effect (Stehle and Seeger, 1956; Seeger, 1957; Seeger and Haasen, 1958). The nonlinear elasticity description of the dislocations is, however, mathematically cumbersome, and simple solutions are usually not feasible (Zubov, 2001).

2.2.2 Chemical effect

The dislocations usually dissociate into partials. In fcc for example, the stacking fault ribbon between two Schokley partials is a few layers of atoms in hcp structure. Some solute atoms tend to segregate into the stacking fault ribbon, if the solubility of the solute elements in the matrix is lower than that in the stacking fault. The segregation leads to an enrichment of the solute atoms in the stacking fault ribbon between the partials (Suzuki, 1952, 1983).

Suppose the concentration of the solute is c and c_f in the matrix and the stacking fault, respectively. The extra shear stress $\tau_{chemical}$ required to move the solute enriched dislocation is (Flinn, 1958, 1962):

$$\Delta\tau_{chemical} = \frac{1}{b}\frac{\partial\gamma}{\partial c_f}(c_f - c) \tag{2.11}$$

where γ is the stacking fault energy and b is the Burger's vector.

2.2.3 Electrostatic effect

In the strain field of an edge dislocation, the electrons flow from the compressed side to the expanded side, which results in an electrostatic dipole. The solute atoms have different number

of the valence electrons which also results in an electrostatic field around them. Those two electrostatic fields interact with each other (Fiore and Bauer, 1968).

The early investigations showed that the electrostatic effect energy is only 1/5 of the elastic effect energy which might be ignored (Cottrell et al., 1953; Friedel, 1964). However, the later study by Sugiyama suggested that the electrostatic energy might be as 1 to 4 times as the elastic one (Sugiyama, 1966). Unfortunately, this aspect is still inadequately treated.

It is worth mentioning that it is claimed this effect is of great importance in Ni solid solutions because of the d-d hopping interaction of the solute elements and Ni (Mishima et al., 1986; Shinoda et al., 1987). This conclusion was later invalidated by conducting more careful experiments (Choi et al., 1990) and including the atomic relaxation in the tight-binding calculations (Shinoda et al., 1990b).

2.2.4   Short range ordering (SRO)

The solute atoms are rarely randomly or homogeneously distributed in the matrix. Especially in the stress field of the dislocations, short range ordering (SRO) might occur. The interaction between the dislocations and SRO is more like the super dislocation mechanism in intermetallics. When one dislocation passes the SRO by cutting, the next moving dislocation on the same slip plane is exerted much less force (Fisher, 1954; Flinn, 1958, 1962).

2.3 Statistical treatment

In order to obtain the average force of a collection of solute atoms exerted on a dislocation, the the interaction between a single solute atom and a single dislocation should be treated by a statistical model. The average interaction between the solute atoms and the dislocation can be expressed in following form:

$$\Delta\tau_c = A\epsilon^n c^m \begin{cases} \text{n=3/2, m=1/2, Friedel-Fleischer limit (Friedel, 1964; Fleischer, 1964)} \\ \text{n=4/3, m=2/3, Mott-Labusch limit (Labusch, 1970, 1972)} \end{cases}$$

(2.12)

where $\Delta\tau_c$ is the increase in CRSS; A is a constant. ϵ is the strengthening parameter; and c is the atomic fraction of the solute atoms. The applicability of the those two limits in Equation (2.12) depends on a dimensionless parameter (Labusch, 1970; Haasen, 1979, 1996):

$$\beta = \frac{w}{l_s} \cdot \left(\frac{2T}{f_{max}}\right)^{1/2} = \frac{\sqrt{c}}{b} \cdot w \cdot \left(\frac{2T}{f_{max}}\right)^{1/2}$$

(2.13)

Friedel-Fleischer limit, $\beta \ll 1$,   dilute but strong and localized obstacles.
Mott-Labusch limit, $\beta > 1$,   concentrated but weak and diffused obstacles.

where l_s is the solute atom spacing; w is the interaction range; T is the line tension of the dislocation, $T = \frac{1}{2}Gb^2$; f_{max} is the maximum elementary interaction force.

Those two limits can be better illustrated in Figure 2.4 (Nabarro, 1977). In Friedel-Fleischer limit, when the dislocation breaks from B to D (Figure 2.4(a)), no motion of the dislocation outside A and C. In Mott-Labusch limit (Figure 2.4(b)), when the same scenario occurs, the motion of the dislocation occurs outside A and C over many obstacles. However, which limit should be applied is defined in a very ambiguous way, and there is a gap between $\beta \ll 1$ and $\beta > 1$, which means in real experiments any scaling of the concentration c is possible.

Besides those two statistical models, other models were also proposed, see Riddhagni and Asimow (1968); Nabarro (1977); Gypen and Deruyttere (1977a,b); Zaiser (2002).
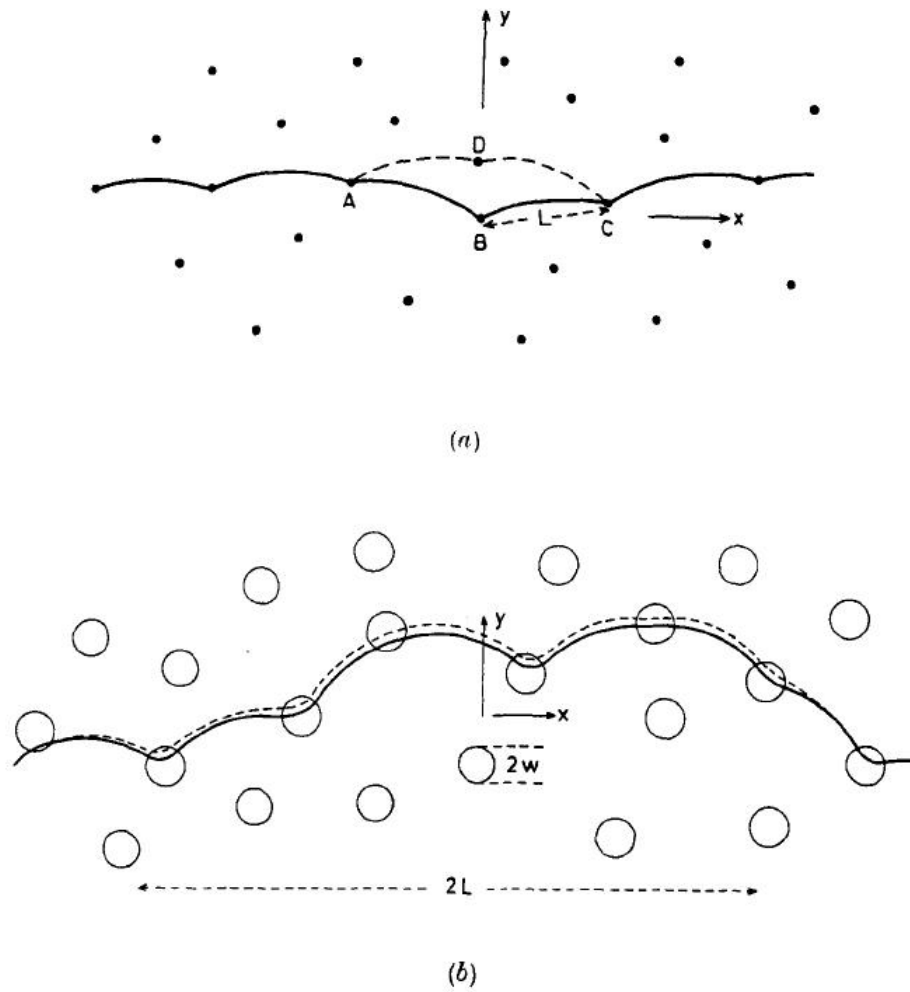
Figure 2.4: Illustration of (a) Friedel-Fleischer limit (b) Mott-Labusch limit. In Friedel-Fleischer limit, when the dislocation breaks from *B* to *D*, no motion of the dislocation outside *A* and *C*. In Mott-Labusch limit, when the same scenario occurs, the motion of the dislocation occurs outside *A* and *C* over many obstacles (Nabarro, 1977)

2.4 Difficulties in experiments and alternatives

Regarding the experiments in measuring solid solution strengthening, Haasen (Haasen, 1979) pointed out the difficulties simple mechanical tests: (1) the heterogeneous deformation; (2) the mobility of the solute atoms (the serration flow and Portevin-LeChatelier effect); (3) the influence of the solute alloying on the the dislocation structure (different grown-in dislocation densities). All of them lead to the uncertainties of the measurements of the CRSS or the yield stress as well as the subsequent interpretations.

Alternatively, the binding energy of the dislocation and the solute atoms can be measured by the internal friction (IF) measurements (Granato and Lücke, 1956; Fiore and Bauer, 1964, 1968; Kosugi and Kino, 1993). Ide et al. also proposed a method of determining the flow stress at the strain at the magnitude of 10^{-9} from the amplitude dependent internal friction (ADIF) measurements (Ide et al., 1999). The method of IF is, however, an indirect way of studying the micro-plasticity, and ADIF is extremely sensitive to the microstructure (Blanter et al., 2010). The interpretation requires considerable expertise and caution.

2.5 Electronic correlations of the solid solution strengthening

e/a ratio (electron-atom ratio) and difference in valency

Allen et al. showed that with approximately the same e/a ratio the stress-strain curves of Cu-Zn, Cu-Ga, Cu-Ge, and Cu-As solid solutions nearly superimpose (Allen et al., 1951). Hibbard conducted the experiments in Cu-Ge, Cu-Ga, Cu-Al, and Cu-Zn which have nearly the same grain size and the lattice parameters, and the yield stress correlates very well with the e/a ratio (Hibbard, 1958).

Kratochvil correlated the valency difference of the solute and the solvent elements and the strength of the solid solutions, and concluded that the more difference in valency the more strengthening effect (with exceptions) (Kratochvil, 1970).

Electric conductivity and solubility

Collings proposed that if the electronic perturbation by the solute element is large in the solid solutions, then the strengthening effect is "rapid" (Collings and Gegel, 1973; Collings, 1975). This perturbation can be characterized by the electric conductivity or solubility of the solute elements. And those two properties can be correlated with the strengthening effects of the solute elements (Nakagawa and Hirano, 1968; Shinoda et al., 1990a; Nagarjuna et al., 1999).

Chapter 3

Theoretical methods used in this thesis

3.1 Density Functional Theory (DFT)

Density functional theory (DFT) is a quantum mechanical calculation method, studying the groundstate properties of the matters. Instead of solving Schrödinger equation, the problem lies in DFT is to solve the Kohn-Sham equation on the basis of Hohenberg-Kohn theorem. In this section, the key elements of DFT are briefly outlined along with major technical issues, such as the exchange-correlation functionals and the accuracy and efficiency related parameters.

3.1.1 General formulation of DFT

The core of DFT consists of two key elements: the Hohenberg-Kohn theorem and the Kohn-Sham equation. One offers the possibility, and another one realizes it.

Hohenberg-Kohn theorem (Hohenberg and Kohn, 1964)

The Hohenberg-Kohn theorem states that: the knowledge of the groundstate electron density $n(\mathbf{r})$ uniquely determines the external potential $V[n(\mathbf{r})]$. This also means $n(\mathbf{r})$ further uniquely determines the groundstate wavefunction $\Psi[n(\mathbf{r})]$ and the groundstate total energy $E[n(\mathbf{r})]$, as well as the other observables.

In non-relativistic Coulomb system, the Hohenberg-Kohn theorem can be reformulated into three important statements (Capelle, 2006):

1. The groundstate wave function can be uniquely expressed by the groundstate electron density ($n_0(\mathbf{r})$):

$$\Psi_0(\mathbf{r_1},\mathbf{r_2},...\mathbf{r_N}) = \Psi[n_0(\mathbf{r})] \tag{3.1}$$

2. The total energy consists of three contributions which are the functionals of the electron density:

$$E[n] = T[n] + U[n] + V[n] = F[n] + V[n] \tag{3.2}$$

where T is the kinetic energy; U is the electron-electron Coulombic repulsion; V is the external potential which is expressed as:

$$V[n] = \int n(\mathbf{r})v(\mathbf{r})d^3r \tag{3.3}$$

where $v(\mathbf{r})$ depends on the specific problem, and usually it is the nucleus-electron Coulombic attraction (in atomic units):

$$v(\mathbf{r}) = -\sum_{\alpha} \frac{Z_{\alpha}}{|\mathbf{r} - \mathbf{R}_{\alpha}|} \tag{3.4}$$

where Z_α is the nuclear charge of nucleus α. Since T and U are independent of $v(\mathbf{r})$, they are usually grouped as the universal functionals, F.

3. If the electron density is not the groundstate electron density, the total energy determined by this electron density is always greater than the groundstate total energy.
   This statement offers the possibility of using the variational principle to minimize the total energy to find the groundstate electron density. This problem is solved by the Kohn-Sham equation.

Kohn-Sham equation (Kohn and Sham, 1965)

The Kohn-Sham equation was adopted from Hartree-Fock (HF) theory. In HF theory, the exchange energy is explicitly treated by the Slater determinant, but the correlation energy is missing. The the universal functional F (in Equation (3.2)) can be rewritten as:

$$F = T + U = T_0 + E_C + V_H + E_X = T_0 + V_H + E_{XC} \tag{3.5}$$

where T_0 is the kinetic energy of a non-interacting system as in HF theory; E_C and E_X are the correlation and exchange energy respectively, and they are grouped as the exchange-correlation energy E_{XC}; V_H is the Hartree potential which is essentially the electron-electron Coulombic repulsion. Then the Kohn-Sham Hamiltonian can be constructed (in atomic units, $\widehat{}$ indicates operator):

$$\begin{aligned} \widehat{H}_{KS} &= \widehat{T}_0 + \widehat{V}_H + \widehat{V} + \widehat{E}_{XC} \\ &= -\frac{1}{2}\nabla^2 + \int \frac{n(\mathbf{r}')}{|\mathbf{r} - \mathbf{r}'|} d^3r + v(\mathbf{r}) + \widehat{E}_{XC} \end{aligned} \tag{3.6}$$

Then the Kohn-Sham equation is:

$$\widehat{H}_{KS}\phi_n(\mathbf{r}) = \epsilon_i \phi_n(\mathbf{r}) \tag{3.7}$$

And the electron density is:

$$n(\mathbf{r}) = \sum_n \langle \phi_n(\mathbf{r})|\phi_n(\mathbf{r})\rangle \tag{3.8}$$

Since Equation (3.7) and (3.8) are interlinked, the problem can be solved in a self-consistent manner:

1. generate a initial electron density, $n^0(\mathbf{r})$.

2. use $n^0(\mathbf{r})$ to calculate V_H, V, and E_{XC}.

3. put V_H, V, and E_{XC} into the Kohn-Sham equation, solve it, and obtain wavefunction $\phi_n^0(\mathbf{r})$

4. use the wavefunction $\phi_n^0(\mathbf{r})$ to calculate electron density, $n^1(\mathbf{r})$.

5. compare newly obtained electron density ($n^1(\mathbf{r})$) with the initial guess ($n^0(\mathbf{r})$). If the difference between them is within a certain tolerance, then stop the calculation. The obtain electron density $n^1(\mathbf{r})$ is the groundstate electron density. Otherwise go back to step **2** using $n^1(\mathbf{r})$ as the input, until the convergence criterion is fulfilled.

After the groundstate electron density is obtained, the total energy is also obtained naturally:

$$E = -\sum_i^{occupied} \int \phi_i^*(\mathbf{r})\frac{\nabla^2}{2}\phi_i(\mathbf{r})d^3r + \frac{1}{2}\int\int \frac{n(\mathbf{r})n(\mathbf{r}')}{|\mathbf{r}-\mathbf{r}'|}d^3r d^3r' + \int n(\mathbf{r})v(\mathbf{r})d^3r + E_{XC} \quad (3.9)$$

The total energy of a electron-ion system should also include the ion-ion Coulombic repulsion. According to the Born-Oppenheimer approximation, the kinetic energy of the ions can be considered to be zero, and the ion-ion Coulombic repulsion is a constant:

$$E_{nn} = \sum_{\alpha,\beta} \frac{Z_\alpha Z_\beta}{|\mathbf{R}_\alpha - \mathbf{R}_\beta|} \quad (3.10)$$

For a many-electron system, the number of the variables in the Kohn-Sham equation is much lower than in the Schrödinger equation. Essentially the Kohn-Sham equation is a single electron Schrödinger equation. In the Kohn-Sham equation, the single electron is only a mathematical quantity, and it has no direct physical meaning. Only the final convergent result, the groundstate electron density has direct physical meaning.

3.1.2 Exchange-correlation functional

HEAVEN OF CHEMICAL ACCURACY
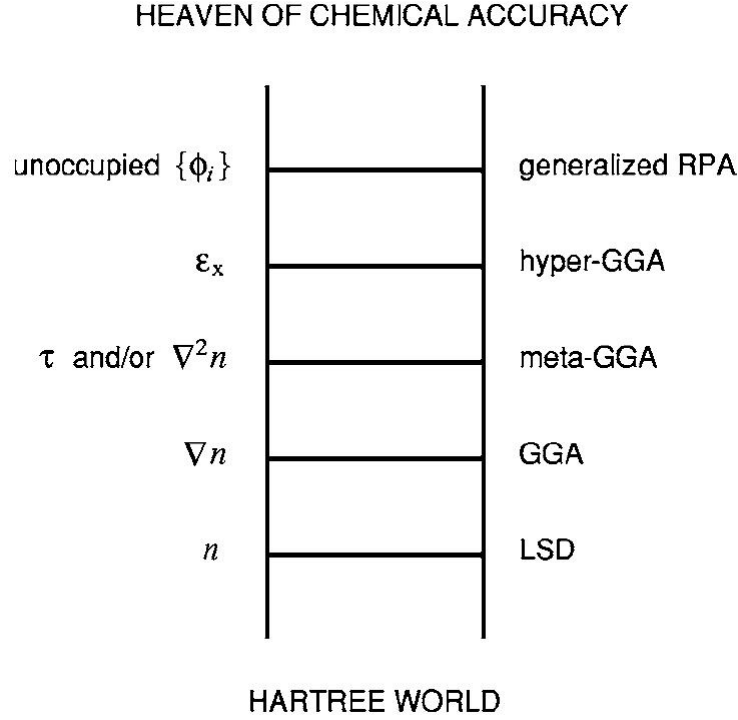
Figure 3.1: Jacob's ladder of exchange-correlation energy approximations in DFT (Perdew et al., 2005) (Note: LSD (local spin density) on the first rung of the ladder is a general description of LDA, LSD takes the spin directions into account)

In Equation (3.6) of the Kohn-Sham Hamiltonian, the exact form of the exchange-correlation functional (E_{XC}) is not known except for the homogeneous electron gas. Thus, a certain approximation has to be made to make the application of DFT possible. The current exchange-correlation functionals include LDA (local density approximation), GGA (generalized gradient approximation), and etc. (see Figure 3.1). The ladder rungs are arranged according to the information included in determining E_{XC}. The more information included, the higher rung is. Among them, LDA and GGA are currently widely used.

LDA (local density approximation)

LDA is the first rung of Jacob's ladder of the exchange-correlation functional. The exchange-correlation functional takes the following form:

$$E_{XC}^{LDA} = \int n(\mathbf{r})\epsilon_{XC}(n(\mathbf{r}))d^3r, \quad \widehat{E_{XC}^{LDA}} = \epsilon_{XC}(n(\mathbf{r})) \tag{3.11}$$

where $\epsilon_{XC}(n)$ is the exchange-correlation energy function (not functional!) of the homogeneous electron gas. The total energy of the homogeneous electron gas can be calculated numerically

by quantum Monte Carlo (Ceperley and Alder, 1980). $\epsilon_{XC}(n)$ can be obtained by subtracting the non-interaction kinetic energy (T_0) and the Hartree potential (V_H) from the total energy. $\epsilon_{XC}(n)$ should be tabulated (Ceperley and Alder, 1980) or parameterized (Perdew and Zunger, 1981; Perdew and Wang, 1992) for a series electron densities beforehand. In the calculation, the system is imagined to be divided into infinitesimally small volumes, and each infinitesimally small volume can be approximated as a volume filled with the homogeneous electron gas. Equation (3.11) is applied to each of the infinitesimal volume.

GGA (generalized gradient approximation)

The second rung of Jacob's ladder of the exchange-correlation functional is GGA (Perdew and Yue, 1986). The general form of GGA is:

$$E_{XC}^{GGA} = \int f(n(\mathbf{r}), \nabla n(\mathbf{r})) d^3 r \tag{3.12}$$

Besides the local electron density, in GGA, the local electron density gradient is also taken into account. Since there is no unique way of incorporating the electron density gradient in the expression of the exchange-correlation functionals, there are different versions of GGA. At the moment in the field of physics, the most widely used one is PBE[1] (Perdew et al., 1996), and GGA is also claimed to perform better than LDA (Ziesche et al., 1998), specifically e.g. for 3d metals, such as Fe.

Assessment of LDA and PBE

The performance of the LDA and PBE (both are widely used) in solids has been thoroughly investigated. Some of the assessments are summarized as the following:

1. Lattice parameter
   In general, LDA predicts smaller lattice parameters, and PBE larger (Kurth et al., 1999; Staroverov et al., 2004; Ropo et al., 2008; Csonka et al., 2009; Haas et al., 2009, 2010). In comparison with the experiments, the relative error of LDA is $-5\% \sim 0.2\%$, and PBE is $-0.8\% \sim 3\%$ (Haas et al., 2009, 2010).

2. Bulk modulus
   In general, too stiff by LDA and too soft by PBE (Kurth et al., 1999; Staroverov et al., 2004; Ropo et al., 2008; Csonka et al., 2009). According to these assessments, the relative error from experiments is $-10\% \sim 40\%$ for LDA, and $-22\% \sim 17\%$ for PBE. Of course, the measurement of the bulk modulus might not be as precise as the lattice parameters, thus uncertainties in the measured bulk moduli might also make the relative error larger.

---

[1]PBE denotes the GGA functional proposed by Perdew, Burke and Ernzerhof (Perdew et al., 1996), and there are variations of PBE (see Pedroza et al. (2009))

3. Vacancy

   the study of the formation energy of the vacancy in Al, Cu and Ni indicates that LDA is the most reliable one (Delczeg et al., 2009).

4. Phonon spectrum

   The study of the phonon spectra of a series pure fcc metals indicates that the experimental measurements lie between the predictions by LDA and PBE, and consequently so do the measured heat capacity and thermal expansion (Grabowski et al., 2007)[2].

It is worth mentioning that there is a variant of PBE, called PBEsol (Perdew et al., 2008). The prediction of the lattice parameters and the bulk modulus by PBEsol lies between the predictions by LDA and PBE. And the relative error is $-2.5\% \sim 1.5\%$ for the lattice parameters, and $-17\% \sim 24\%$ for the bulk moduli (Ropo et al., 2008; Csonka et al., 2009; Haas et al., 2009; Pedroza et al., 2009; Haas et al., 2010).

3.1.3 Accuracy and efficiency in DFT calculations

In DFT calculation, the compromise should be made between the accuracy and the efficiency. The main parameters which are related to this issue are the cut-off energy, the k-point sampling, the σ value, and the pseudopotential.

3.1.3.1 Cut-off energy

According to the Bloch's theorem, the Kohn-Sham wavefunction, $\phi_{\mathbf{k},i}(\mathbf{r})$ solved from the Kohn-Sham equation (Equation (3.7)) can by expanded by the plane waves:

$$\phi_{\mathbf{k},n}(\mathbf{r}) = \sum_{\mathbf{G}} c_{\mathbf{k},n}(\mathbf{G})\, e^{i(\mathbf{G}+\mathbf{k})\cdot\mathbf{r}} \tag{3.13}$$

where $\mathbf{k}$ is the wave vector, and $\mathbf{G}$ are the reciprocal lattice vectors. Thus, the wavefunction should be evaluated at certain number of $\mathbf{k}$ in the Brillouin zone (see next section) involving an infinite number of possible $\mathbf{G}$. In practice, the infinite sum is truncated by specifying a cut-off length G_{cutoff}:

$$\phi_{\mathbf{k},i}(\mathbf{r}) = \sum_{|\mathbf{G}+\mathbf{k}|<G_{\text{cutoff}}} c_{\mathbf{k},i}(\mathbf{G})\, e^{i(\mathbf{G}+\mathbf{k})\cdot\mathbf{r}} \tag{3.14}$$

The cut-off length is usually characterized by the cut-off energy:

$$E_{\text{cutoff}} = \frac{h}{2m}G_{cut}^2 \tag{3.15}$$

---

[2]In Grabowski et al. (2007), Al and Au do not behave like the other studied fcc pure metals. In case of Al, The deviation of the thermal capacity and the heat capacity from the experiments at elevated temperatures is due to the vacancy (Grabowski et al., 2009). In case of Au the difference is caused by lack of description of the van der Waals force both in LDA and PBE.

As can be recognized in Equation (3.14), G_{cutoff} determines how good the Kohn-Sham wavefunction is described by the plane waves. Therefore, G_{cutoff} should be large enough to achieve a certain precision. On the other hand, if G_{cutoff} is too large, then it becomes computationally expensive.

3.1.3.2 k-point sampling

As mentioned in the previous section, the Kohn-Sham wavefunction should be evaluated at a certain number of $\mathbf{k}$ in the Brillouin zone. After the wavefunction is expanded by the plane waves, the electron density can be written as:

$$n(\mathbf{r}) = \sum_{\mathbf{k},n} \sum_{\mathbf{G},\mathbf{G}'} c_{\mathbf{k},n}^{*}\left(\mathbf{G}'\right) c_{\mathbf{k},n}\left(\mathbf{G}\right) e^{i(\mathbf{G}-\mathbf{G}')\cdot\mathbf{r}} \tag{3.16}$$

If Equation (3.16) is used to evaluate different energy contributions in Equation (3.9), they may take a general form:

$$f = \frac{\Omega}{(2\pi)^3} \int_{BZ} f\left(\mathbf{k}\right) d\mathbf{k} \tag{3.17}$$

where Ω is the volume of the cell, BZ is short for Brillouin zone, and f is a certain quantity, such as the kinetic energy, and the other potentials[3].

In DFT calculations, the integral in Equation (3.17) is usually evaluated on a discrete set of k-points (Monkhorst and Pack, 1976):

$$f = \frac{\Omega}{(2\pi)^3} \sum_{\mathbf{k}} \omega_{\mathbf{k}} f\left(\mathbf{k}\right) \tag{3.18}$$

where $\omega_{\mathbf{k}}$ is the weight of the k-point. Therefore, it is necessary to have enough k-points sampled in the Brillouin zone so that the energetics can be calculated with enough precision. On the other hand, the integral over the Brillouin zone takes much of the computational effort in DFT. Thus, if the k-point sampling in the Brillouin zone is too dense, the calculation would be lengthy.

3.1.3.3 Fermi surface smearing

In metals, the energy band is partially filled. The integral of a function over the partially filled Brillouin zone is:

$$f = \frac{\Omega}{(2\pi)^3} \sum_{\mathbf{k}} \theta\left(\epsilon_{\mathbf{k}} - \epsilon_F\right) \omega_{\mathbf{k}} f\left(\mathbf{k}\right) \begin{cases} \theta\left(\epsilon_{\mathbf{k}} - \epsilon_F\right) = 1 & \text{if } \epsilon_{\mathbf{k}} < \epsilon_F \\ \theta\left(\epsilon_{\mathbf{k}} - \epsilon_F\right) = 0 & \text{if } \epsilon_{\mathbf{k}} > \epsilon_F \end{cases} \tag{3.19}$$

---

[3]In most of the DFT calculations, the Hartree potential, the external potential, and the ion-ion Coulombic repulsion are not calculated separately, but grouped together in order to avoid the divergence (Nogueira et al., 2003).

where ϵ_F is the Fermi-level, $\theta(\epsilon_\mathbf{k} - \epsilon_F)$ is the Dirac step function. $\epsilon_\mathbf{k} < \epsilon_F$ the band is occupied, and $\epsilon_\mathbf{k} > \epsilon_F$ empty. Because of the partial occupancy of the energy band, any function $f(\mathbf{k})$ is discontinuous at the Fermi-level so that a very dense k-point sampling in the Brillouin zone is necessary. In order to avoid a very dense k-point sampling, the Dirac step function needs to be replaced by a smooth function, but without losing any physical significance. Replacing the Dirac step function by a smooth function is called the Fermi surface smearing.

Methfessel-Paxton smearing   Among ever proposed smearing methods, Methfessel-Paxton smearing method is the most widely used smearing method for metals (Methfessel and Paxton, 1989). The idea is to expand the Dirac step function in a set of orthogonal functions, replacing $\theta(\epsilon_\mathbf{k} - \epsilon_F)$ by $\theta_N(x)$:

$$\theta_N(x) = \theta_0(x) + \sum_{n=1}^{N} A_n H_{2n-1}(x) e^{-x^2}, \text{ where } x = \frac{\epsilon_\mathbf{k} - \epsilon_F}{\sigma} \tag{3.20}$$

$$\theta_0(x) = \frac{1}{2}(1 - erf(x)) = \frac{1}{2}(1 - \frac{2}{\sqrt{\pi}}\int_x^\infty e^{-t^2}dt) \tag{3.21}$$

$$A_n = \frac{(-1)^n}{n!4^n\sqrt{\pi}} \tag{3.22}$$

$$H_n(x) = (-1)^n e^{x^2/2}\frac{d^n}{dx^n}e^{-x^2/2} \text{ (Hermite polynomials)} \tag{3.23}$$

The successive approximation to the step function $\theta_N(x)$ is shown in the left of Figure 3.2. Methfessel-Paxton smearing method is characterized by two parameters: σ and N (Equation (3.2)). σ value should be chosen very carefully. If it is small, Methfessel-Paxton smearing method will lose its essence which ends up with highly densed k-point sampling for convergence. If it is too large, the results might be wrong. N, of course, according to Figure 3.2, should be as large as possible, but it is shown that N=1 and N=2 give very similar results for Al shown in the right of Figure 3.2.
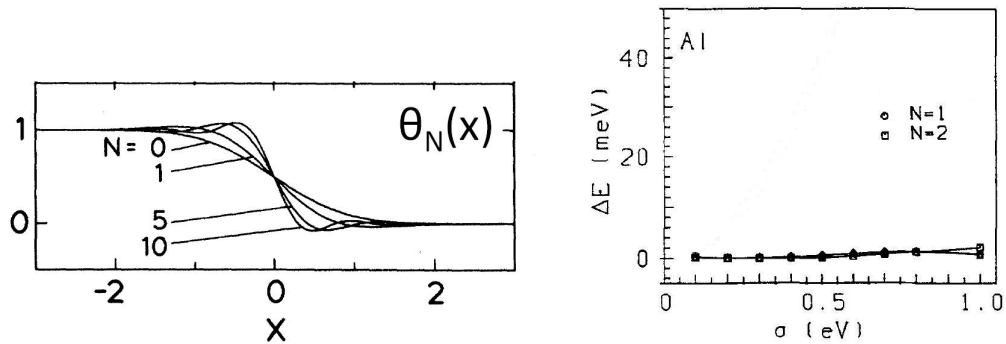

Figure 3.2: Left: successive approximation to the step function $\theta_N(x)$ (Methfessel and Paxton, 1989). Right: convergence of the free energy for Methfessel-Paxton smearing method (N=1, N=2) with respect to σ (Kresse and Furthmüller, 1996).

Fermi smearing   Fermi smearing is to replace $\theta\left(\epsilon_{\mathbf{k}} - \epsilon_F\right)$ by the Fermi-Dirac function:

$$\theta\left(\frac{\epsilon_{\mathbf{k}} - \epsilon_F}{\sigma}\right) = \frac{1}{e^{\frac{\epsilon_{\mathbf{k}} - \epsilon_F}{\sigma}} + 1} \tag{3.24}$$

This smearing includes the excitation of the electrons in the calculation, thus the final result is the one at a certain electronic temperature.

Tetrahedron method   In the tetrahedron method, the Brillouin zone is divided into small tetrahedra which fill the reciprocal space by using discrete k-points as shown in Figure 3.3. The function being integrated within each tetrahedron is determined by interpolation (linear or beyond). In this way, the integral can be done not only on the original discrete k-points but also the entire space (Blöchl et al., 1994).
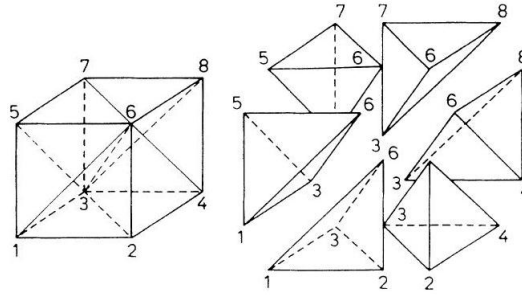

Figure 3.3: The reciprocal space is divided into small tetrahedron by using the discrete k-points (Blöchl et al., 1994)

3.1.3.4   Pseudopotential

The formulation in Section 3.1.1 is the formulation of the all-electron DFT calculation which involves all the electrons including the core and valence electrons. Such all-electron calculations usually are computationally expensive and not always necessary for the following two reasons: (1) the core electrons which are near the nucleus are associated with the wavefunctions which oscillate with short wave length in real space, and this kind of wavefunctions can be expanded into a large number of plane waves which in fact ends up with very high cut-off energy; (2) the important chemical or physical phenomena occur with the valence electrons, and the core electrons hardly participate. Based on these two reasons, the electron density of a chosen set of core electrons is replaced by a smooth density which should reproduce important physical properties of the real ion core. The replacement is illustrated in Figure 3.4.

There are two main issues of the pseudopotential: softness and transferability. Softness means the number of the plane waves needed when a pseudopotential is used. If only a few, then this pseudopotential is considered to be soft and the calculations are faster and less expensive, otherwise hard. If a pseudopotential can be used in any kinds of environments (atom, molecule,

cluster, solid, alloy, surface...), then this pseudopotential is called transferable.

At the moment, there are two kinds of widely used pseudopotentials: US-PP (ultrasoft-pseudopotential (Vanderbilt, 1990)) and PAW (projector augmented-wave) (Blöchl, 1994). The construction of US-PP needs a few empirical parameters, and PAW method is more physical based. According to the study of Kresse and Joubert (Kresse and Joubert, 1999), well-constructed US-PPs and the PAW method give identical results. More importantly, their results are also in good agreement with all-electron calculations.
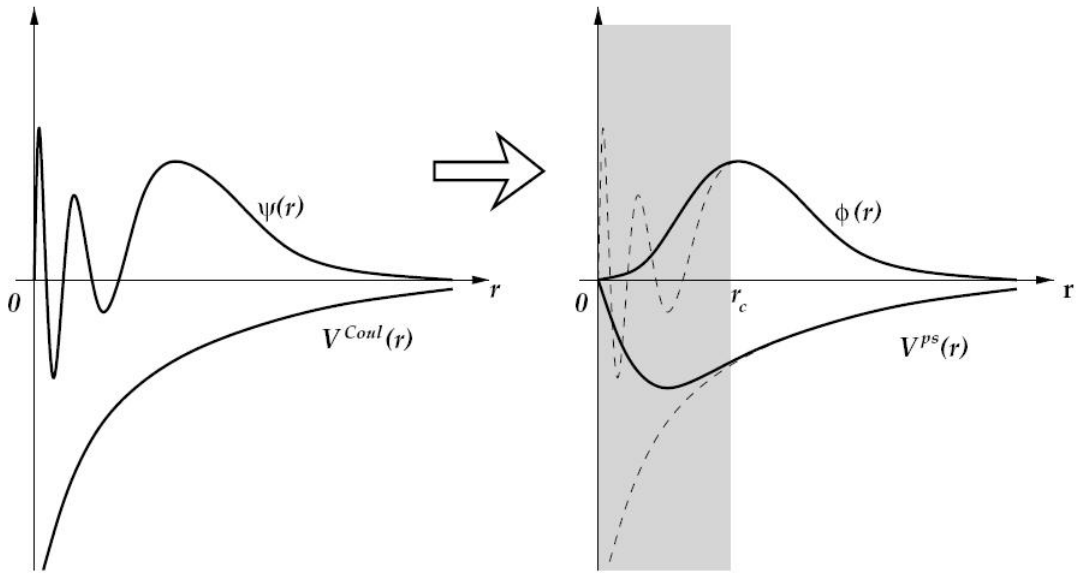

Figure 3.4: Schematics for explaining the replacement of the real valence wavefunction $\Psi(r)$ and the Coulomb potential $V^{Coul}(r)$ by the pseudo-wavefunction $\phi(r)$ and the pseudopotential $V^{ps}(r)$. Keep $\phi(r)$ close to $\Psi(r)$ outside r_c, and make $\phi(r)$ smooth inside r_c (Kaxiras, 2003).

3.2 Equation of States (EOS)

In this thesis, the EOS means the relation between the total energy and the volume of a solid body, and it is used to determine the equilibrium volume, the bulk modulus, and the equilibrium total energy. By using DFT, the total energies at a series of volumes are calculated. The calculated energy-volume curve is fitted by a EOS model. The aforementioned properties can be obtained from the fitting parameters.

To be precise, the EOS is the relation of the total energy and the applied hydrostatic pressure. Therefore, if the solid body does not have cubic crystal structure, the shape relaxation should be activated during the calculation in order to make sure the solid body is under a hydrostatic pressure.

There are a few models ever proposed (Stacey et al., 1981; Poirier, 2000). Among them, there are two widely used EOS: the Murnaghan EOS (Murnaghan, 1944), and the Birch-Murnaghan EOS (Murnaghan, 1937; Birch, 1938, 1947).

3.2.1 Murnaghan EOS

The basic assumption of the Murnaghan EOS is that the bulk modulus depends on the applied pressure. And it is characterized by a constant, the bulk modulus pressure derivative:

$$B' = -\left(\frac{\partial B}{\partial P}\right)_T \tag{3.25}$$

Then the bulk modulus is:

$$B = B_0 + B'P \tag{3.26}$$

$$B = -V\left(\frac{\partial P}{\partial V}\right)_T \tag{3.27}$$

where B_0 is the bulk modulus at zero pressure. Combining Equation (3.26) and Equation (3.27) leads to:

$$\frac{dV}{V} = -\frac{dP}{B_0 + B_0'P} \tag{3.28}$$

Integrating Equation (3.28):

$$P(V) = \frac{B_0}{B'}\left(\left(\frac{V_0}{V}\right)^{B'} - 1\right) \tag{3.29}$$

Inserting Equation (3.29) into $E = E_0 - \int P dV$, then the Murnaghan EOS is obtained:

$$E(V) = E_0 + \frac{B_0 V}{B'}\left(\frac{(V_0/V)^{B'}}{B' - 1} + 1\right) - \frac{B_0 V_0}{B' - 1} \tag{3.30}$$

3.2.2 Birch-Murnaghan EOS

The derivation of the Birch-Murnaghan EOS is not as straightforward as the Murnaghan EOS. In the Birch-Murnaghan EOS, the Eulerian strain tensor is used to express the finite strain:

$$\epsilon_{ij} = \frac{1}{2}\left(\delta_{ij} - \frac{\partial a_k}{\partial x_i}\frac{\partial a_k}{\partial x_j}\right) = \frac{1}{2}\left(\frac{\partial u_i}{\partial x_i} + \frac{\partial u_j}{\partial x_j}\right) - \frac{1}{2}\frac{\partial u_k}{\partial x_i}\frac{\partial u_k}{\partial x_j}$$
$$\text{with } i,j,k = 1,2,3 \tag{3.31}$$

where x_k is the deformed coordinate, a_k is the undeformed coordinate, δ_{ij} is the Kronecker tensor, u_k is the displacement vector, and Einstein's summation rule is applied. Essentially, in Eulerian strain tensor, the deformed coordinates is the reference, while in Lagrangian strain tensor, the undeformed coordinates is the reference.

If only the hydrostatic pressure is applied, a single strain component can be used to determine the strain tensor:

$$\epsilon_{ij} = \epsilon\delta_{ij} \tag{3.32}$$
$$\text{with } i,j = 1,2,3$$

The relation between ϵ in Equation (3.33) and the volume is:

$$\frac{V}{V_0} = (1 - 2\epsilon)^{-\frac{3}{2}} = (1 + 2f)^{-\frac{3}{2}} \tag{3.33}$$

$$f = \frac{1}{2}\left(\left(\frac{V}{V_0}\right)^{-\frac{3}{2}} - 1\right) \tag{3.34}$$

where V_0 is the volume at zero pressure; f is only for the sake of convenience. The total energy is expanded in terms of f (Murnaghan, 1937; Birch, 1938):

$$E = E_0 + af^2 + bf^3 + cf^4 + \cdots \tag{3.35}$$

where E_0 is the total energy of the undeformed body; $a,b,c...$ are the coefficients expressed by V_0, B_0, $B_0'\cdots$ (see below).

3.2.2.1 2nd order Birch-Murnaghan EOS

If E in Equation (3.35) is only expanded up to 2nd order:

$$E \approx E_0 + af^2 \tag{3.36}$$

Differentiate Equation (3.36) by using the following relations:

$$P = -\left(\frac{\partial E}{\partial V}\right)_T = -\left(\frac{\partial E}{\partial f}\frac{\partial f}{\partial V}\right)_T \tag{3.37}$$

$$B_0 = -V\left(\frac{\partial P}{\partial V}\right)_{T,P=0} \tag{3.38}$$

a is found to be:

$$a = \frac{9}{2}B_0 V_0 \tag{3.39}$$

Then the pressure in the 2nd order Birch-Murnaghan EOS is:

$$P_{2nd} = \frac{3B_0}{2}\left[\left(\frac{V}{V_0}\right)^{-\frac{7}{3}} - \left(\frac{V}{V_0}\right)^{-\frac{5}{3}}\right] \tag{3.40}$$

Accordingly, the total energy is:

$$E_{2nd}(V) = E_0 + \frac{9}{8}B_0 V_0 \left[\left(\frac{V}{V_0}\right)^{-\frac{2}{3}} - 1\right]^2 \tag{3.41}$$

3.2.2.2 3rd order Birch-Murnaghan EOS

If E in Equation (3.35) is only expanded up to 3rd order:

$$E \approx E_0 + af^2 + bf^3 \tag{3.42}$$

Another relation is used to differentiate Equation (3.42) together with the relations in Equation (3.37) and Equation (3.38):

$$B_0' = \left(\frac{\partial B}{\partial P}\right)_{T,P=0} \tag{3.43}$$

b is found to be:

$$b = \frac{9}{2}B_0 V_0 \left(B_0' - 4\right) \tag{3.44}$$

The pressure in the 3rd order Birch-Murnaghan EOS is:

$$P_{3rd} = \frac{3B_0}{2}\left[\left(\frac{V}{V_0}\right)^{-\frac{7}{3}} - \left(\frac{V}{V_0}\right)^{-\frac{5}{3}}\right]\left\{1 + \frac{3}{4}\left(B_0' - 4\right)\left[\left(\frac{V}{V_0}\right)^{-\frac{2}{3}} - 1\right]\right\} \tag{3.45}$$

The total energy corresponding to the 3rd order Birch-Murnaghan EOS is:

$$E_{3rd}(V) = E_0 + \frac{9V_0 B_0}{16}\left\{\left[\left(\frac{V}{V_0}\right)^{-\frac{2}{3}} - 1\right]^3 B_0' + \left[\left(\frac{V}{V_0}\right)^{-\frac{2}{3}} - 1\right]^2\left[6 - 4\left(\frac{V}{V_0}\right)^{-\frac{2}{3}}\right]\right\} \tag{3.46}$$

Birch showed that in cubic systems, B_0' can be expressed by the elastic constants (Birch, 1947)[4]

$$B_0' = 1 - \frac{1}{3} \cdot \frac{C_{111} + 6C_{112} + 2C_{123}}{C_{11} + 2C_{12}} = 1 - \frac{1}{3} \cdot \frac{B_{0,3rd}}{B_0} \tag{3.47}$$

where C_{ij} and C_{ijk} are the 2nd and 3rd order elastic constants. B_0 and $B_{0,3rd}$ are the second and the third order bulk modulus. This means B_0' is also an indication of the higher order elastic modulus.

---

[4]The expression of Equation 3.47 is different from the original version, because in the original paper the Birch's definition of the third order elastic constants (C_{ijk}^{B}) was used. C_{ijk}^{B} is related to the current C_{ijk} as: $C_{111}^{B} = \frac{1}{6}C_{111}$, $C_{112}^{B} = \frac{1}{2}C_{112}$, $C_{123}^{B} = C_{123}$ (Hiki, 1981).

3.3 Energy-strain relation of an elastic body

In this thesis, the elastic constants are calculated by fitting DFT calculated energy-strain curves. In this section, the relation of the elastic energy and the strain of an elastic body in cubic symmetry is briefly discussed. The energy-strain relation of two specific deformation modes (tetragonal shear and trigonal shear) are further discussed. By applying these two shear strains, $C_{11} - C_{12}$ and C_{44} can be calculated. Together with the bulk modulus ($3B_0 = C_{11} + 2C_{12}$) from the equation of state (previous section), individual elastic constants, C_{11}, C_{12}, and C_{44} of an elastic body in cubic symmetry are obtained.

3.3.1 General formulation of energy-strain relation of an elastic body in cubic symmetry

When an solid body is deformed elastically at a constant temperature, the elastic energy can be expanded in terms of the elastic constants (Birch, 1947; Hiki, 1981):

$$U(\eta) = U_0 \quad + \quad \frac{1}{2!}V \sum_{i,j,k,l=1}^{3} C_{ijkl}\eta_{ij}\eta_{kl} + \frac{1}{3!}V \sum_{i,j,k,l,m,n=1}^{3} C_{ijklnm}\eta_{ij}\eta_{kl}\eta_{mn} +$$

$$\frac{1}{4!}V \sum_{i,j,k,l,m,n,p,q=1}^{3} C_{ijklmnpq}\eta_{ij}\eta_{kl}\eta_{mn}\eta_{pq} + \dots \tag{3.48}$$

where U_0 is the total energy of the solid body under no strain; V is the volume of solid body. η is the Lagrangian strain component which is defined as:

$$\eta_{ij} = \frac{1}{2}\left(\frac{\partial x_k}{\partial a_i}\frac{\partial x_k}{\partial a_j} - \delta_{ij}\right) = \frac{1}{2}\left(\frac{\partial u_i}{\partial a_i} + \frac{\partial u_j}{\partial a_j}\right) + \frac{1}{2}\frac{\partial u_k}{\partial a_i}\frac{\partial u_k}{\partial a_j} \tag{3.49}$$
$$\text{with } i,j,k = 1,2,3$$

where x_k and a_k are the deformed and undeformed coordinates; δ_{ij} is the Kronecker tensor; and u_k is the displacement vector. And Einstein's summation rule is applied. The notation of the elastic constants can be simplified by Voigt notation listed in Table 3.1.

Table 3.1: Voigt notation

$$
\begin{array}{ll}
11 \longrightarrow 1 & \eta_{11} \longrightarrow \eta_1 \\
22 \longrightarrow 2 & \eta_{22} \longrightarrow \eta_2 \\
33 \longrightarrow 3 & \eta_{33} \longrightarrow \eta_3 \\
23 \longrightarrow 4 & \eta_{23} \longrightarrow \eta_4/2 \\
31 \longrightarrow 5 & \eta_{31} \longrightarrow \eta_5/2 \\
12 \longrightarrow 6 & \eta_{12} \longrightarrow \eta_6/2
\end{array}
$$

For cubic symmetry, there are 3 independent SOECs (second order elastic constants), 6 independent TOECs (third order elastic fonstants), 11 independent FOECs (fourth order elastic constants) listed in Table 3.2.

Table 3.2: Independent SOECs (second order elastic constants), TOECs (third order elastic fonstants), FOECs (fourth order elastic constants) of cubic systems.

SOECs	C_{11}, C_{12}, C_{44}
TOECs	$C_{111}, C_{112}, C_{123}, C_{144}, C_{155}, C_{456}$
FOECs	$C_{1111}, C_{1112}, C_{1122}, C_{1123}, C_{1144}, C_{1155}, C_{1255}, C_{1266}, C_{1456}, C_{4444}, C_{4455}$

According to Table 3.1, Table 3.2, and Equation (3.48), the elastic energy density of a solid body in cubic symmetry can be written as (Birch, 1947; Ghate, 1964):

$$[U(\eta) - U_0] V^{-1} = u(\eta) = u_2(\eta) + u_3(\eta) + u_4(\eta) + \cdots \tag{3.50}$$

$$u_2(\eta) = \frac{1}{2}C_{11}(\eta_1^2 + \eta_2^2 + \eta_3^2) + C_{12}(\eta_1\eta_2 + \eta_2\eta_3 + \eta_3\eta_1) + \frac{1}{2}C_{44}(\eta_4^2 + \eta_5^2 + \eta_6^2) \tag{3.51}$$

$$
\begin{aligned}
u_3(\eta) \quad = \quad & \frac{1}{6}C_{111}(\eta_1^3 + \eta_2^3 + \eta_3^3) + \frac{1}{2}C_{112}(\eta_1\eta_2^2 + \eta_2\eta_3^2 + \eta_3\eta_1^2 + \eta_1^2\eta_2 + \eta_2^2\eta_3 + \eta_3^2\eta_1) \\
& + C_{123}\eta_1\eta_2\eta_3 + \frac{1}{2}C_{144}(\eta_1\eta_4^2 + \eta_2\eta_5^2 + \eta_3\eta_6^2) \\
& + \frac{1}{2}C_{155}(\eta_2\eta_4^2 + \eta_3\eta_4^2 + \eta_1\eta_5^2 + \eta_3\eta_5^2 + \eta_1\eta_6^2 + \eta_2\eta_6^2) \\
& + C_{456}\eta_4\eta_5\eta_6 \tag{3.52}
\end{aligned}
$$

$$
\begin{aligned}
u_4(\eta) \quad = \quad & \frac{1}{24}C_{1111}(\eta_1^4 + \eta_2^4 + \eta_3^4) + \frac{1}{6}C_{1112}[\eta_1^3(\eta_2 + \eta_3) + \eta_2^3(\eta_3 + \eta_1) + \eta_3^3(\eta_1 + \eta_2)] \\
& + \frac{1}{4}C_{1122}(\eta_1^2\eta_2^2 + \eta_2^2\eta_3^2 + \eta_3^2\eta_1^2) + \frac{1}{2}C_{1123}(\eta_1^2\eta_2\eta_3 + \eta_2^2\eta_3\eta_1 + \eta_3^2\eta_1\eta_2) \\
& + \frac{1}{4}C_{1144}(\eta_1^2\eta_4^2 + \eta_2^2\eta_5^2 + \eta_3^2\eta_6^2) + \frac{1}{4}C_{1155}(\eta_1^2(\eta_5^2 + \eta_6^2) + \eta_2^2(\eta_4^2 + \eta_6^2) + \eta_3^2(\eta_4^2 + \eta_5^2)) \\
& + \frac{1}{2}C_{1255}(\eta_1\eta_2(\eta_4^2 + \eta_5^2) + \eta_2\eta_3(\eta_5^2 + \eta_6^2) + \eta_1\eta_3(\eta_4^2 + \eta_6^2)) \\
& + \frac{1}{2}C_{1266}(\eta_1\eta_2\eta_6^2 + \eta_2\eta_3\eta_4^2 + \eta_1\eta_3\eta_5^2) + C_{1456}\eta_4\eta_5\eta_6(\eta_1 + \eta_2 + \eta_3) \\
& + \frac{1}{24}C_{4444}(\eta_4^4 + \eta_5^4 + \eta_6^4) + \frac{1}{4}C_{4455}(\eta_4^2\eta_5^2 + \eta_5^2\eta_6^2 + \eta_6^2\eta_4^2) \tag{3.53}
\end{aligned}
$$

3.3.2 Tetragonal and trigonal shear ($C_{11} - C_{12}$ and C_{44})

In this thesis, two specific deformation modes are applied to calculate the second order elastic constants. These modes are the tetragonal and trigonal shear. The elastic constants are calculated in the following way:

1. Apply a series of strains to the supercell, and conserve the volume.

37

2. Calculate the total energy of the strained supercells.

3. Plot the total energy against the applied strain.

4. Fit the energy-strain curve with a polynomial function (usually second order). The second order coefficient of the fitted function is the desired second order elastic constants.

The basic information of the tetragonal and trigonal shear is listed in Table 3.3.

Table 3.3: Basic information of the tetragonal and trigonal shear.

	Tetragonal shear	Trigonal shear	Note
Strain variable	ε_3	ε_{12}	This strain is used plot the energy-strain curve
Undeformed and deformed coordinates	$x_1 = (\varepsilon_1 + 1)a_1$ $x_2 = (\varepsilon_1 + 1)a_2$ $x_3 = (\varepsilon_3 + 1)a_3$	$x_1 = a_1 + \varepsilon_{12}a_2$ $x_2 = a_2 + \varepsilon_{12}a_1$ $x_3 = (\varepsilon_3 + 1)a_3$	a_k, undeformed coordinates x_k, deformed coordinates $(k = 1,2,3)$
Constraint	$\varepsilon_1 = (\varepsilon_3 + 1)^{-1/2} - 1$	$\varepsilon_3 = (1 - \varepsilon_{12}^2)^{-1} - 1$	This ensures volume conservation
Lagrangian strain tensor	$\eta_1 = \eta_2 = \frac{1}{2}\varepsilon_1^2 + \varepsilon_1$ $\eta_3 = \frac{1}{2}\varepsilon_3^2 + \varepsilon_3$ $\eta_4 = \eta_5 = \eta_6 = 0$	$\eta_1 = \eta_2 = \frac{1}{2}\varepsilon_{12}^2$ $\eta_3 = \frac{1}{2}\varepsilon_3^2 + \varepsilon_3$ $\eta_4 = \eta_5 = 0$ $\eta_6 = 2\varepsilon_{12}$	In Voigt notation (see Table 3.1)
Second order coefficient in fitted function	$\frac{3}{4}(C_{11} - C_{12})$	$2C_{44}$	

3.4 Homogenization method of elastic constants

In this thesis, the homogenization mothd is used to obtain the polycrystalline Young's modulus and shear modulus from the calculated elastic constants. The homogenization method is to homogenize a tensorial quantity into a scalar quantity.

The primitive homogenization methods assume strain or stress homogeneity at the mesoscale, namely Voigt's (Voigt, 1910) and Reuss' (Reuss, 1929) model:

$$C_{ijkl}^V = W^{-1} \sum_{n=1}^{N} w(g^n) g_{ip}^n g_{jq}^n g_{kr}^n g_{ls}^n C_{pqrs}^C \quad \text{(Voigt's model)} \tag{3.54}$$

$$S_{ijkl}^R = W^{-1} \sum_{n=1}^{N} w(g^n) g_{ip}^n g_{jq}^n g_{kr}^n g_{ls}^n C_{pqrs}^C \quad \text{(Reuss' model)} \tag{3.55}$$

The superscript, V, R, C, means Voigt's model, Reuss' model model, and the single crystal elastic constants, respectively. C and S are the elastic stiffness and compliance tensor. $g_{ip}^n g_{jq}^n g_{kr}^n g_{ls}^n$ is the tensor transforming from crystal coordinates to sample coordinates. $w(g^n)$ is the weight assigned to the orientation, W is the sum of the weights, and N is the total number of the orientations. For the crystals in which the orientations of the grains are randomly distributed, the homogenized shear modulus takes the following form:

$$G_V = \frac{C_{11} - C_{12} + 3C_{44}}{5} \quad \text{(Voigt's model)} \tag{3.56}$$

$$G_R = \frac{5}{4(S_{11} - S_{12}) + 3S_{44}} \quad \text{(Reuss's model)} \tag{3.57}$$

Hill realized that Voigt's and Reuss' model are the upper and lower bounds of the true elastic behavior (Hill, 1952). In Hill's model, the homogenized shear modulus takes the arithmetic or geometric average of the shear modulus from Voigt's and Reuss' model:

$$C_{ijkl}^H = \frac{1}{2}\left(C_{ijkl}^V + \left(S_{ijkl}^R\right)^{-1}\right) \text{ or } C_{ijkl}^H = \left(C_{ijkl}^V \cdot \left(S_{ijkl}^R\right)^{-1}\right)^{\frac{1}{2}} \tag{3.58}$$

Hershey's model (Hershey, 1954) is similar to self-consistent model, and a similar approach is proposed by Kröner (Kröner, 1958). In Hershey's model, individual grains are assumed to be spherical and the orientations are randomly distributed. The homogenized shear modulus is obtained by solving the following equation:

$$\begin{aligned}
& 64G_H^4 + 16\left(4C_{11} + 5C_{12}\right)G_H^3 \\
& + \left[3\left(C_{11} + 2C_{12}\right)\left(5C_{11} + 4C_{12}\right) - 8\left(7C_{11} - 4C_{12}\right)C_{44}\right]G_H^2 \\
& - \left(29C_{11} - 20C_{12}\right)\left(C_{11} + 2C_{12}\right)C_{44}G_H \\
& - 3\left(C_{11} + 2C_{12}\right)^2\left(C_{11} - C_{12}\right)C_{44} = 0
\end{aligned} \tag{3.59}$$

After the homogenized shear modulus is obtained, the Young's modulus and Poisson's ratio can be obtained via the relations in the isotropic linear elasticity theory:

$$E = \frac{9BG}{3B + G} \qquad (3.60)$$

$$\nu = \frac{9B - 2G}{6B + 2G} \qquad (3.61)$$

where B is the bulk modulus from EOS.

Besides the above mentioned analytical methods, certain numerical methods are also available, such as crystal elasticity finite element method (CEFEM) and crystal elasticity fast Fourier transform (CEFFT) (Roters et al., 2010).

3.5 Atomic volume determined by Bader Analysis

In this thesis, Bader analysis is used to obtain the atomic volume of an atom in the crystals. The atomic volume is determined by the topological analysis on the electron density. The volume determined in this way should give more physical insight than the geometrical analysis, such as Voronoi construction.

The main difference of Bader analysis from Voronoi construction is that in Bader analysis the atoms in the crystals are divided by the "zero-flux" surfaces. At a "zero-flux" surface the electron flux in the normal of this surface is zero which fulfill the following relation:

$$\Delta\rho\left(r_s\right) \cdot n\left(r_s\right) = 0 \tag{3.62}$$

where r_s is any point on the "zero-flux" surface. This is illustrated in Figure 3.5
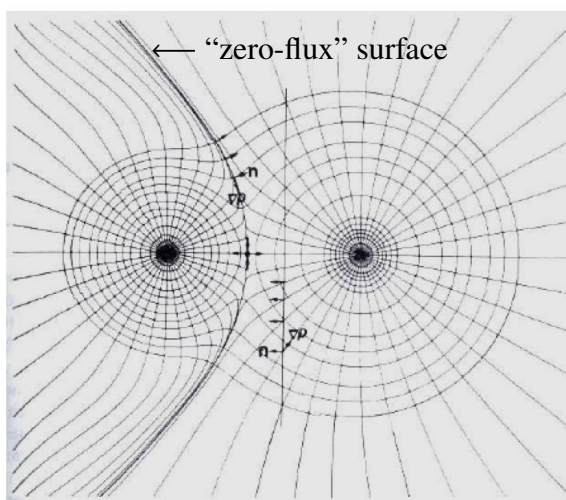
Figure 3.5: Contour map of NaCl overlaid with trajectories of $\Delta\rho$ (Bader, 1994).

Once such surfaces are identified, the volume bounded by the surface in association with the nucleus is the atomic volume of the atom in a particular crystal. Naturally, the electron density in this volume can be integrated to obtain the total charge, so that the charge transfer can be studied when an atom is put into a foreign environment.

In this thesis, Bader analysis was performed by using the algorithm and the package developed by Henkelman and co-workers (Henkelman et al., 2006; Sanville et al., 2007; Tang et al., 2009).

3.6 Ashby's materials property and design chart

In this thesis, various calculated materials properties enter Ashby's materials property and design charts.

According to Ashby's materials property and design charts, it is suggested that one material property is plotted against another (Ashby, 2005). An example is shown in Figure 3.6.
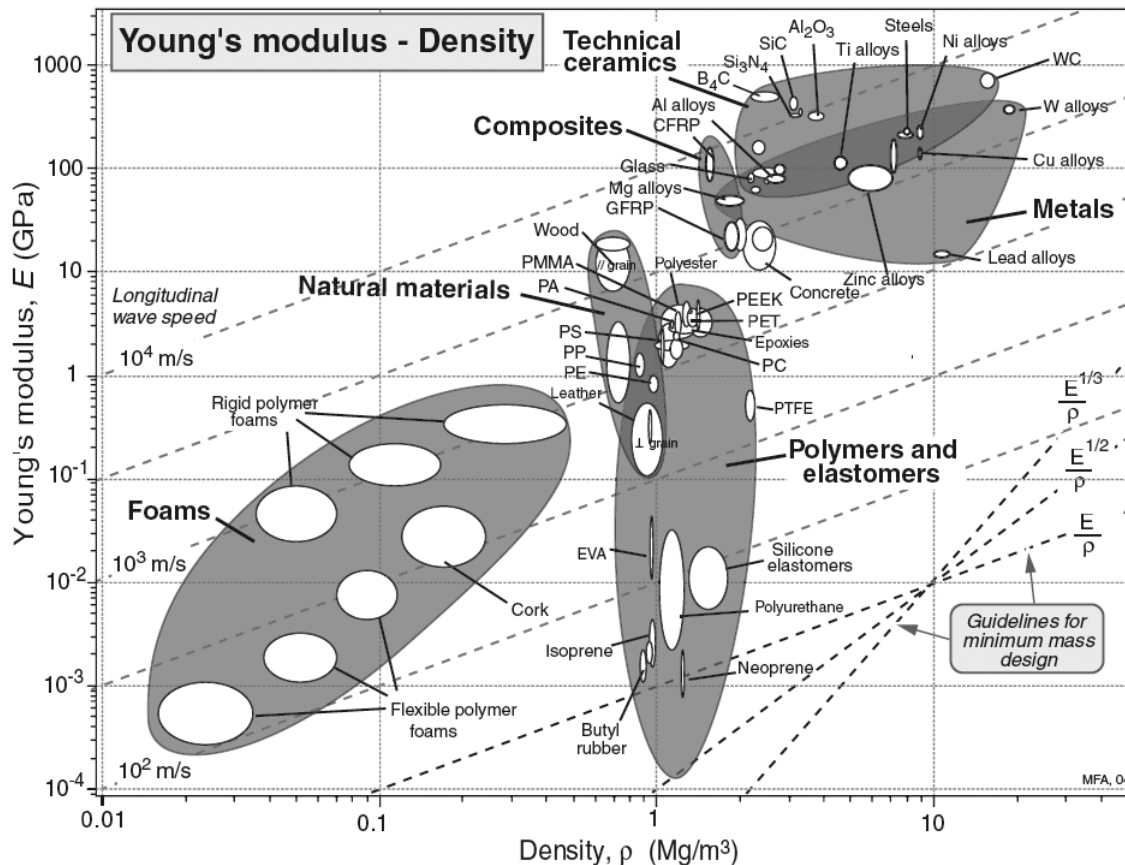
Figure 3.6: Young's modulus-density chart (Ashby, 2005).

Two features of this kind of plots should be noted:

1. The logarithmic scale.

2. The straight guidelines associated with the corresponding material indices.

The reason for such a kind of plot can be explained by the following example. A material is to be selected to make the aircraft wing spars shown in Figure 3.7. Too high density or too low stiffness leads to undesirable performance of the wing spars.
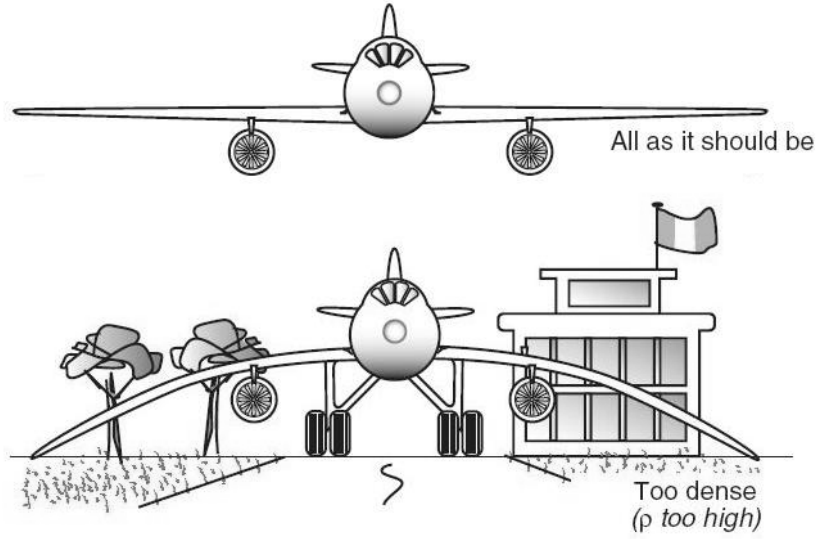
Figure 3.7: The desired (top) and undesired (bottom) performance of the wing spars of an aircraft (Ashby et al., 2007).

In a simple manner, the performance of the materials in such a task is characterized by the following equation:

$$\epsilon = \frac{\sigma}{E} = \frac{mg/A}{E} = \frac{LA\rho g/A}{E} = Lg \cdot \frac{\rho}{E} \quad (3.63)$$

where g is the strength of the gravitational field, L and A is the length and the cross section area of the wing spar, all of which should be constants in a task; ρ and E is the density and the Young's modulus, respectively, both of which depend on the specific materials. In the process of selecting materials, the material should have maximum ratio of E/ρ in order to minimize ϵ. By drawing straight lines parallel to the existing guideline of E/ρ in Figure 3.6, an engineer can find the material with the maximum E/ρ in that chart. In this particular example, E/ρ is the material indices, and Equation (3.63) is called equation performance. Without the logarithmic scale, the guidelines associated with the material indices cannot be drawn as a straight line which makes it far less convenient.

In the same manner, there are other materials indices corresponding to other performance equations. The selected material indices and corresponding descriptions are listed in Table 3.4 (Ashby, 2005). Those listed material indices are to be used for the discussion in Chapter 8.

Table 3.4: Material indices used in this thesis. To fulfill the task, the corresponding material indices should be maximized. All the descriptions are from Ashby (2005). E, Young's modulus; ρ, density; σ_f, failure stress (yield or fracture).

Material indices	Task
	Stiffness-limited design at minimum mass
E/ρ	Tie (tensile structure) Stiffness, length specified; section area free
	Beam (loaded in bending) Stiffness, length, height specified; width free
	Cylinder with internal pressure Elastic distortion, pressure and radius specified; wall thickness free
$E^{1/2}/\rho$	Beam (loaded in bending) Stiffness, length, shape specified; section area free
	Column (compression structure, failure by elastic buckling) Buckling load, length, shape specified; section area free
$E^{1/3}/\rho$	Beam (loaded in bending) Stiffness, length, width specified; height free
	Panel (flat plate, loaded in bending) Stiffness, length, width specified, thickness free
	Plate (flat plate, compressed in-plane, buckling failure) Collapse load, length and width specified, thickness free
	Strength-limited design at minimum mass
σ_f/ρ	Tie (tensile structure) Stiffness, length specified; section area free
	Shaft (loaded in torsion) Load, length, outer radius specified; wall thickness free
	Beam (loaded in bending) Load length, height specified; width free
	Column (compression structure) Load, length, shape specified; section area free
	Cylinder with internal pressure Elastic distortion, pressure and radius specified; wall thickness free
	Spherical shell with internal pressure Elastic distortion, pressure and radius specified, wall thickness free
	Flywheels, rotating disks Maximum energy storage per unit mass; no failure
$\sigma_f^{1/2}/\rho$	Shaft (loaded in torsion) Load, length, wall-thickness specified; outer radius free
	Beam (loaded in bending) Load, length, width specified; height free
	Panel (flat plate, loaded in bending) Stiffness, length, width specified, thickness free
	Plate (flat plate, compressed in-plane, buckling failure) Collapse load, length and width specified, thickness free

Continued on next page

Table 3.4 Continued

Material indices	Task
$\sigma_f^{2/3}/\rho$	Shaft (loaded in torsion)
	Load, length, shape specified, section area free
	Beam (loaded in bending)
	Load, length, shape specified; section area free
Strength-limited design for maximum performance	
σ_f/E	Elastic hinges
	Radius of bend to be minimized (max flexibility without failure)
$\sigma_f^{3/2}/E$	Knife edges, pivots
	Minimum contact area, maximum bearing load
	Compression seals and gaskets
	Maximum conformability; limit on contact pressure
	Diaphragms
	Maximum deflection under specified pressure or force
σ_f^2/E	Springs
	Maximum stored elastic energy per unit volume; no failure
σ_f/ρ	Rotating drums and centrifuges
	Maximum angular velocity; radius fixed; wall thickness free
Vibration-limited design	
E/ρ	Ties, columns
	Maximum longitudinal vibration frequencies
	Beams, all dimensions prescribed
	Maximum flexural vibration frequencies
	Panels, all dimensions prescribed
	Maximum flexural vibration frequencies
$E^{1/2}/\rho$	Beams, length and stiffness prescribed
	Maximum flexural vibration frequencies
$E^{1/3}/\rho$	Panels, length, width and stiffness prescribed
	Maximum flexural vibration frequencies

Part II

Results and Discussion

Chapter 4

Equation of states of studied Al binary solid solutions

4.1 Equation of states of selected elements in pure bulk phases

Table 4.1 and Table 4.2 list the groundstate properties of the selected elements in bulk phases. The most accurate prediction is a_0 or V_0 (lattice parameter and equilibrium atomic volume). The error of DFT deviating from the experiments is less than 1%. For B_0 (bulk modulus), the error is less than 6% except Zn ($\sim$40%). The bulk modulus pressure derivatives (B'_0) predicted by DFT also align with the measurements.

Table 4.1: The groundstate lattice parameter (a_0 in Å), bulk modulus (B_0 in GPa), bulk modulus pressure derivative (B'_0), equilibrium total energy per atom (E_0 in eV) of Al, Cu, Ca, Sr, and Ir. M: Murnaghan EOS; BM: Birch-Murnaghan EOS.

	Crystal structure	Method	a_0	B_0	B'_0	E_0
Al	fcc	M	4.040	77.15	4.62	-3.745
		BM	4.040	77.47	4.64	-3.745
		exp.	4.032[a]	79.38[b]	4.72[c]	
Cu	fcc	M	3.637	136.06	5.01	-3.718
		BM	3.637	136.75	5.05	-3.718
		exp.	3.602[a]	142.03[d] 141.33[e] 142.04[f] 144.46[g]	5.277±0.022[h] 5.278[i]	
Ca	fcc	M	5.529	17.32	3.30	-2.004
		BM	5.529	17.37	3.32	-2.004
		exp.	5.57[j]	18.36[j]	3.6[j]	
Sr	fcc	M	6.040	11.72	3.12	-1.684
		BM	6.040	11.76	3.14	-1.684
		exp.	6.050[j]	12.35[j]	2.37[j]	
Ir	fcc	M	3.877	344.21	5.11	-8.857
		BM	3.877	346.05	5.15	-8.857
		exp.	3.835[a] 3.834[k]	366[l]	5.47[m]	

[a] From Grabowski et al. (2007), T=5K
[b] From Kamm and Alers (1964), from T=4.2 extrapolated to T=0K
[c] From Rose et al. (1984), T=0K
[d] From Overton and Gaffney (1955), from T=4.2 extrapolated to T=0K
[e] From Rayne (1959), T=4.2K
[f] From Waldorf (1960), T=4.2K
[g] From Ledbetter (1981), T=5K on polycrystal
[h] From van't Klooster et al. (1979), the adiabatic B'_0, T=79K
[i] From van't Klooster et al. (1979), the isothermal B'_0, T=79K
[j] From Anderson et al. (1990), T=0K
[k] From Arblaster (2010), from T=4 extrapolated to T=0K
[l] From MacFarlane et al. (1966), from T=4.2K extrapolated to T=0K
[m] From Steinberg (1982), unknown temperature

Table 4.2: The groundstate lattice parameter (a_0 in Å) or equilibrium atomic volume (V_0 in Å^3), bulk modulus (B_0 in GPa), bulk modulus pressure derivative (B'_0), equilibrium total energy per atom (E_0 in eV) of Li, Mg, and Zn. M: Murnaghan EOS; BM: Birch-Murnaghan EOS.

	Crystal structure	Method	a_0	B_0	B'_0	E_0
Li	fcc	M	4.329	14.14	3.04	-1.905
		BM	4.329	14.18	3.07	-1.905
	bcc	M	3.439	13.48	2.19	-1.903
		BM	3.439	13.54	2.27	-1.903
		exp.	3.491[a] 3.478[b] 3.5092[c]	13.8[d] 13.2[e] 13.1[f] 12.95[g]	3.3[f] 3.49[h] 3.51[i]	

	Crystal structure	Method	V_0	B_0	B'_0	E_0
Mg	fcc	M	23.116	35.36	4.66	-1.582
		BM	23.116	35.51	4.68	-1.582
	hcp	M	22.962	35.81	4.07	-1.595
		BM	22.962	35.93	4.09	-1.595
		exp.	22.878[j]	36.39[k]	3.9[l]	
Zn	fcc	M	15.260	68.41	5.24	-1.244
		BM	15.259	68.79	5.30	-1.244
	hcp	M	15.259	56.09	6.56	-1.266
		BM	15.338	56.71	6.72	-1.266
		exp.	15.080[m]	78.14[n] 80.40[o]	6.4[l]	

[a] From Barrett (1956), T=78K

[b] From Berliner et al. (1989), T=20K

[c] From Chiarotti (1993), T=5K

[d] From Nash and Smith (1959), T=78K

[e] From Slotwinski and Trivisonno (1969), T=78K

[f] From Day and Ruoff (1974),from T=85K extrapolate to T=0K

[g] From Felice et al. (1977), ^{7}Li, from T=90K extrapolate to T=0K

[h] From Felice et al. (1977), ^{7}Li, the adiabatic B'_0, T=195K

[i] From Felice et al. (1977), ^{7}Li, the isothermal B'_0,T=195K

[j] From Rossouw and Venkatesan (2001), T=103K

[k] From Slutsky and Garland (1957), from T=4.2 extrapolated to T=0K

[l] From Steinberg (1982), unknown temperature

[m] Extrapolate V_0 at T=273.3K (Owen and Yates, 1934) to T=0K through the thermal expansion data (Meyerhoff and Smith, 1962)

[n] From Garland and Dalven (1958), from T=4.2K extrapolated to T=0K

[o] From Alers and Neighbours (1958), T=4.2K

4.2 Lattice parameters (a_0) and bulk moduli (B_0) of studied Al binary solid solutions

4.2.1 a_0 and B_0 calculated by DFT

Figure 4.1 shows the compositional dependence of the lattice parameter and the bulk modulus of the studied Al binary solid solutions. Both of them almost linearly depend on the concentration. Among the solute elements, Ca, Sr and Ir change these two properties of Al more drastically than Cu, Mg, Li and Zn.
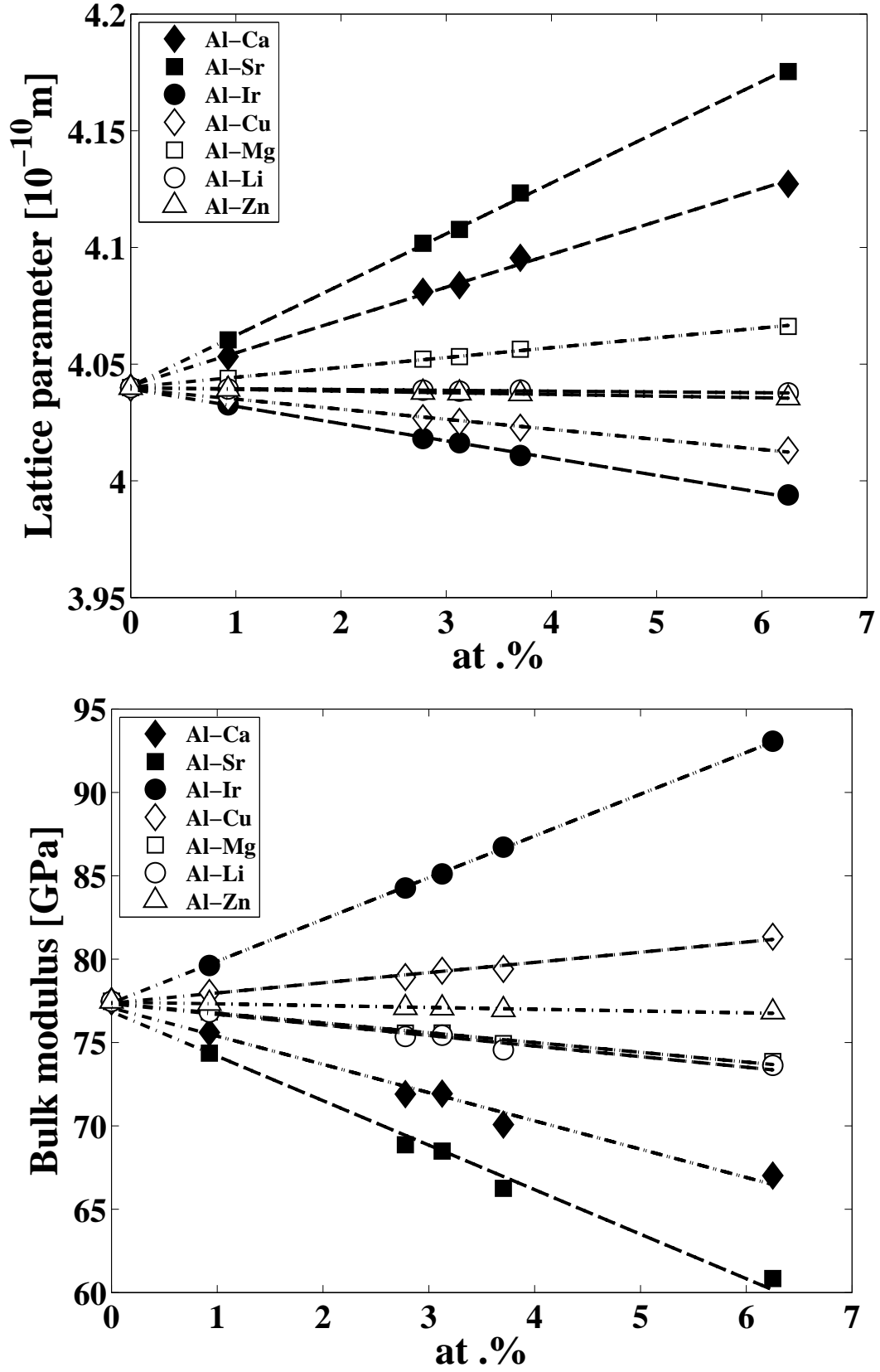
Figure 4.1: The lattice parameters (top) and the bulk moduli (bottom) of the studied Al binary solid solutions on the dependence of the concentration calculated by DFT.

4.2.2 Comparison of a_0 and B_0 by DFT and experiments

Figure 4.2 shows the comparison of the calculated and measured (at 25 °C or room temperature)
lattice parameter and bulk modulus.

For the lattice parameter, the calculated and measured almost have the same compositional
dependence, despite the fact of the thermal expansion.

For the bulk modulus, The agreement between the calculation and the measurement is not as
good as the lattice parameter. All the bulk modulus measurements[1] were conducted by the
ultrasonic method on single crystals except Al-Cu. The bulk modulus of Al-Cu solid solutions
were measured on the polycrystals by the resonance method (Masafumi and Takefumi, 1988).
This method might not be as precise as the ultrasonic method. Especially, the bulk modulus
of pure Al reported by Masafumi et al. (Masafumi and Takefumi, 1988) is ~4 GPa lower than
those in the other measurements (Gault et al., 1977; Müller et al., 1986).

---

[1]The measured bulk modulus are calculated from the elastic constants measured on the single crystals
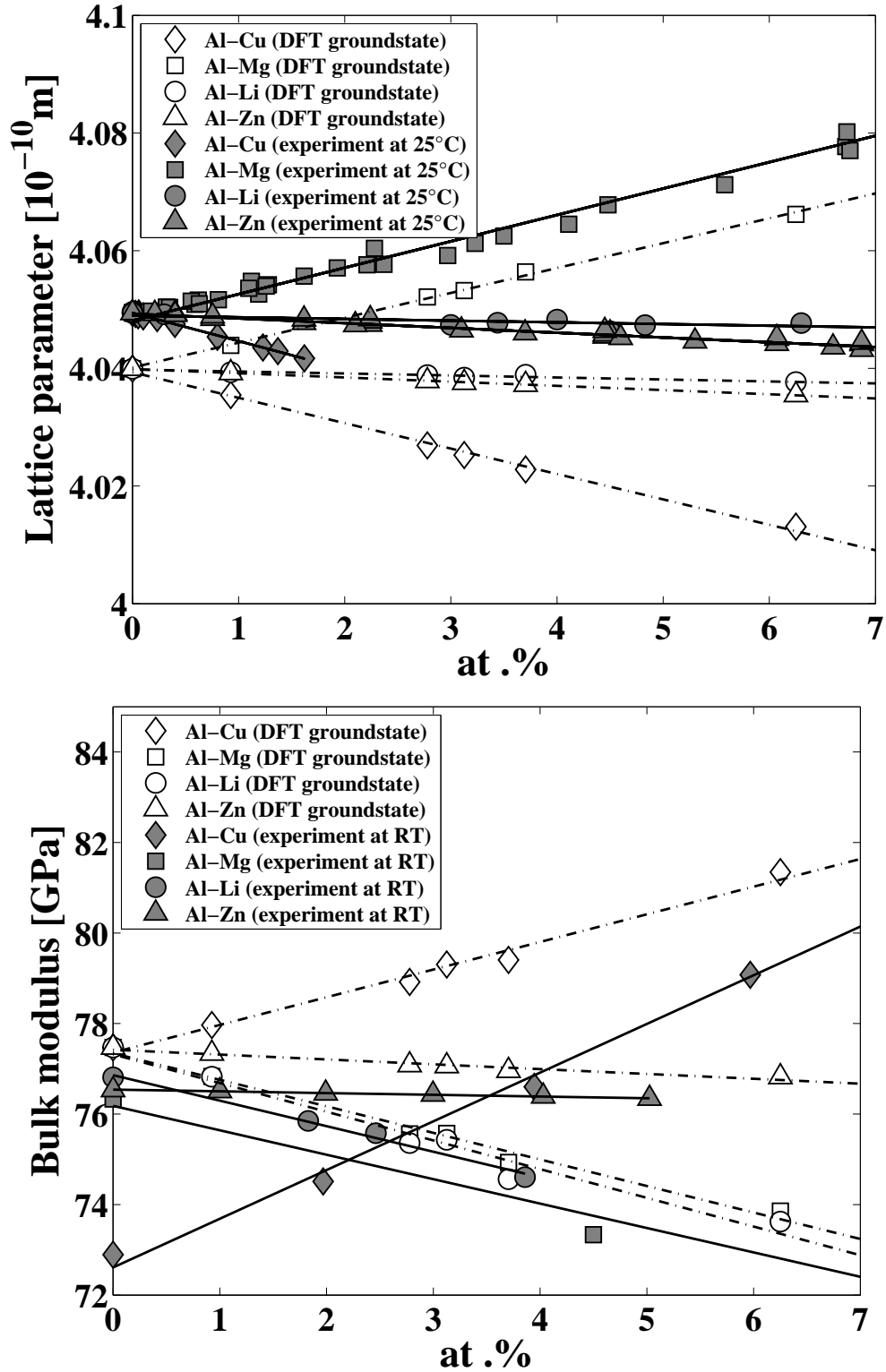
Figure 4.2: The lattice parameters (top) and the bulk moduli (bottom) of the studied Al binary solid solutions calculated by DFT compared with measurements at 25°C or room temperature. References of the experiments: Lattice parameter: Al-Cu, Murray (1985); Al-Mg, Murray (1982); Al-Li, McAlister (1982); Al-Zn, Murray (1983). Bulk modulus: Al-Cu, Masafumi and Takefumi (1988); Al-Mg, Gault et al. (1977); Al-Li and Al-Zn, Müller et al. (1986).
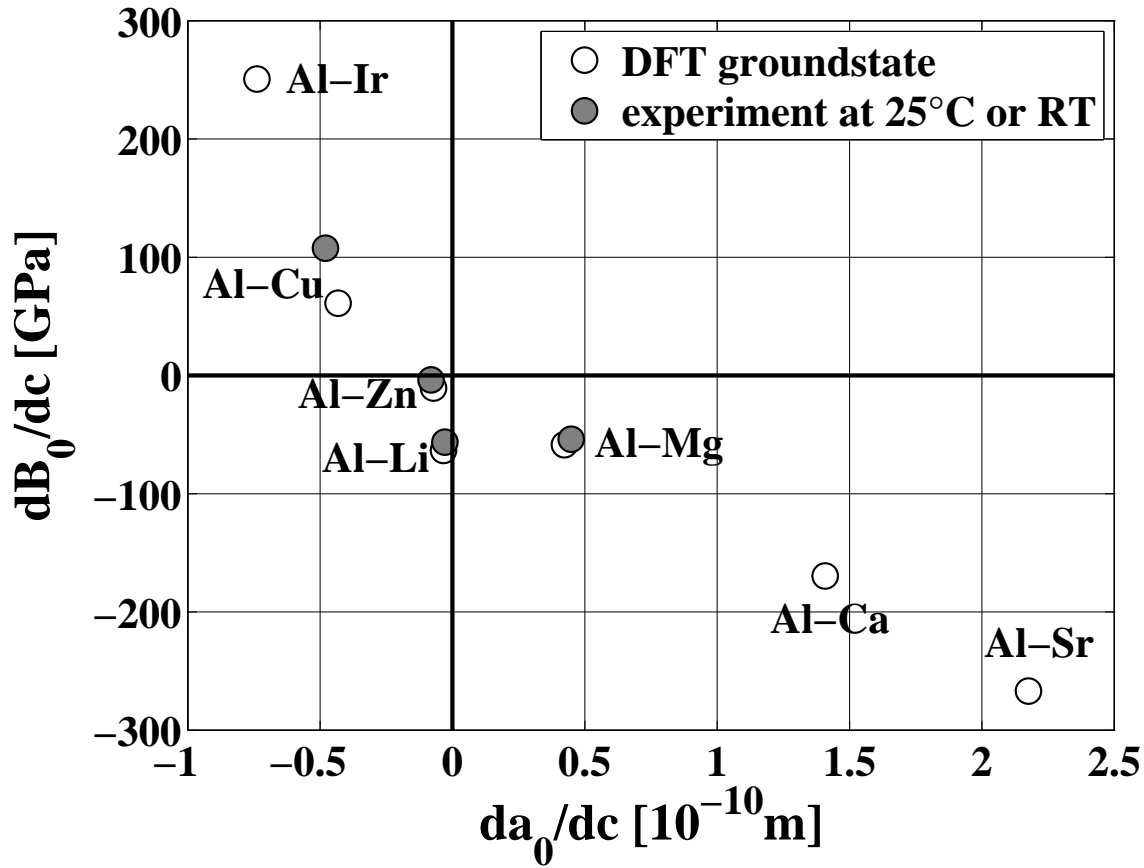
Figure 4.3: dB_0/dc vs. da_0/dc of the studied Al binary solid solutions calculated by DFT compared with experiments at 25°C or room temperature. References of the experiments are listed in the caption of Figure 4.2.

Figure 4.3 shows the comparison of the calculated and measured compositional dependence of the lattice parameter and the bulk modulus. This plot reveals that the lower the bulk modulus the larger the lattice parameter. But it does not mean the volume contraction introduced by the solute elements definitely leads to a higher bulk modulus. As shown in Figure 4.3, Li and Zn introduce the volume contraction but lower the bulk modulus which is confirmed by both the calculation and the measurement.

4.2.3 Comparison of DFT with Vegard's law

Figure 4.4 shows the comparison of the compositional dependence of the lattice parameters by DFT and Vegard's law. The end members in Vegard's law are the lattice parameters of fcc Al and fcc X. The deviation of Vegard's law from DFT is listed in Table 4.3.

Vegard's law can only qualitatively reproduce the lattice parameters of solid solutions. The lattice parameter of Li in fcc structure is larger than Al (Table 4.2), however, Li introduces volume contraction in Al, which is the reason for the large discrepancy between DFT and Vegard's law.
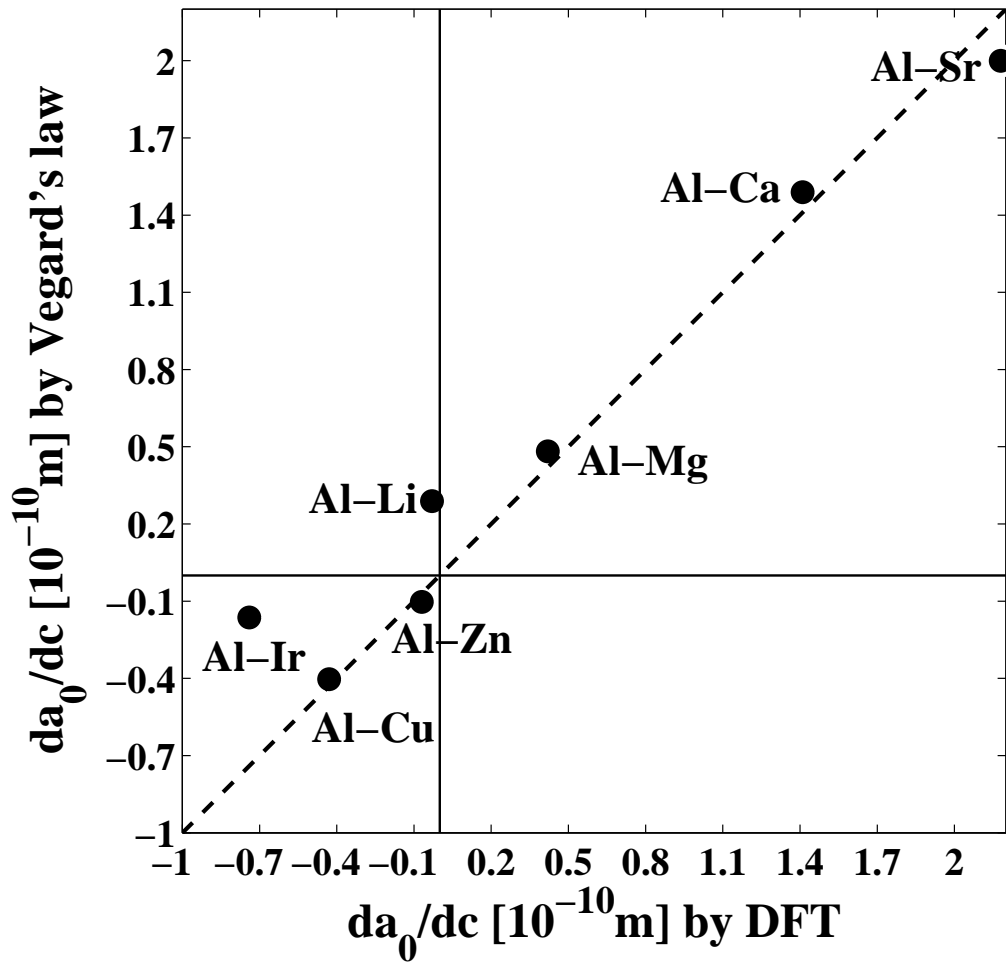
Figure 4.4: The compositional dependence of the lattice parameters of the studied Al binary solid solutions by DFT and Vegard's law. The end members in Vegard's law are the lattice parameters of fcc Al and fcc X.

Table 4.3: Deviation of the Vegard's law from DFT according to Figure 4.4.

	Al-Ca	Al-Sr	Al-Ir	Al-Cu	Al-Mg	Al-Li	Al-Zn
Deviation [%]	5.6	-8.3	-78.0	-6.3	14.8	-1062.5	46.6

4.3 Enthalpies of studied Al binary solid solutions

Solubility is an important knowledge in the context of the solid solution strengthening. In principle, a phase diagram can be fully reproduced or predicted by DFT, but the non-configurational entropies, the vibrational entropy and the magnetic entropy, are computationally expensive. For simplicity, it is focused on the enthalpies, especialy the enthalpies related to the solubility in this thesis.

4.3.1 Denotation of enthalpies

Before the calculated enthalpies are discussed, the denotation of the enthalpies should be described:

(a) Enthalpy of mixing per atom, ΔH_{mix}.

$$\Delta H_{mix} = E^{fcc}_{Al_{1-c}X_c} - (1-c) \cdot E^{fcc}_{Al} - c \cdot E^{eq}_{X} \tag{4.1}$$

where E is the equilibrium total energy per atom; the subscript denotes the chemical composition; the superscript denotes the crystal structure. For pure X, the crystal structure is the equilibrium crystal structure at groundstate (see Table 4.1 and 4.1). $E^{fcc}_{Al_{1-c}X_c}$ is calculated by using dilute ordered supercells to approximate the solid solutions with randomly distributed solute atoms.

(b) Solubility enthalpy per atom, ΔH_{sol}.

$$\Delta H_{sol} = E^{fcc}_{Al_{1-c}X_c} - (1-c) \cdot E^{fcc}_{Al} - c \cdot (E^{eq}_{Al_mX_n} - \frac{m}{m+n} \cdot E^{fcc}_{Al}) \cdot \frac{m+n}{n} \tag{4.2}$$

where $E^{eq}_{Al_mX_n}$ is the equilibrium total energy of the binary intermetallic compound immediate next to the primary Al solid solutions. The difference between ΔH_{mix} and ΔH_{sol} is one of the end members. For ΔH_{mix}, the end members are pure Al and X both in equilibrium crystal structure. For ΔH_{sol}, the end members are pure Al and the chemical potential of X in the intermetallic compound Al_mX_n. In the studied Al binary alloys, the supersaturated solid solutions do not decompose into pure Al and X, but rather Al and the intermetallic compounds. Thus ΔH_{sol} should give better insight into the solubility of X in Al.

(c) Enthalpy of mixing per solute, $\Delta H_{mix}(\text{per solute})$, and solubility enthalpy per solute, $\Delta H_{sol}(\text{per solute})$.
Both ΔH_{mix} and ΔH_{sol} approach 0 when c approaches 0. But the enthalpy of mixing per solute and the solubility enthalpy per solute do not vanish when c approaches 0, and they are defined as:

$$\Delta H_{mix}(\text{per solute}) = \frac{1}{c} \cdot \Delta H_{mix} \tag{4.3}$$

$$\Delta H_{sol}(\text{per solute}) = \frac{1}{c} \cdot \Delta H_{sol} \tag{4.4}$$

Pictorial speaking, if ΔH_{mix} and ΔH_{sol} are plotted against c, ΔH_{mix}(per solute) and ΔH_{sol}(per solute) are the slopes of these enthalpies as c approaches 0.

4.3.2 Enthalpy of mixing of studied Al binary solid solutions

4.3.2.1 Enthalpy of mixing per atom, ΔH_{mix} of studied Al binary solid solutions
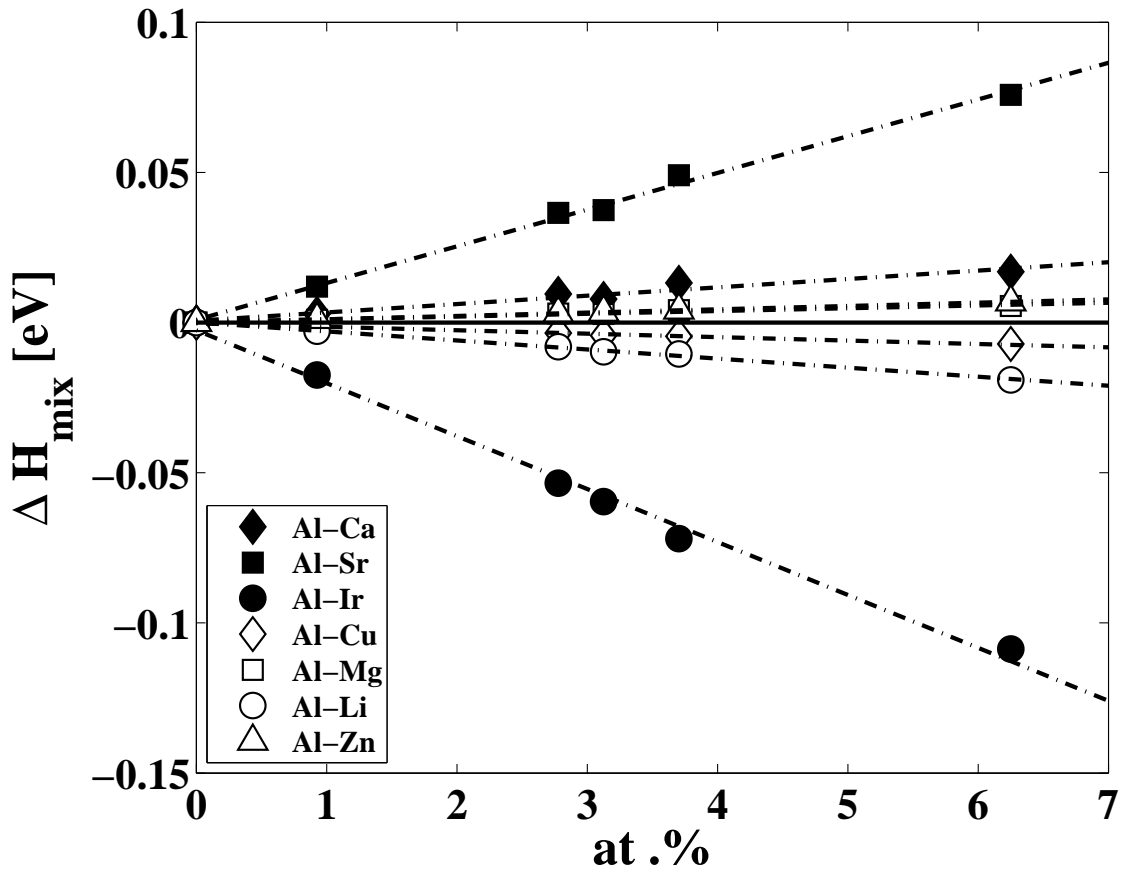
Figure 4.5: The enthalpies of mixing per atom (Equation (4.1)) of the studied Al binary solid solutions.

Figure 4.5 shows the enthalpies of mixing per atom of the studied Al binary systems. The enthalpies of mixing per atom are negative in Al-Ir, Al-Cu, and Al-Li, while they are positive in other systems.
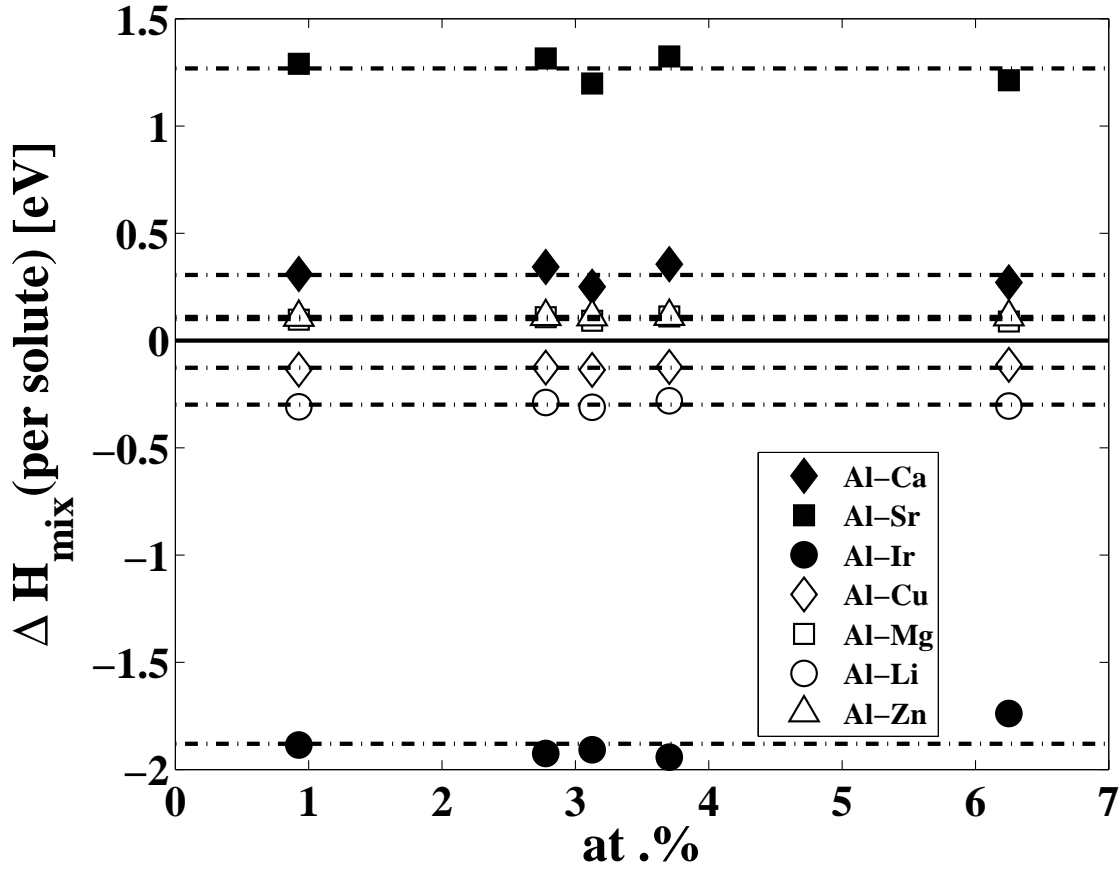
Figure 4.6: The enthalpy of mixing per solute (Equation (4.3)), ΔH_{mix}(per solute) of the studied Al binary solid solutions.

4.3.2.2 Enthalpy of mixing per solute, ΔH_{mix}(per solute) of studied Al binary solid solutions

The enthalpies of mixing per solute of the studied Al binary systems are shown in Figure 4.6. Within the studied concentration range, the enthalpies of mixing per solute for each solute element are almost identical at different concentrations.

The enthalpies of mixing per solute calculated in this thesis are compared with other theoretical studies shown in Table 4.4.

Wolverton and Ozoliņš performed very similar calculations (Wolverton and Ozoliņš, 2006). One major difference is the exchange-correlation functional. They used LDA, but PBE was employed in this thesis. The largest discrepancy between this thesis and (Wolverton and Ozoliņš, 2006) is in Al-Mg with the deviation from this thesis being ∼50 %. The source of this large discrepancy is currently unknown.

The other studies are conducted on higher concentrations by using special treatments on the solid solutions, such as SQS and CPA (see Table 1.2). ΔH_{mix}(per solute) of Al-Ir and Al-Zn in this thesis can reproduce the calculation by using SQS (Jiang and Gleeson, 2006) or CPA

(Smirnova et al., 2002). For Al-Cu, the agreement with Wang et al. (2009) is only satisfactory. The largest discrepancy occurs in Al-Mg. The predictions in this thesis and the one by using SQS (Zhong et al., 2005) are at different order of magnitude. The source of this large discrepancy is currently also unknown.

Table 4.4: The enthalpy of mixing per solute, ΔH_{mix}(per solute) of the studied Al binary solid solutions compared with other theoretical studies. Method lists: (1) the exchange-correlation functional; (2) the method of mimicking the randomness of the solid solution (OSC: ordered supercell; SQS: special quasi-random structure; CPA: coherent potential approximation).

	This study		Other work			
	c	ΔH_{mix} (per solute)	c	ΔH_{mix} (per solute)		
System	[at.%]	[eV]	[at.%]	[eV]	Method	Reference
Al-Ca	0.926	0.310				
	2.778	0.343				
	3.125	0.250				
	3.704	0.356				
	6.25	0.271				
Al-Sr	0.926	1.290	1.5625	1.04	LDA	Wolverton and Ozoliņš (2006)
	2.778	1.315	3.125	0.88	OSC	
	3.125	1.198				
	3.704	1.324				
	6.25	1.213				
Al-Ir	0.926	-1.886	25	-1.704	PW91	Jiang and Gleeson (2006)
	2.778	-1.925			SQS	
	3.125	-1.908				
	3.704	-1.942				
	6.25	-1.739				
Al-Cu	0.926	-0.136	6.25	-0.0750	PW91	Wang et al. (2009)
	2.778	-0.126	12.5	-0.0907	SQS	
	3.125	-0.137	18.75	-0.113		
	3.704	-0.123	1.5625	-0.080	LDA	Wolverton and Ozoliņš (2006)
	6.25	-0.114	3.125	-0.100	OSC	
Al-Mg	0.926	0.097	25	0.0154	PBW96	Zhong et al. (2005)
	2.778	0.108			SQS	
	3.125	0.092	1.5625	0.05	LDA	Wolverton and Ozoliņš (2006)
	3.704	0.112			OSC	
	6.25	0.089				
Al-Li	0.926	-0.309	1.5625	-0.38	LDA	Wolverton and Ozoliņš (2006)
	2.778	-0.289	3.125	-0.37	OSC	
	3.125	-0.311				
	3.704	-0.281				
	6.25	-0.305				
Al-Zn	0.926	0.108	10	0.124	PBE	Smirnova et al. (2002)
	2.778	0.111	20	0.102	CPA	
	3.125	0.110	30	0.0804		
	3.704	0.112	1.5625	0.11	LDA	Wolverton and Ozoliņš (2006)
	6.25	0.110			OSC	

4.3.3 Solubility enthalpy of studied Al binary solid solutions

4.3.3.1 Studied Al binary intermetallic compounds

To calculate ΔH_{sol}, the knowledge of the total energy of the relevant intermetallic compound is required. The crystal structures of the intermetallic compounds immediate next to the Al primary solid solutions are listed in Table 4.5.

Table 4.5: Crystal structures of the intermetallic compounds immediate next to the Al primary solid solutions of the studied Al binary systems. Whether calculated: whether this compound is calculated in this thesis.

System	Compound	Strukturbericht	Prototype	Whether calculated
Al-Ca	Al_4Ca	$D1_3$	Al_4Ba	Yes
Al-Sr	Al_4Sr	$D1_3$	Al_4Ba	Yes
Al-Ir	Al_9Ir_2	$D8_d$	Co_2Al_9	No
Al-Cu	Al_2Cu	C16	Al_2Cu	Yes
Al-Mg	$Al_{140}Mg_{89}$		Cd_2Na	No
Al-Li	AlLi	B32	NaTl	Yes
Al-Zn				

In this thesis, not all the listed compounds were calculated as indicated in Table 4.5. The total energy of those which were not calculated were obtained in the following way:

Al_9Ir_2 The formation enthalpies of Al_9Ir_2 and AlIr (B2 structure) were calculated by Jiang and Gleeson (Jiang and Gleeson, 2006). In this thesis, the formation enthalpy of AlIr was calculated and compared with Jiang and Gleeson (2006). This difference allows to speculate the formation enthalpy of Al_9Ir_2 under the calculation setup in this thesis. The total energy of Al_9Ir_2 was calculated according to the speculated formation enthalpy of Al_9Ir_2, and the total energies of pure fcc Al and Ir in this thesis. The difference of the formation enthalpy of AlIr between this thesis and Jiang and Gleeson (2006) is ~1 %.

$Al_{140}Mg_{89}$ Due to the limitation of the computational power, the calculation of $Al_{140}Mg_{89}$ is not feasible. The total energy of $Al_{140}Mg_{89}$ was approximated by the total energies of the compounds with the composition close to $Al_{140}Mg_{89}$. The total energies of three Laves phases C15, C14, C36 at the composition of Al_2Mg were calculated by Zhong et al. (Zhong et al., 2005). It is found that Al_2Mg (C36) has the minimum total energy. Therefore, in this thesis, the total energy of Al_2Mg (C36) calculated by Zhong et al. (Zhong et al., 2005) was used as an approximated total energy of $Al_{140}Mg_{89}$. Since there is no stable Al_2Mg C36 phase in Al-Mg binary system, the calculated solubility enthalpy by using the approximated total energy of $Al_{140}Mg_{89}$ must be lower than the true values. Hence it cannot be fully trusted.

In Al-Zn binary system, there is no intermetallic compound. Therefore, the solubility enthalpy is equivalent to the enthalpy of mixing in Al-Zn system.

4.3.3.2 Solubility enthalpy per atom, ΔH_{sol} of studied Al binary solid solutions
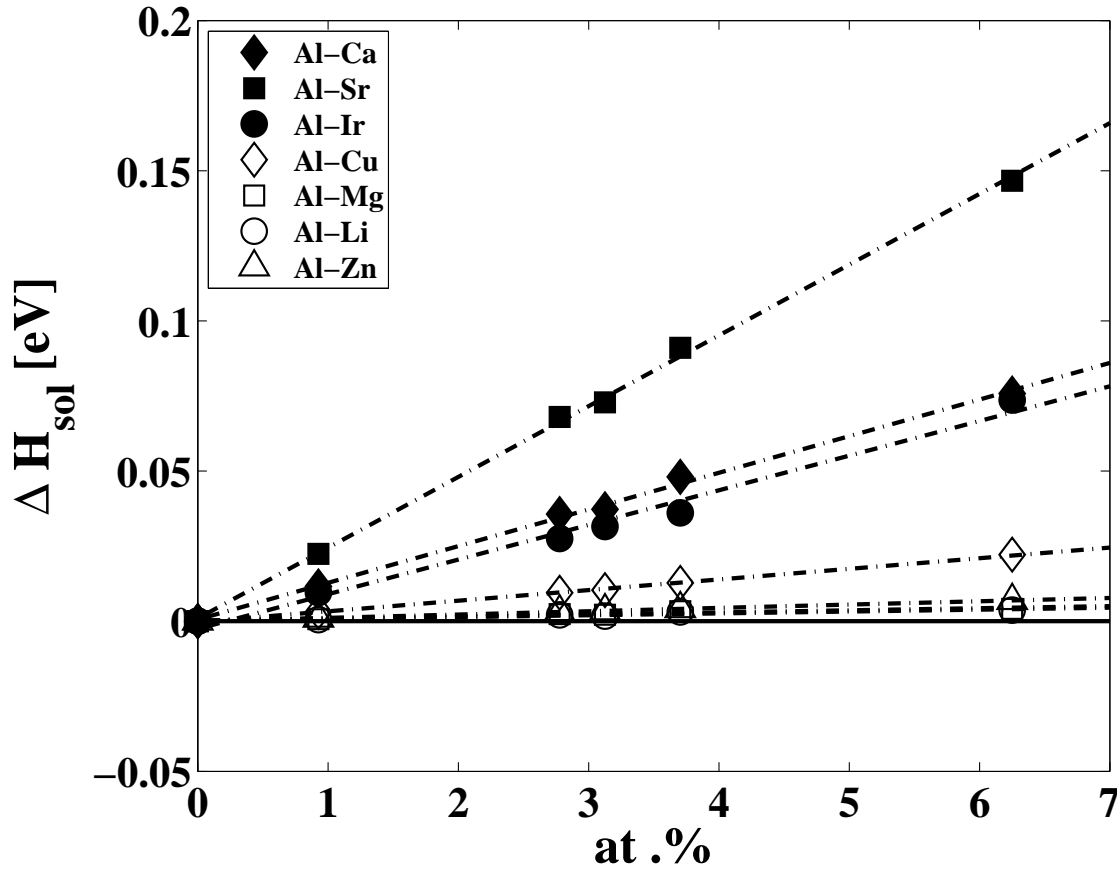
Figure 4.7: The solubility enthalpies per atom (Equation (4.2)) of the studied Al binary solid solutions.

The solubility enthalpies per atom of the studied Al binary systems are shown in Figure 4.7. All the calculated solubility enthalpies per atom are positive. This is consistent with the solubility of the studied solute elements in Al, because the solubilities of them are usually very low except at elevated temperature.

4.3.3.3 Solubility enthalpy per solute, ΔH_{sol}(per solute) of studied Al binary solid solutions
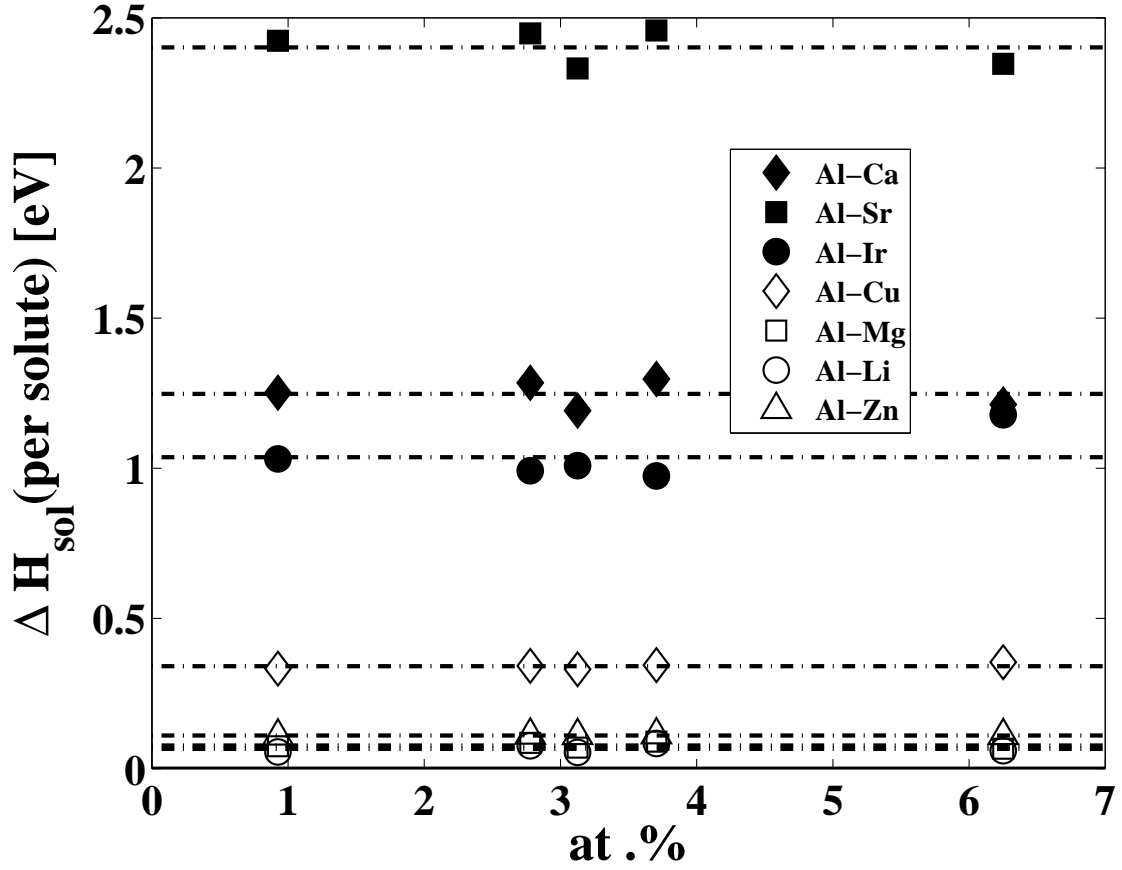
Figure 4.8: The solubility enthalpies per solute (Equation (4.4)) of the studied Al binary solid solutions.

The solubility enthalpies per solute of the studied Al binary systems are shown in Figure 4.8. The solubility enthalpy, however, does not correspond to the solubility of the solute element in Al. For instance, Zn has a wide solubility in Al up to ~67 at.%, and the maximum solubility of Li in Al is ~14 at.%. In Figure 4.8, the solubility enthalpy of Al-Li is lower than that of Al-Zn.
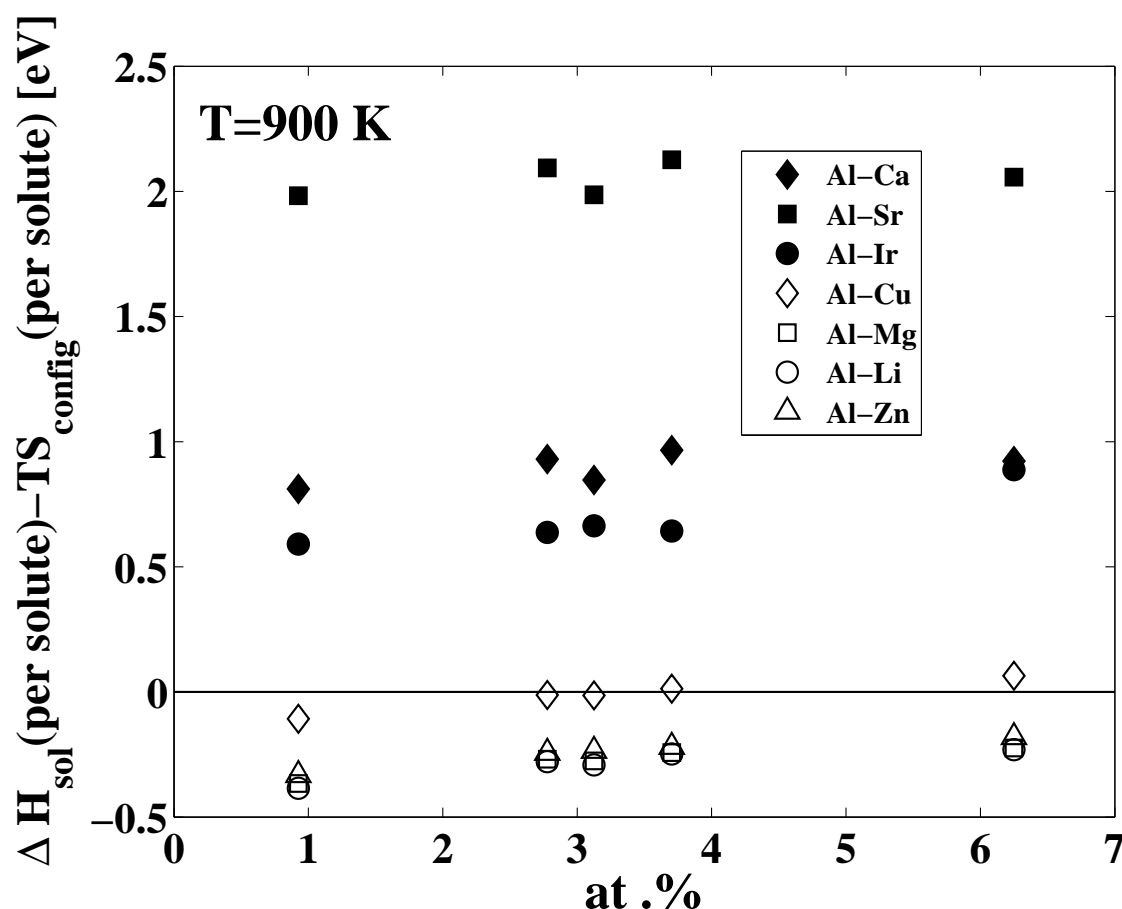
Figure 4.9: The solubility free energy (without vibrational entropy) per solute of the studied Al binary solid solutions at 900 K. 900 K is approximately the melting point of pure Al.

Another factor which determines the solubility is the entropy. The solubility free energy without the vibrational entropy per solute at 900 K are plotted in Figure 4.9. According to Figure 4.9, Cu has a limited solubility even at 900 K (<3 at.%). Li and Zn dissolve in Al readily at least up to 6.25 at.%. These observations are consistent with the Al-Cu (Murray, 1985), Al-Li (McAlister, 1982) and Al-Zn (Murray, 1983) phase diagrams. The solubility free energy of Al-Mg indicates that Mg dissolve in Al up to 6.25 at.% which is consistent with the Al-Mg phase diagram (Murray, 1982). As stated in Section 4.3.3.1, the total energy of the intermetallic compound in Al-Mg binary system was approximated in this thesis. Thus, the solubility free energy per solute of Al-Mg in Figure 4.9 cannot be fully trusted, although the observation is consistent with the phase diagram.

According to Figure 4.9, Ca, Sr, and Ir have no solubility in Al even at 900 K. However, the solubilities of Ca (Nowotny et al., 1940) and Ir (Axler et al., 1989; Hill et al., 1998) in Al have been experimentally observed. This indicates that the solublity of Ca and Ir in Al is driven by the vibrational entropy.

Chapter 5

Elastic properties of studied Al binary solid solutions

5.1   Elastic constants of selected pure elements in fcc structure

The elastic constants of selected pure elements in fcc structure are listed in Table 5.1. The agreement between the calculated and the measured elastic constants is not as good as the properties from the equation of states (Table 4.1 and Table 4.2). For Al, Cu and Ir, the error of the calculation from the measurements (close to 0 K, e.g. 4.2 K) is within ±8%. The measurements of the elastic constants of Ca and Sr are conducted at higher temperatures. Nevertheless, the magnitude of the calculated elastic constants of Ca and Sr are at least in reasonable agreement with the measurements, and the differences are ranged within 0.3~5 GPa.

Table 5.1: The elastic constants [GPa] of the selected pure elements in fcc structure.

		C_{11}	C_{12}	C_{44}	Reference
Al	this study	111.2	59.9	34.1	
	exp.	114.43	61.92	31.62	Kamm and Alers (1964)[a]
Cu	this study	171.0	119.6	77.3	
		176.2	124.94	81.77	Overton and Gaffney (1955)[a]
	exp.	176.2	124.94	81.76	Rayne (1959)[b]
		176.99	124.97	81.45	Waldorf (1960)[b]
Ir	this study	579.3	229.4	254.5	
	exp.	596	242	270	MacFarlane et al. (1966)[a]
Ca	this study	22.6	14.8	15.4	
		25±3	15±1	20±1	Buchenau et al. (1981)[c]
	exp.	27.801	16.304	18.225	Stassis et al. (1983)[c]
		22.8	16±0.6	14±3	Heiroth et al. (1986)[d]
Sr	this study	15.9	9.7	10.7	
	exp.	15.6	10.2±0.4	12.1±0.9	Buchenau et al. (1984)[e]

[a] From T=4.2 extrapolated to T=0K
[b] At T=4.2K
[c] Calculated from the phonon dispersion curves measured at room temperature.
[d] Calculated from the phonon dispersion curves measured at 300 K.
[e] Calculated from the phonon dispersion curves measured at 100 K.

5.2 Elastic constants of studied Al binary solid solutions

5.2.1 $C_{11} - C_{12}$ and C_{44} of Al-Ca and Al-Sr solid solutions

The calculated elastic constants ($C_{11} - C_{12}$, and C_{44}) of Al-Ca and Al-Sr solid solutions are shown in Figure 5.1 and 5.2.

The compositional dependences of $C_{11} - C_{12}$ and C_{44} of Al-Ca and Al-Sr are very similar, while Sr is more effective in decreasing both elastic constants. Especially, C_{44} of the Al-Sr solid solution at 6.25 at.% ($Al_{30}Sr_2$) is even close to C_{44} of pure Sr (Table 5.1).

In Figure 5.1 and 5.2, one may notice that by using different supercells, the compositional dependences are different. Such a supercell size dependence is more pronounced in $C_{11} - C_{12}$ than C_{44}. It creates a great uncertainty in predicting the compositional dependence of the elastic properties. The supercell size dependence is also notable in other studied systems. This phenomenon is to be explained and discussed in Section 5.3.
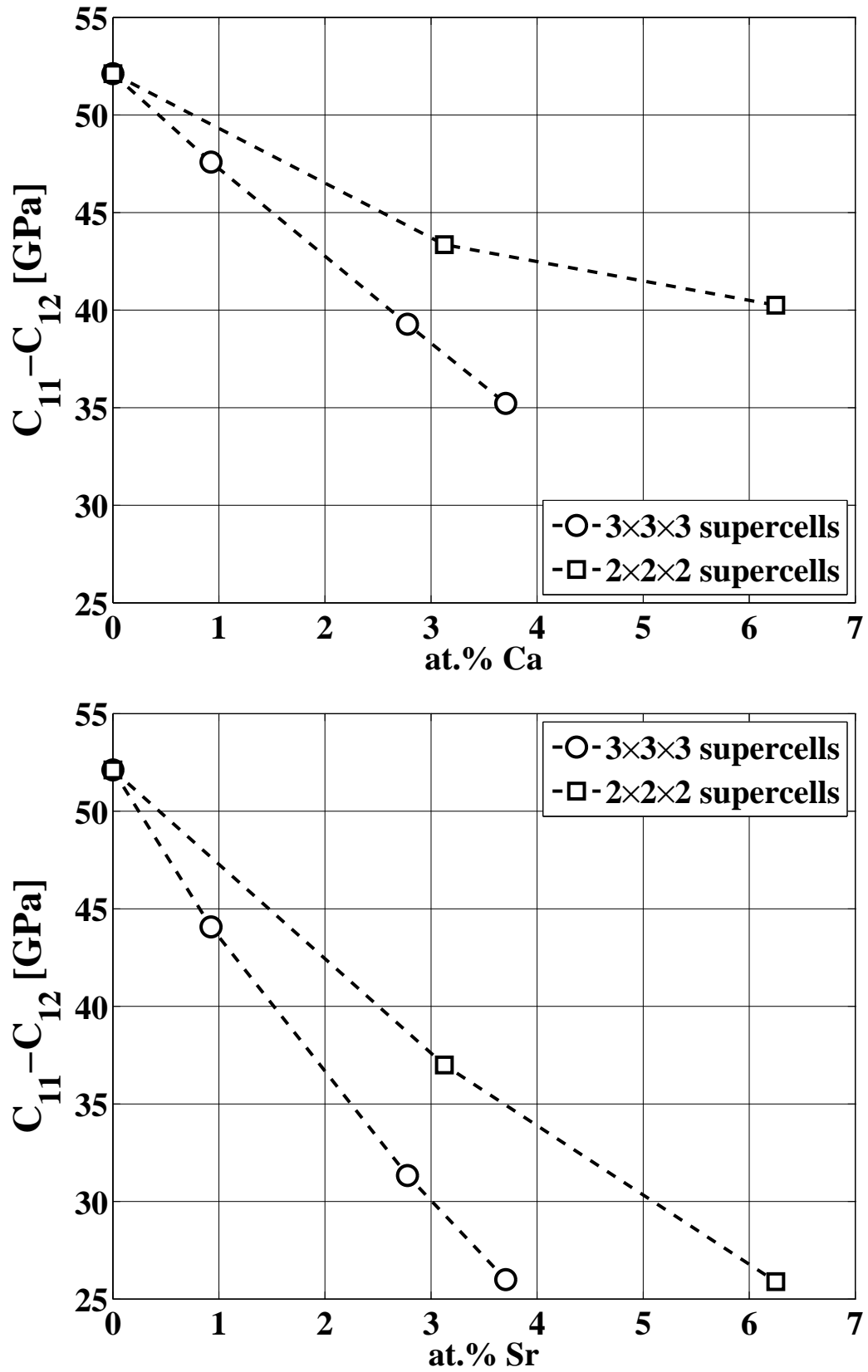
Figure 5.1: $C_{11} - C_{12}$ of Al-Ca (top) and Al-Sr (bottom) solid solutions. Open circle: calculated by using 3×3×3 supercells; open square: calculated by using 2×2×2 supercells.
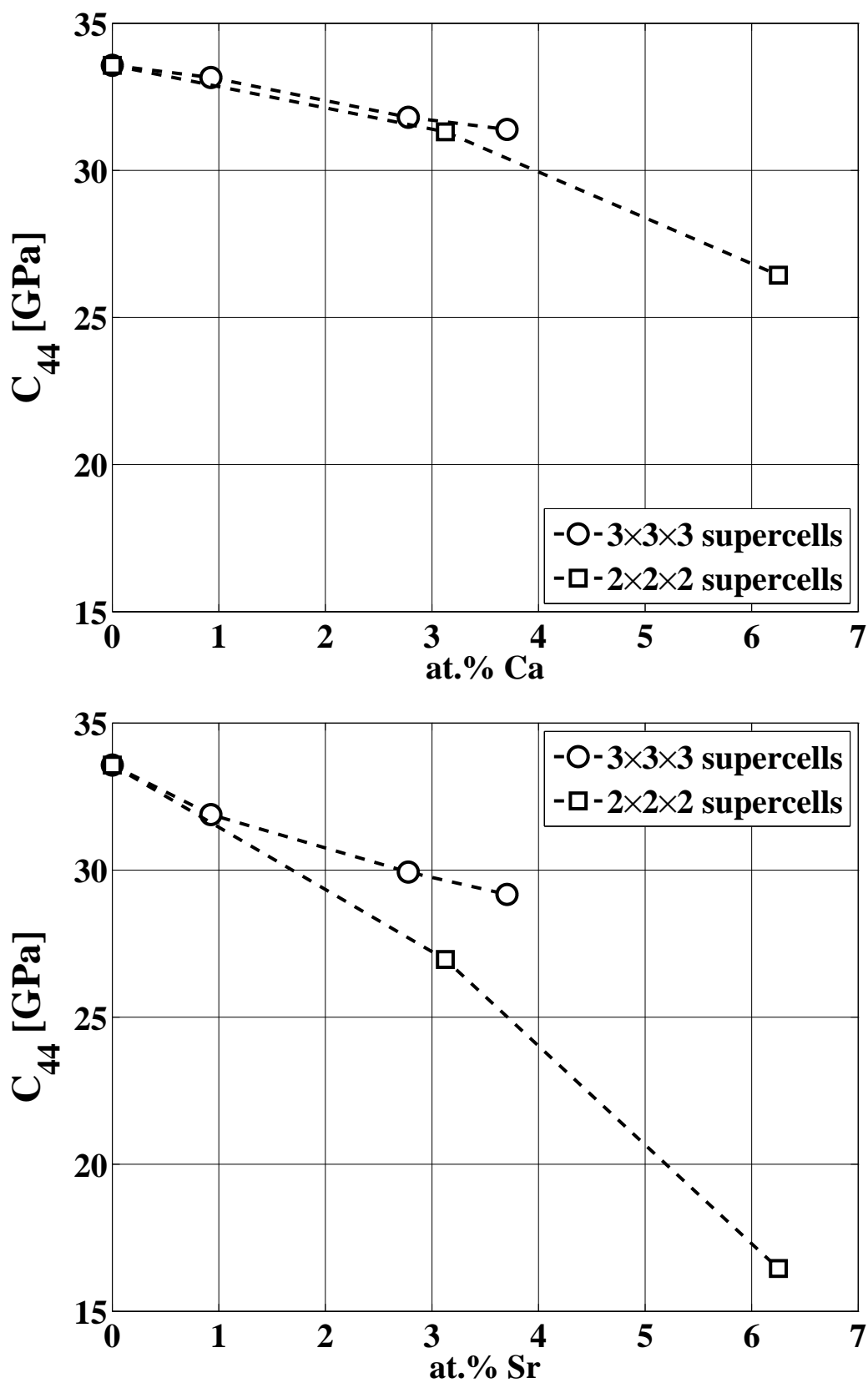
Figure 5.2: C_{44} of Al-Ca (top) and Al-Sr (bottom) solid solutions. Open circle: calculated by using 3×3×3 supercells; open square: calculated by using 2×2×2 supercells.

5.2.2 $C_{11} - C_{12}$ and C_{44} of Al-Ir and Al-Cu solid solutions

The calculated elastic constants of Al-Ir and Al-Cu solid solutions are shown in Figure 5.3 and 5.4.

Ir increases both $C_{11} - C_{12}$ and C_{44} of Al, but not monotonically. From 3.704 or 3.125 at.% (Al$_{104}$Ir$_4$ or Al$_{30}$Ir$_2$), $C_{11} - C_{12}$ and C_{44} start to decrease.

$C_{11} - C_{12}$ of Al-Cu solid solutions increases monotonically up to 3.125 or 3.704 at.% (Al$_{31}$Cu$_1$ or Al$_{104}$Cu$_4$), but $C_{11} - C_{12}$ of Al-6.25 at.% Cu (Al$_{30}$Cu$_2$) is even lower than pure Al. On the other hand, C_{44} of Al-Cu increases monotonically up to Al-6.25 at.% Cu (Al$_{30}$Cu$_2$). Apparently, the change of the elastic constants of Al by Cu is not as pronounced as by Ca, Sr, or Ir. The maximum change in $C_{11} - C_{12}$ and C_{44} of Al-Cu within the studied concentration is only ~3 and ~1 GPa.
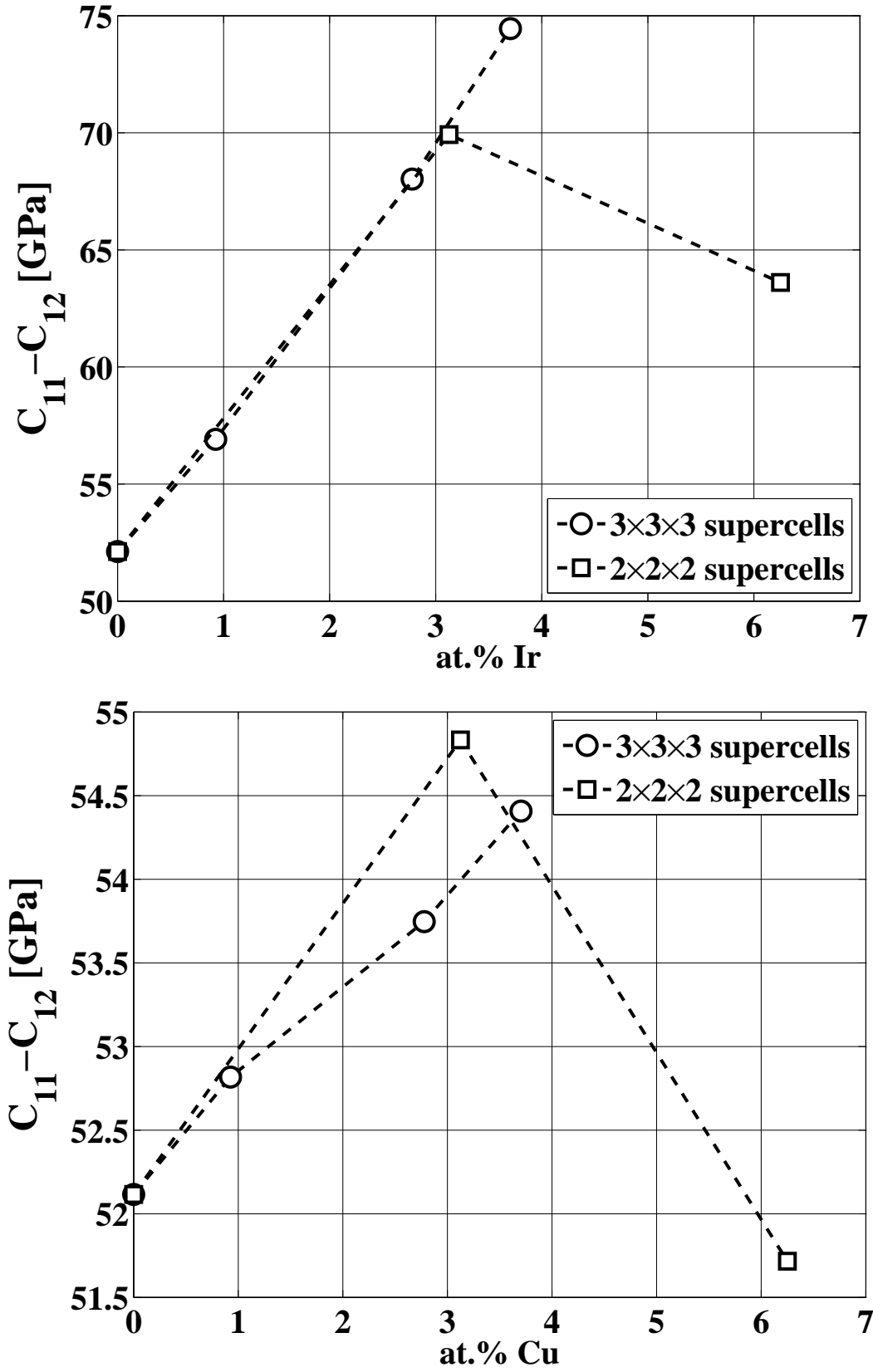
Figure 5.3: $C_{11} - C_{12}$ of Al-Ir (top) and Al-Cu (bottom) solid solutions. Open circle: calculated by using 3×3×3 supercells; open square: calculated by using 2×2×2 supercells.
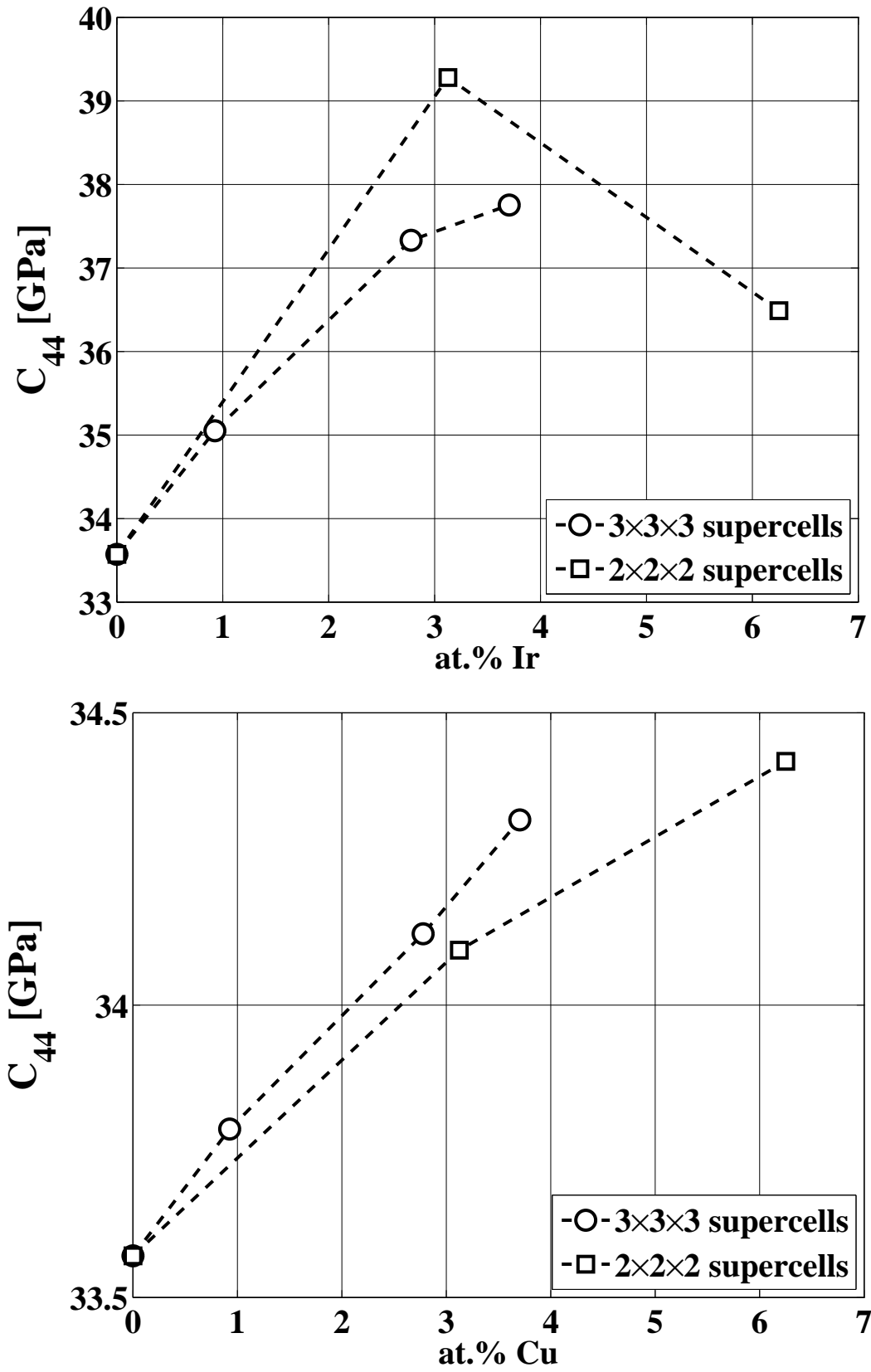
Figure 5.4: C_{44} of Al-Ir (top) and Al-Cu (bottom) solid solutions. Open circle: calculated by using 3×3×3 supercells; open square: calculated by using 2×2×2 supercells.

5.2.3 $C_{11} - C_{12}$ and C_{44} of Al-Mg and Al-Li solid solutions

The calculated elastic constants of Al-Mg and Al-Li solid solutions are shown in Figure 5.5 and 5.6. The calculated elastic constants are compared with previous theoretical work by using coherent potential approximation (CPA) (Taga et al., 2005; Zander et al., 2007) and the experiments at room temperature (Gault et al., 1977; Müller et al., 1986).

For Al-Mg solid solutions, the supercell size dependence is notable. Especially, $C_{11} - C_{12}$ of Al-Mg solid solutions calculated by 2×2×2 supercells are almost constant within studied concentrations. By using 3×3×3 supercells, $C_{11} - C_{12}$ decreases ~2 GPa from pure Al to Al-3.7037 at.%Mg. The measured $C_{11} - C_{12}$ of Al-Mg solid solutions slowly decreases as the concentration increases. From pure Al to 12 at.%Mg, $C_{11} - C_{12}$ of Al-Mg decreases ~1.1 GPa. The prediction of the compositional dependence of $C_{11} - C_{12}$ in this study is in satisfactory agreement with the experiments. The calculated C_{44} of Al-Mg increases as the concentration increases, which is in agreement with the experiments. The compositional dependence predicted by 3×3×3 supercell is ~0.0379 GPa/at.% which is close to the experiment, ~0.0313 GPa/at.%. By using 2×2×2 supercell, it is ~1.1356 GPa/at.%.

The calculated $C_{11} - C_{12}$ of Al-Li increases up to 2.778 at.% or 3.125 at.% ($Al_{105}Li_3$ or $Al_{31}Li_1$), and then decreases. The measured $C_{11} - C_{12}$ increases even up to ~4 at.% which is in good agreement with the CPA calculations (Taga et al., 2005). The compositional dependence of C_{44} of Al-Li by 2×2×2 supercells is ~0.5972 GPa/at.% which is relatively close to the the experiments, ~0.678 GPa/at.%, and it is ~0.2083 GPa/at.% by 3×3×3 supercells.
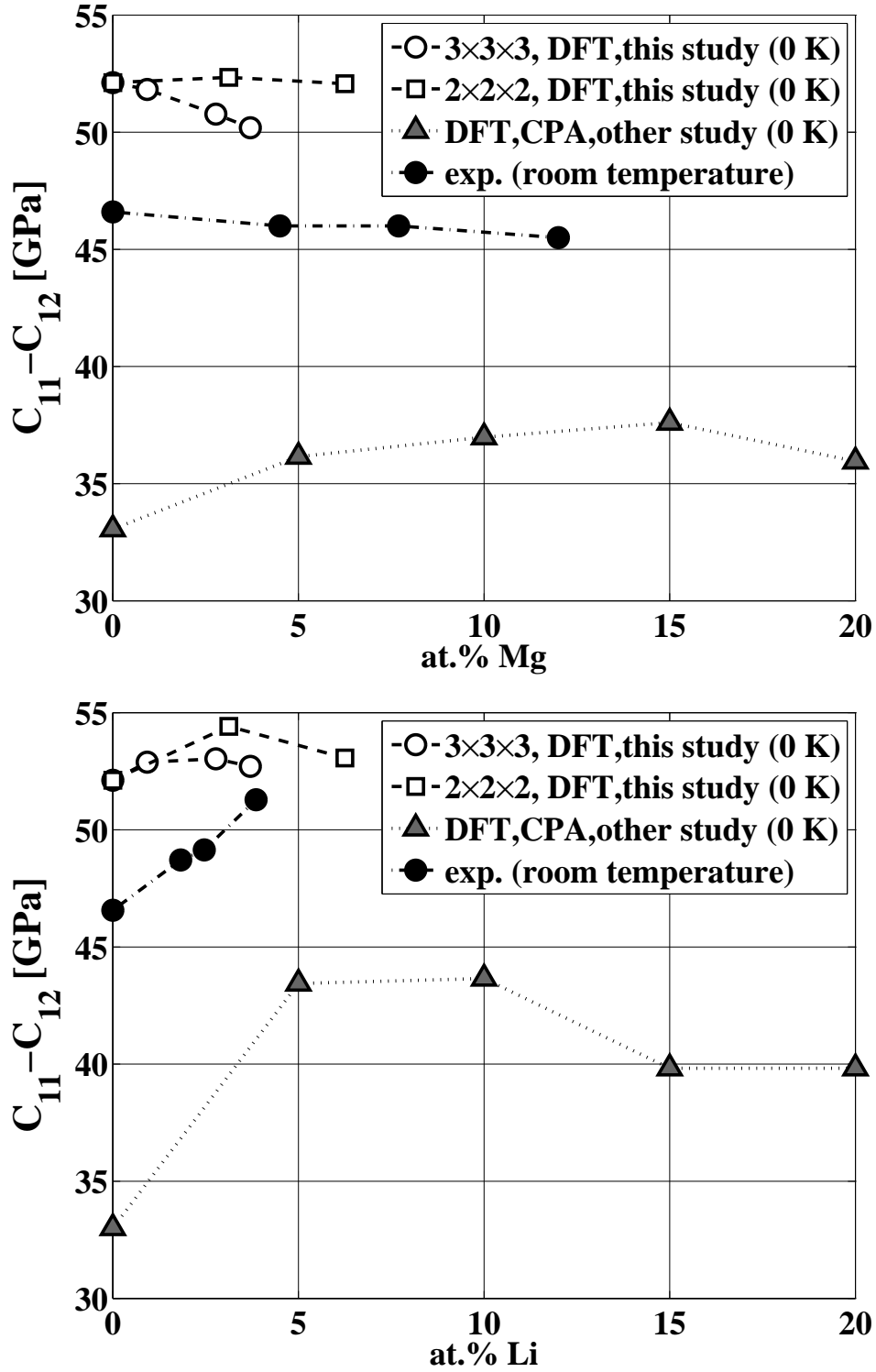
Figure 5.5: $C_{11} - C_{12}$ of Al-Mg (top) and Al-Li (bottom) solid solutions.

Open circle:	DFT, this study.	3×3×3 supercells
Open square:	DFT, this study.	2×2×2 supercells
Solid gray triangle:	DFT, CPA, other work,	Al-Mg, (Zander et al., 2007).
		Al-Li, (Taga et al., 2005).
Solid black circle:	experiments,	Al-Mg, (Gault et al., 1977).
		Al-Li, (Müller et al., 1986).
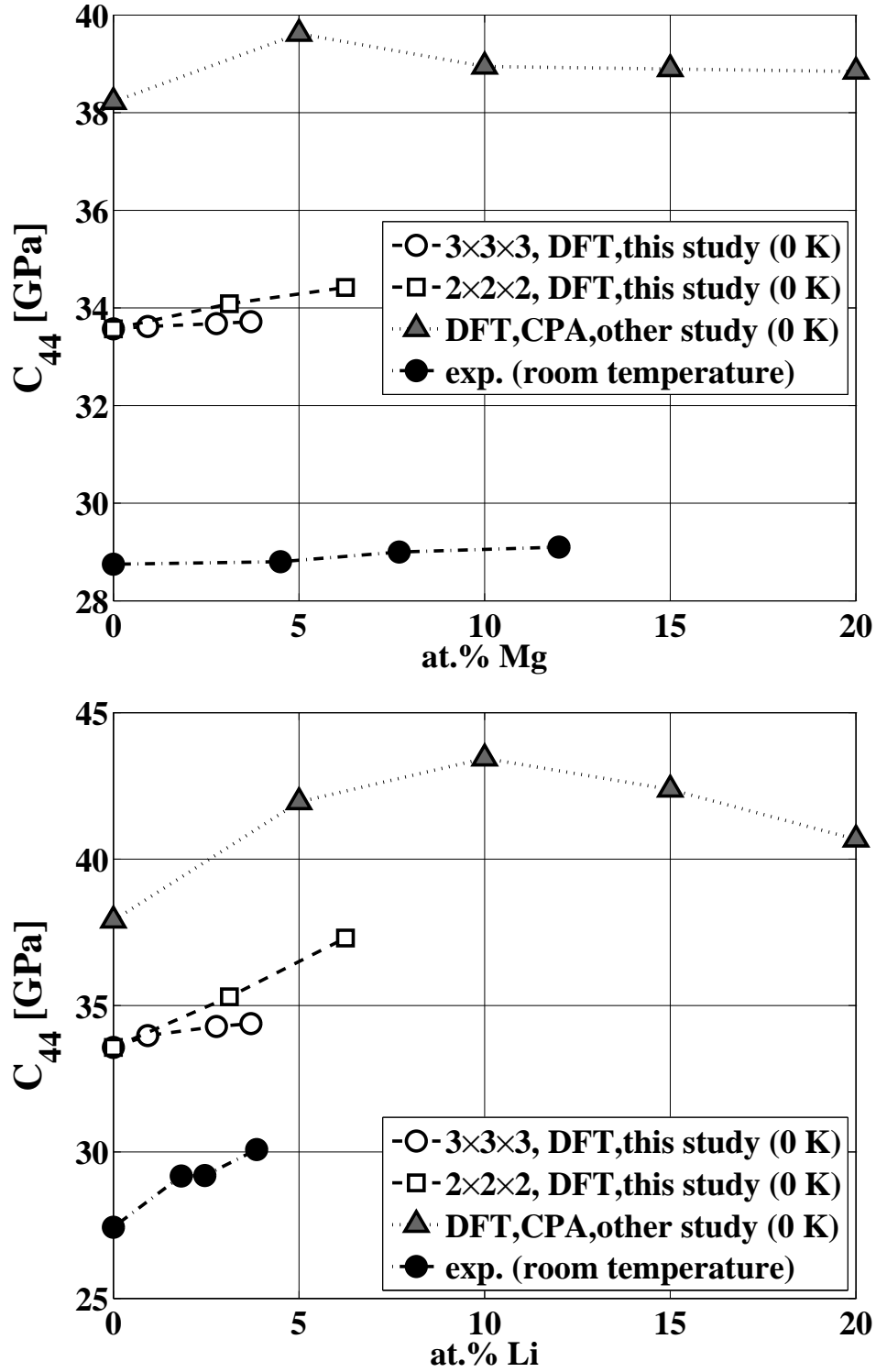
Figure 5.6: C_{44} of Al-Mg (top) and Al-Li (bottom) solid solutions.

Open circle:	DFT, this study.	3×3×3 supercells
Open square:	DFT, this study.	2×2×2 supercells
Solid gray triangle:	DFT, CPA, other work,	Al-Mg, (Zander et al., 2007).
		Al-Li, (Taga et al., 2005).
Solid black circle:	experiments,	Al-Mg, (Gault et al., 1977).
		Al-Li, (Müller et al., 1986).

5.2.4 $C_{11} - C_{12}$ and C_{44} of Al-Zn solid solutions

The calculated elastic constants of Al-Zn solid solutions are shown in Figure 5.7 compared with the experiments (Müller et al., 1986).

The calculated compositional dependence of $C_{11} - C_{12}$ does not agree with the experiments at all. As the concentration increases, the calculated $C_{11} - C_{12}$ decreases but the measured one increases.

In Figure C.16 in Appendix C, it shows that if calculation is conducted with σ=0.4 eV, the increase of $C_{11} - C_{12}$ of Al-Zn observed in the experiments can be reproduced by DFT. But it is shown that the converged results can be obtained with σ=0.8 eV (Appendix C).

Siebke and Fridrich investigated the influence of Guinier-Preston (GP) zones on the elastic constants in an Al-6.8 at.% Zn alloy (Siebke and Friedrich, 1980). As the size of the GP zones increases, $C_{11}-C_{12}$ increases and C_{44} decreases. If it is assumed that the higher the concentration the higher possibility of the formation of the GP zones, the decrease of $C_{11} - C_{12}$ of Al-Zn solid solutions is disguised by the formation of the GP zones. Since the microstructure of the Al-Zn alloys in the experiments (Müller et al., 1986) is unknown, it is not conclusive to state the elastic constants calculated in this thesis are wrong.
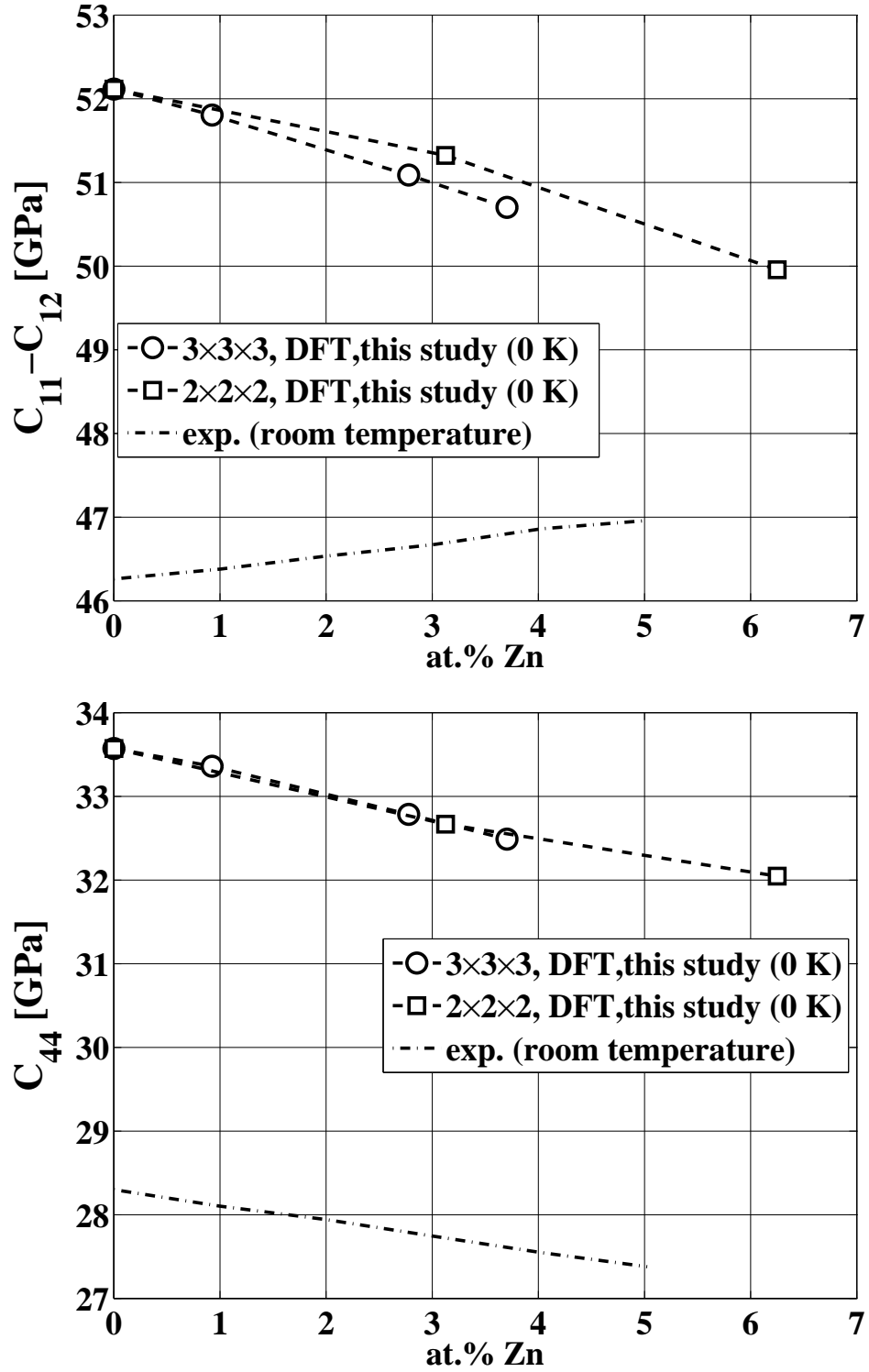
Figure 5.7: $C_{11} - C_{12}$ (too) and C_{44} of Al-Zn solid solutions.
Open circle: DFT, this study.   3×3×3 supercells
Open square: DFT, this study.   2×2×2 supercells
plain dash line: experiments,   Al-Li, (Müller et al., 1986).

5.3 Discussion on supercell size dependence

An important feature, the supercell size dependence, is observed in most of the calculated elastic constants as shown in the previous section.

In this thesis, the solid solutions were mimicked by ordered supercells. And two kinds of supercells were employed: 3×3×3 or 2×2×2 supercells. In one system, the calculated elastic constants may following the same compositional dependence but different slopes developed depending on the supercell size. This is most obvious in Al-Ca and Al-Sr solid solutions (see Figure 5.1 and 5.2).

An intuitive explanation of this phenomenon is the lack of the description of the solute atom randomness. A comparative study of the elastic constants of Al-Ti solid solutions calculated by SQSs (special quasi-structures) and the standard supercell was performed by von Pezold et al. (von Pezold et al., 2010). According to the comparative study, a 6×6×6 supercell (864 atoms in fcc) containing randomly distributed solute atoms is large enough for a good description of a disordered Al-Ti solid solution[1]. The comparative study also indicates that if the solid solution is dilute, by using smaller supercells, the supercell approximation can satisfactorily reproduce the elastic constants calculated by SQSs.

In the light of this comparative study, two aspects are responsible for the supercell size dependence: the local atomic environment and the range of the chemical interaction.

Local atomic environment Apparently the ordering of the atoms has great effect on the calculated elastic constants. Table 5.2 lists the number of the nearest Al neighbors per solute atom in each supercells. All of the solute atoms have 12 first nearest Al neighbors, but in 3×3×3 supercells, each solute atom has 6 second nearest Al neighbors, and in 2×2×2, it has only 3.

Range of the perturbation (chemical interaction) In this thesis, the perturbation caused by the solute elements was investigated by studying the average electron density of the solvent Al atoms. It is to be demonstrated that the perturbation is usually long-ranged. In some extreme cases, such as Al-Ca and Al-Sr, a 3×3×3 supercell is not large enough to cover the perturbation caused by a single solute atom. The more perturbation the solute atom causes, the more pronounced supercell size dependence there would be. This aspect is to be discussed in more detail in Chapter 7.

---

[1]In that particular study (von Pezold et al., 2010), the Al-Ti EAM potential was employed. The cut-off radius in the EAM potential is 5.77 Å. Therefore, a 6×6×6 supercell (864 atoms in fcc) containing randomly distributed solute atoms is only sufficiently large, if the chemical interaction is around 5.77 Å. If the chemical interaction is more long-ranged, namely >5.77 Å, a 6×6×6 supercell might not be sufficient.

Table 5.2: The number of nearest Al neighbors (NN) per solute atom in each supercell in this thesis.

	Concentration [at.%]	Supercell	NN								
			1st	2nd	3rd	4th	5th	6th	7th	8th	9th
$Al_{107}X_1$	0.926	3×3×3	12	6	24	12	12	8	24	3	6
$Al_{105}X_3$	2.778	3×3×3	12	6	$10\frac{2}{3}$	4	2	$\frac{1}{3}$			
$Al_{31}X_1$	3.125	2×2×2	12	3	12	3	1				
$Al_{104}X_4$	3.704	3×3×3	12	6	8						
$Al_{30}X_2$	6.25	2×2×2	12	3							

5.4 Homogenized elastic moduli of studied Al binary solid solutions

For simplicity, the modulus effect (di-elastic, see Section 2.2.1) can be treated in the framework of the isotropic elasticity. It is more applicable to Al alloys, because the Zener's ratios[2] of Al and studied Al binary solid solutions are close to unity[3]. The calculated elastic constants (tensorial quantity) should be homogenized into isotropic elastic modulus (scalar quantity). In this thesis, Hershey's homogenization method (Hershey, 1954) was used. Details of Hershey's homogenization method and other methods are presented in Section 3.4.

5.4.1 Homogenized elastic moduli of Al-Ca and Al-Sr solid solutions

The homogenized elastic moduli of Al-Ca and Al-Sr solid solutions are shown in Figure 5.8 and 5.9. Ca and Sr both decrease the homogenized shear modulus of Al. Especially, Sr decreases the homogenized shear modulus and Young's modulus of Al down to roughly half of those of pure Al.

---

[2]Zener's ratio: $A_Z = \frac{C_{11} - C_{12}}{C_{44}}$, a measure of the elastic anisotropy for the cubic symmetry. $A_Z = 1$ means elastically isotropic.

[3]The exception is Al-Sr solid solutions. The Zener's ratio could be above 2.
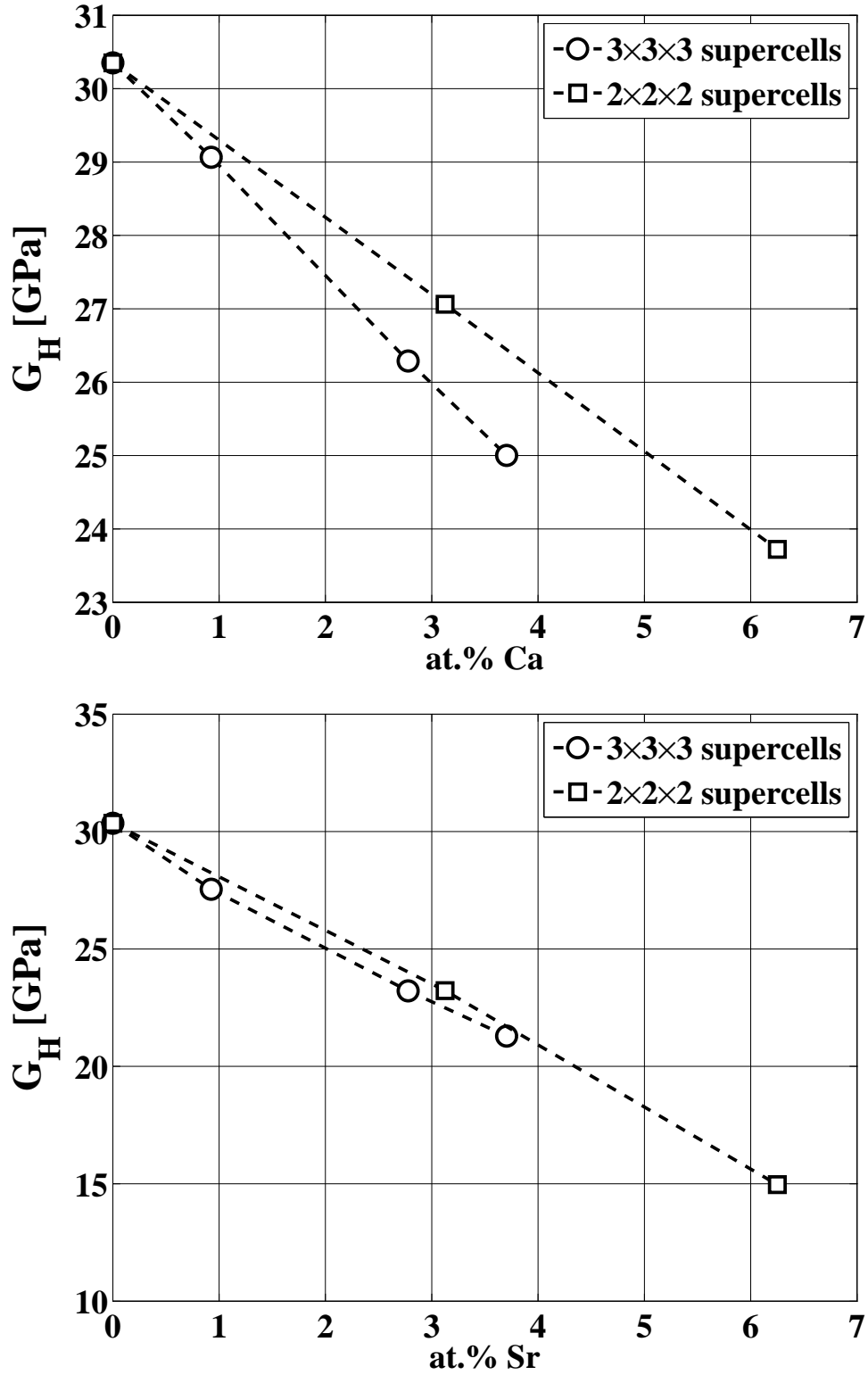
Figure 5.8: Homogenized shear moduli (G_H) of Al-Ca (top) and Al-Sr (bottom) solid solutions. Open circle: DFT, this study.
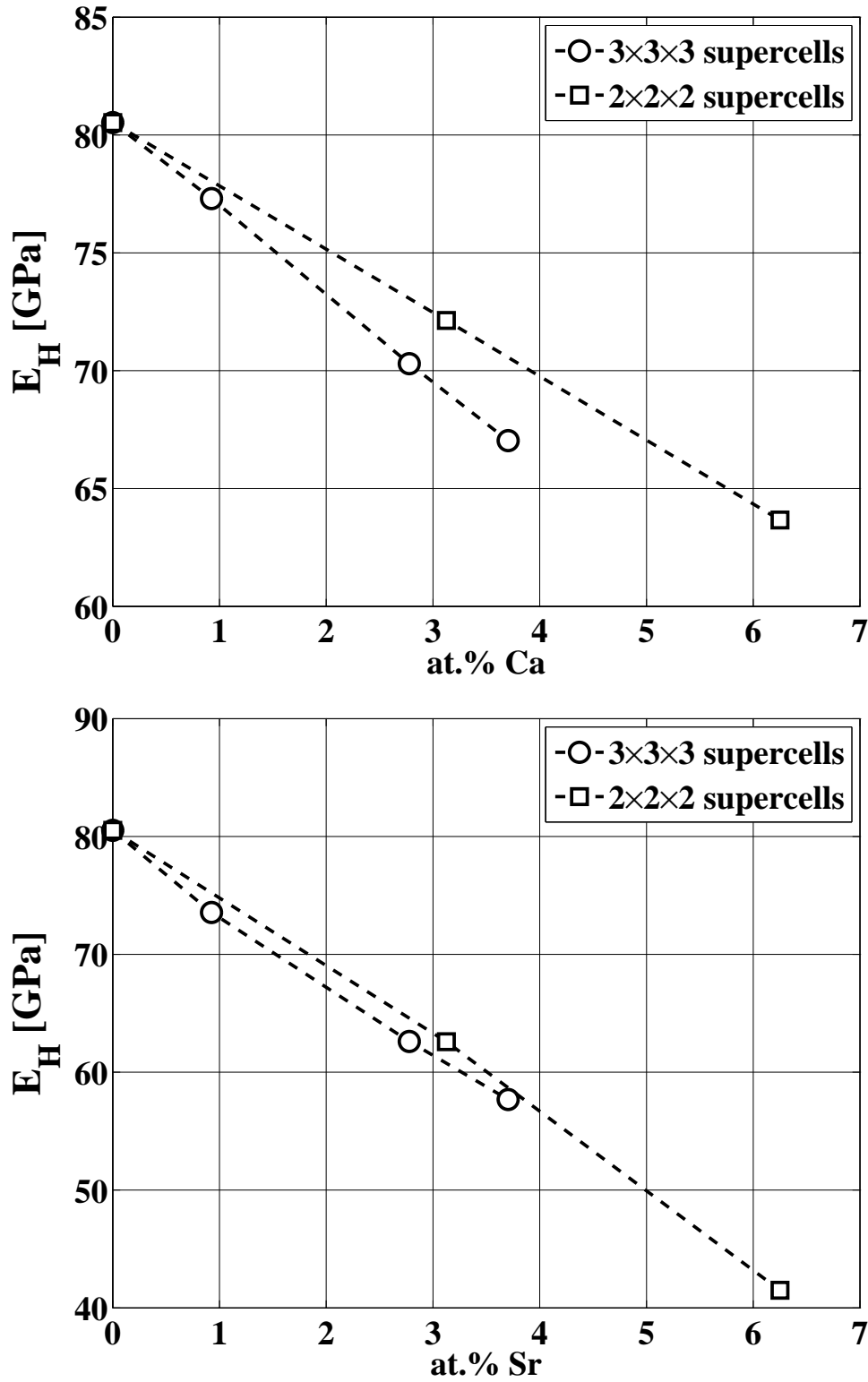
Figure 5.9: Homogenized Young's moduli (E_H) of Al-Ca (top) and Al-Sr (bottom) solid solutions. Open circle: DFT, this study.

5.4.2 Homogenized elastic moduli of Al-Ir and Al-Cu solid solutions

The homogenized elastic modulus of Al-Ir and Al-Cu solid solutions are shown in Figure 5.10 and 5.11.

Ir increases the homogenized shear modulus of Al, but not monotonically. Above the concentration of 3.125 at.% or 3.704 at.% Ir ($Al_{31}Ir_1$ or $Al_{104}Ir_4$), the homogenized shear modulus starts to decrease.

The homogenized shear moduli of Al-Cu solid solutions predicted in this study approximatedly linearly depends on the concentration below 3.125 at.% or 3.704 at.% Cu ($Al_{31}Cu_1$ or $Al_{104}Cu_4$). In this concentration range, the homogenized shear modulus increases ~0.2572 GPa/at.%, while it is ~0.3855 GPa/at.% in the measurements. The increase of the homogenized shear modulus in this thesis is underestimated compared with the measurements. This underestimation is also observed in the bulk modulus of Al-Cu solid solutions (see Figure 4.2). The monotonic increase of the shear modulus of Al-Cu solid solution is observed in the measurements up to ~8 at.% which is, however, not reproduced in this thesis.
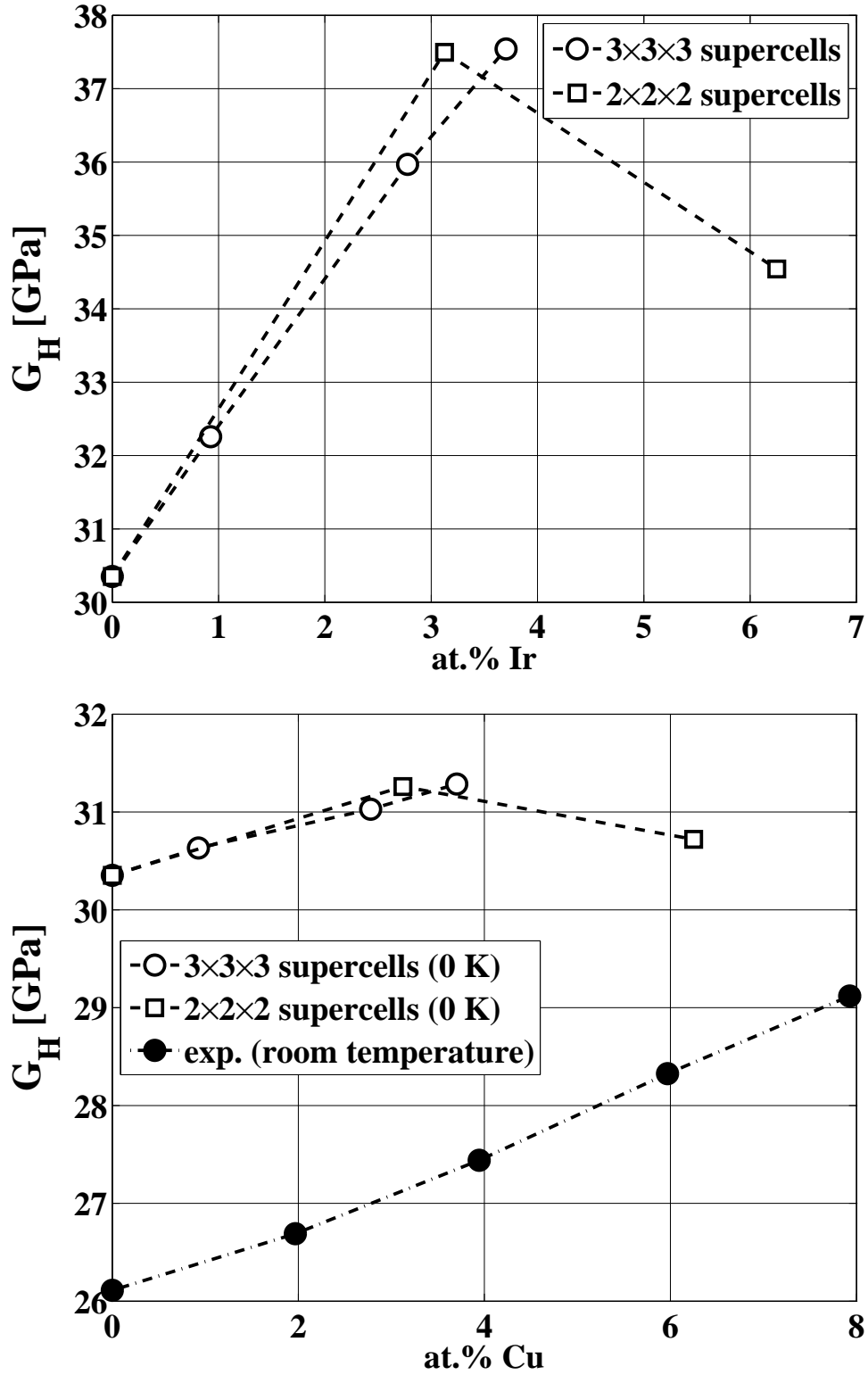
Figure 5.10: Homogenized shear moduli (G_H) of Al-Ir (top) and Al-Cu (bottom) solid solutions.

Open circle: DFT, this study.

Solid circle: experiments on polycrystals (Masafumi and Takefumi, 1988).
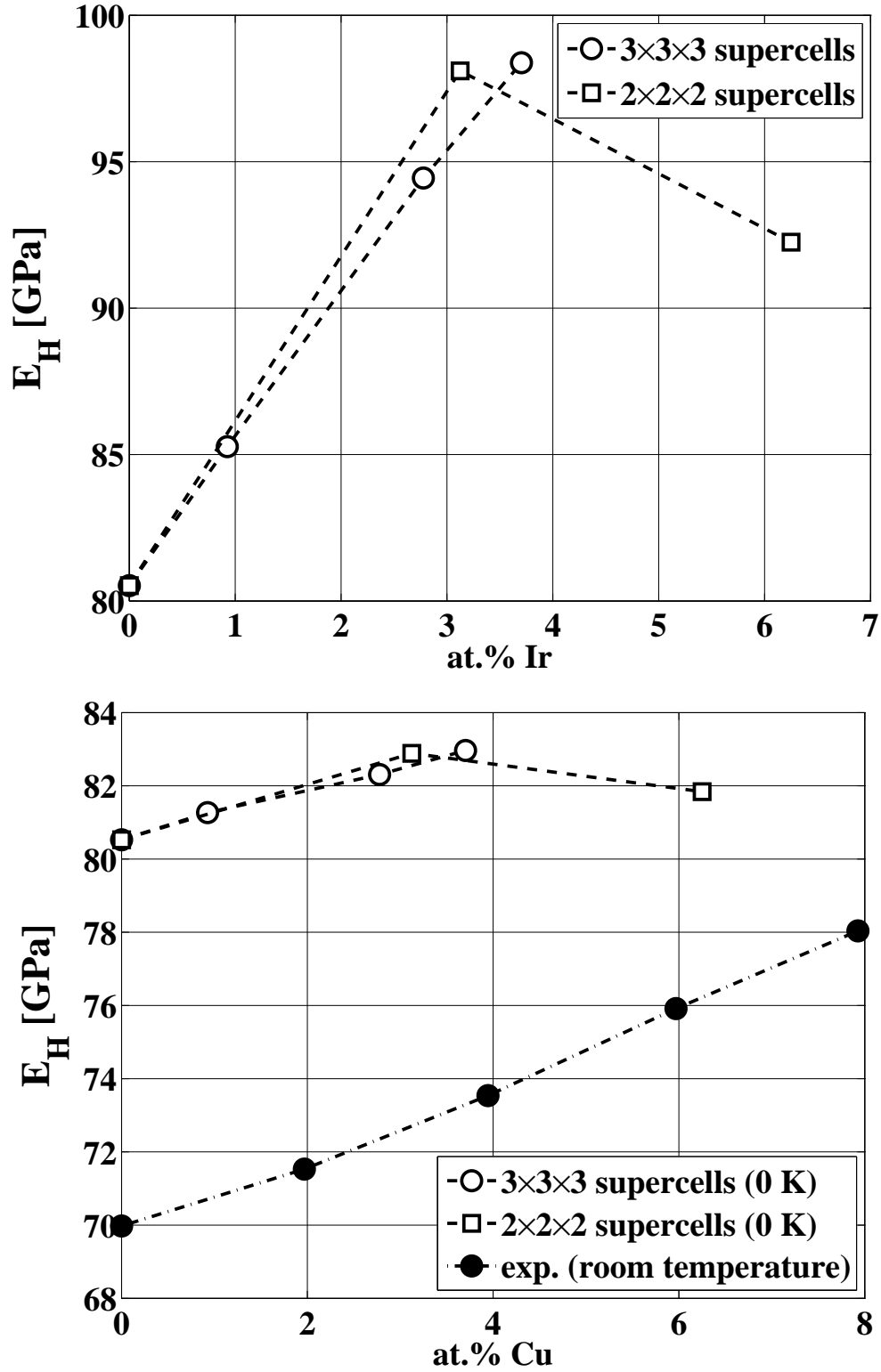
Figure 5.11: Homogenized Young's moduli (E_H) of Al-Ir (top) and Al-Cu (bottom) solid solutions.

       Open circle: DFT, this study.

       Solid circle: experiments on polycrystals (Masafumi and Takefumi, 1988).

5.4.3 Homogenized elastic moduli of Al-Mg and Al-Li solid solutions

The homogenized elastic modulus of Al-Mg and Al-Li solid solutions are shown in Figure 5.12 and 5.13.

The homogenized shear moduli of Al-Mg solid solutions have a very unique compositional dependence. The compositional dependence predicted by 2×2×2 supercells is increasing, and by 3×3×3 supercells it is decreasing. The homogenized shear moduli from the measured elastic constants (Gault et al., 1977) practically has no change ($\sim \pm 0.1$ GPa) over the studied concentrations. The measured shear modulus of polycrystals (Raju and Reddy, 1980) slightly decreases (~ 0.15 GPa) from 6.18 to 11.09 at.%Mg, and drops ~ 0.7 GPa at 14.44 at.%Mg. Such a compositional dependence is reproduced by CPA, but if only the homogenized shear moduli of Al-Mg solid solutions are considered and the pure Al is disregarded.

The homogenized shear moduli of Al-Li solid solutions also indicates a supercell size dependence, but the compositional dependence increases as predicted by both 2×2×2 and 3×3×3 supercells. The increase predicted is ~ 0.3563 GPa/at.% and ~ 0.1465 GPa/at.% by 2×2×2 and 3×3×3 supercells, respectively. However, neither of them reproduces the measurements, i.e., ~ 0.6455 GPa/at.%.

The homogenized Young's moduli from the measured elastic constants of Al-Mg solid solutions slightly decrease as the Mg concentration increases. The Young's modulus measured on polycrystals decrease more rapidly. Such a compositional dependence, however, is not reproduced in this study. Instead, a supercell size dependent compositional dependence is observed.

The compositional dependence of the homogenized Young's modulus of Al-Li solid solutions calculated by 2×2×2 supercells in this study are in good agreement with the homogenized Young's modulus from the measured elastic constants, but not with the experiments on the polycrystals. On the other hand, the homogenized Young's modulus from the elastic constants by CPA is in good agreement with the measurements on polycrystals in the concentration range of 0-5 at.%.
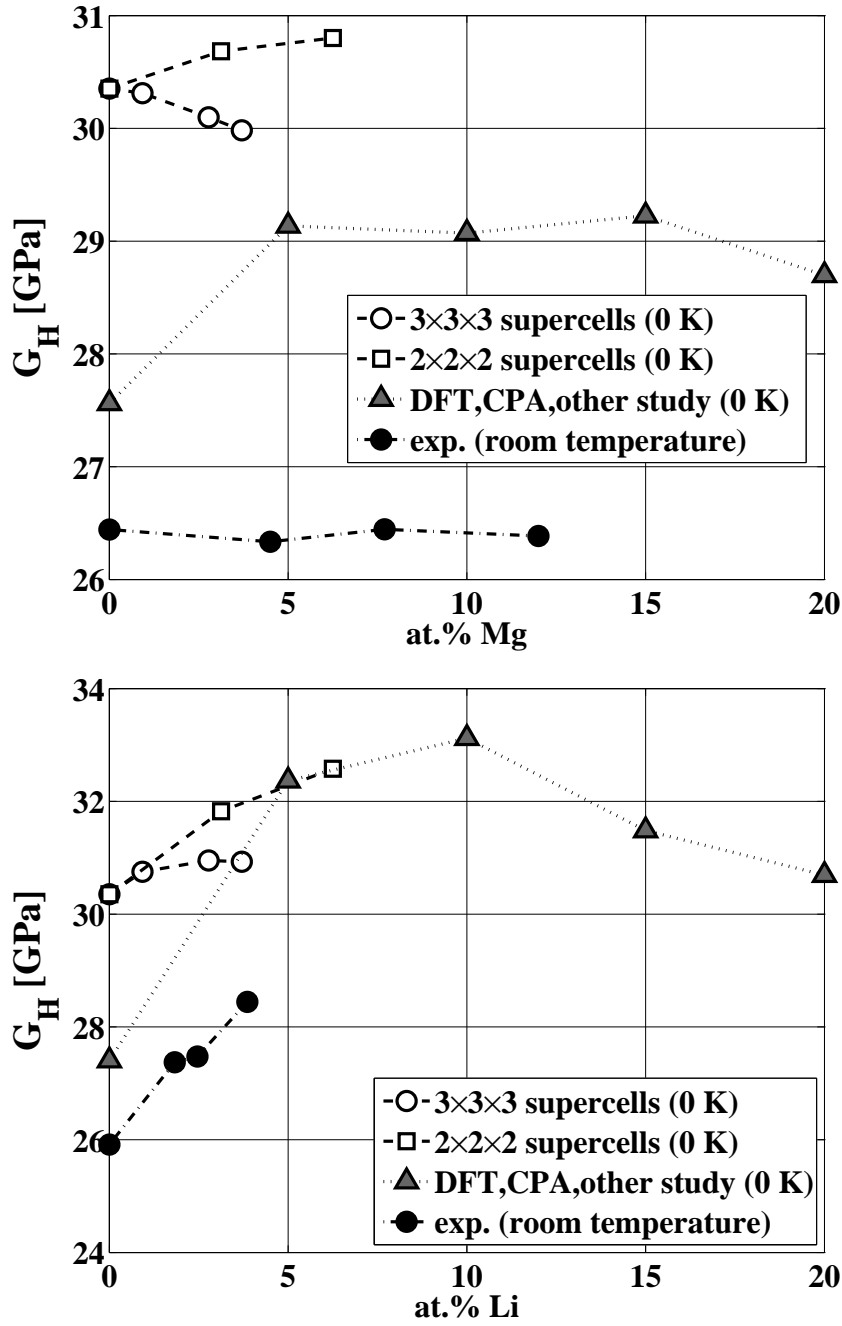
Figure 5.12: Homogenized shear moduli (G_H) of Al-Mg (top) and Al-Li (bottom) solid solutions.

Open circle:	DFT, this study.		
Gray solid triangle:	DFT, CPA, other work,	Al-Mg	(Zander et al., 2007).
		Al-Li	(Taga et al., 2005).
Black solid symbol:	experiments,	Al-Mg,	circle, H (Gault et al., 1977).
			square, P (Raju and Reddy, 1980).
		Al-Li,	circle, H (Müller et al., 1986).

P: measurement on polycrystals.

H: homogenized elastic modulus from the measured elastic constants of single crystals.
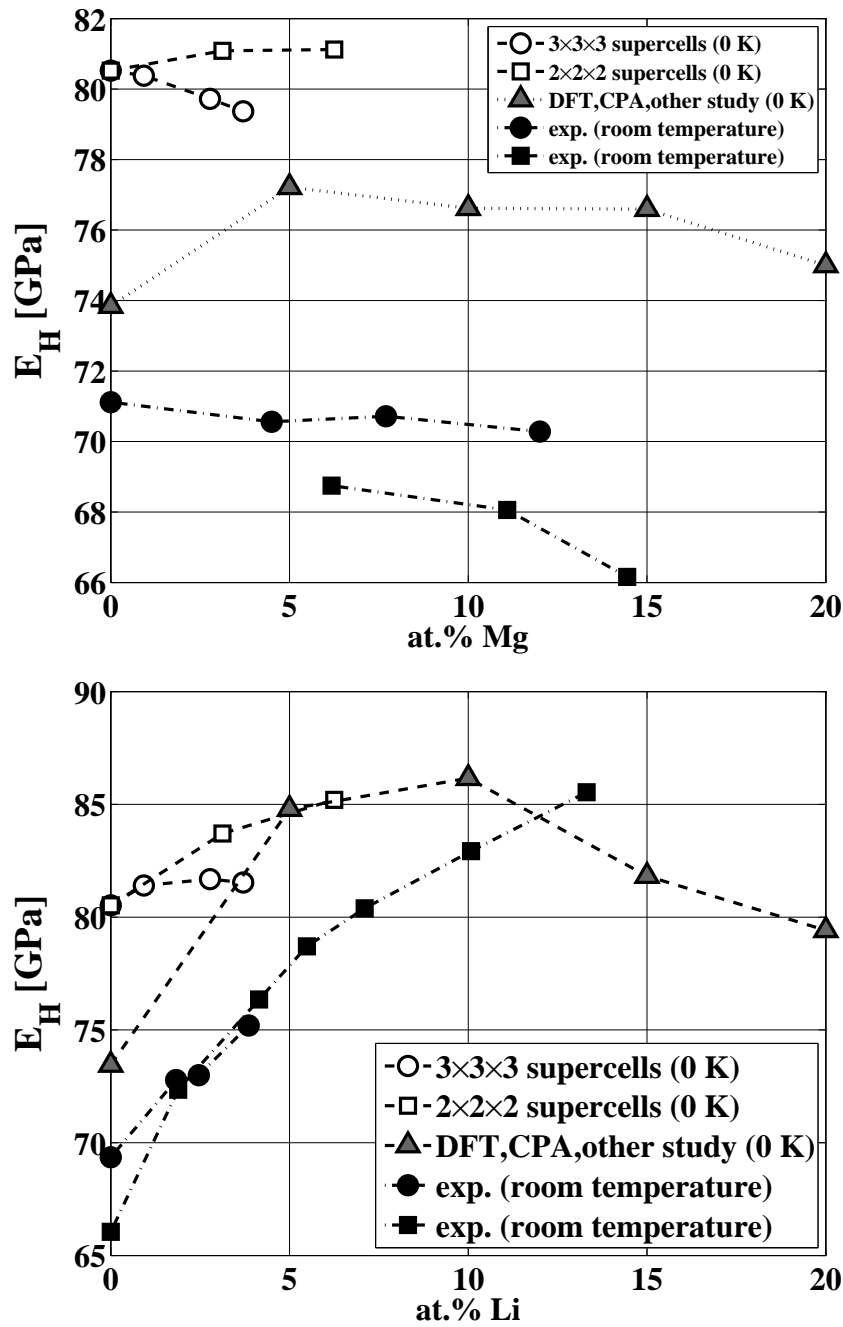
Figure 5.13: Homogenized Young's moduli (E_H) of Al-Mg (top) and Al-Li (bottom) solid solutions.

Open circle:	DFT, this study.		
Gray solid triangle:	DFT, CPA, other work,	Al-Mg	(Zander et al., 2007).
		Al-Li	(Taga et al., 2005).
Black solid symbol:	experiments,	Al-Mg,	circle, H (Gault et al., 1977).
			square, P (Raju and Reddy, 1980).
		Al-Li,	circle, H (Müller et al., 1986).
			square, P (Noble et al., 1982).

P: measurement on polycrystals.

H: homogenized elastic modulus from the measured elastic constants of single crystals.

5.4.4 Homogenized elastic moduli of Al-Zn solid solutions

The homogenized elastic moduli of Al-Zn solid solutions is shown in Figure 5.14.

Despite of the discrepancy between the calculated and the measured $C_{11} - C_{12}$ (see Figure 5.7), the calculated homogenized shear modulus is in satisfactory agreement with the homogenized shear modulus from the measured elastic constants.

The compositional dependence of the homogenized Young's modulus of Al-Zn solid solutions in this study is in good agreement with the measurements on the polycrystals of Al-Zn alloys at ~400 °C where Al-Zn alloy is in disordered solid solution state (Kardashe et al., 1968). The calculated compositional dependence of the homogenized Young's modulus still agrees well with the measurements on the polycrystals.
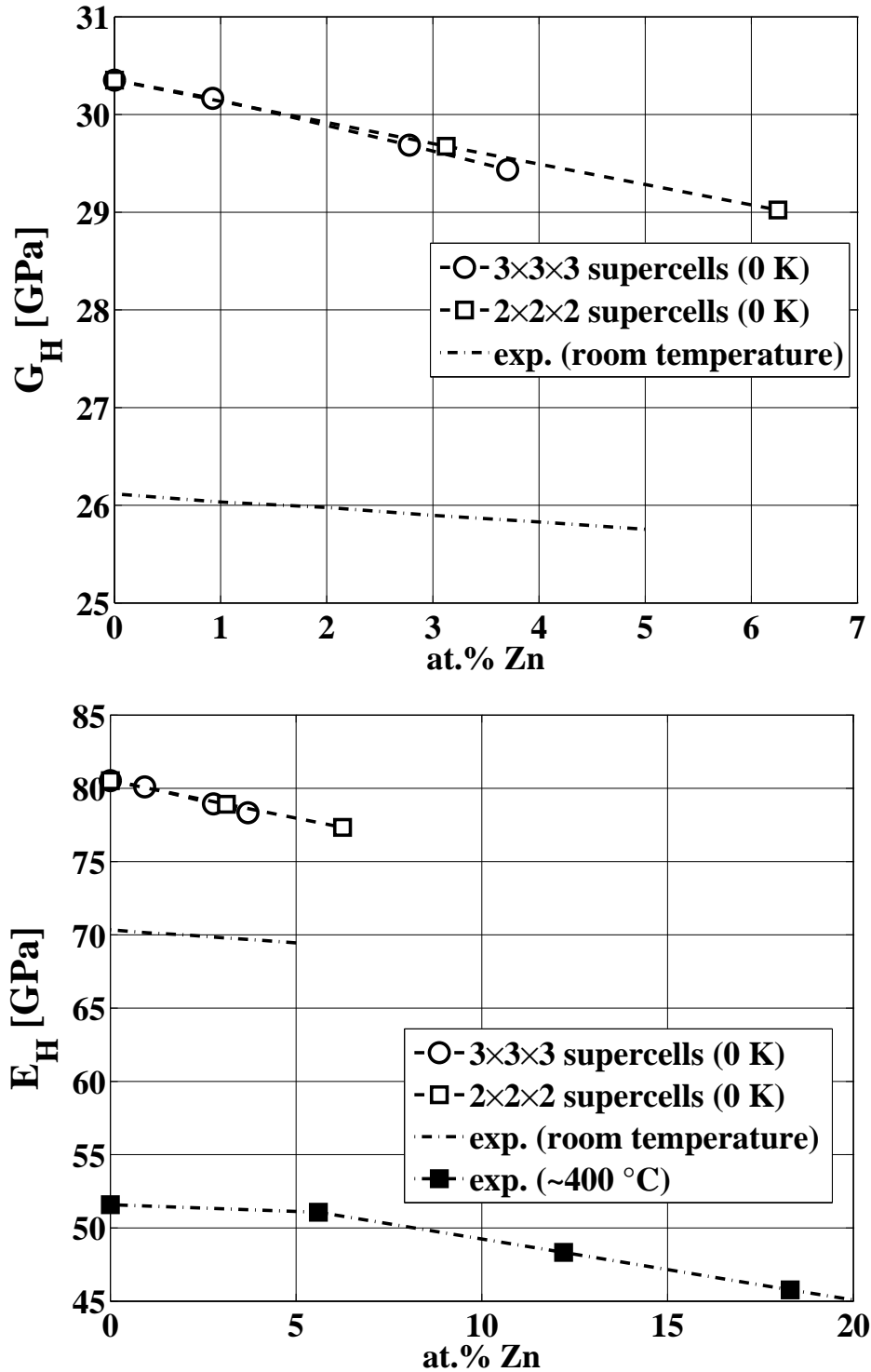
Figure 5.14: Homogenized shear moduli (G_H, top) and homogenized Young's moduli (E_H, bottom) of Al-Zn solid solutions.

Open circle: DFT, this study.

Experiments: Plain dash line, H (Müller et al., 1986).

Black solid square, P (Kardashe et al., 1968).

P: measurement on polycrystals.

H: homogenized modulus from the measured elastic constants of single crystals.

Chapter 6

Strengthening parameters of studied Al solid solutions

6.1 Validation of calculated strengthening parameters

6.1.1 Model parameters

Table 6.1: δ_b, η_B, and η_G of the studied Al solid solutions calculated by DFT compared with available experimental results. Due to the strong nonlinear compositional dependence of the elastic constants at Al-6.25 at.%X ($Al_{30}X_2$) by DFT, the properties calculated at this concentration are disregarded.

System	δ_b		η_B		η_G	
	this study	exp.	this study	exp.	this study	exp.
Al-Ca	0.364	0.465[a]	-2.192		-4.375	
Al-Sr	0.540		-3.452		-7.746	
Al-Ir	-0.183		3.240		6.769	
Al-Cu	-0.106	-0.119[b]	0.790	1.391[c]	0.847	1.270[c]
Al-Mg	0.104	0.111[d]	-0.758	-0.698[e]	-0.125	-0.007[e*]
Al-Li	-0.007	-0.007[f]	-0.820	-0.729[g]	0.786	2.127[g*]
Al-Zn	-0.017	-0.020[h]	-0.138	-0.049[g]	-0.795	-0.236[g*]

[a] (Nowotny et al., 1940), alloys were quenched from 888K.
[b] (Murray, 1985), measured at 25 °C.
[c] (Masafumi and Takefumi, 1988), measured at room temperature on polycrystals.
[d] (Murray, 1982), measured at 25 °C.
[e] (Gault et al., 1977), measured at room temperature.
[f] (McAlister, 1982), measured at 25 °C.
[g] (Müller et al., 1986), measured at room temperature.
[h] (Murray, 1983), measured at 25 °C.
[*] homogenized from the measured elastic constants by using Hershey's model (Hershey, 1954).

The ingredients of calculating the strengthening parameters are listed in Table 6.1. The best agreement with the experiments is in δ_b. And the worst is in η_G, mostly because of the supercell size dependence. These parameters are inserted into the solid solution strengthening models to obtain δ_b, P and ϵ_L (Section 2.2.1).

6.1.2 Strengthening parameters

The calculated strengthening parameters are listed in Table 6.2, along with the experimental results and direct DFT results All the quantities in Table 6.2 are normalized by the corresponding parameters of Al-Cu.

In each system, the normalized $|\delta_b|$ and $|P/c|$ are close to each other. When the modulus mismatch is included (ϵ_L), Al-Ir has higher strengthening capability than Al-Ca, while $|\delta_b|$ and $|P/c|$ predicts higher strengthening capability of Al-Ca than that of Al-Ir.

According to the normalized strengthening parameters of Al-Cu and Al-Mg solid solutions, the

solid solution strengthening of Al-Mg is slightly lower than that of Al-Cu. This is, however, rarely observed in the simple mechanical tests. Nevertheless, the relative interaction energy by ADIF (Kosugi and Kino, 1993), the energy barrier and the CRSS at 0 K by the direct DFT calculation (Leyson et al., 2010) are consistent with the strengthening parameters calculated in this thesis. Even if the modulus mismatch effect is disregarded and only $|\delta_b|$ and $|P/c|$ are used, the agreement is already very good.

According to the calculated normalized strengthening parameters of Al-Li and Al-Zn, Li and Zn have much lower strengthening capability in Al than that of Cu and Mg. This is consistent with the experiments. In this thesis, the strengthening effect of Zn is predicted to be higher than Li. In the experiments, however, this is not so clear that whether Zn has higher strengthening capability than Li. In some experiments, the strengthening capability of Li is higher than that of Zn. This uncertainty from the experiments is probably related to the microstructure in Al-Li and Al-Zn. The cluster formation in Al-Zn (Dash and Fine, 1961) and metastable phase δ' in Al-Li (Furukawa et al., 1985) occurs even in as-quenched state.

The strengthening parameters of Al-Ca, Al-Sr and Al-Ir are much higher than the other systems. In current commercial Al alloys, a small amount of Ca and Sr is added to Al-Si alloys. But the purpose of that is not to strengthen the alloys by solid solution strengthening but to refine the eutectic phase. Higher amount of Ca or Sr causes other drawbacks, such as porosity of the castings, deterioration of the ductility and high pick-up of the hydrogen (ASM Handbook, 1990).

Table 6.2: The strengthening parameters calculated in this study compared with what is observed in the experiments and the direct DFT. Note: all the quantities are normalized by the corresponding quantities of Al-Cu.

System	DFT (this study)			From stress-strain curves at RT				ADIF[a]		Direct DFT (other study)[b]	
	$\|\delta_b\|$	ϵ_L $\alpha=16$	$\|P/c\|$	$\Delta\tau_c/$at.% [c]	$\Delta\sigma_0/$at.% [d]	[e]	[f]	IE	CS	$\Delta E_b/c^{1/3}$	$\tau_{y0}/c^{2/3}$
Al-Ca	3.43	3.84	3.27								
Al-Sr	5.09	6.12	5.01								
Al-Ir	1.73	3.89	1.96								
Al-Cu	1	1	1	1	1	1	1	1	1	1	1
Al-Mg	0.98	0.88	0.99	0.32~0.38	0.20~0.99	0.67		0.97	0.48	0.99	
Al-Li	0.07	0.42	0.07	0.20~0.21	0.03~0.11	0.15					0.98
Al-Zn	0.16	0.16	0.16	0.13~0.28	0.08~0.52	0.41	0.09	0.56	0.06		

[a] (Kosugi and Kino, 1993). ADIF: amplitude dependent internal friction; IE: interaction energy; CS: critical stress.

[b] (Leyson et al., 2010). ΔE_b is the energy barrier for a curved dislocation to move over a characteristic distance; τ_{y0} is CRSS at 0 K. c is the atomic concentration.

[c] single crystal, Al-Cu: (Carlsen and Honeycombe, 1955; Jaoul, 1955; Dew-Hughes and Robertson, 1960). Al-Mg: (Asada et al., 1967; Podkuiko et al., 1972; Tensi et al., 1970; Podkuyko and Pustovalov, 1975), Al-Li: (Miura et al., 1987, 1988), Al-Zn: (Jaoul, 1955; Dash and Fine, 1961; Auer et al., 1964; Haberkorn and Gerold, 1966).

[d] polycrystal, Al-Cu: (Sanders et al., 1986; Deschamps et al., 1996; Gandin et al., 2002; Churyumov et al., 2007a; Zolotorevsky et al., 2009), Al-Mg: (Sanders et al., 1986; Ryen et al., 2006; Churyumov et al., 2007a,b; Zolotorevsky et al., 2009), Al-Li: (Jones and Das, 1960; Fomenko et al., 1993; Isaev et al., 1994, 1996), Al-Zn: (Sanders et al., 1986).

[e] (ASM Handbook, 1990)

[f] (Noble et al., 1982)

6.2 Limitations and applicabilities of modulus and volume mismatch parameters

As demonstrated in Table 6.2, the strengthening parameters reasonably agree with the experiments. On the other hand, if only the volume mismatch parameter is considered, the strengthening parameters of Al-Cu and Al-Mg correlate perfectly with the strengthening effect calculated by direct DFT calculations (Leyson et al., 2010). The strengthening parameters in this thesis are based on very crude but reasonable models. Therefore the limitation and applicability of those approximations should be discussed. The discussion is focused on the mismatch parameters, including η_G, δ_b and P (see Section 2.2.1)

6.2.1 Modulus mismatch model parameter

Fleischer's original formulation of the di-elastic parameter (η_G) was adopted from the study of composite materials (Fleischer, 1963). In composite materials, given the sufficient knowledge of the distribution and the shape of the inclusions, the modulus of the inclusion can be obtained from the macroscopic modulus (e.g. Torquato (1991)). This is based on the physical invariance that adding stiffer inclusions results in stiffer materials and vice versa. In a quantum mechanical system, however, this is not always true. As shown in Figure 5.3, $C_{11} - C_{12}$ at Al-6.025 at.%Cu is lower than pure Al, but below that concentration, $C_{11} - C_{12}$ of Al-Cu solid solutions are higher than pure Al. It can be further illustrated in Table 6.3. In some cases, such as Al-Ca and Al-Sr, the elastic constants of $L1_2$ Al_3X_1 (25 at.%) are much higher than pure Al, but those of $Al_{31}X_1$ (3.125 at.%) are lower than pure Al. These observations are in contradiction with the concept in composite materials.

Table 6.3: The elastic constants of Al (0 at.%), $Al_{31}X_1$ (0.926 at.%), and Al_3X_1 (25 at.%).

	$C_{11} - C_{12}$ [GPa]			C_{44} [GPa]		
	Al	$Al_{31}X_1$	Al_3X_1	Al	$Al_{31}X_1$	Al_3X_1
Al-Ca		43.4	101.5		31.3	59.4
Al-Sr		37.0	79.9		27.0	48.0
Al-Ir		69.9	120.1		39.3	61.9
Al-Cu	52.1	54.8	116.5	33.6	34.1	25.9
Al-Mg		52.3	62.0		34.1	35.1
Al-Li		54.4	91.5		35.3	40.1
Al-Zn		51.3	43.5		32.7	25.9

On the other hand, with the presence of a dislocation, the shear deformation is very heterogeneous. Most of the shear occurs between the adjacent planes directly above and below the dislocation, e.g. in Al (Woodward et al., 2008). The relevant property to this shear is the γ-

surface[1] which, however, does not necessarily correlate with the shear modulus. A famous example is the comparison between Al and Cu. The shear modulus of Cu is higher than Al, but the intrinsic and the unstable stacking fault energy of Al are both higher than Cu (Ogata et al., 2002; Brandl et al., 2007; Jahnátek et al., 2009). Therefore, a more reasonable di-elastic parameter should be related to the γ-surface. Yasi et al. proposed a slip mismatch parameter to replace the modulus mismatch parameter (Yasi et al., 2010). The slip mismatch is defined as:

$$\epsilon_{SFE} = \frac{1}{\gamma_{I2}} \cdot \frac{d\gamma_{I2}}{dc} \tag{6.1}$$

where γ_{I2} is the I2 intrinsic stacking fault energy; and c is the atomic fraction of solute atoms on the stacking fault. This parameter is apparently more pertinent than η_G in the context of the solid solution strengthening.

From the technical point of view, by using ordered supercells, the supercell size dependence is observed in all the calculated elastic constants (see Chapter 5). Because of that, there is a great uncertainty in the compositional dependence of the elastic constants. This uncertainty makes the prediction of η_G unreliable. Besides that, it is not possible to make any extrapolation or interpolation of the elastic modulus. Therefore, the di-elastic parameter, η_G, is physically ill defined and technically unreliable (when ordered supercells are used).

6.2.2   Volume mismatch model parameter

The volume mismatch model parameters include δ_b and $|P/c|$. The relevant properties to these two parameters are the lattice parameters and the bulk modulus. Unlike the elastic constants, the calculated lattice parameters and the bulk modulus are not sensitive to the supercell size[2]. Therefore, the calculated compositional dependences of these two properties are more trustworthy than η_G, not to mention their better agreement with the experiments than η_G (see Table 6.1).

Within the calculated concentration of Al binary solid solutions, the lattice parameters and bulk modulus both linearly depend on the concentration. The question is up to which concentration the linear dependence is still valid. This question is related to the computational efficiency, because in general, at high concentrations, only a small number of atoms is required to perform DFT calculations. These two properties of Al_3X_1[3] ($1\times1\times1$ supercell) were calculated, and

---

[1]γ-surface is also called the generalized stacking fault which was firstly proposed by Vitek (Vitek, 1968). Given a description of the atomic interaction, such as DFT or the atomic potentials, the γ-surface is calculated in the following way: a perfect crystal is cut along a given crystallographic plane; the upper part is displaced by a vector **t** parallel to the cutting plane; the total energy of such a faulted crystal is subtracted by the total energy of the perfect crystal; then the fault energy corresponding to the displacement vector **t** is obtained. By repeating this procedure for a series of **t** within the periodic cell on the given crystal plane, a two dimensional energy-displacement surface is obtained, and this surface is called γ-surface. In this kind of calculations, the atomic relaxation is allowed perpendicular to the given crystal plane, but forbidden parallel to the given crystal plane.

[2]If one closely inspects Figure 4.1, one can find the slight supercell size dependence in the bulk modulus, e.g. Al-Ca, Al-Sr, Al-Mg and Al-Li.

[3]In fact, Al_3X_1 is in $L1_2$ structure

compared with extrapolations from the dilute solid solutions ($2\times2\times2$ and $3\times3\times3$ supercells) shown in Figure 6.1 and 6.2. It can be observed that the deviation of the extrapolated lattice parameters of Al_3X_1 deviate from the calculated within -1~2.5%. The deviation of the bulk modulus, however, can go up to -80%. This observation enables fast evaluation of the volume mismatch parameter, δ_b, of Al binary solid solutions with the solute elements throughout the periodic table. This result is presented in next section where a chemical trend of the solid solution strengthening is observed on the periodic table.
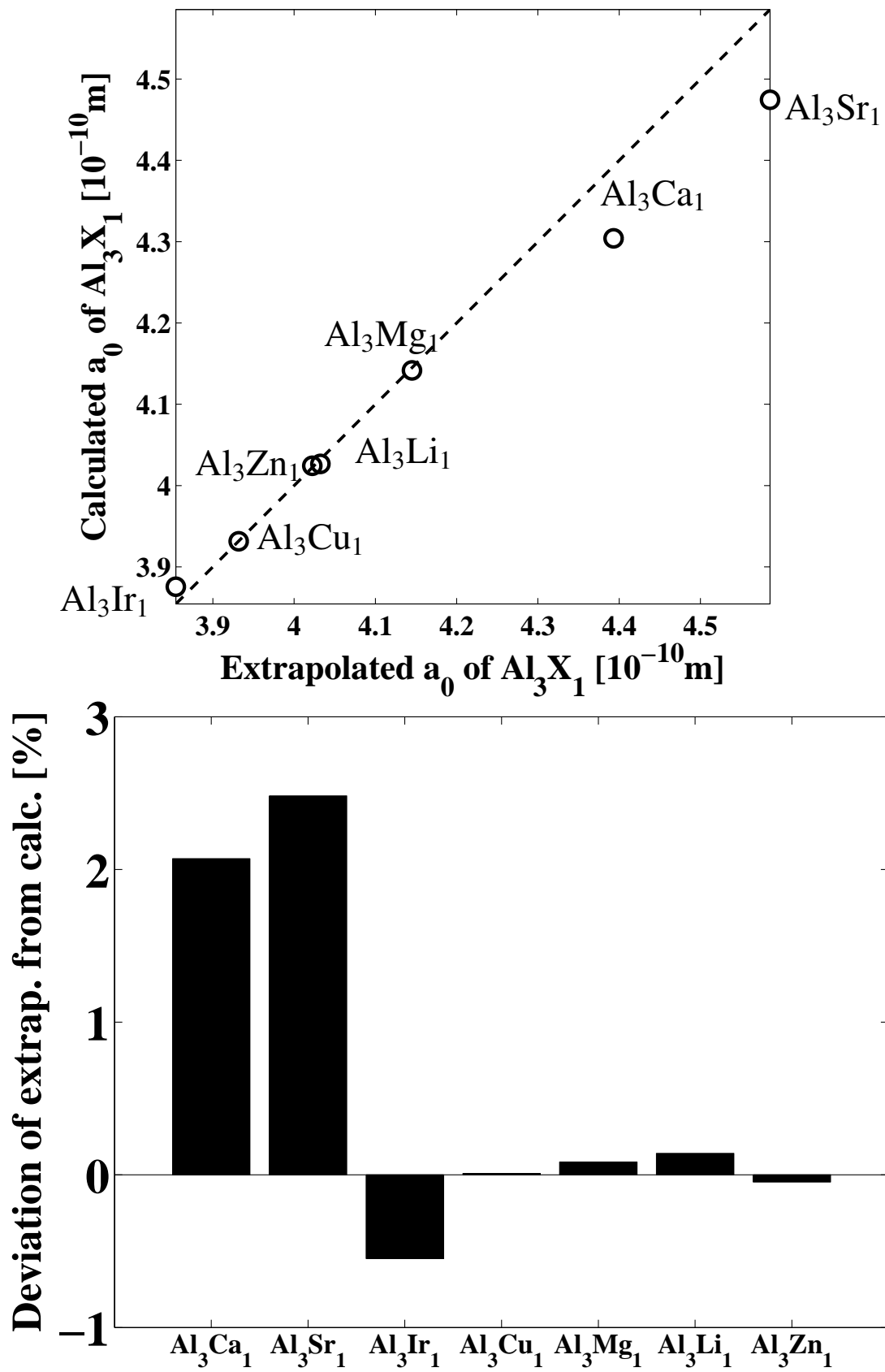
Figure 6.1: Top: the comparison of the extrapolated and calculated lattice parameter of $L1_2$ Al_3X_1. Bottom: the deviation of the extrapolation from the calculated lattice parameter.
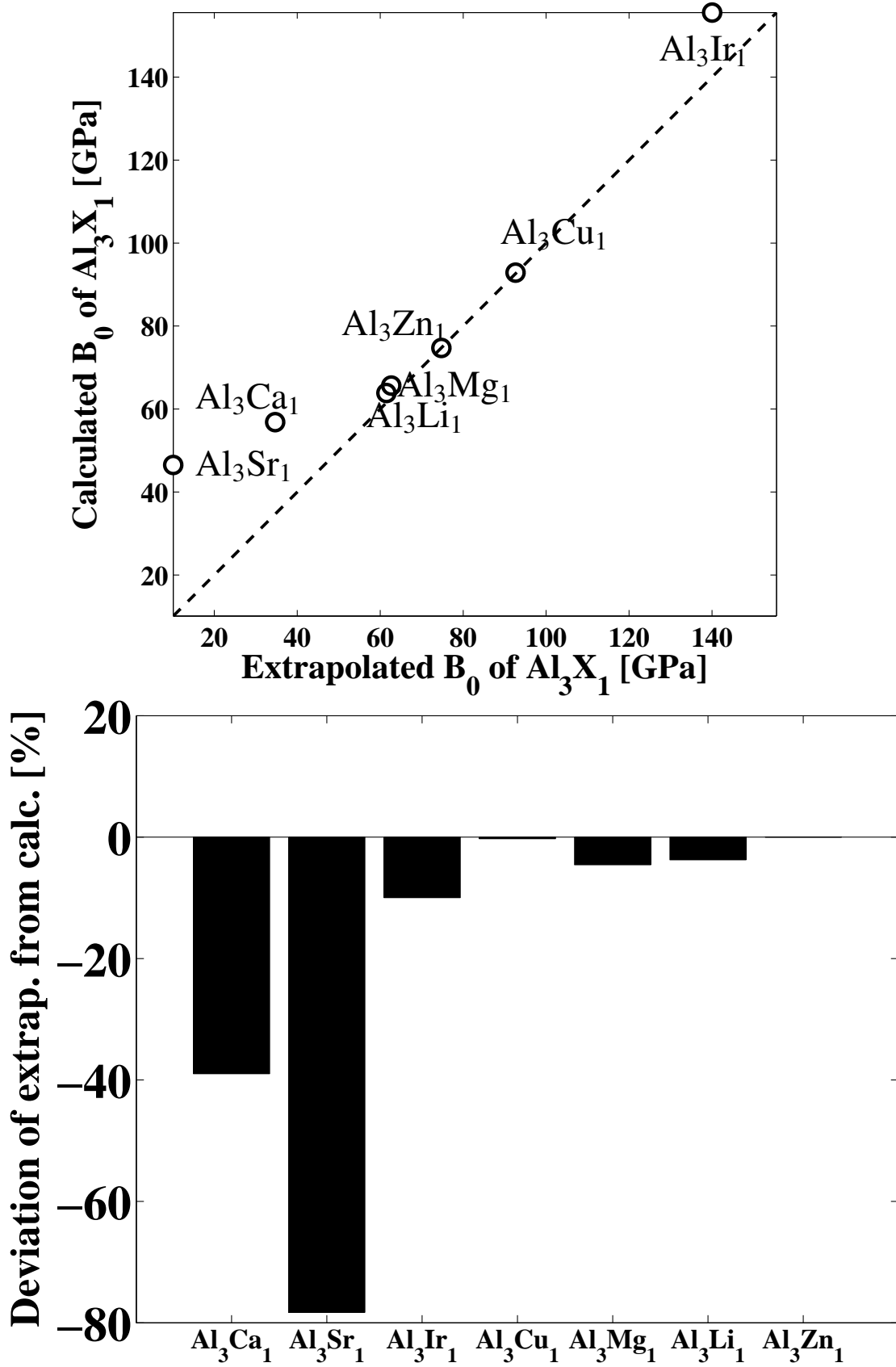
Figure 6.2: Top: the comparison of the extrapolated and calculated bulk modulus of $L1_2$ Al_3X_1. Bottom: the deviation of the extrapolation from the calculated bulk modulus.

6.3   Chemical trend of solid solution strengthening on periodic table

6.3.1   Chemical trend of solid solution strengthening in Al binary systems

According to the last section, the lattice parameters of the studied Al binary solid solutions have linear compositional dependence up to 25 at.% (Al_3X_1). If the aforementioned observations apply to other Al binary solid solutions, the volume mismatch parameter can be quickly and reliably evaluated by performing calculations on Al_3X_1 (1×1×1 supercell).

With the solute elements throughout the periodic table, the lattice parameters of Al_3X_1 were calculated, and their differences from pure fcc Al are shown in Figure 6.3. It should be mentioned that the calculations were not carried out for the some light elements (H, He, C, N, O and F), 3d magnetic elements (Cr, Mn, Fe, Co and Ni), some radioactive elements in 6th period (Po, At and Rn), Lanthanoid elements and 7th period elements.

Three features can be observed in Figure 6.3:

1. **Parabolic shape.** Within the same period, the curve of the lattice parameter difference vs. group number resembles a parabolic curve. The noble gas and alkaline metals cause largest volume expansion, and the middle transition metals, e.g. group 8 or 9, introduce largest volume contraction. Although 3d magnetic elements were not calculated, according to the trend, it is reasonable to believe that Fe would cause the largest volume contraction within the 4th period.

2. **From group 13 to group 15.** From group 13 to group 15 (e.g. Ga, Ge, As), the rate in changing the lattice parameter is not as steep as that before group 13 and after group 15.

3. **Transition metals in 5th and 6th period.** If the solute elements are in the same group, and in 5th and 6th period, the lattice parameters of Al_3X_1 are close to each other. The exceptions are Y and La.

The above features are not very surprising, because the same features are also observed in the atomic volumes of pure X in 4th, 5th and 6th period (Gschneidner Jr., 1964). Then the question is how Figure 6.3 looks when the lattice parameters of Al_3X_1 are determined by Vegard's law.

Figure 6.3: The lattice parameter difference between Al_3X_1 and pure Al. Note: some light elements (H, He, C, N, O and F), 3d magnetic elements (Cr, Mn, Fe, Co and Ni), some radioactive elements in 6th period (Po, At and Rn), Lanthanoid elements and 7th period were not calculated.
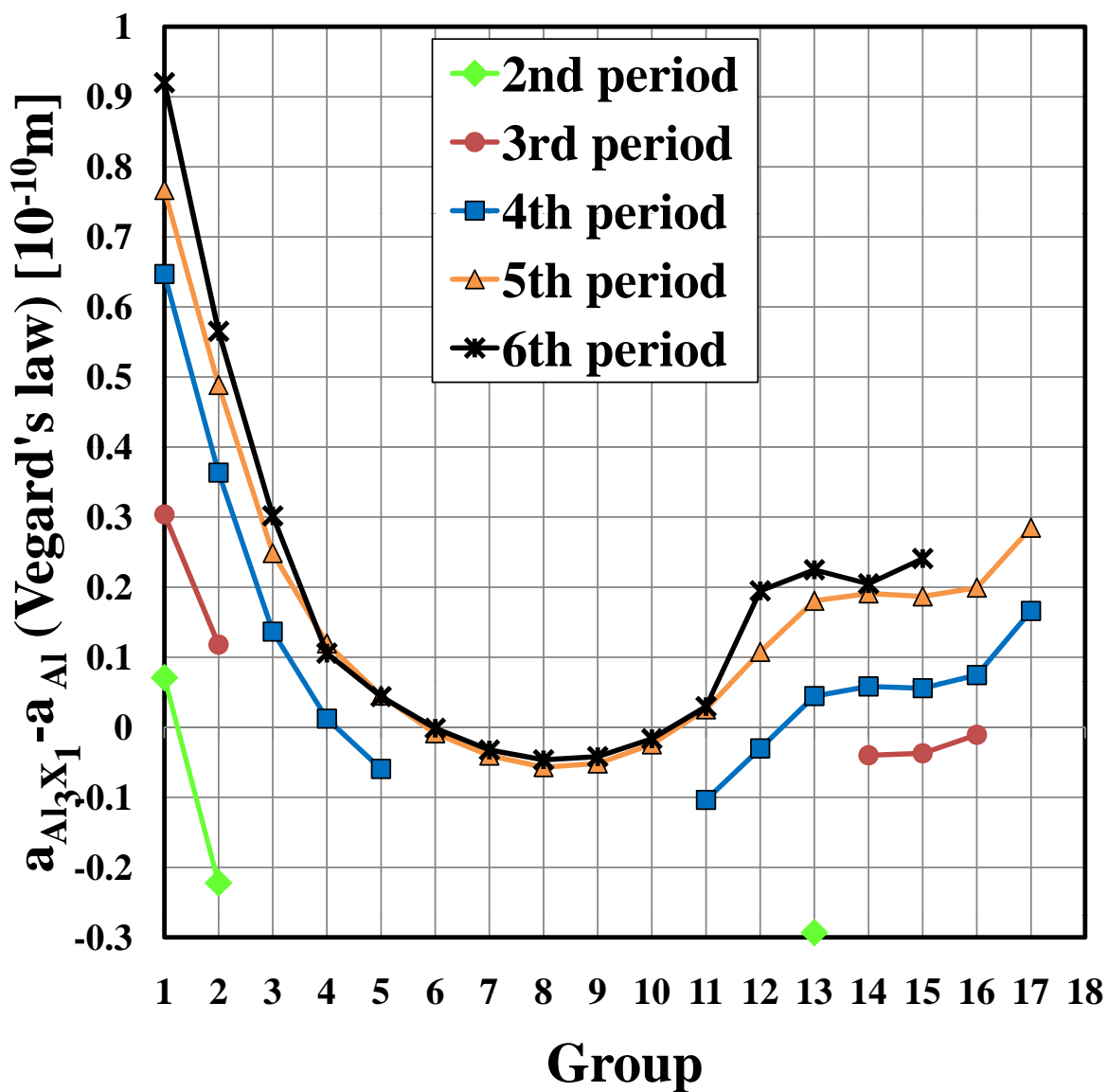
Figure 6.4: The lattice parameter difference between Al_3X_1 and pure Al determined by Vegard's law. The end members for applying Vegard's law are the lattice parameters of pure Al and X in fcc structure adopted from Shang et al. (2010a) (DFT calculation).

Figure 6.4 shows the difference of the lattice parameter between Al_3X_1 and pure Al determined by Vegard's law. Qualitatively, the general features observed in Figure 6.3 are preserved in Figure 6.4. There are two limitations of using Vegard's law:

- The deviation of Vegard's law from DFT calculation is within -6~4 % shown in Figure 6.5, but the compositional dependence of the lattice parameters are usually in great discrepancy between Vegard's law and DFT calculation, e.g. in Al-Li, the deviation could be more than 1000 % (see Table 4.4). Thus, Vegard's law might not be a good approximation for some individual systems.

- As to be shown in Section 6.3.2.2, starting from group 12 or 13, the lattice parameters of Ni binary systems decreases, which is inconsistent with the observation in the atomic volume of pure solute elements. Such a feature is similar to that of the atomic radii of pure elements (e.g. empirical atomic radii (Slater, 1964)). In other words, there are variations in the end members used in the Vegard's law to determine the correct trend on the periodic table. In Al binary systems, the lattice parameter of the pure elements in fcc might be good, but in Ni binary systems, the atomic radii of pure elements might be the good ones.
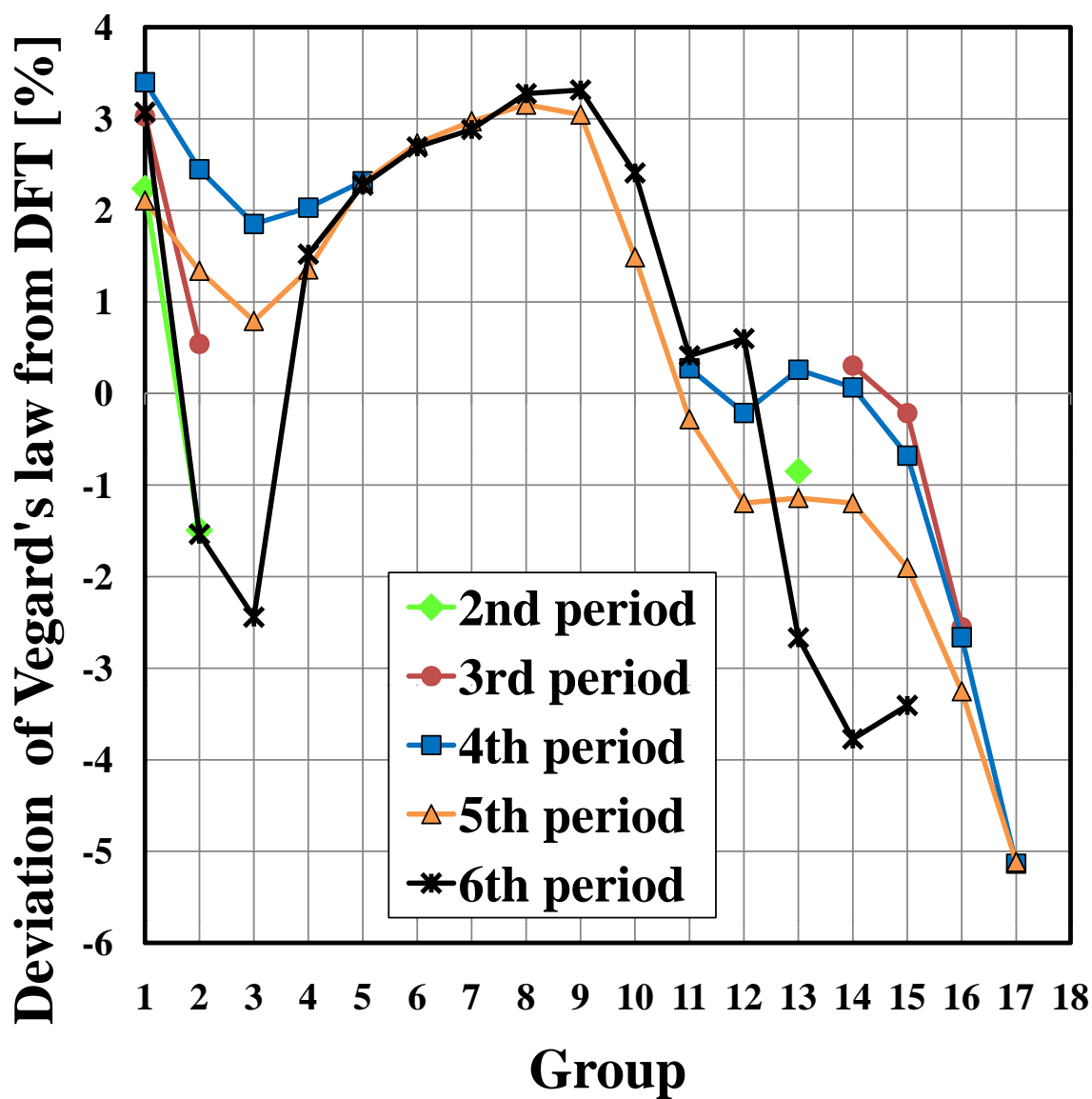
Figure 6.5: The deviation of Figure 6.4 (Vegard's law) from Figure 6.3 (DFT).

The volume mismatch parameters were estimated by using the lattice parameter of Al_3X_1 and pure Al. Their absolute values are plotted in Figure 6.6.

Figure 6.6 indicates the strengthening capability of the solute elements in Al, if only the volume mismatch is considered. The most effective solid solution strengtheners revealed in Figure 6.6 are the alkaline metals in 4th, 5th and 6th period, and noble gas elements in 3rd, 4th, 5th (and possibly 6th) period. The least effective ones are at the beginning and end of the transition metals in each period, e.g. group 3, 4, 11 or 12. Although 3d magnetic elements were not calculated, according to the trend, it is reasonable to assume that their strengthening capabilities are at the intermediate level.

Table 6.4 lists the orders of the strengthening capabilities of the investigated solute elements in Al in previous studies. And they are compared with order revealed in Figure 6.6. If Ge, Ag, and Li are disregarded, Figure 6.6 can exactly reproduce the orders of the strengthening capabilities observed in experiments or the direct DFT calculation. However, one may realize that even in the experiments the order of the strengthening capabilities of Ge and Ag are not consistent in different studies. As mentioned before, in Al-Li, the metastable precipitates can form upon quenching (Furukawa et al., 1985). Similarly, in Al-Ag, the metastable precipitates can also form upon quenching (Hirano, 1969) which makes the measured compositional dependence of the lattice parameters inconsistent in different studies (Roberge and Herman, 1973). Thus, the discrepancy might be due to different heat treatments and the sample handling in different experiments.

Figure 6.6: The absolute values of the volume mismatch parameters of Al binary solid solutions estimated by using the lattice parameter of Al_3X_1 and pure Al. Note: some light elements (H, He, C, N, O and F), 3d magnetic elements (Cr, Mn, Fe, Co and Ni), some radioactive elements in 6th period (Po, At and Rn), Lanthanoid elements and 7th period were not calculated.

According to the above demonstration and discussion, it seems the volume mismatch alone can fairly reasonably reproduce the order of solute elements' strengthening capabilities in Al.

Table 6.4: The strengthening capabilities of the solute elements in Al determined by previous studies and compared with those from Figure 6.6. The solute elements in previous studies whose strengthening capabilities are in discrepancy with Figure 6.6 are in round bracket. The strengthening capabilities of Mn and Cr are assumed to be higher than Cu, according to the trend in Figure 6.6.

Reference	Previous studies		This thesis
	Method	Strengthening capabilities	Figure 6.6
Dorn et al. (1950)	exp.	Cu>(**Ge**)>Mg>Ag>Zn	Cu>Mg>Ge>Ag>Zn
Tensi et al. (1970)	exp.	Cu>(**Ag**)>Mg>Si>Zn	Cu>Mg>Si>Ag>Zn
Borchers and Dropmann (1972)	exp.	Cu>Mg>Si>Ga>Zn	Cu>Mg>Si>Ga>Zn
Noble et al. (1982)	exp.	Mn>Cu>Mg>(**Ag**)≥(**Ge**)>(**Li**)>Zn	Mn>Cu>Mg>Ge>Ag>Zn>Li
Leyson et al. (2010)	direct DFT	Cr>Cu>Mg>Si	Cr>Cu>Mg>Si

The question is whether slip mismatch parameter (di-elastic parameter, see Section 6.2.1) still plays a role. To answer this question an expression combining ϵ_b and ϵ_{SEF}, similar to $\epsilon_L = \left(\delta_b^2 + \alpha^2 \eta_G^2\right)^{\frac{1}{2}}$, should be explicitly known. Within the scope of this thesis, such an expression is not known for Al solid solutions. But the study of the solid solution strengthening on Mg basal slip (Yasi et al., 2010) may shed some light on it.

By using direct DFT calculations, Yasi et al. worked out a strengthening parameter expressed by the volume mismatch parameter (ϵ_b) and the slip mismatch parameter (ϵ_{SFE}) (Yasi et al., 2010). Similar to ϵ_L, Yasi's expression also has weighting factors for the mismatch parameters. The weighting factor for ϵ_b^2 is as >1000 times as that for ϵ_{SEF}^2. This means the volume mismatch usually takes the dominant part of the strengthening effect.

On the other hand, the volume and slip mismatch parameter are correlated. The slip mismatch parameters of Al solid solutions are shown in Figure 6.7. It seems there is also a chemical trend, at least in the 4th period. If one compares Figure 6.7 and Figure 6.3, one may notice a general tendency. The volume expansion results in a decrease in the stacking fault energy, and vice versa. Thus, if the slip parameters are included, the actual values might change, but the general chemical trend revealed by the volume mismatch parameter alone should not be changed significantly.
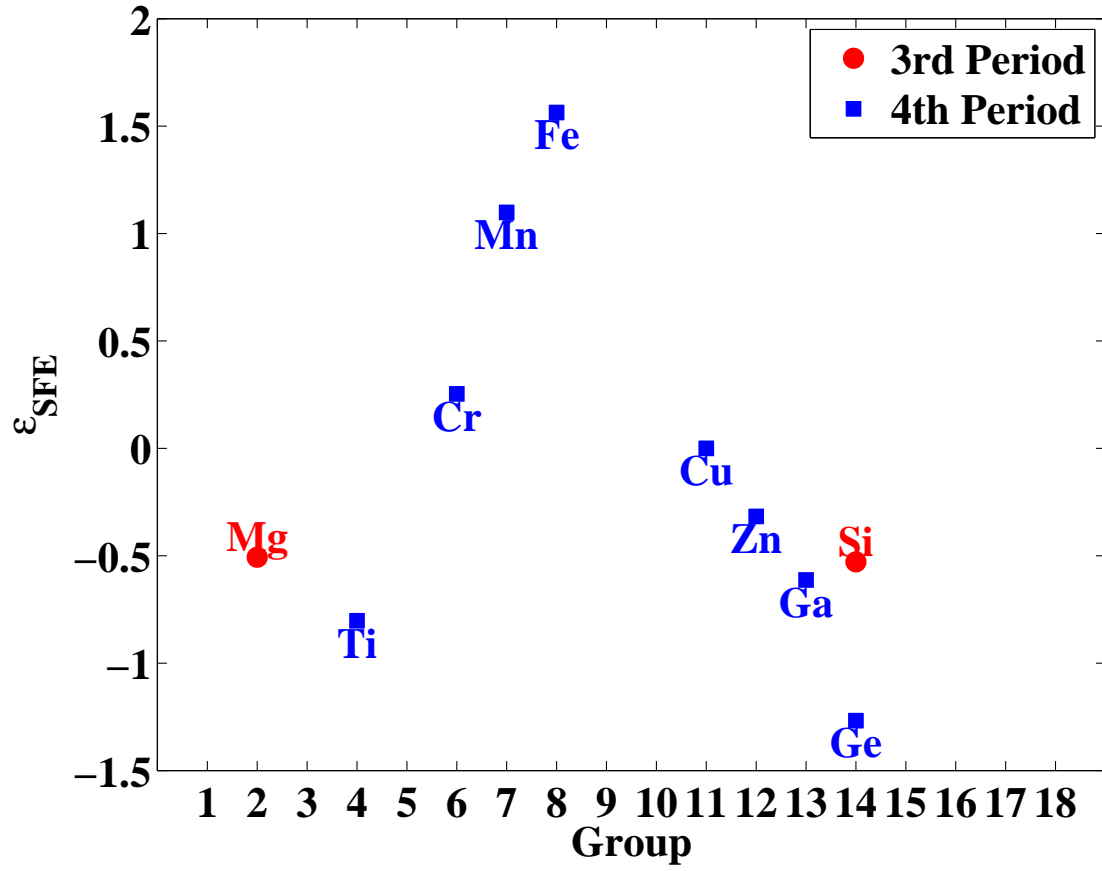
Figure 6.7: The slip mismatch parameter, ϵ_{SEF} of Al binary systems calculated by DFT. The plotted data are from Qi and Mishra (2007)

6.3.2 Chemical trend of solid solution strengthening in previous studies

In last section, it shows that the mismatch parameters of Al binary systems follow a trend on the periodic table. Thus it is speculated that the similar trend should also exist in other systems. Therefore in this section, the previous studies in other systems are re-analyzed in the same manner as last section. It will be shown that such a chemical trend also exists in other systems.

The selected previous studies are either carefully conducted experiments or the quantum mechanical calculations (DFT or tight-binding) performed directly on dislocations.

6.3.2.1 Mg based binary systems

The volume and slip mismatch parameters of Mg binary systems on the basal slip are plotted in Figure 6.8. The general trends resemble to Figure 6.3 and Figure 6.7, except the elements in 2nd period, Li and Be.

The maximum resistance forces imposed by the solute atoms against an edge dislocation on basal slip are plotted in Figure 6.9. Approximately, in the same period, the least effective strengtheners are in group 3, 4, 12 or 13, and the most effective ones are the alkaline metals and group 9. This trend is very similar to Figure 6.6.
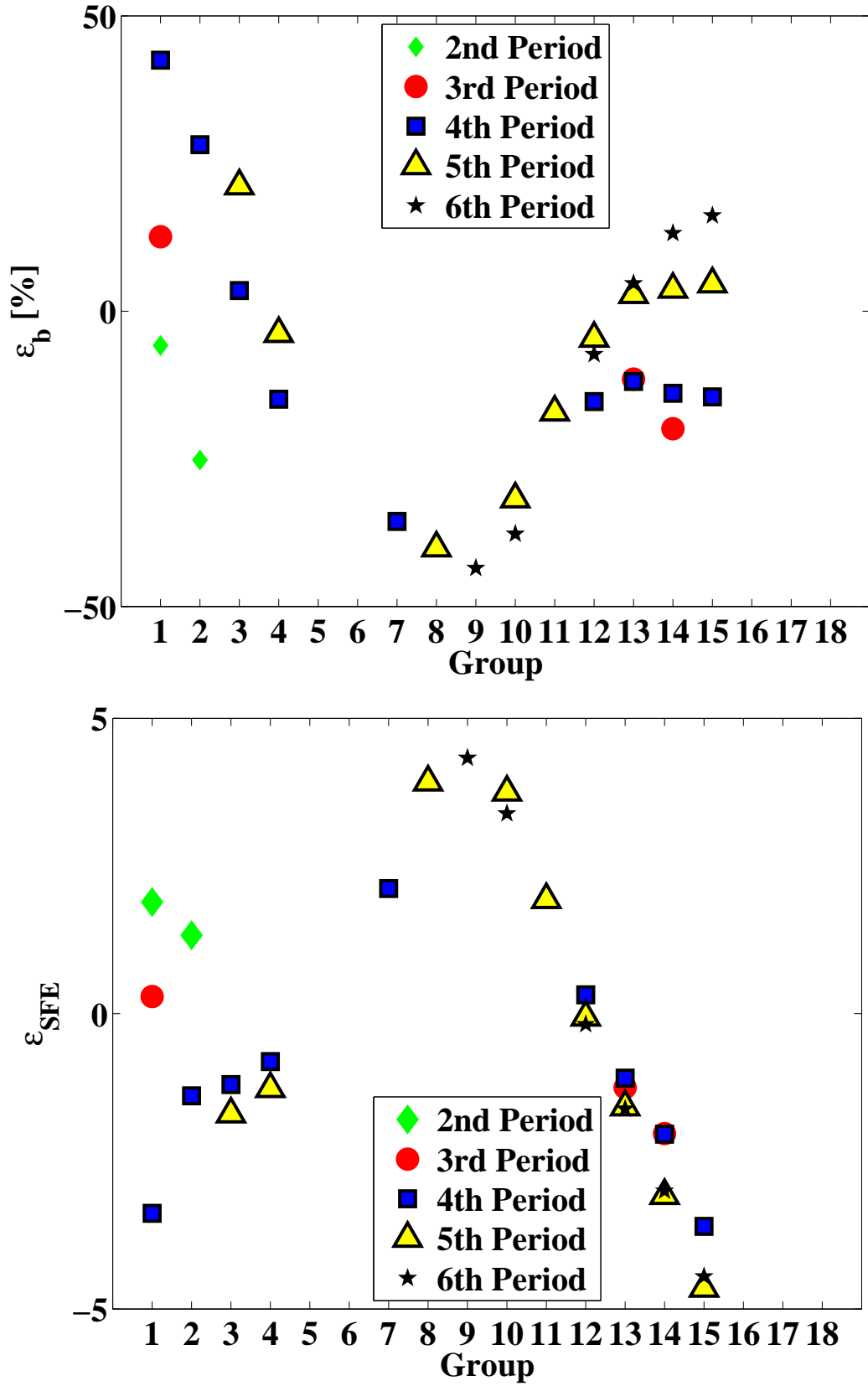
Figure 6.8: The DFT determined strengthening parameters, ϵ_b (top) and ϵ_{SFT} (bottom), in Mg basal slip. The definition of these two parameters is described in the text. The plotted data are from Yasi et al. (2010).
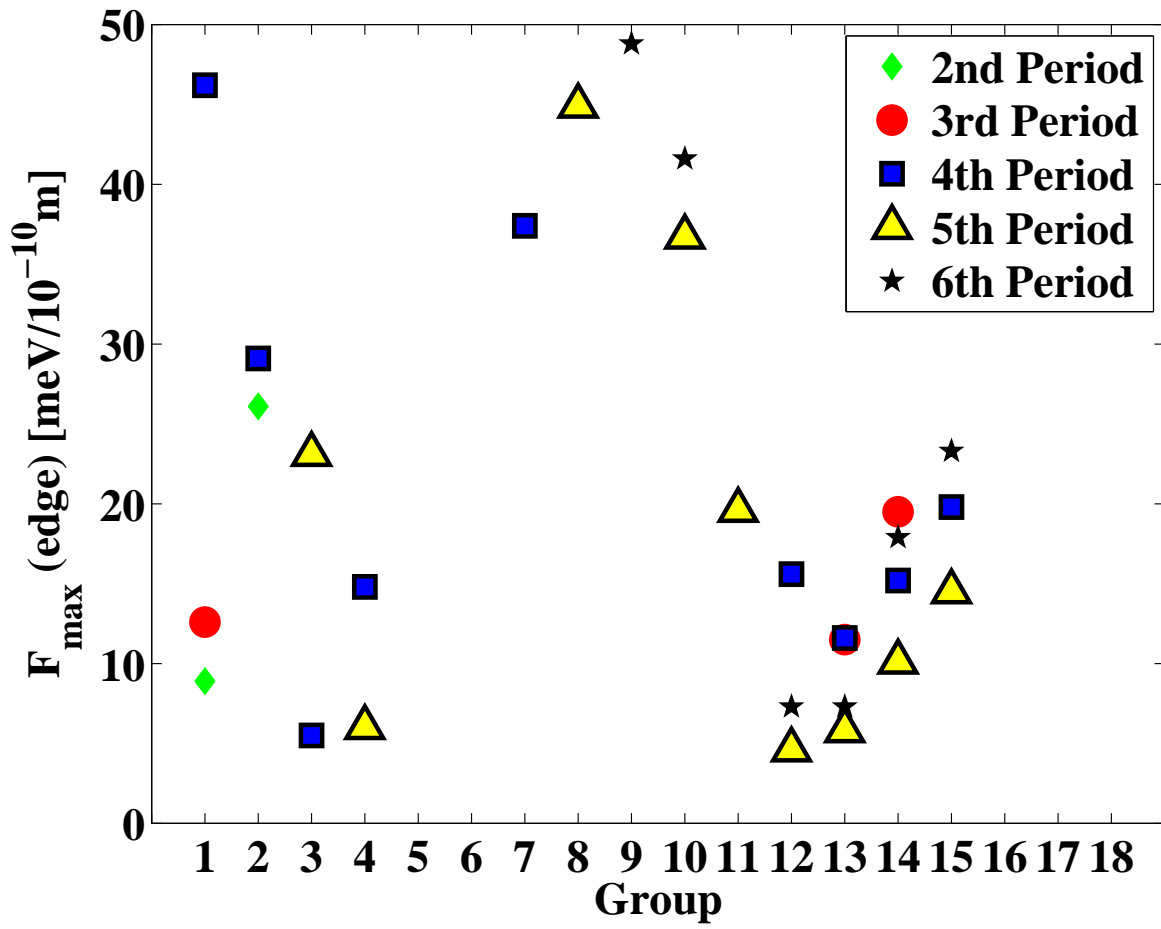
Figure 6.9: The DFT determined maximum interaction force between the solute atom and an edge dislocation in Mg basal slip. The plotted data are from Yasi et al. (2010)

6.3.2.2 Ni based binary systems

The solid solution strengthening in Ni binary systems have been very well studied experimentally (Mishima et al., 1986; Choi et al., 1990)[4] and theoretically (Shinoda et al., 1990b). The solid solution strengthening effects determined by experiments, and the solute-dislocation interaction energies calculated by tight-binding in Ni binary systems are shown in Figure 6.10. The calculated solute-dislocation interaction energies reasonably agree with experimentally determined strengthening effect.

The chemical trend in Figure 6.10 is different from that in Al and Mg binary solid solutions (see Figure 6.6 and 6.9). Since there is no data of alkaline and alkaline earth metals, conservatively speaking, in each period, the most effective strengtheners are group 3 and 13, and the least ones are group 9 or 10.

This trend is similar to the trend of the volume mismatch parameters in Ni binary solid solutions shown in Figure 6.11. One may notice that it seems from group 13 the volume mismatch parameter decreases, which is in contradiction with the trend of Al or Mg solid solutions (Figure 6.3 and 6.8[5]). In fact, this trend resembles the trend of the atomic radii of the pure elements (e.g. empirical atomic radii (Slater, 1964)). The general trend of the atomic radii is as the atomic number increases the atomic radius decreases. In alkali, alkali earth and transition metals, the atomic radii vs. atomic number takes a parabolic shape, which means in each period from left to right, there is a local atomic radii maximum in group 12.

---

[4]The data of Ni-X (X=In, Sn and Sb) in (Mishima et al., 1986) are disregarded. The data of Ni-X (X=Sn and Sb) are from (Choi et al., 1990).

[5]In Figure 6.8, from group 13 to group 15, the volume mismatch parameter slightly decreases.
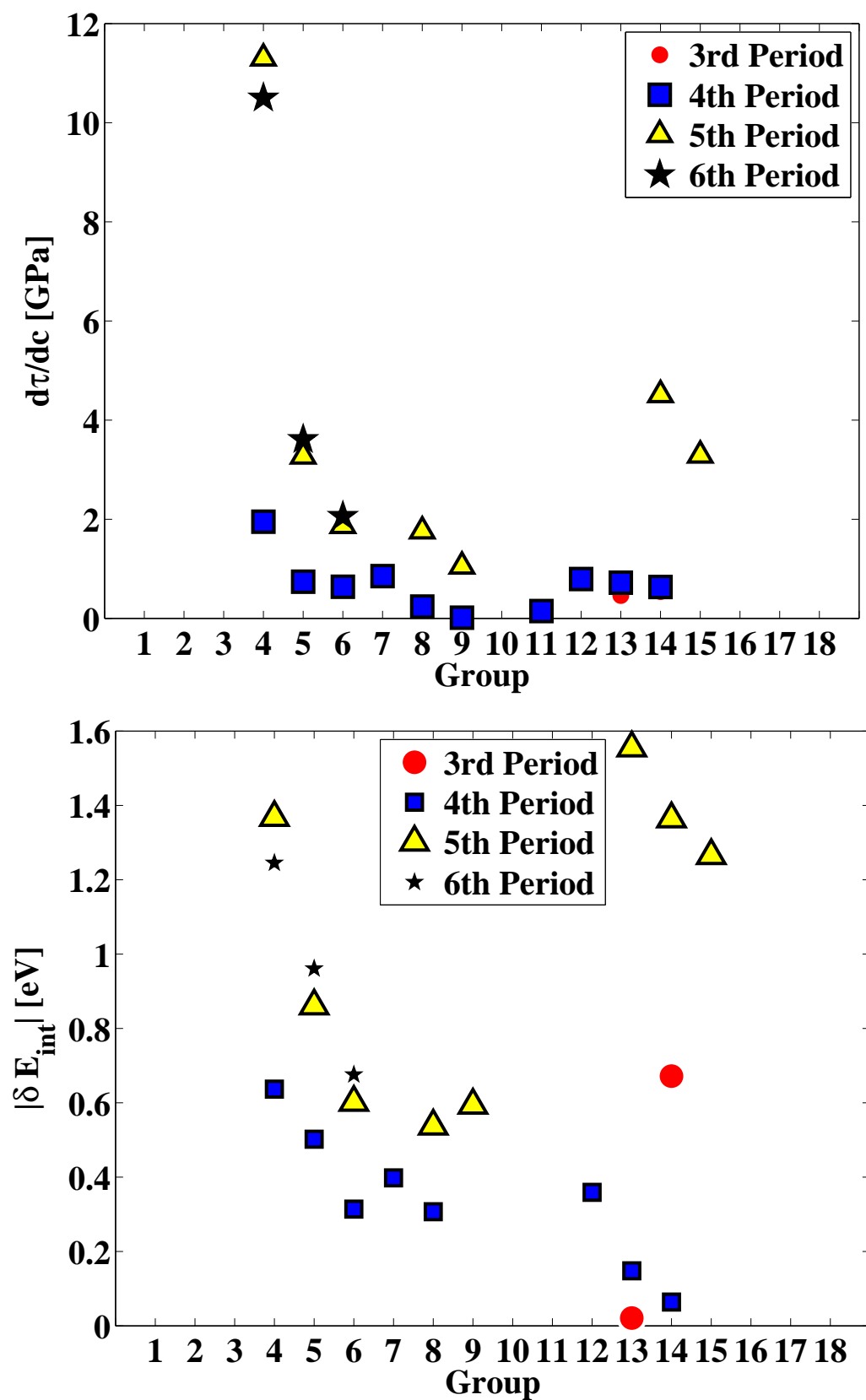
Figure 6.10: The solid solution strengthening in Ni solid solutions. Top: experimentally determined rate of solid solution hardening per one at.% (Mishima et al., 1986) (Sn and Sb are from (Choi et al., 1990)). Bottom: the interaction energy between the solute atom and the dislocation determined by tight-binding (Shinoda et al., 1990b).
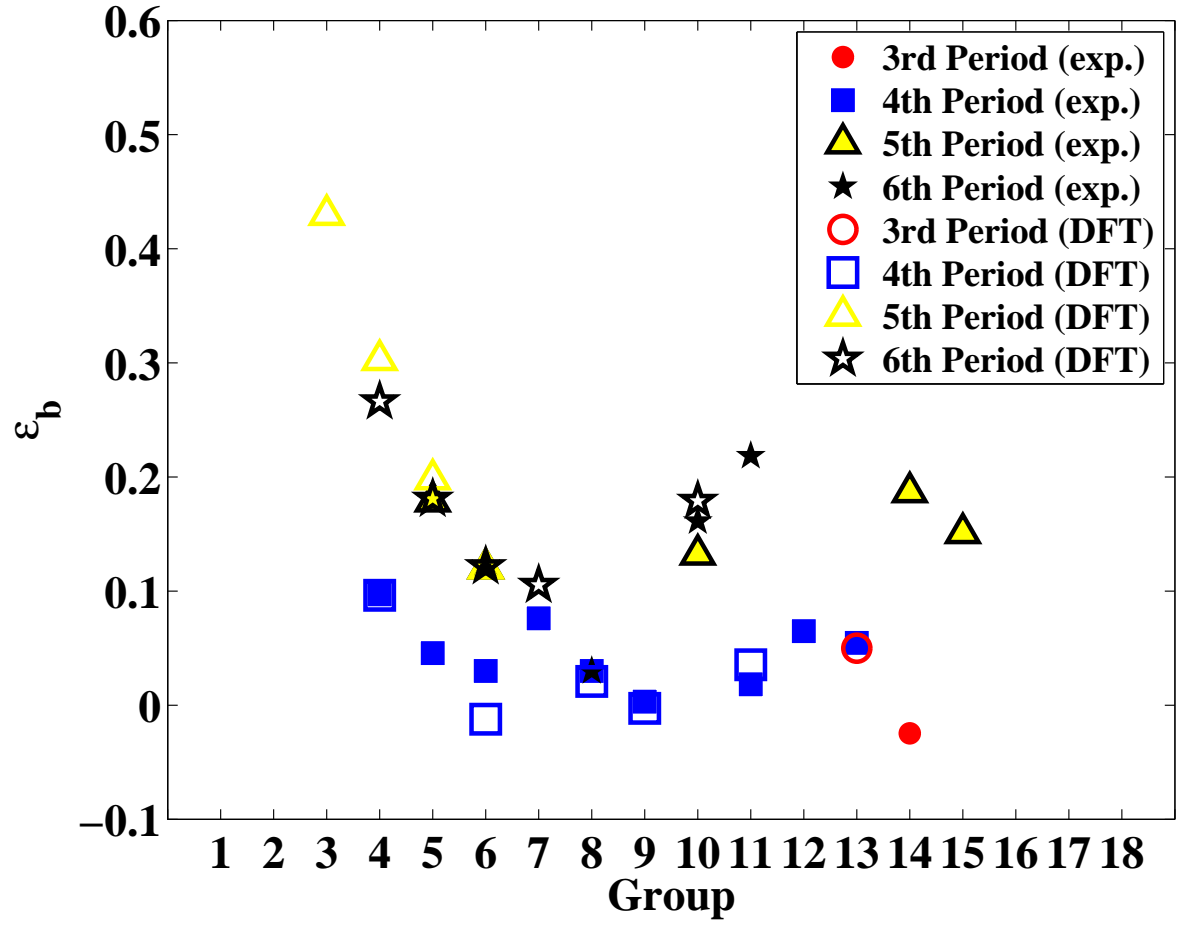
Figure 6.11: The volume mismatch parameter, ϵ_b, of Ni solid solutions. The plotted data are from Pearson (1964) (exp.) and Kim et al. (2009) (DFT).

6.3.3 Discussion of the chemical trend

It is observed that there is a chemical trend of the solid solution strengthening in Al, Mg (basal slip) and Ni binary alloys. This trend is based on the idea that the decisive properties, the atomic volume and the stacking fault energy, follow a trend on the periodic table. Some points should be made to further clarify the trend.

1. For the volume mismatch parameter of Al and Mg binary systems, the concave-up parabolic trend is similar to that of the atomic volume of the pure elements (Gschneidner Jr., 1964). As for Ni binary systems, the feature that the volume mismatch parameter decreases as the group number increases starting from group 12 or 13 resembles the trend of the atomic radii of the pure elements (e.g. empirical atomic radii (Slater, 1964)).

2. As shown in Figure 6.3, Figure 6.7 and Figure 6.8, within one period the volume and slip mismatch parameters roughly takes a concave-up parabolic and concave-down curve, respectively. If a simplified trend of the volume and slip mismatch parameters is assumed, as shown in Figure 6.12, one may notice that the positions of the least effect strengtheners depend on where $\delta_b = 0$ and $\epsilon_{SEF} = 0$ are placed. In Al and Mg binary systems, as shown in Figure 6.3, 6.7, and 6.8, $\epsilon_b \rightarrow 0$ and $\epsilon_{SEF} \rightarrow 0$ in group 3, 4 or 12, 13, therefore the least effective strengtheners are in these groups.
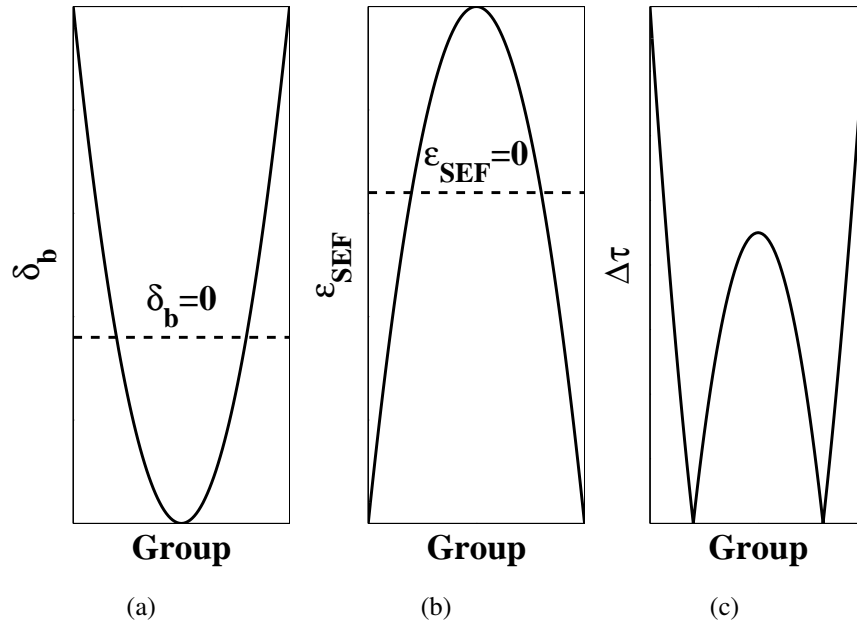
Figure 6.12: Schematics of the simplified trend of (a) the volume mismatch parameter, (b) the slip mismatch parameter, and (c) the increased shear stress. Dash line indicates where $\epsilon_b = 0$ or $\epsilon_{SEF} = 0$ is.

3. The parabolic trend is followed better in the metallic elements ranging from group 1 to group 12 in 4th, 5th and 6th period. And it might be violated in alkali and alkali earth metals in 2nd and 3rd period, and the elements in the main groups except group 1 and 2. Examples of this violation are:

   - The slip mismatch parameters of Mg binary systems on basal slip in the 2nd period in Figure 6.8

   - The volume mismatch parameters of Ni binary systems in groups 13 to 15 in Figure 6.11.

4. In some cases, when the solute elements are from the groups starting from group 12 or 13, the volume mismatch parameter alone cannot be correlated with the strengthening effect. Here are some examples:

   - As shown in Figure 6.13, for the solute elements being from group 1 to 12 in Mg on basal slip, the volume mismatch parameter almost correlates perfectly with the maximum interaction force. For the solute elements in group 13 to 15, the volume mismatch parameter only correlates with the maximum interaction force within one period.

   - In (Shinoda et al., 1990b), it shows that the volume mismatch parameter is almost correlated with the solute-dislocation interaction energy. The absolute value of the

119

volume mismatch parameter of Si in Ni is the smallest of the studied solute elements, but Si-dislocation interaction energy is still higher than some of the solute elements (see Figure 6.10).

- In Cu, Ag and Au binary systems (Jax et al., 1970), most of the strengthening effect can be correlated with the volume mismatch parameter. In Au binary systems, among the studied solute elements of Ga, Cd, Zn, In, Ag and Pd, the volume mismatch parameter of Ga is only higher than Ag, but the strengthening effect of Ga in Au is the highest in all these 6 solute elements. In (Jax et al., 1970), such a phenomenon was attributed to the extraordinarily high modulus mismatch parameter of Ga in Au. As recognized in (Yasi et al., 2010), it is speculated that Ga should significantly change the stacking fault energy of Au.
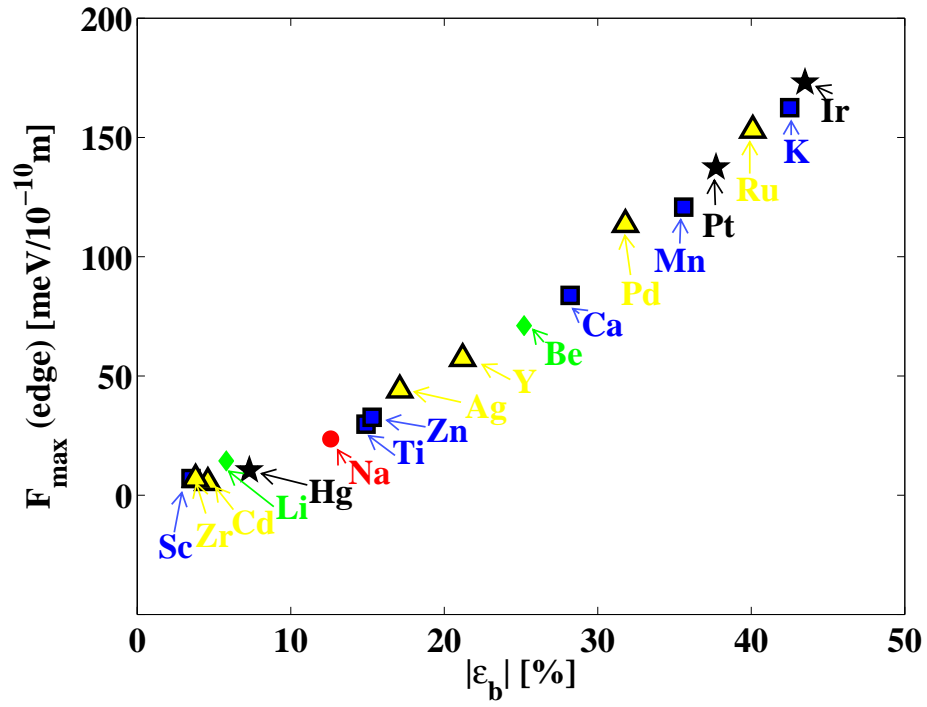
(a) Group: 1~12
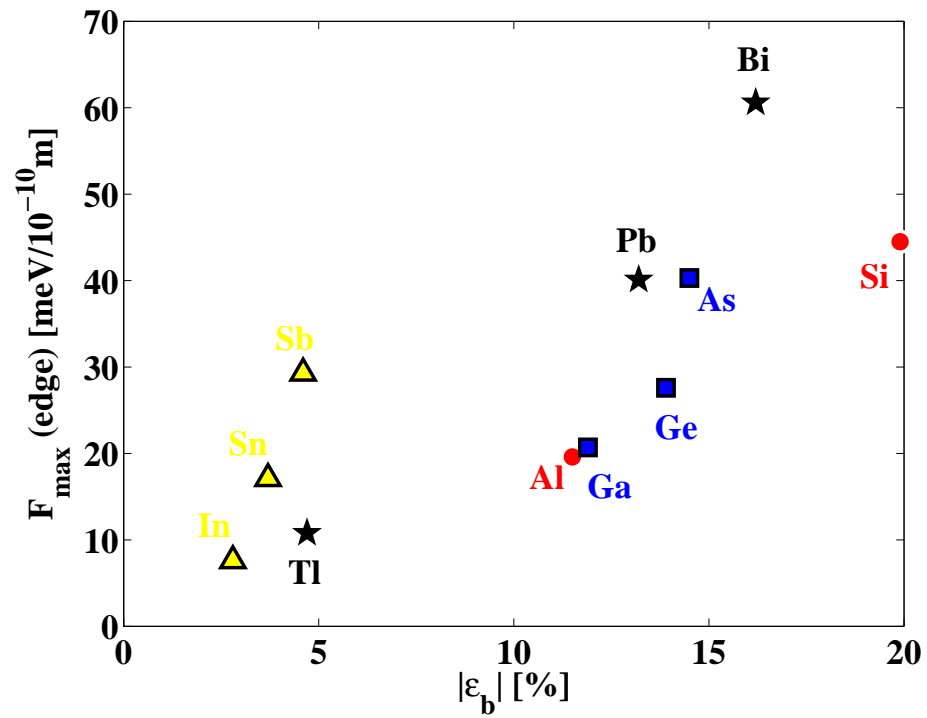
(b) Group: 13~15

Figure 6.13: Correlation between the volume mismatch parameter and the maximum interaction force between the solute atom and an edge dislocation on Mg basal slip. Top: solute elements are from group 1 to 12. Bottom: the solute elements are from 13 to 15. The plotted data are from Yasi et al. (2010). Color code: see Figure 6.8

6.4 Correlation between solubility and strengthening parameter

In the last section, the chemical trend of the solid solution strengthening in Al binary solid solutions on the periodic table is observed. With this trend the most and least effective strengtheners can be identified. This leads to a question whether those most effective strengtheners are dissoluble. Without any further investigation, this question can be readily and approximately answered. One of the Hume-Rothery rules states that the atomic radii of the solute and solvent atoms should not differ from each other more than 15 %, otherwise the solubility would be low. On the other hand, the predominant part of the solid solution strengthening is the volume mismatch. Therefore, if the volume mismatch parameter is large, the solubility of the corresponding element would be low. It has been shown that the strengthening effect could be correlated with the maximum solubility of the solute elements in Ni, Cu and Au binary solid solutions (Shinoda et al., 1990a), α-Fe binary solid solutions (Nakagawa and Hirano, 1968).

In this section, the correlation between the solubility and the strengthening effect is further discussed. The solubility was calculated by using the solubility enthalpy per solute ($\Delta H_{sol}(per\ solute)$) in Section 4.3.3.3. The strengthening effect is represented by the absolute value of the volume mismatch parameter ($|\delta_b|$). The uncertainties and related alloy design limit is to be discussed.
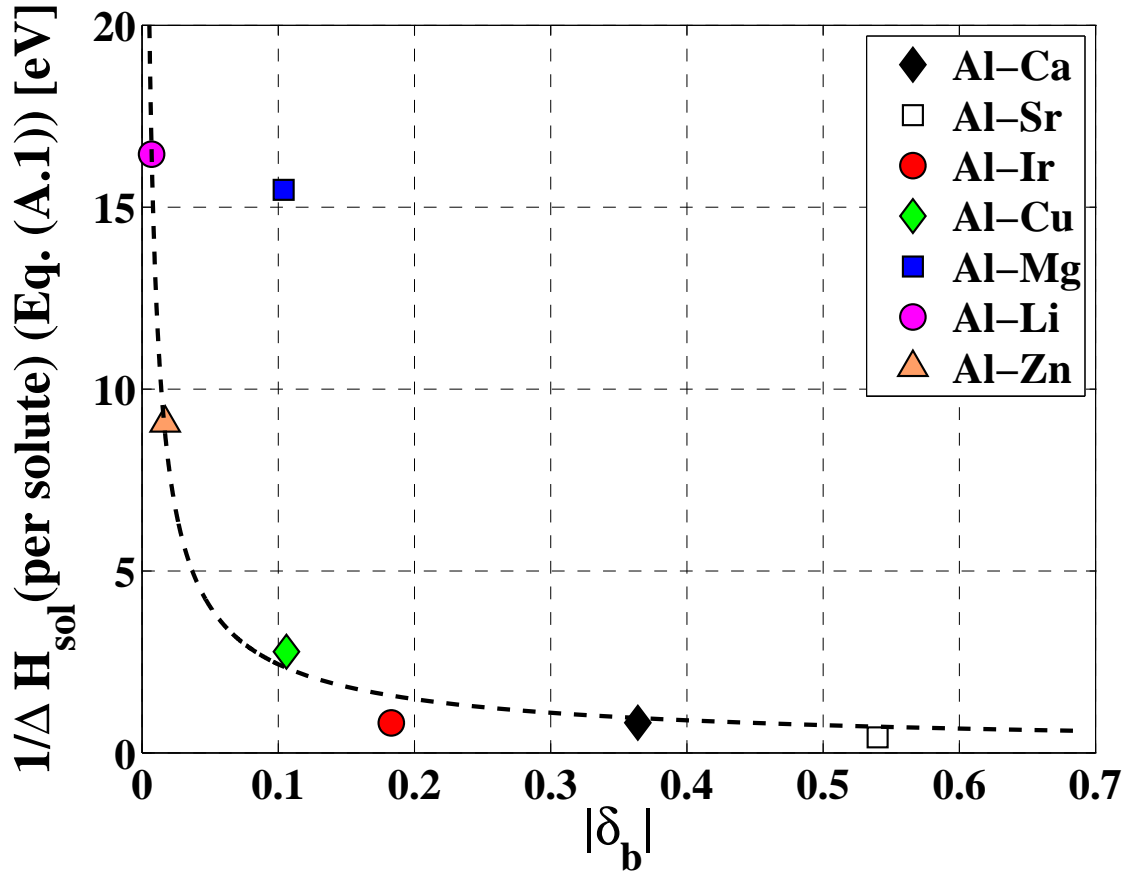
Figure 6.14: The reciprocals of the solubility enthalpy per solute vs. the absolute values of the volume mismatch parameter. Note: the solubility enthalpies of Al-Mg solid solutions cannot be fully trusted, because the total energy of the immediate intermetallic compound to the Al primary solid solution in the phase diagram was based on another compound which has similar composition (see Section 4.3.3.1). The black dash line is the fitted curve (Equation (6.2)).

Figure 6.14 shows the correlation between the solubility enthalpy per solute and the volume mismatch parameter. Please note that the solubility enthalpies of Al-Mg solid solutions cannot be fully trusted (see Section 4.3.3.1). If the solubility enthalpy per solute of Al-Mg is disregarded, the rest of the data points approximately fall on a power-law curve.

$$\frac{1}{\Delta H_{\text{sol}}(\text{per solute})} = A \cdot \frac{1}{|\delta_b|^n}, \, (n > 0) \tag{6.2}$$

where A and n are fitting parameters which is 0.46 and 0.72, respectively. The goodness of fit, R^2 is 0.9953 which indicates almost perfect correlation between the calculated data and the fitting curve.

If the entropy is neglected, Equation (6.2) allows to approximate the solubility limits on the

basis of $|\delta_b|$:

$$c_{\max} = \exp\left(-\frac{\Delta H_{\text{sol}}(\text{per solute})}{k_B T}\right) = \exp\left(-\frac{|\delta_b|^n}{A k_B T}\right) \tag{6.3}$$

At $c_{\max}$ and T, the shear resistance imposed by the solute atoms against the dislocation (τ_c) is (Leyson et al., 2010):

$$\tau_c(c_{max}, T) = \varepsilon \cdot c_{max}^p \cdot \left[1 - \left(\frac{k_B T}{\Delta E_b} \ln \frac{\dot{\epsilon}_0}{\dot{\epsilon}}\right)^{2/3}\right] \tag{6.4}$$

where

- ε is the strengthening potency.

- c_{max} is from Equation (6.3). $p = 2/3$, if Labusch statistics (Labusch, 1970, 1972; Leyson et al., 2010) is followed.

- $1 - (k_B T / \Delta E_b \cdot \ln \dot{\epsilon}_0 / \dot{\epsilon})^{2/3}$ is the temperature dependence of τ_c, where ΔE_b is the energy barrier for a flexible dislocation to overcome an array of solute atoms (Leyson et al., 2010).

The above three factors represent three competing processes:

- ε increases as $|\delta_b|$ increases.

- c_{max} increases as $|\delta_b|$ decreases according to Equation (6.3).

- $1 - (k_B T / \Delta E_b \cdot \ln \dot{\epsilon}_0 / \dot{\epsilon})^{2/3}$ decreases as the temperature increases. If ΔE_b is large, $1 - (k_B T / \Delta E_b \cdot \ln \dot{\epsilon}_0 / \dot{\epsilon})^{2/3}$ is less dependent on the temperature. ΔE_b, on the other hand, depends on c_{max} and $|\delta_b|$.

If ε and ΔE_b can be also expressed in terms of $|\delta_b|$ as c_{max} in Equation (6.3), the maximum $\tau_c(c_{max}, T)$ at an optimal $|\delta_b|$ can be estimated. This is realized by using the findings in (Leyson et al., 2010). In (Leyson et al., 2010), ε and ΔE_b in four Al binary alloys were calculated by using FB-DFT (flexible-boundary DFT). Both ε and ΔE_b almost linearly depend on the extra volume ΔV shown in Figure 6.15. If the linear correlations are assumed for any other Al binary systems, ε and $\Delta E_b / c^{1/3}$ can be calculated for other systems by using the knowledge of δ_b, because there is a relation between ΔV and δ_b:

$$\Delta V = 3a_{Al}^2 \cdot \frac{da}{dc}\bigg|_{c=0} = 3a_{Al}^3 \cdot \frac{1}{a} \cdot \frac{da}{dc}\bigg|_{c=0} = 3a_{Al}^3 \cdot \delta_b \tag{6.5}$$
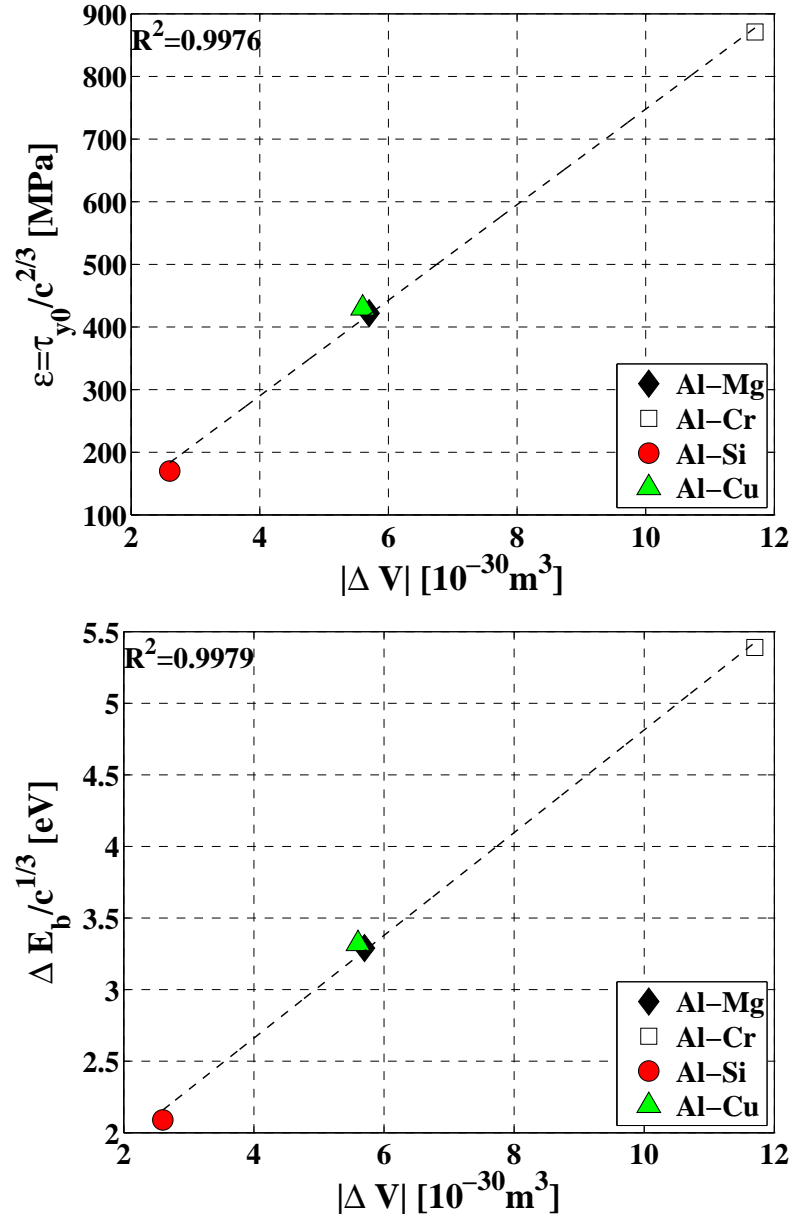
Figure 6.15: The correlation of the absolute extra volume ($|\Delta V|$) with (a) $\varepsilon = \tau_{y0}/c^{2/3}$ and (b) $\Delta E_b/c^{1/3}$. The goodness of fit (R^2) is shown on the figures. The plotted data are from (Leyson et al., 2010).
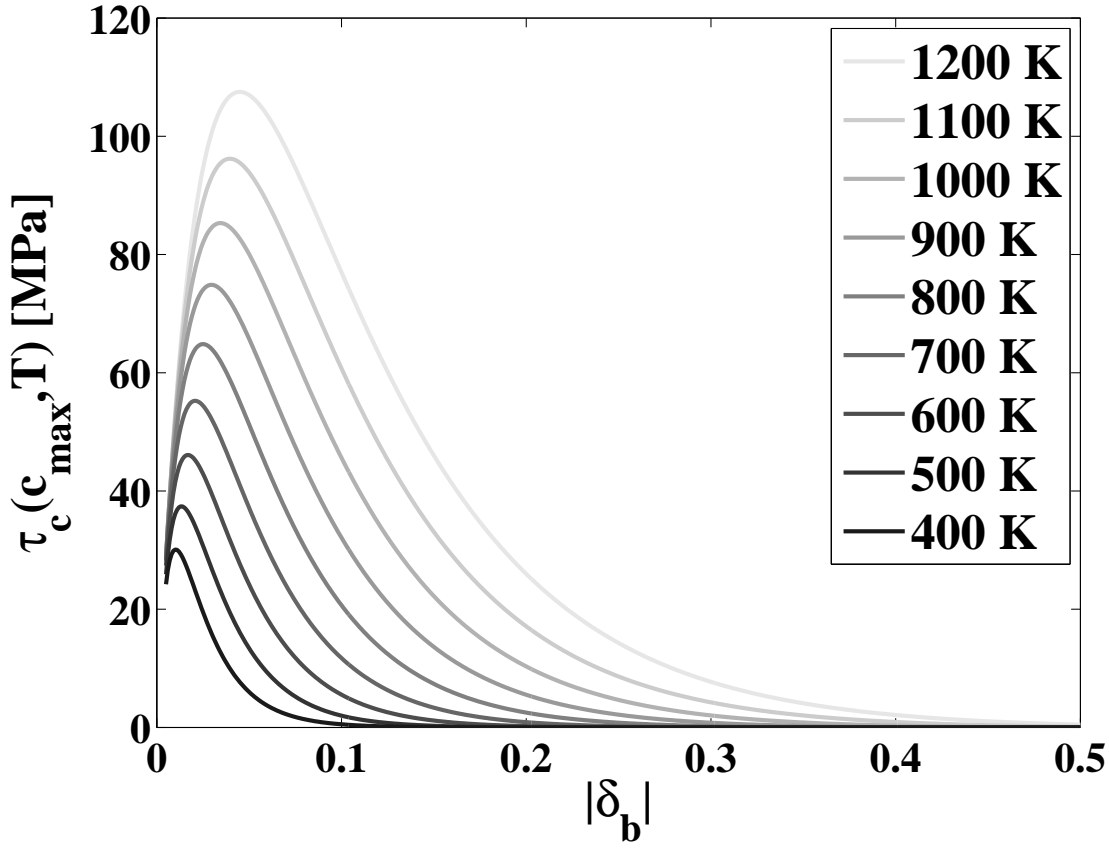
Figure 6.16: $\tau_c(c_{max},T)$ at various temperatures vs. $|\delta_b|$ by using Equation (6.4).

Thus, $\tau_c(c_{max},T)$ can be expressed in terms of $|\delta_b|$ and T, and plotted against $|\delta_b|$ at various temperatures shown in Figure 6.16[6]. One may notice that only high temperatures were analyzed. This is because that the solubility was calculated by using the solubility enthalpy per solute and neglecting the entropy effect, but as shown in (Ozoliņš and Asta, 2001; Ozoliņš et al., 2005; Ravi et al., 2006), the uncertainty introduced by the entropy effect is 200~600 K. For example, if the solubility limit is predicted to be c at T with the entropy effect, the same solubility limit (c) would be at T+200~600 K without the entropy. Therefore, the analysis was only conducted at the elevated temperatures (400~1200 K). Figure 6.16 shows:

- The optimal $|\delta_b|$ is usually smaller (e.g. <0.1).

- The optimal $|\delta_b|$ increases as the temperature increases.

- If $|\delta_b|$ is large, $\tau_c(c_{max},T)$ is very limited by low solubility limit (c_{max}).

However, cautions should be taken when Figure 6.16 is approached, because it is very qualitative analysis. Though the general feature that there exists an optimal $|\delta_b|$ will not be changed, there are a few limitations in the above analysis:

---

[6]$\dot{\epsilon}_0$ and $\dot{\epsilon}$ were chosen to be 10^{-4} and 10^{-6} in Equation (6.4). The general feature of Figure 6.16 is not sensitive to the actual values of $\dot{\epsilon}_0$ and $\dot{\epsilon}$.

- As aforementioned, without considering the entropy effect, there could be 200~600 K uncertainty.

- The temperature dependence of τ_c $(1 - (k_B T/\Delta E_b \cdot \ln \dot{\epsilon}_0/\dot{\epsilon})^{2/3})$ do not produce the "stress plateau", which means this temperature dependence is only valid before the plateau temperature.

- In this thesis, the end members used to calculated the solubility enthalpy are the pure fcc Al and the stable intermetallic compound immediate next to the primary Al solid solutions. If the metastable intermetallic compound is considered, the solubility enthalpy could be changed. The validation of the power-law correlation between the solubility enthalpy and the volume mismatch parameter (Equation 6.2) is an open question.

- When the concentration in the solid solution exceeds the solubility limit and the diffusion is significantly suppressed, the above analysis is not valid any more.

Chapter 7

Perturbation caused by solute atoms in studied Al binary solid solutions

7.1 Purpose of this chapter

As stated in Section 1.1, the application of quantum mechanics in materials science is not only aimed at obtaining the materials properties, but also at achieving understanding from the electronic origin. In this chapter, an attempt was made in this direction. Specifically, the perturbation caused by the solute elements in the Al matrix was studied.

Quantum mechanically speaking, the perturbation means that the periodic potential acting on the electrons in a pure crystal is locally changed by the solute elements. Therefore, the pertinent investigation of this problem should be the wavefunctions or energy bands, as well as other analysis, such as the electron density difference[1] or the electron localization function (ELF)[2]. All these analysis are considerably sophisticated and complex. Moreover, none of them provide a simple and intuitive physical picture.

A simple and intuitive picture could be the property changes on a per atom basis. Such a picture allows us to see up to which range the effect of the solute atom becomes negligible.

Then the question is how to identify an atom in a crystal. A simple method can be Voronoi construction. But this method is purely based on geometry. When the atoms are in an alloy crystal, the identification of the atomic boundaries is too arbitrary. A more reasonable method would be Bader analysis which identifies the atomic boundaries based on the topology of the electron density (see Section 3.5 for details).

In this thesis, perturbation caused by the solute atoms is characterized by the average electron density of each of the Al atoms in an Al solid solution. The average electron density is calculated by the total charge divided by the atomic volume, both of which were determined by Bader analysis. The idea of the average electron density is similar to the free electron theory, because in the free electron theory, the electron density is assumed to be homogeneous throughout the crystal. Al is a simple metal, and the density of states of pure fcc Al resembles to that of the free electrons. Therefore, the idea of the average electron density is not a bad approximation to Al.

In this chapter, the atomic volume and the charge transfer of the solute atoms in studied Al solid solutions are presented. Then the average electron density of each Al atoms in those solid solutions is presented. In order to further reveal the perturbation by the solute atoms, the average electron density of each Al atom in non-relaxed crystals is investigated. It will be demonstrated that the atomic relaxation (elastic effect) has the great contribution to the perturbation.

---

[1]For example, the electron density difference ($\Delta\rho_{A_nB_m}$) of a binary system (A_nB_m) is calculated in the following way: (1) calculate the electron density of A_nB_n, $\rho_{A_nB_m}$; (2) replace the constituent A by vacancies ($\square$) in A_nB_m, and calculate the electron density of $\square_nB_m$, $\rho_{\square_nB_m}$; (3) replace the constituent B by vacancies ($\square$) in A_nB_m, and calculate the electron density of $A_n\square_m$, $\rho_{A_n\square_m}$; (4) then $\Delta\rho_{A_nB_m}$ is obtain by $\Delta\rho_{A_nB_m} = \rho_{A_nB_m} - \rho_{A_n\square_m} - \rho_{\square_nB_m}$. In step (2) and (3), the atomic relaxation is not allowed in the calculation.

[2]The electron localization function (ELF) is a measure for the localization of the electrons. ELF ranges between 0 and 1. ELF=0 is for the extreme delocalization, ELF=1 is for extreme localization respectively, and 0.5 is for free electrons.

7.2 Atomic volume and charge transfer of solute atoms in studied Al binary solid solutions

The atomic volume and the charge transfer of the solute atoms in studied Al binary solid solutions are shown in Figure 7.1. The following observations are made:

1. **When the solute gives charges to Al, its atomic volume decreases, and vice versa.**
   Figure 7.1 shows Ca, Sr, Mg, and Li give charges to the surrounding Al which makes themselves smaller. All of them except Sr are even smaller than the atomic volume of the pure Al, but the volume decrease of Sr in Al from its original volume is significantly large. Ir, Cu, and Zn, on the other hand, take charges from Al which makes them larger even than pure Al.

2. **In most of the studied systems, when the solute gives charges to Al, the lattice parameter increases, and vice versa. The exception is Li.**
   If one recalls the lattice parameters of those solid solutions in Figure 4.1, one may recognize that the lattice parameter increases when the solute atom gives charges to Al (e.g. Ca, Sr and Mg), and vice versa. Taking Ca for example, the process should be: when an Al atom is substituted by Ca, it gives charges to Al; this charge transfer makes Al larger and Ca smaller; but the volume increase of Al is larger than the decrease of Ca; thus the overall volume increases. For Li, the volume increase of Al cannot compensate the volume decrease of Li, therefore the overall volume is decreased.

3. **As long as the solute atom has 12 first nearest Al neighbors, the amount of the charge transfer is almost independent of the concentration..**
   Figure 7.1 shows that the charge transfer and the atomic volume of the solute atom in Al binary solid solutions are almost independent of the concentration. It only depends on the immediate atomic environment. The charge transfer and the atomic volume of the solute atoms in $L1_2$ Al_3X_1 especially are practically the same as in the dilute solid solutions. The exception is Ir. Probably because the amount of the charge transfer from Al to Ir is too large, the charge transfer deviates from the linear behavior.

4. **The atomic relaxation has only small effect on the charge transfer between the solute atom and Al.**
   Figure 7.2 shows the difference in the atomic volume and the charge transfer between the solute atoms in relaxed and non-relaxed supercells. The atomic relaxation indeed has a certain contribution to the charge transfer and the atomic volume change. However, the difference in the charge transfer is one order of magnitude lower than the charge transfer of the solute atoms in relaxed supercells (see Figure 7.1). For Mg, Li, and Zn, the atomic relaxation almost has no effect on the event and the amount of the charge transfer. For Ca, Sr, Ir, and Cu, the atomic relaxation just promotes the charge transfer.
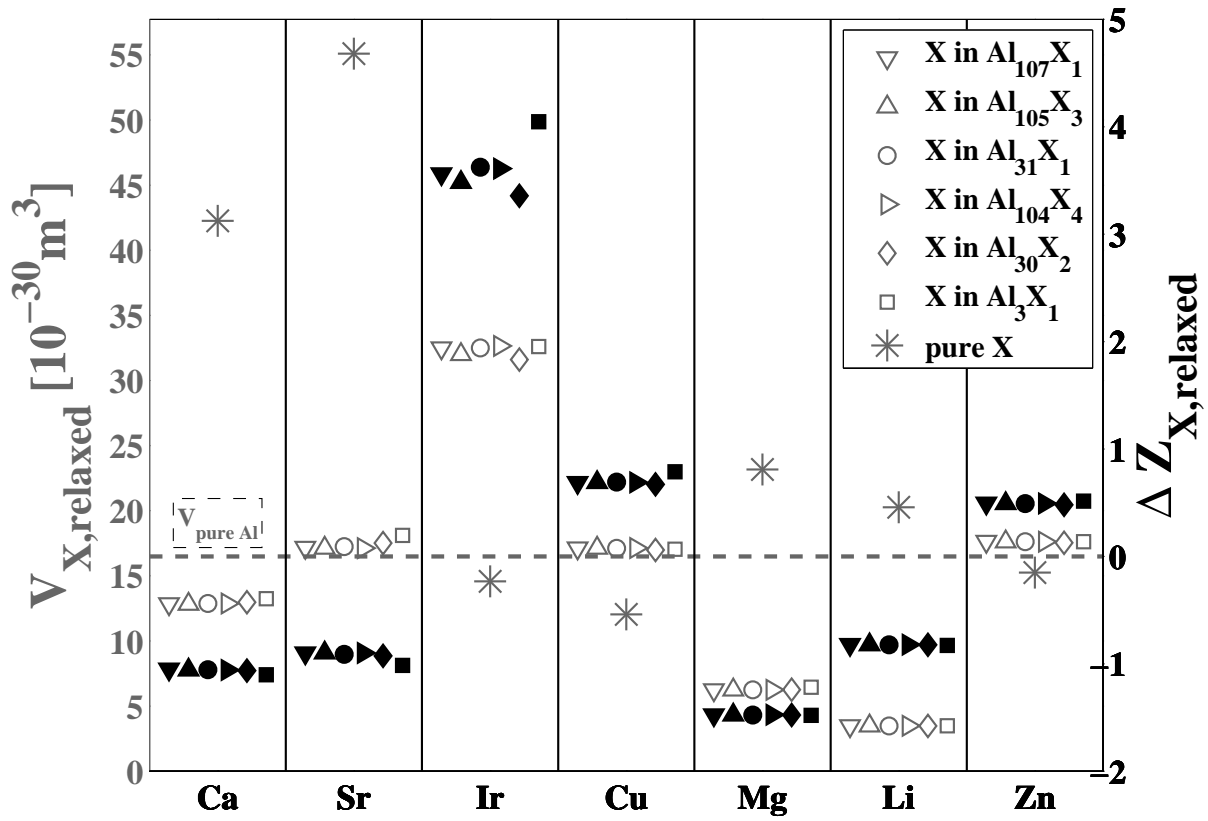
Figure 7.1: The atomic volume (left y axis) and the charge transfer (right y axis) of the solute
atoms in studied Al binary solid solutions in relaxed supercells. Relaxed means that the
atomic positions are externally and internally relaxed. Open symbol: atomic volume on
the left y axis. Solid symbols: charge transfer (positive: take charge from Al; negative:
give charge to Al) on the right y axis. The gray horizontal dashed line is the equilibrium
atomic volume of pure Al in the bulk phase.
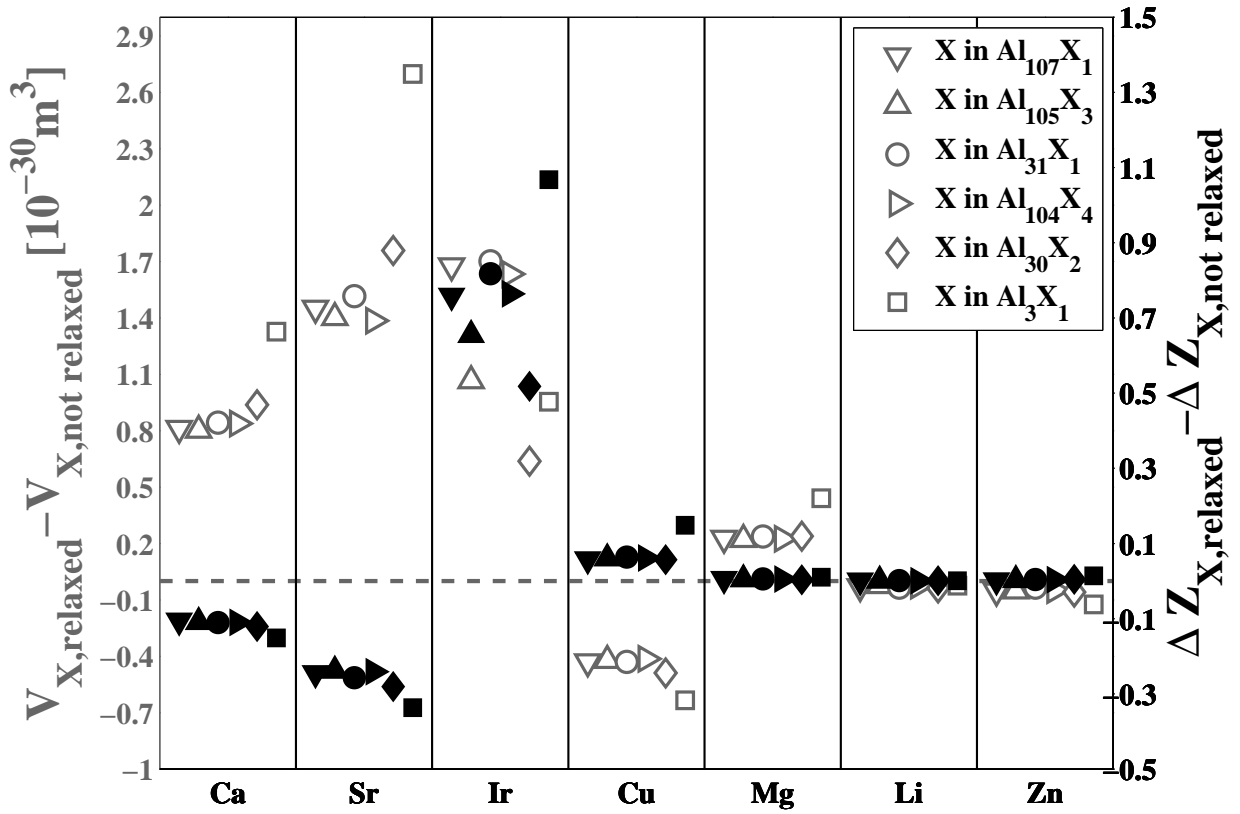
Figure 7.2: The effect of the atomic relaxation on the atomic volume (left y axis) and the charge transfer (right y axis) of the solute atoms in studied Al binary solid solutions. Open symbol: on the left y axis. Solid symbols: on the right y axis. The gray horizontal dashed line is zero for both sides of the y axis.

7.3 Average electron density of each Al atom in studied Al binary solid solutions

7.3.1 Separating elastic and chemical effect

Among the possible sources of the supercell size dependence (Castleton et al., 2009), the elastic effect, namely the local atomic relaxation, is probably the main source of the supercell size dependence in metallic solid solutions. Thus, in this study, three kinds of supercells were employed to separate the elastic effect and the chemical effect:

relaxed $Al_{(1-c)}X_c$ The supercell is fully relaxed externally and internally. The calculated properties presented in Chapter 4 and Chapter 5 are from this kind of supercells. This supercell includes both the elastic effect and the chemical effect.

$Al_{(1-c)}Al_c$ (relaxed as $Al_{(1-c)}X_c$) The solute atom(s) in **relaxed $Al_{(1-c)}X_c$** is/are replaced by Al atom(s), and the atoms are fixed at their original positions as if they are still in **relaxed $Al_{(1-c)}X_c$**. This supercell is pure Al with disordered lattice structure, and it only includes the elastic effect.

non-relaxed $Al_{(1-c)}X_c$ This supercell has perfect fcc structure and the lattice parameter of pure Al. This supercell only has the chemical effect.

The results of the first kind of supercells are shown in Section 7.3.2, and the last two kinds are shown in Section 7.3.3.

7.3.2 Average electron density of each Al atom in relaxed supercells (elastic effect and chemical effect)

In this section, the average electron density of each Al atom in relaxed solid solution supercells is presented. The average electron densities are arranged according the the neighboring postions of the Al atoms to the solute atoms. Some of the binary solid solutions have similar average electron density vs. Al-solute neighboring position profiles:

- Al-Mg, Al-Ca and Al-Sr: the average electron densities of Al atoms are changed even beyond the third nearest neighbors to the solute.

- Al-Ir and Al-Cu: the largest change in the average electron density of Al atom is not at the first nearest neighbors, but at the second nearest neighbors to the solute.

- Al-Li and Al-Zn: the change in the average electron density of Al at the second nearest neighbors to solute is nearly negligble.

7.3.2.1 Average electron density of each Al atoms in Al-Ca, Al-Sr and Al-Mg solid solutions
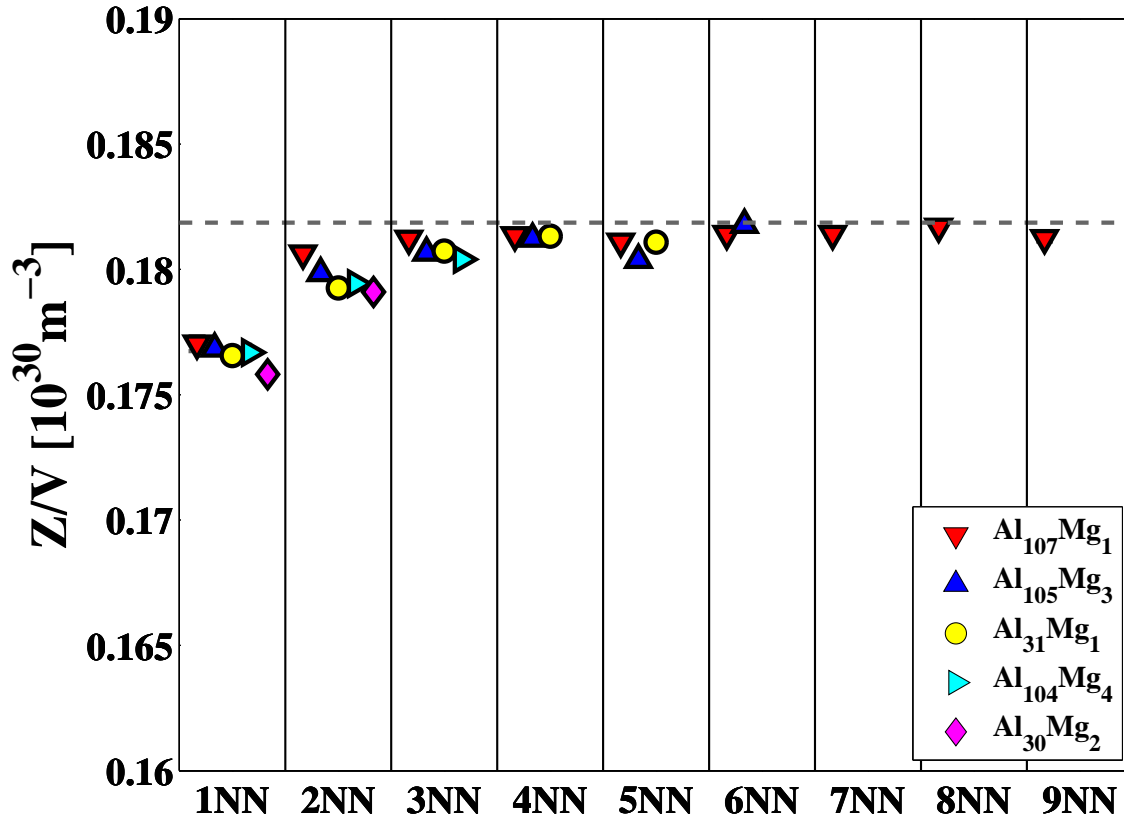
Figure 7.3: The average electron density (Z_{Al}/V_{Al}) of each Al atom in Al-Mg solid solutions in relaxed supercells. iNN: the ith nearest neighbor to the solute atoms. The gray horizontal dashed line is the average electron density of pure Al in the bulk phase.

The average electron densities of each Al atoms in Al-Mg, Al-Ca and Al-Sr solid solutions are shown in Figure 7.3 and 7.4. Probably because Mg, Ca and Sr are in the same group on the periodic table, there are some similarities in Figure 7.3 and 7.4:

- The change in the average electron density of individual Al atoms is even beyond the third nearest Al neighbors to the solute atoms.

- There is a compositional dependence of the change in average electron density of each Al atom at the same neighboring position.

- As the period number increases (Mg is in 3rd period, Ca is in 4th and Sr is in 5th), the change in the average electron density becomes more pronouced and long-ranged.
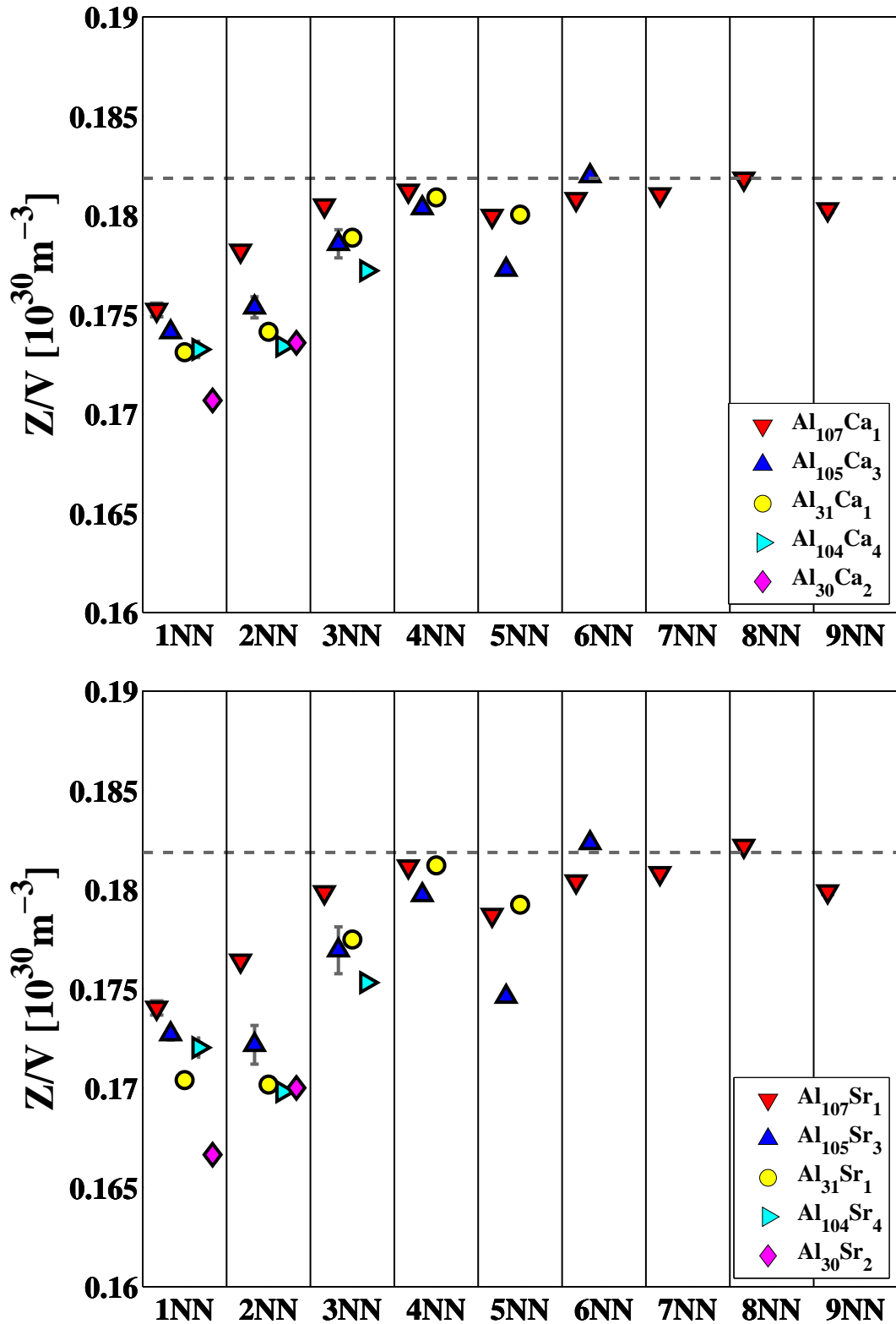
Figure 7.4: The average electron density (Z_{Al}/V_{Al}) of each Al atom in Al-Ca (top) and Al-Sr
(bottom) solid solutions in relaxed supercells. iNN: the ith nearest neighbor to the solute
atoms. The gray horizontal dashed line is the average electron density of pure Al in the
bulk phase.

- In Figure 7.4, the change in the average electron density of Al is long-ranged in Al-Ca and Al-Sr. It seems a 108 atomic supercell (3×3×3) is not sufficiently large enough to describe an isolated Ca or Sr atom in the Al matrix.

7.3.2.2 Average electron density of each Al atom in Al-Ir and Al-Cu solid solutions

In a solid solution, the solvent atom mostly affected should be the first nearest neighbor to the solute atom. But Figure 7.5 shows that in Al-Ir and Al-Ca solid solutions, the largest change in the average electron density of Al occurs at the second nearest neighbors to the solute atom. In Figure 5.3 and Figure 5.4, it shows that there is very strong non-linear compositional dependence of $C_{11} - C_{12}$ of $Al_{30}Ir_2$ and $Al_{30}Cu_2$, C_{44} of $Al_{30}Ir_2$. In $Al_{30}X_2$ supercells, there is no 3rd nearest Al neighbors to the solute atoms (see Table 5.2). The unique change in the average electron density at the second nearest Al neighbors to the solute atoms might be related to the strong non-linearity at the compostion of $Al_{30}X_2$.
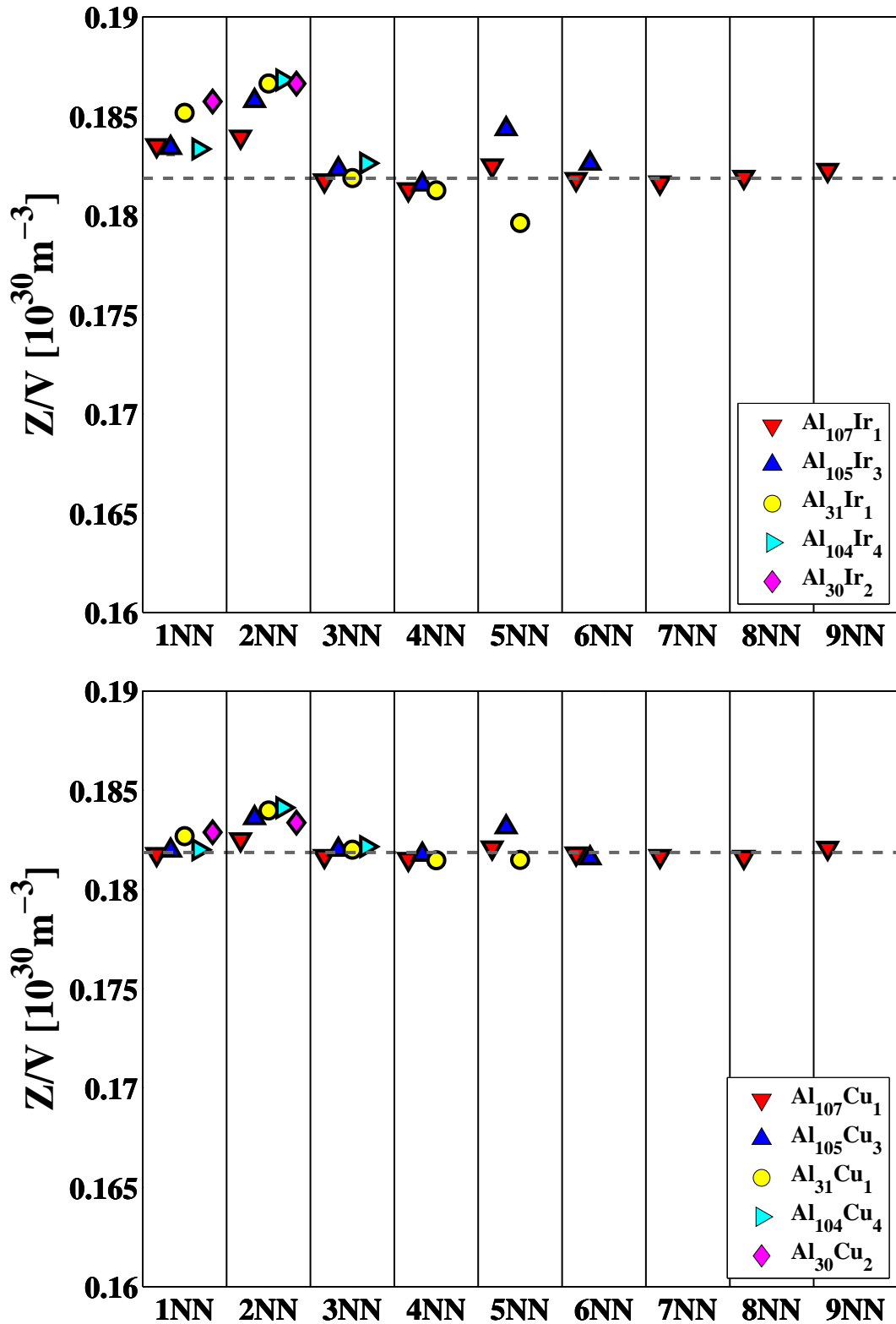
Figure 7.5: The average electron density (Z_{Al}/V_{Al}) of each Al atom in Al-Ir (top) and Al-Cu (bottom) solid solutions in relaxed supercells. iNN: the ith nearest neighbor to the solute atoms. The gray horizontal dashed line is the average electron density of pure Al in the bulk phase.

7.3.2.3 Average electron density of each Al atom in Al-Li and Al-Zn solid solutions

The average electron density of each Al atoms in Al-Li and Al-Zn is shown in Figure 7.6. Compared with other systems, the change in the average electron density is short-ranged. The change at the second nearest Al neighbors to solute atoms is nearly negligble.
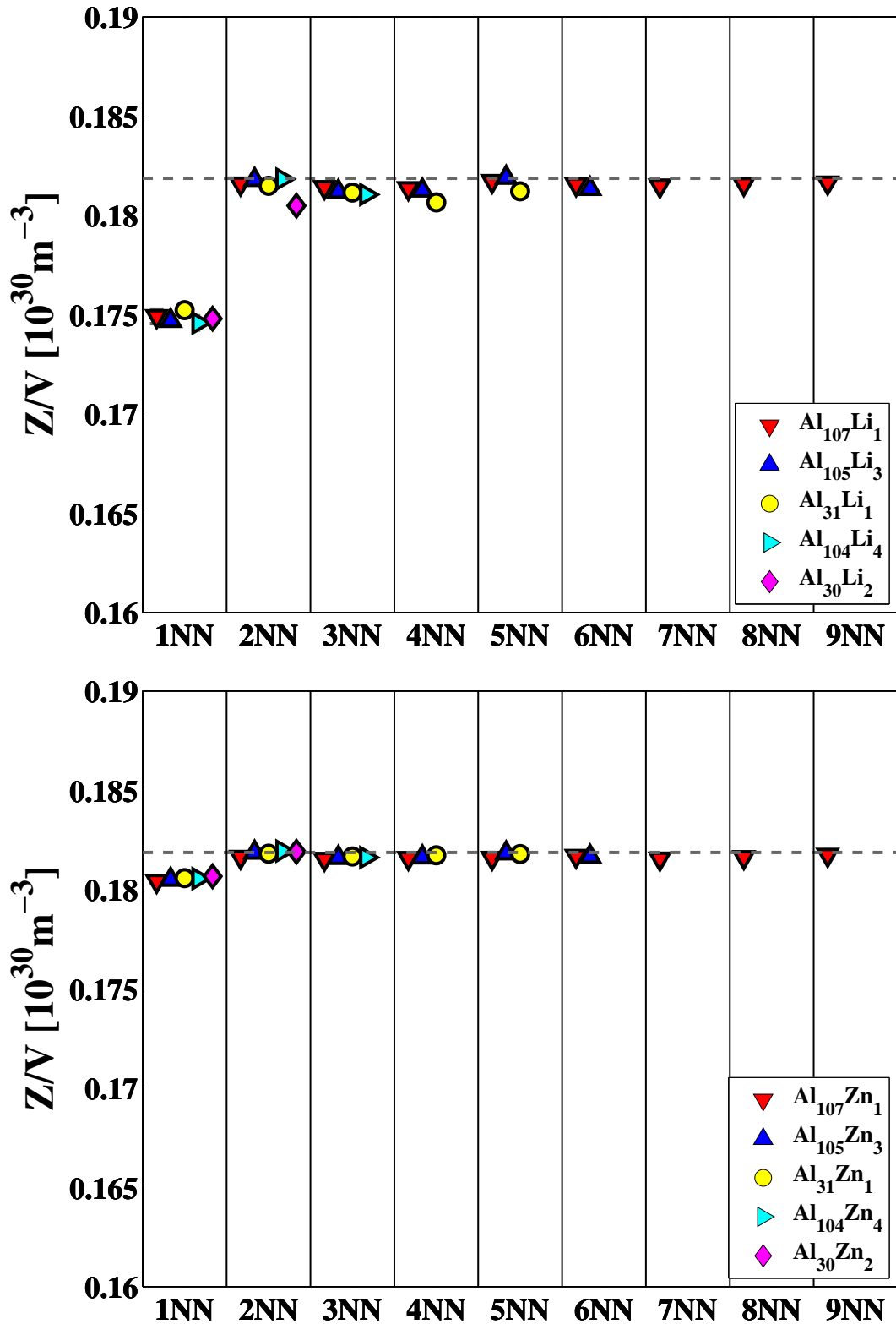
Figure 7.6: The average electron density (Z_{Al}/V_{Al}) of each Al atoms in Al-Li (top) and Al-Zn
(bottom) solid solutions in relaxed supercells. iNN: the ith nearest neighbor to the solute
atoms. The gray horizontal dashed line is the average electron density of pure Al in the
bulk phase.

7.3.3 Average electron densities of each Al atom due to either chemical effect or elastic effect

Compared with the average electron density vs. Al-solute neighboring position profiles in the last section, the following observations can be made in the supercells which has either the elastic effect or the chemical effect (Figure 7.7, Figure 7.8, Figure 7.9, Figure 7.10, Figure 7.11, Figure 7.12 and Figure 7.13):

- In non-relaxed supercells, the change in the average electron density of the first nearest Al neighbors is independent of the concentration. Beyond the first nearest Al neighbors, the rest of the Al atoms nearly have no change in the average electron density.

- In $Al_{(1-c)}Al_c$ supercells (relaxed as $Al_{(1-c)}X_c$), the average electron density vs. Al-solute neighboring position profiles are similar to those of relaxed as $Al_{(1-c)}X_c$ (see last section).

- The atomic relaxation is most responsible for the change in the average electron density of individual Al atoms, except Al-Li and Al-Zn.
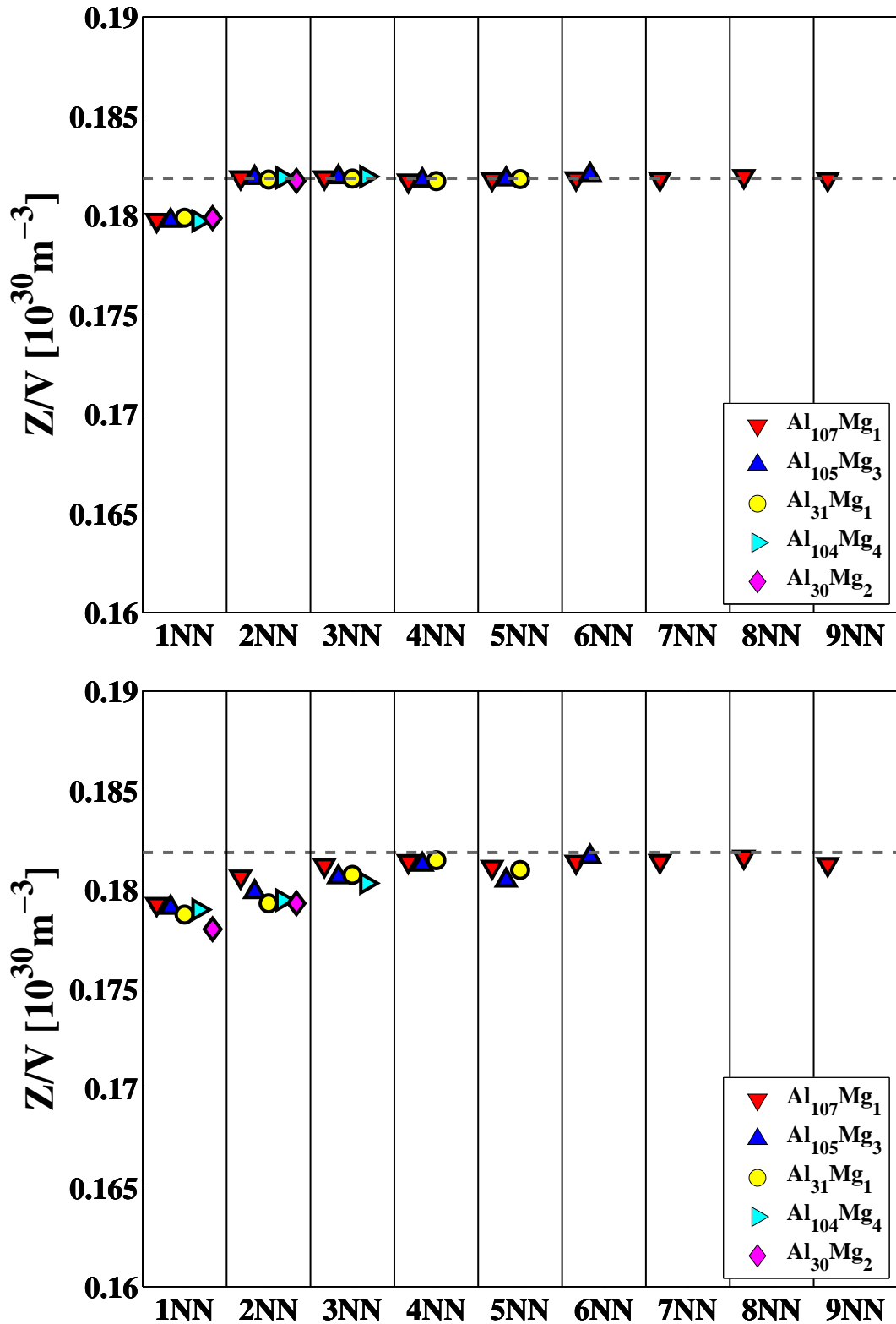
Figure 7.7: The average electron density (Z_{Al}/V_{Al}) of each Al atom in non-relaxed $Al_{(1-c)}X_c$
(top) and $Al_{(1-c)}Al_c$ (relaxed as $Al_{(1-c)}X_c$) (bottom) of Al-Mg solid solutions. iNN: the
ith nearest neighbor to the solute atoms. The gray horizontal dashed line is the average
electron density of pure Al in the bulk phase.
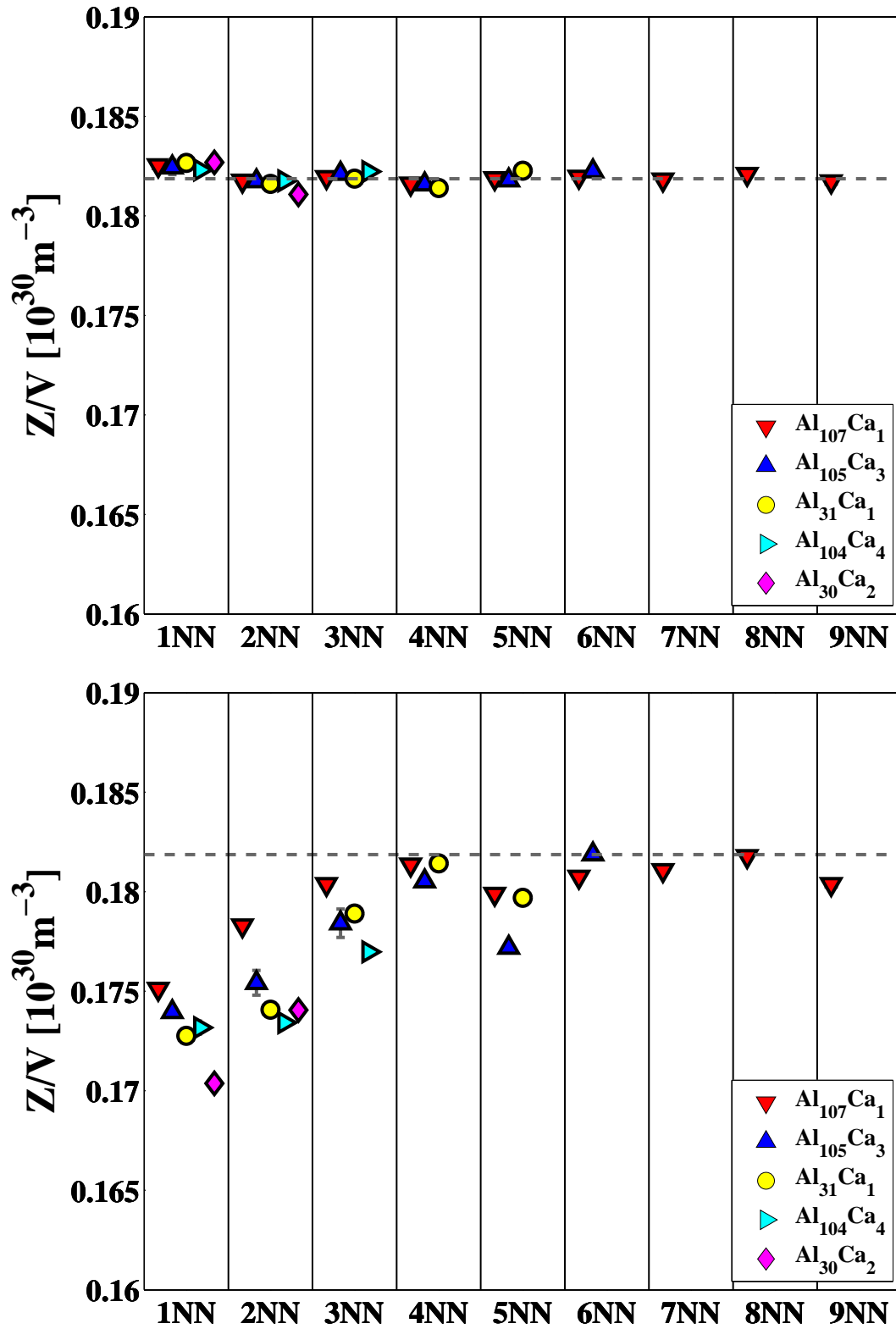
Figure 7.8: The average electron density (Z_{Al}/V_{Al}) of each Al atom in non-relaxed $Al_{(1-c)}X_c$ (top) and $Al_{(1-c)}Al_c$ (relaxed as $Al_{(1-c)}X_c$) (bottom) of Al-Ca solid solutions. iNN: the ith nearest neighbor to the solute atoms. The gray horizontal dashed line is the average electron density of pure Al in the bulk phase.
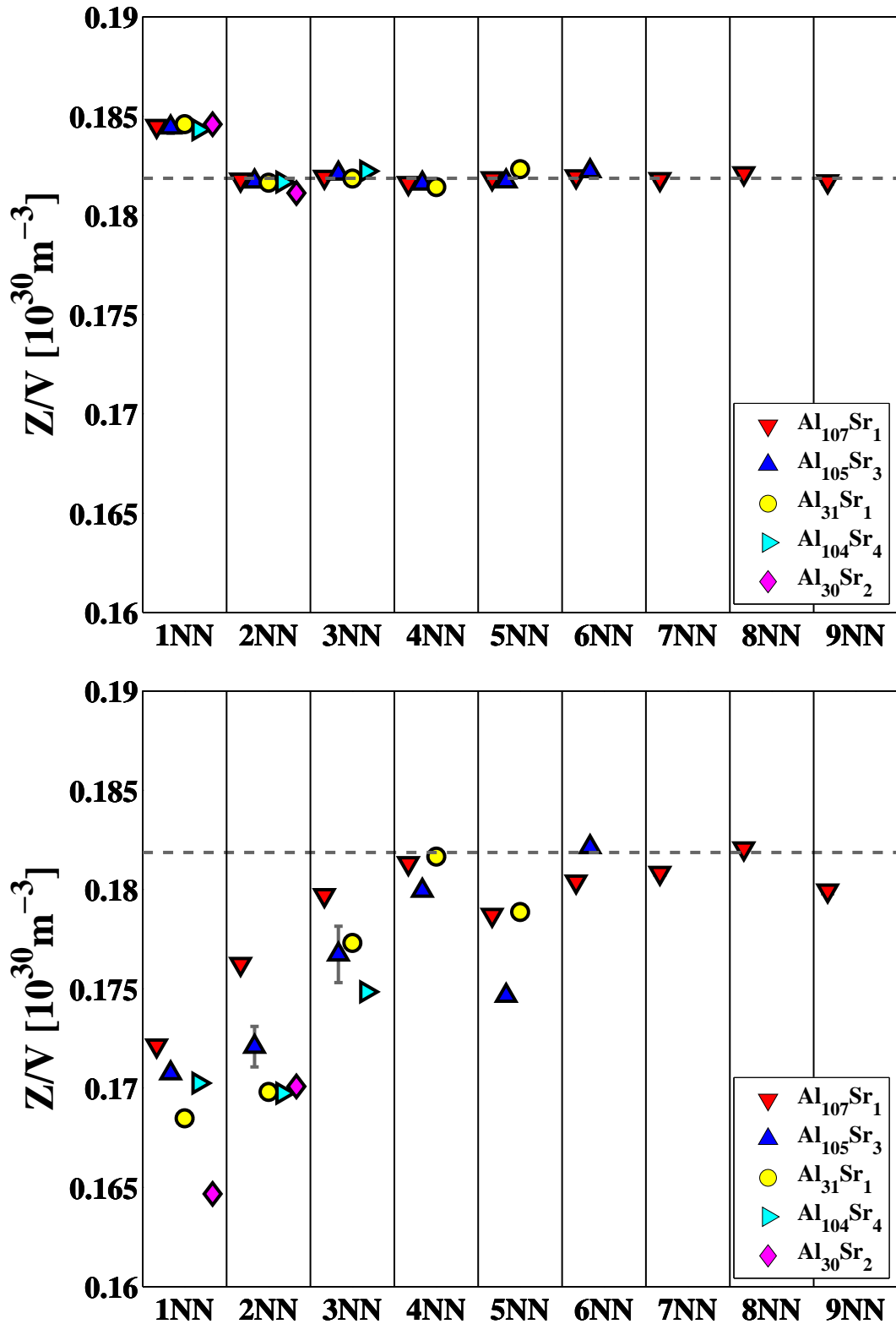
Figure 7.9: The average electron density (Z_{Al}/V_{Al}) of each Al atom in non-relaxed $Al_{(1-c)}X_c$ (top) and $Al_{(1-c)}Al_c$ (relaxed as $Al_{(1-c)}X_c$) (bottom) of Al-Sr solid solutions. iNN: the ith nearest neighbor to the solute atoms. The gray horizontal dashed line is the average electron density of pure Al in the bulk phase.
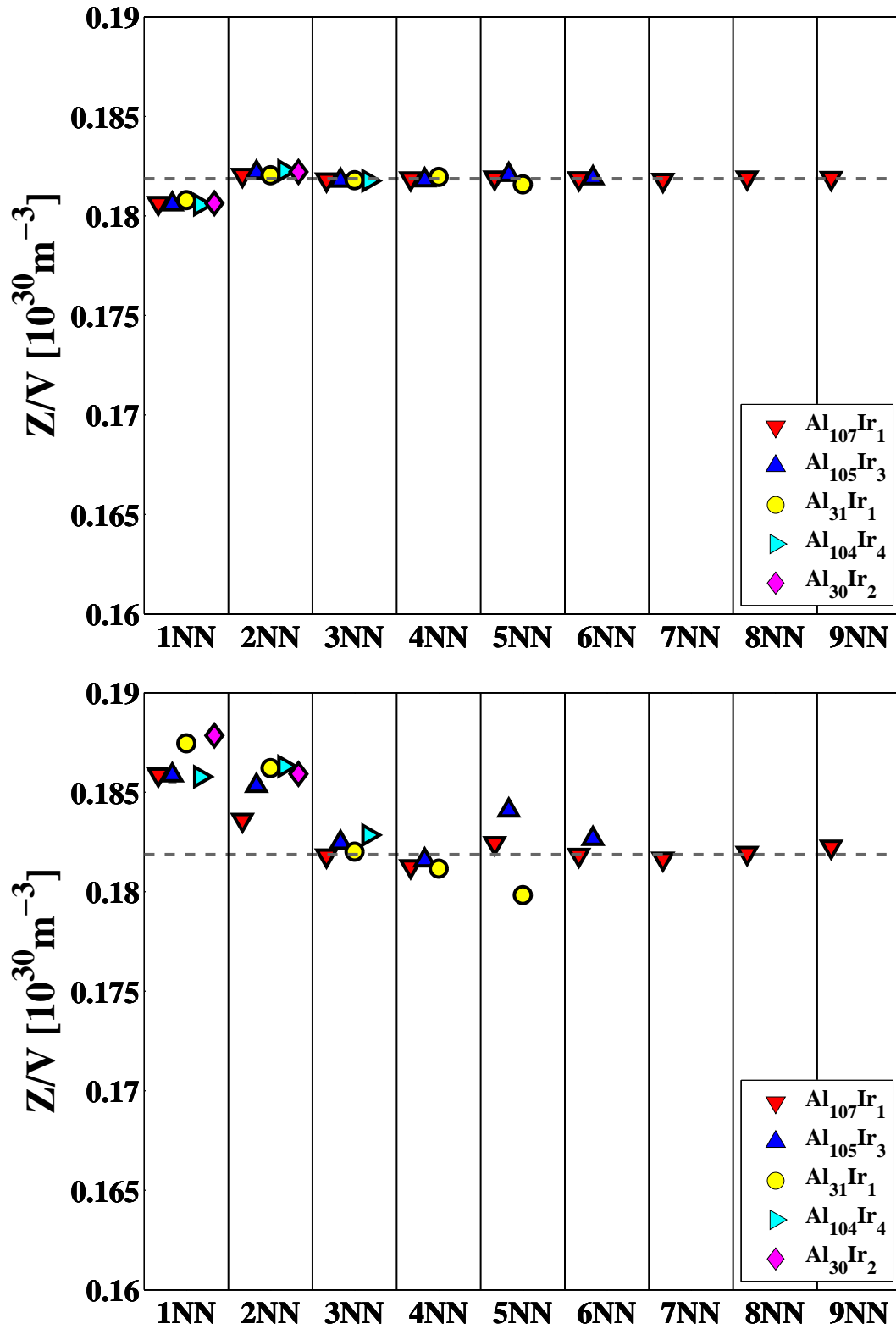
Figure 7.10: The average electron density (Z_{Al}/V_{Al}) of each Al atom in non-relaxed $Al_{(1-c)}X_c$
(top) and $Al_{(1-c)}Al_c$ (relaxed as $Al_{(1-c)}X_c$) (bottom) of Al-Ir solid solutions. iNN: the
ith nearest neighbor to the solute atoms. The gray horizontal dashed line is the average
electron density of pure Al in the bulk phase.
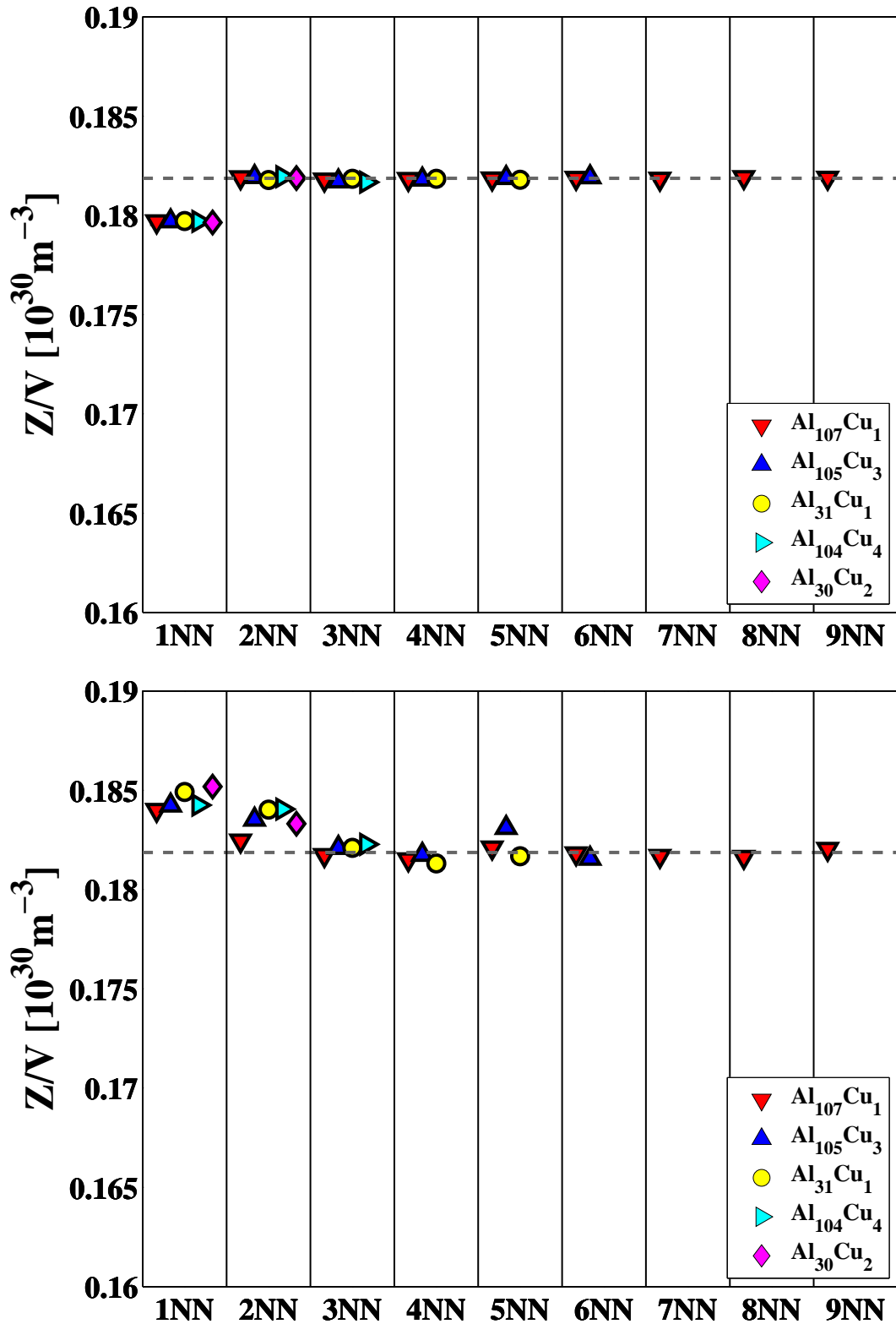
Figure 7.11: The average electron density (Z_{Al}/V_{Al}) of each Al atom in non-relaxed $Al_{(1-c)}X_c$
(top) and $Al_{(1-c)}Al_c$ (relaxed as $Al_{(1-c)}X_c$) (bottom) of Al-Cu solid solutions. iNN: the
ith nearest neighbor to the solute atoms. The gray horizontal dashed line is the average
electron density of pure Al in the bulk phase.
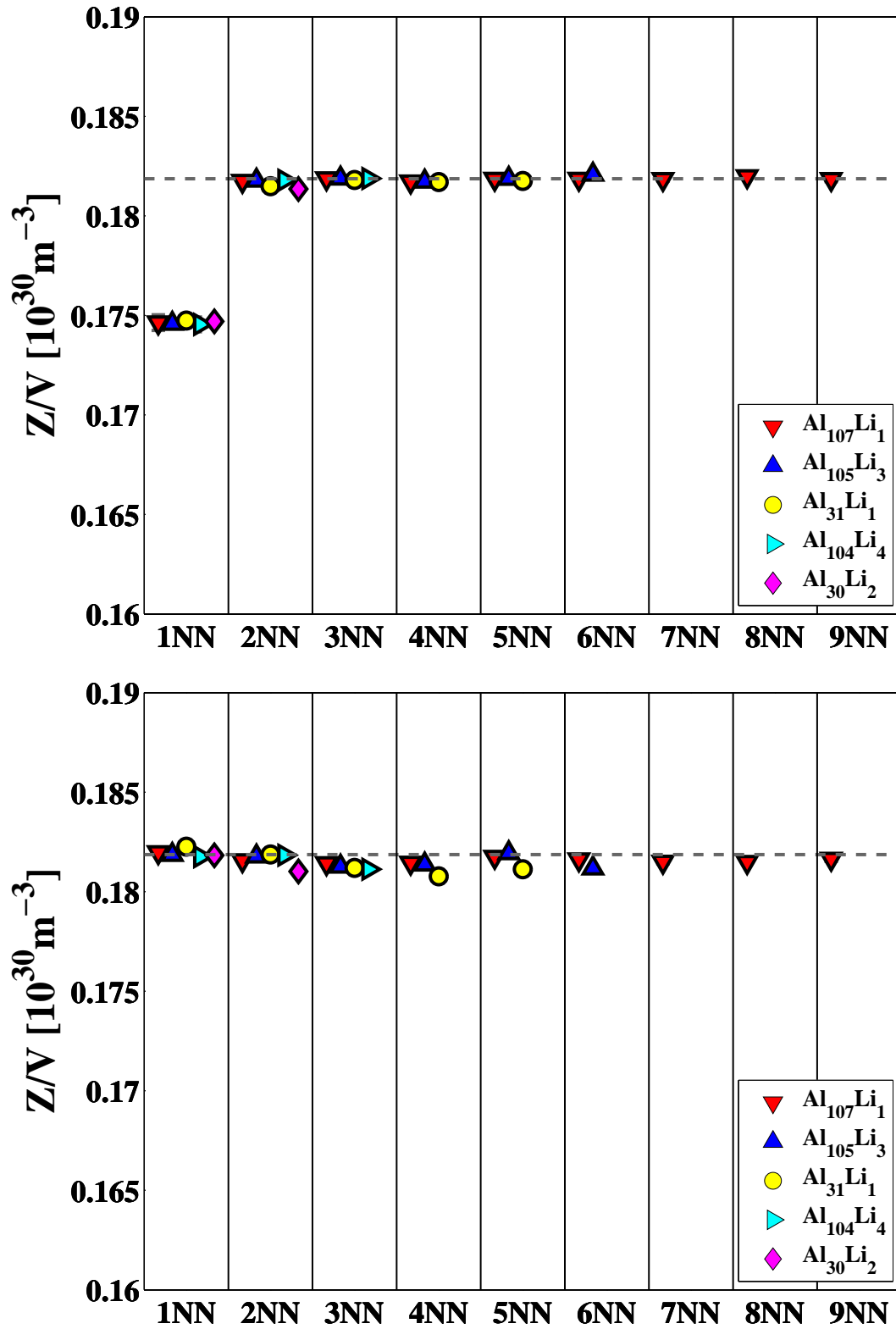
Figure 7.12: The average electron density (Z_{Al}/V_{Al}) of each Al atom in non-relaxed $Al_{(1-c)}X_c$ (top) and $Al_{(1-c)}Al_c$ (relaxed as $Al_{(1-c)}X_c$) (bottom) of Al-Li solid solutions. iNN: the ith nearest neighbor to the solute atoms. The gray horizontal dashed line is the average electron density of pure Al in the bulk phase.
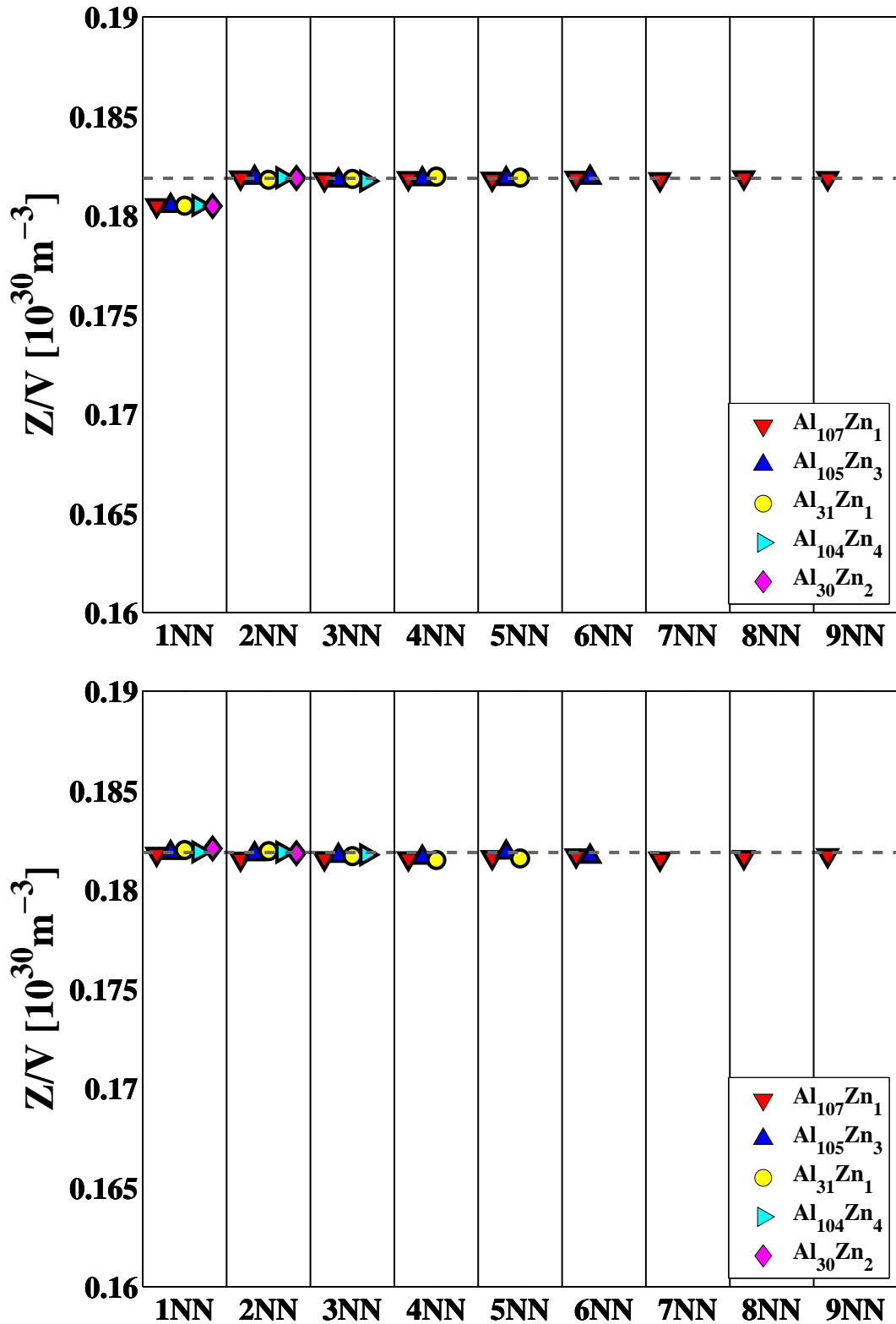
Figure 7.13: The average electron density (Z_{Al}/V_{Al}) of each Al atom in non-relaxed $Al_{(1-c)}X_c$ (top) and $Al_{(1-c)}Al_c$ (relaxed as $Al_{(1-c)}X_c$) (bottom) of Al-Zn solid solutions. iNN: the ith nearest neighbor to the solute atoms. The gray horizontal dashed line is the average electron density of pure Al in the bulk phase.

7.4 Correlation between perturbation and solid solution strengthening

In Section 2.5, it is mentioned that the more there is perturbation by the solute atoms the more solid solution strengthening effect there is (Collings and Gegel, 1973; Collings, 1975). The lattice parameter differences[3] of Al binary solid solutions from pure Al are plotted against the average electron density of all Al atoms in three different supercells (see Section 7.3.2 and 7.3.3) shown in Figure 7.14 and Figure 7.15.

Apparently, the average electron density of all Al atoms in $Al_{(1-c)}Al_c$ (relaxed as $Al_{(1-c)}X_c$) is correlated with the lattice parameter difference better than the other two. Therefore, the atomic relaxation (both external and internal) is closely correlated with the strengthening effect. The chemical effect alone cannot be correlated with the strengthening effect shown in the bottom of Figure 7.15.
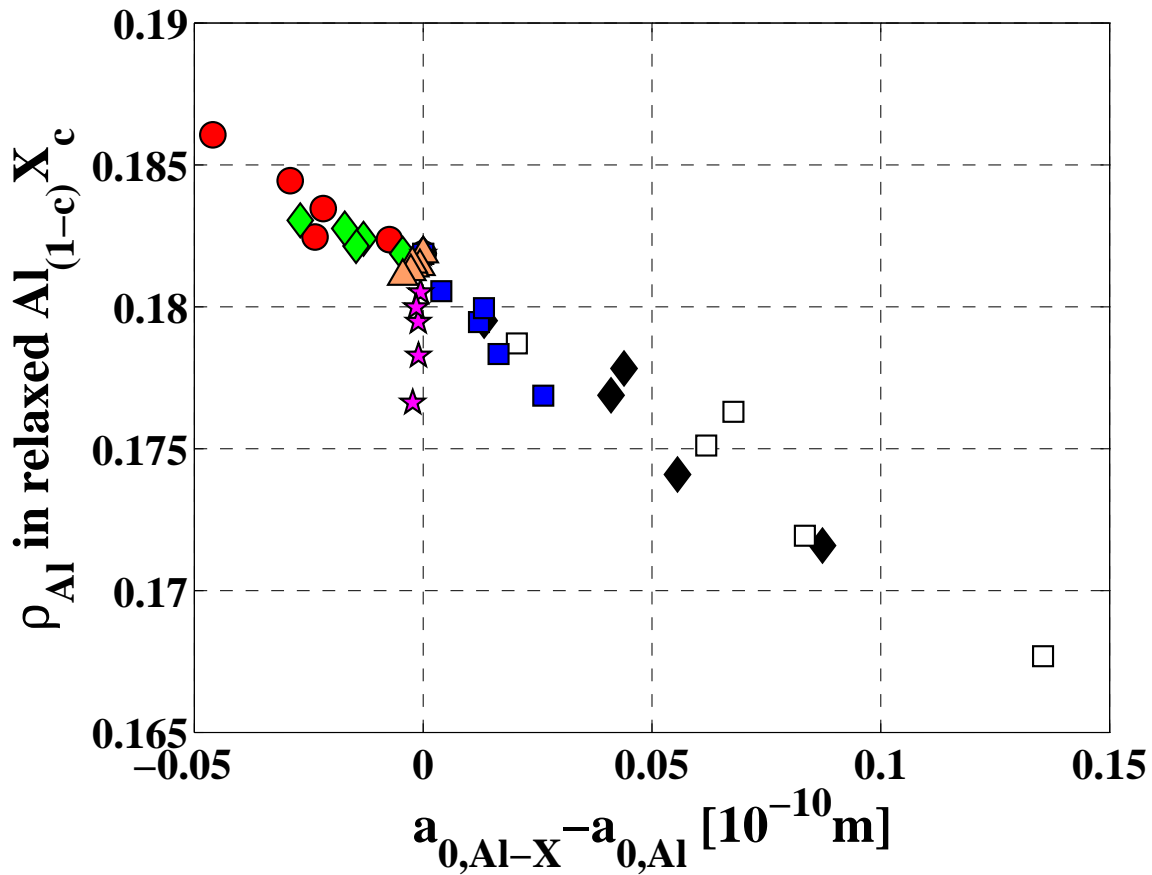
Figure 7.14: The correlation between the lattice parameter difference from pure Al ($a_{0,Al-X} - a_{0,Al}$) and the average electron density of all Al atoms in relaxed $Al_{(1-c)}X_c$.

---

[3]It is essentially equivalent to the volume mismatch parameter.
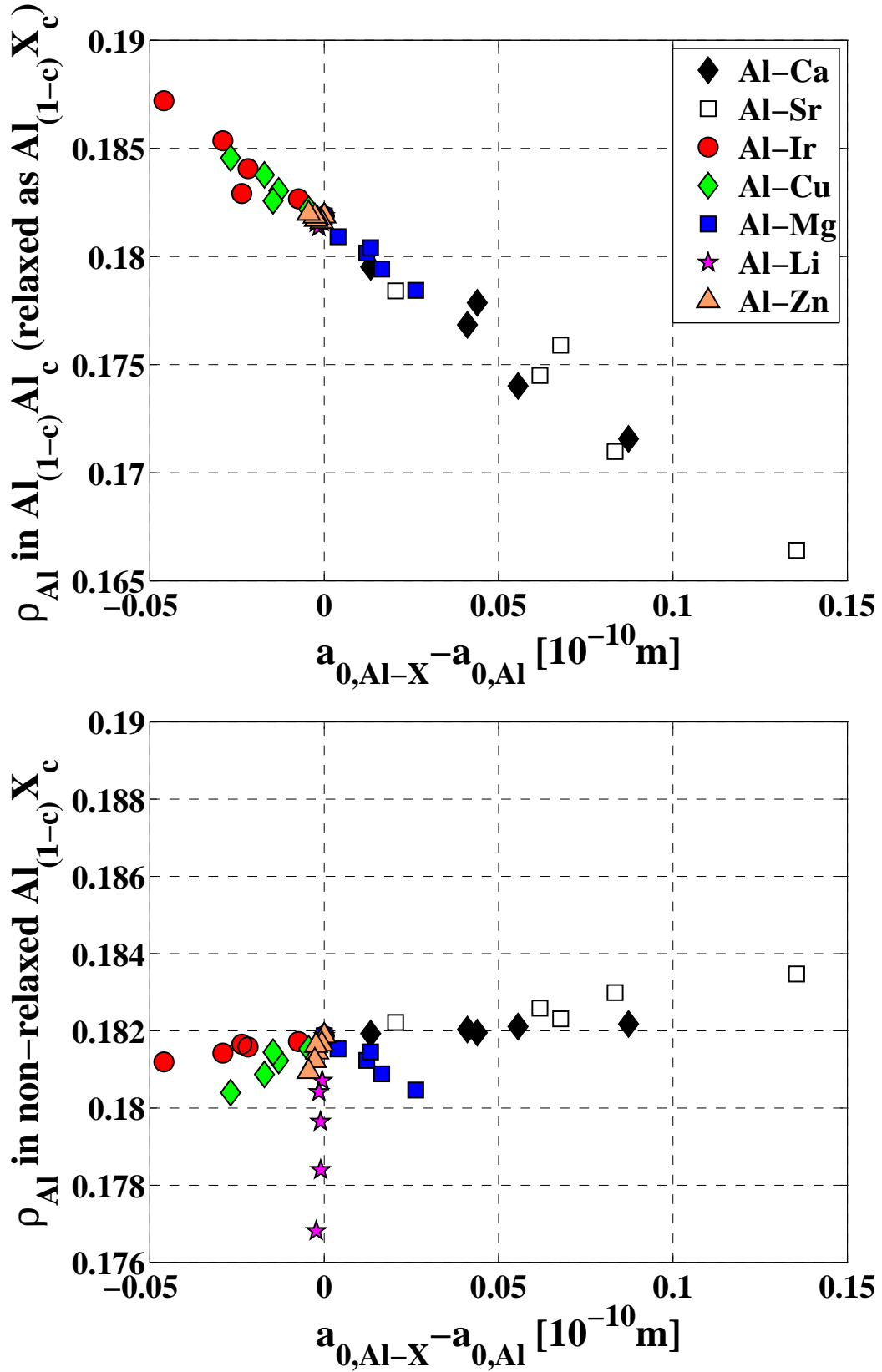
Figure 7.15: The correlation between the lattice parameter difference from pure Al ($a_{0,Al-X} - a_{0,Al}$) and the average electron density of all Al atoms in $Al_{(1-c)}Al_c$ (relaxed as $Al_{(1-c)}X_c$) (top) and non-relaxed $Al_{(1-c)}X_c$ (bottom).

7.5 Correlation between perturabtion and supercell size dependence

As shown in Chapter 5, the calculated elastic constants have supercell size dependence which leads to great uncertainties in the predicting the compositional dependence of the elastic constants. In this section, the supercell size dependence and its correlation with the perturbation caused by the solute atoms (Section 7.3) will be discussed.

The calculated lattice parameters, bulk modulus and the enthalpies of mixing of the studied Al binary solid solutions almost linearly depends on the concentration, because the goodness of linear fit (linear GOF), R^2, is usually above 0.95, except Al-Li whose linear GOF of the lattice parameter is 0.86. The compositional dependences of these properties determined by using different data sets are shown in Figure 7.16. The calculated elastic constants have no linear compositional dependence within the studied concentration. Therefore, the comparison is made only between $Al_{107}X_1$ and $Al_{31}X_1$ shown in Figure 7.17.

The mean values (μ) and standard deviations (σ) of the compositional dependences in Figure 7.16 and Figure 7.17 are listed in Table 7.1. The standard deviations of the compositional dependence of da_0/dc and $d\Delta H/dc$ are usually one or two order magnitude lower the mean values, except Al-Li (da_0/dc) and Al-Mg ($d\Delta H_{mix}/dc$). The standard deviations of the compositional dependent of B_0 are roughly 10% of the mean values. The most supercell size dependent systems are Al-Sr (a_0 and B_0) and Al-Ir (ΔH_{mix}), and the least one is Al-Zn.

The supercell size dependence is much larger in the compositional dependence of the elastic constants than the properties from the equation of state (a_0, B_0 and ΔH_{mix}). The least supercell size dependent system is also Al-Zn, and most one is Al-Sr.
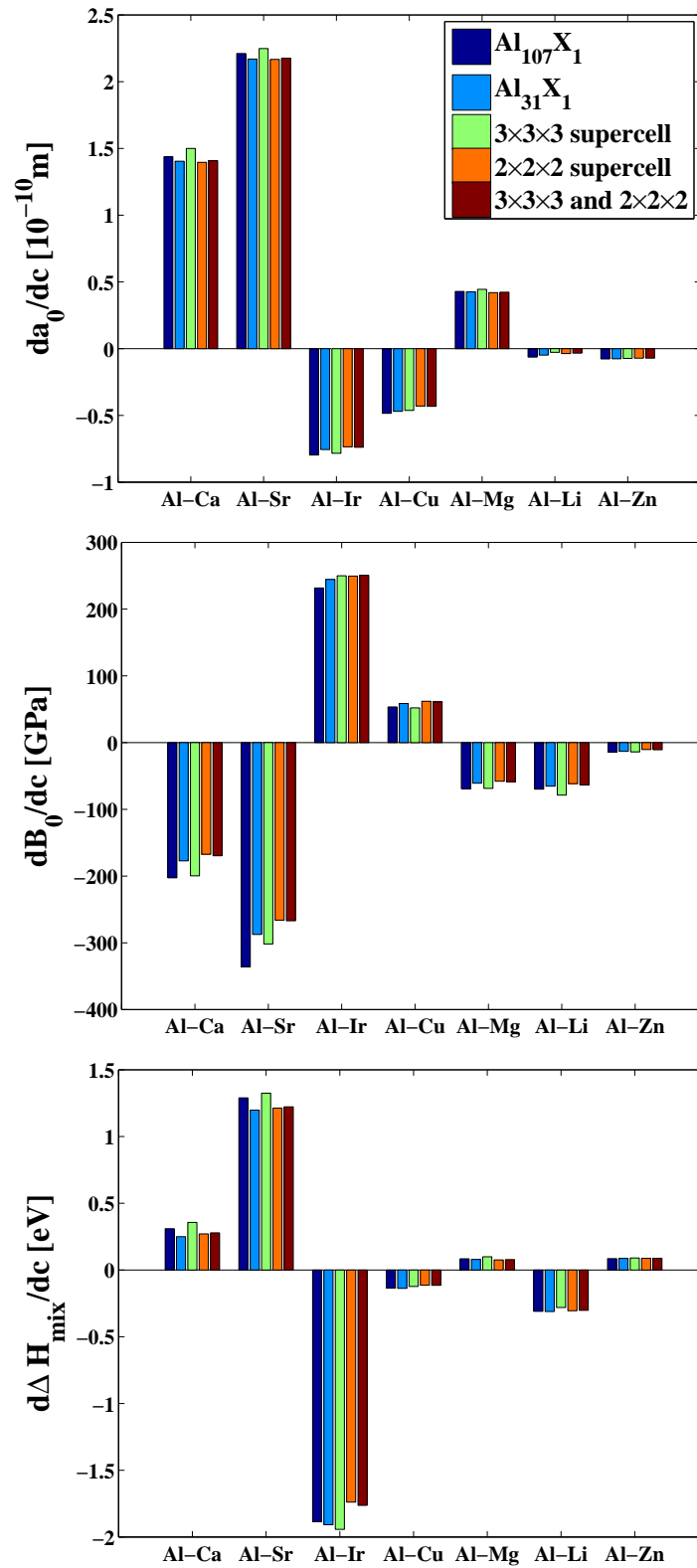
Figure 7.16: The compositional dependence of (top) the lattice parameter, (middle) the bulk modulus and (bottom) and the enthalpies of mixing per atom of studied Al binary solid solutions determined by five data sets: (1) $Al_{107}X_1$, (2) $Al_{31}X_1$, (3) calculations on $3\times3\times3$ supercells (4) calculations on $2\times2\times2$ supercells, (5) calculations on $3\times3\times3$ and $2\times2\times2$ supercells.
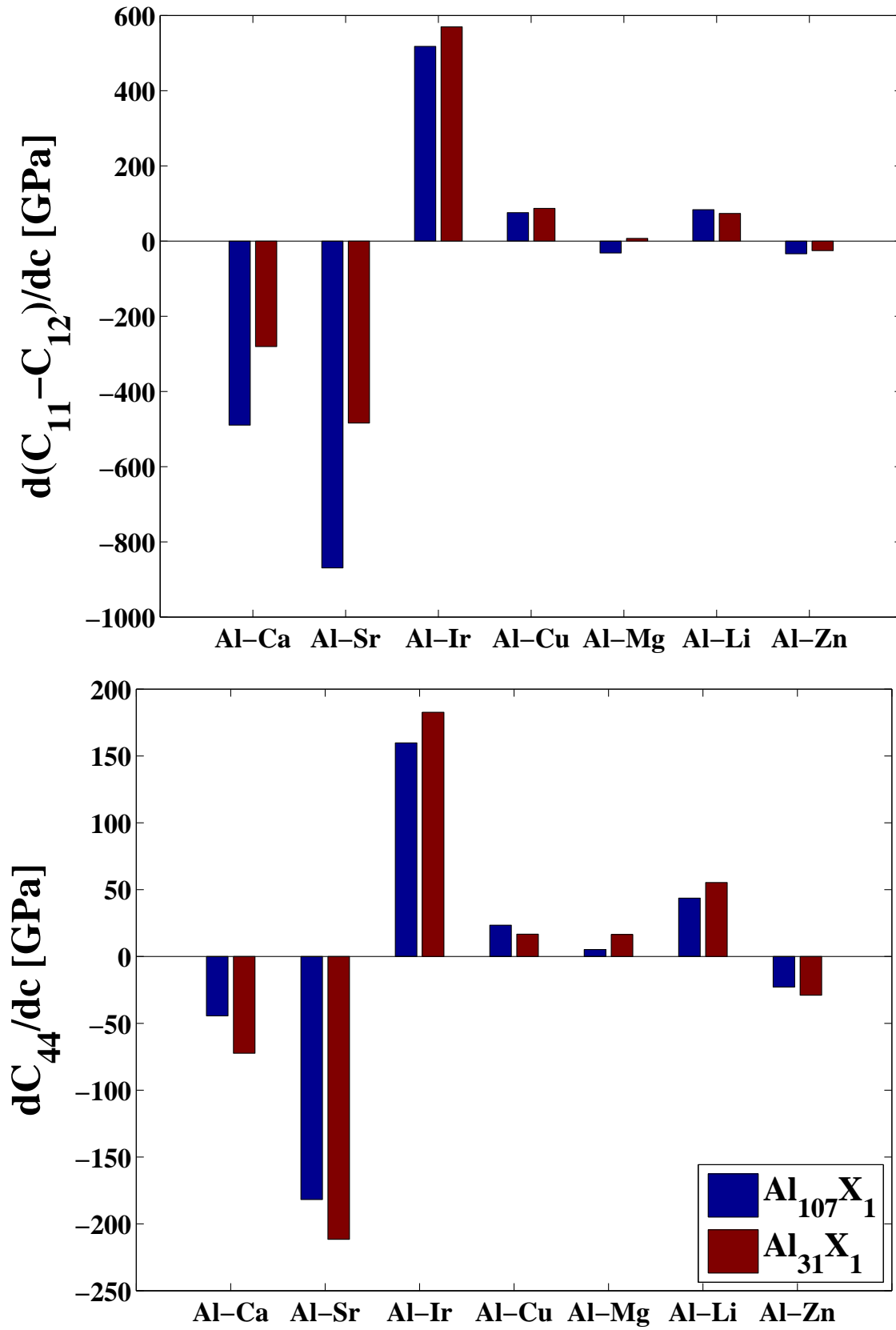
Figure 7.17: The compositional dependence of (top) $C_{11} - C_{12}$ and (bottom) C_{44} of studied Al binary solid solutions determined by $Al_{107}X_1$ and $Al_{31}X_1$.

Table 7.1: The mean values (μ) and standard deviations (σ) of the compositional dependences
determined by different data sets in Figure 7.16 and Figure 7.17

			Al-Ca	Al-Sr	Al-Ir	Al-Cu	Al-Mg	Al-Li	Al-Zn
$\frac{da_0}{dc}$	μ	[Å]	1.4	2.2	-0.8	-0.5	0.4	-0.04	-0.07
	σ	[Å$\times 10^{-2}$]	4.3	3.5	2.7	2.4	1.0	1.4	0.3
$\frac{dB_0}{dc}$	μ	[GPa]	-183.2	-291.6	245.3	57.5	-63.0	-67.7	-12.5
	σ	[GPa]	16.7	29.0	8.0	4.5	5.4	6.8	1.8
$\frac{d\Delta H_{mix}}{dc}$	μ	[eV]	0.3	1.3	-1.9	-0.1	0.08	-0.30	0.09
	σ	[eV$\times 10^{-2}$]	4.1	5.5	9.1	1.1	1.0	1.2	0.2
$\frac{d(C_{11}-C_{12})}{dc}$	μ	[GPa]	-385.0	-676.4	543.9	81.4	-12.2	78.5	-29.5
	σ	[GPa]	147.8	272.4	36.7	7.9	27.4	7.0	5.9
$\frac{dC_{44}}{dc}$	μ	[GPa]	-58.4	-196.6	171.2	20.0	10.8	49.5	-25.9
	σ	[GPa]	19.8	21.1	16.2	4.7	8.0	8.2	4.3

In order to correlate the supercell size dependence and the perturbation caused by the solute
atoms (Section 7.3), the compositional dependences of the average electron density of all Al
atoms[4] are plotted against $\sigma_{dB_0/c}$ and $\sigma_{d(C_{11}-C_{12})/c}$ (Table 7.1) in Figure 7.18, Figure 7.19 and
Figure 7.20.

The chemical effect only has no correlation with the supercell size dependence shown in Figure
7.18. Figure 7.19 shows that there is a correlation between the elastic effect and the supercell
size dependence, except Al-Li. The superposition of the elastic effect and the chemical effect is
also correlated the supercell size dependence shown in the third row of Figure 7.20, because the
elastic effect is the main contribution to the change in the average electron density except Al-Li
and Al-Zn shown in Section 7.3.

If the elastic effect is mainly responsible for the supercell size dependence, the compositional
dependence of the lattice parameter should also be correlated with the supercell size dependence
shown in Figure 7.21. The compositional dependence of the lattice parameter can be used as
good measure to estimate the supercell size dependence. Figure 7.21 shows that Al-Li is a
exception. It is because the chemical effect is much larger than the elastic effect in Al-Li. Thus
the elastic effect sometimes is not the only reason for the supercell size dependence.

---

[4]The average electron density of all Al atoms is defined as $\rho_{all,Al} = \frac{\sum Z_i}{\sum V_i}$, where i is individual Al atom. The
Al atoms at the solute atoms sites in $Al_{(1-c)}Al_c$ (relaxed as $Al_{(1-c)}X_c$) are, of course, not included. $\rho_{all,Al}$ also has
supercell size dependence. $d\rho_{all,Al}/dc$ is obtained from the linear regression.
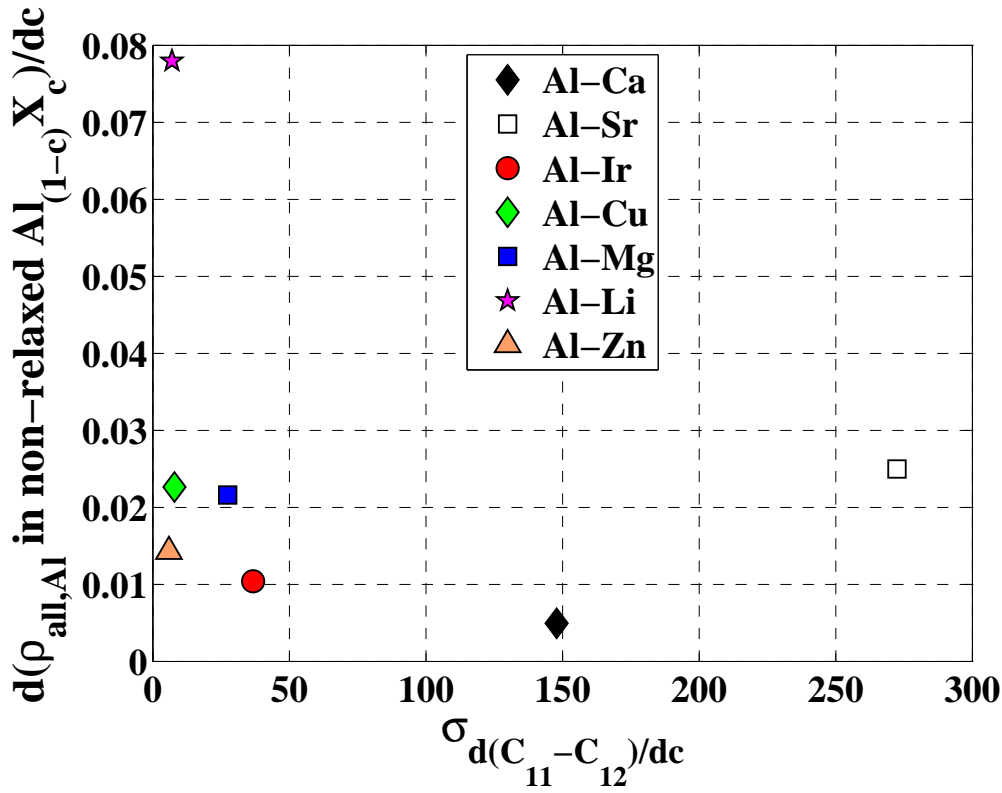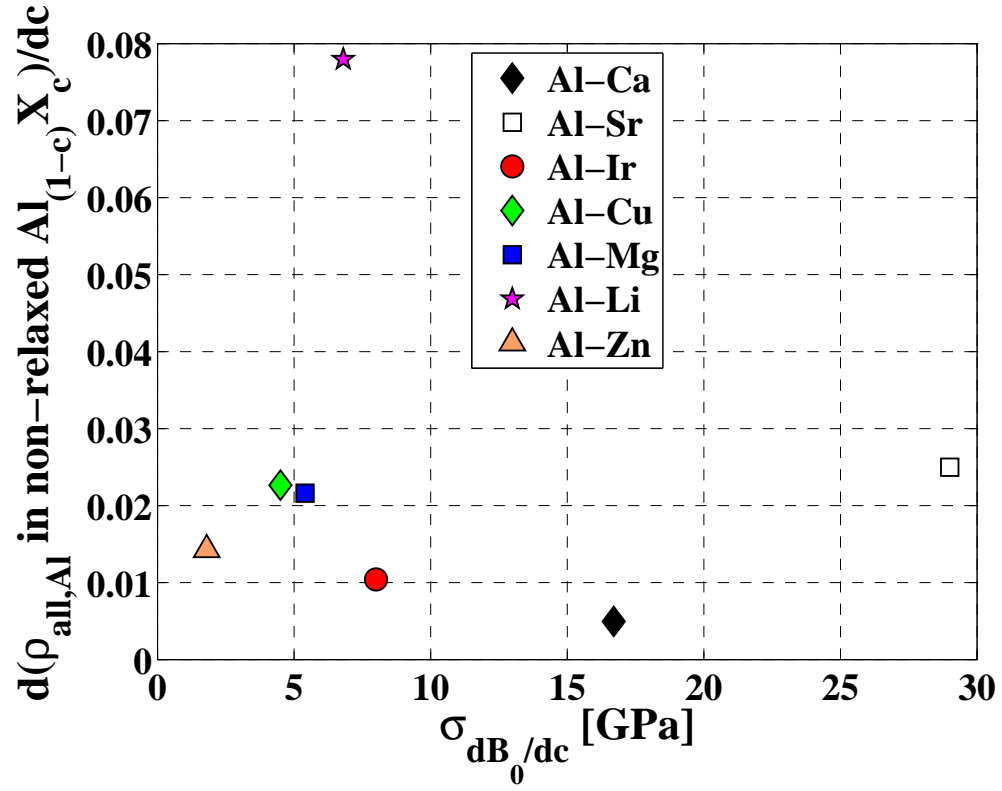
Figure 7.18: $d\rho_{all,Al}/dc$ in non-relaxed $Al_{(1-c)}X_c$ vs. $\sigma_{dB_0/dc}$ (top) and $\sigma_{d(C_{11}-C_{12})/dc}$ (bottom).
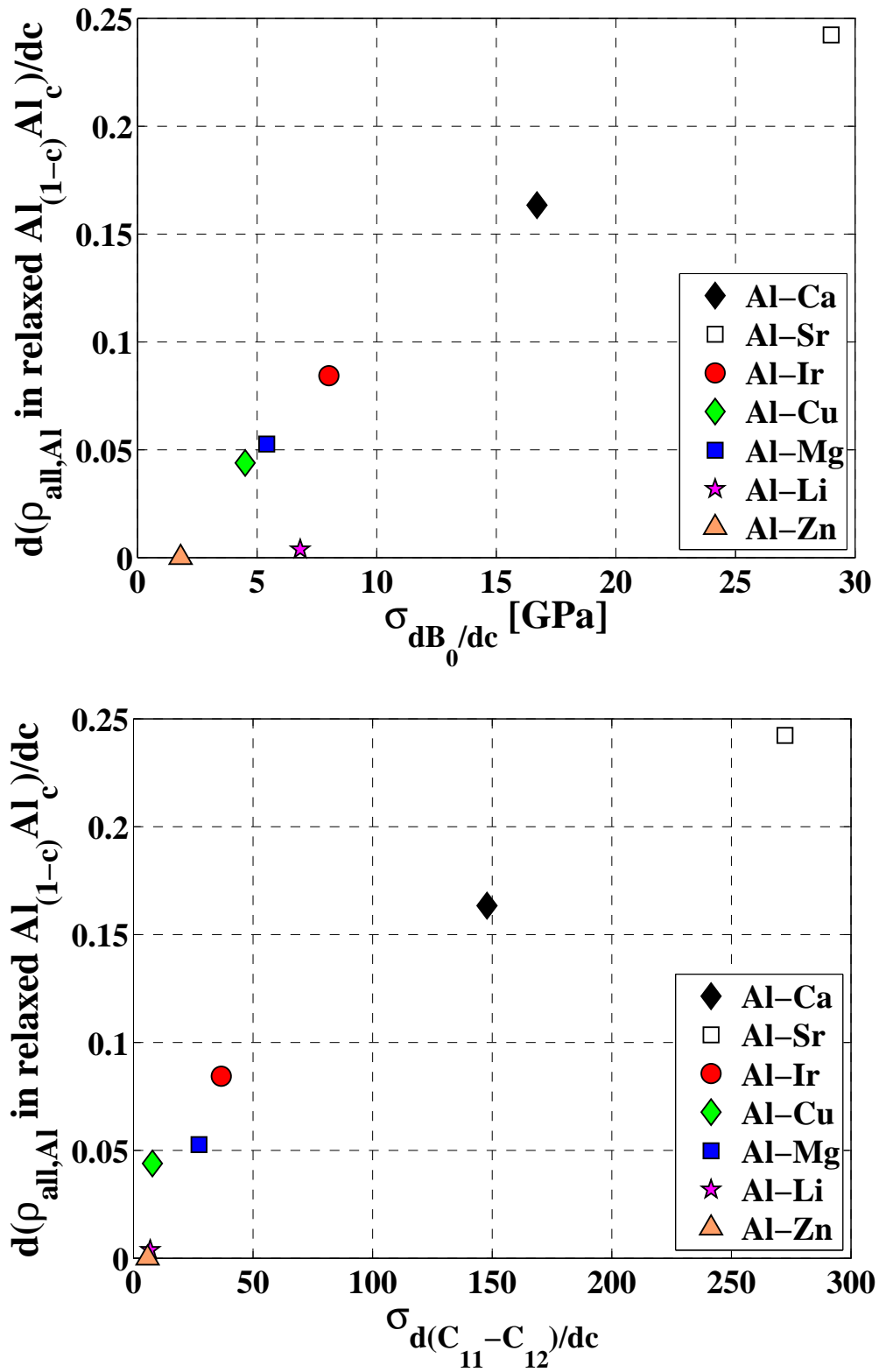
Figure 7.19: $d\rho_{all,Al}/dc$ in $Al_{(1-c)}Al_c$ (relaxed as $Al_{(1-c)}X_c$) vs. $\sigma_{dB_0/dc}$ (top) and $\sigma_{d(C_{11}-C_{12})/dc}$ (bottom).
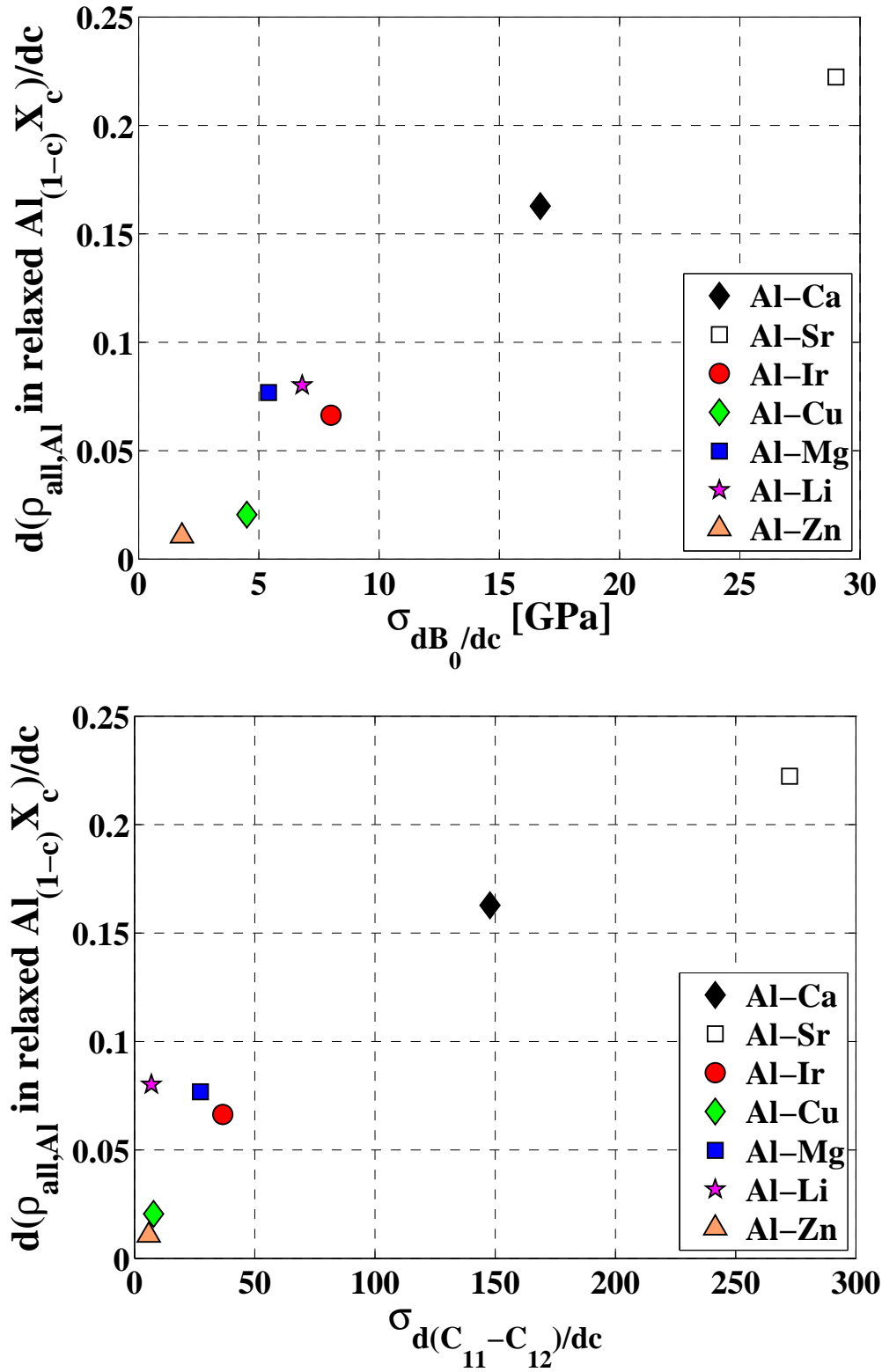
Figure 7.20: $d\rho_{all,Al}/dc$ in relaxed $Al_{(1-c)}X_c$ vs. $\sigma_{dB_0/dc}$ (top) and $\sigma_{d(C_{11}-C_{12})/dc}$ (bottom).
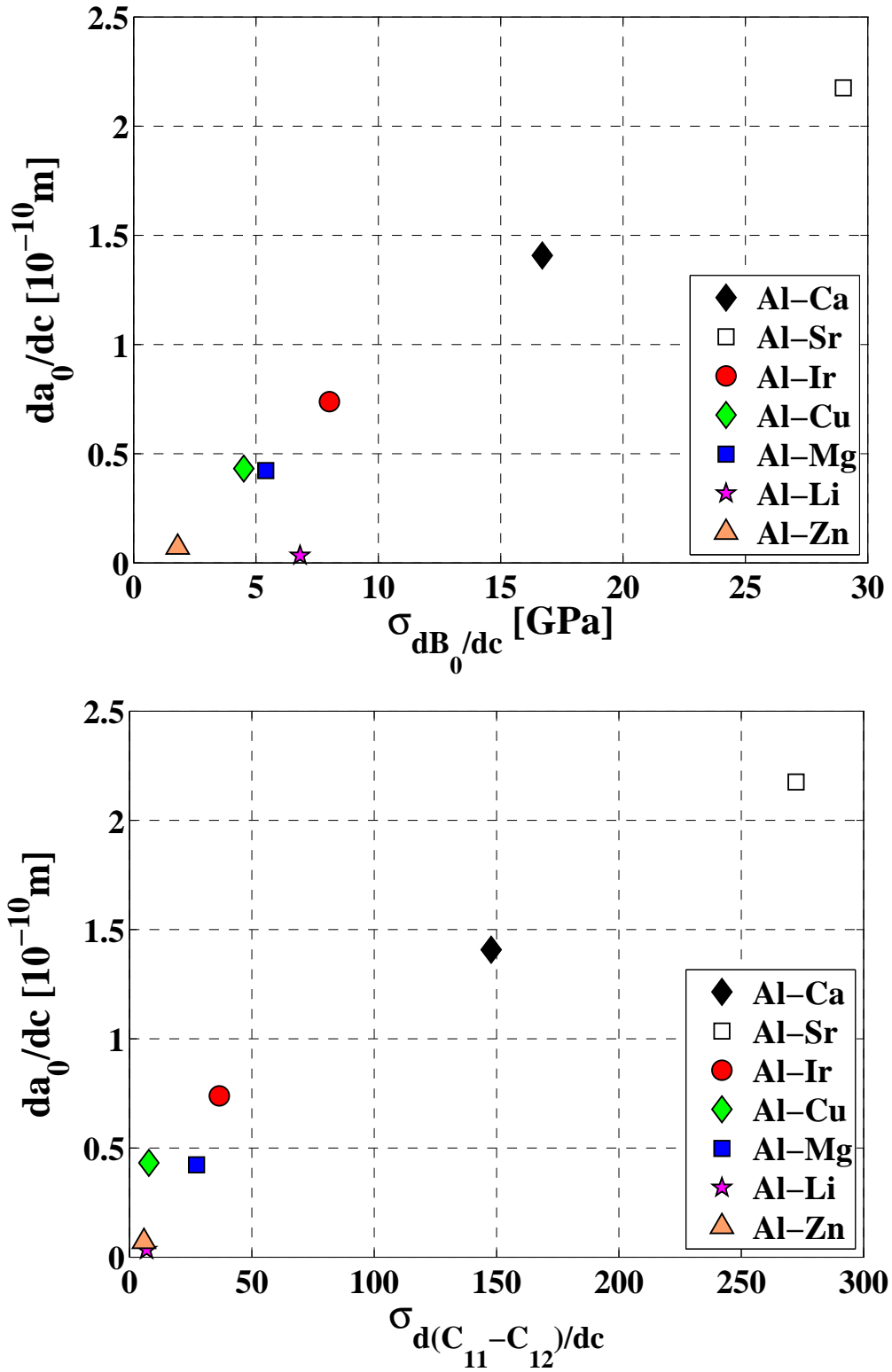
Figure 7.21: da_0/dc vs. $\sigma_{dB_0/dc}$ (top) and $\sigma_{d(C_{11}-C_{12})/dc}$ (bottom).

Chapter 8

DFT guided Ashby's materials property and design charts of studied Al binary solid solutions

8.1 Materials properties from DFT

In ancient times, the iron-made swords were superior to the bronze-made. Among the iron-made swords, the samurai swords were superior to the others, because of its unique heat treatment[1]. In the above example, there are two concepts in making better swords: (1) finding a new material with better performance; (2) manipulating the microstructure of the existing materials to make the performance better. Essentially, these two concepts are dealing with two kinds of the materials properties: intrinsic and extrinsic materials property.

Currently, most of the DFT calculations are only dealing with the intrinsic material properties. The extrinsic materials properties, involving multiple phases, spatial and size distributions or defects interactions, are not very feasible, because of the limited computational power.

On the other hand, in selecting materials, considerations should be made in many aspects. For example, copper-made household pipes are better than iron-based, because the copper rust is much easier to handle than iron rust. It would be, however, very luxury, if copper is used. Therefore a compromise should be made between the performance and the cost. Ashby's material property and design charts help with such a decision making.

As shown in Chapter 6, Ca, Sr and Ir introduce much larger solid solution strengthening effect than the other four studied elements. But the question is whether they also help with improving the performance of Al alloys in other aspects. In this chapter, some of the calculated intrinsic properties of studied Al binary solid solutions are plotted in the manner of Ashby's material property and design charts (see Section 3.6). The performance of the studied solid solutions can be compared in these charts. Two restrictions are applied to those properties: (1) single phases; (2) no texture effect. And those properties are as following:

1. Young's modulus, E

    The calculated elastic constants are homogenized according to certain homogenization methods (Section 3.4) to obtain the homogenized polycrystalline Young's modulus.

2. Density, ρ

    The density is calculated simply by dividing the mass by the equilibrium volume.

3. Yield stress, σ_y

    The yield stress is represented by the absolute value of the elastic dipole in this study. As demonstrated in Section 6.1.2, the elastic dipole is a good measure to characterize the solid solution strengthening. Therefore, it can be considered as a rough measure of the increase in the yield stress. Since the sign of the elastic dipole does not matter, the absolute value of the elastic dipole is used.

---

[1]Before quenching, a thin layer of clay (or nothing at all) covers the edge of the sword, and a thick layer is put on the rest of the sword. Such a process ensures quick cooling on the edge and slow cooling on the spine. The resulting microstructure is the hard but brittle martensite on the edge and soft but tough pearlite on the spine.

4. Ductility

   The ductility is represented by B/G ratio. As shown by Pugh (Pugh, 1954), the higher B/G ratio the higher ductility. Because the bulk modulus, B, characterizes the strength of the chemical bonds, and the shear modulus, G, characterizes the motion of the dislocations.

5. Fatigue property

   The fatigue property is represented by the absolute difference of Zener's ratio (A_Z) from one. As shown in Roters et al. (2010), due to the elastic anisotropy, in an elastically deformed polycrystal with the random texture, there is a stress distribution. High stresses are deemed to be at the vicinity of the grain boundaries. Some local stresses already exceeds the yield stress even the deformation is thought to be elastic. Therefore, the higher elastic anisotropy, the higher stress concentration, consequently the worse fatigue property. However, such a measure should be the lower bound of the fatigue properties because of the following two reasons: (1) the methods used in Roters et al. (2010) do not explicitly consider the contribution of the grain boundary to the deformation. As demonstrated by Ma et al., if the grain boundary is explicitly considered, the stress concentration should be much higher (Ma et al., 2006); (2) the condition of the free surface, such as the micro-cracks, the micro-roughness, or the grain boundary grooves, should have great effect on the fatigue property, which, however, are not considered in this simple model.

8.2 Stiffness-, strength-, and vibration-limited design charts

8.2.1 Young's modulus vs. density
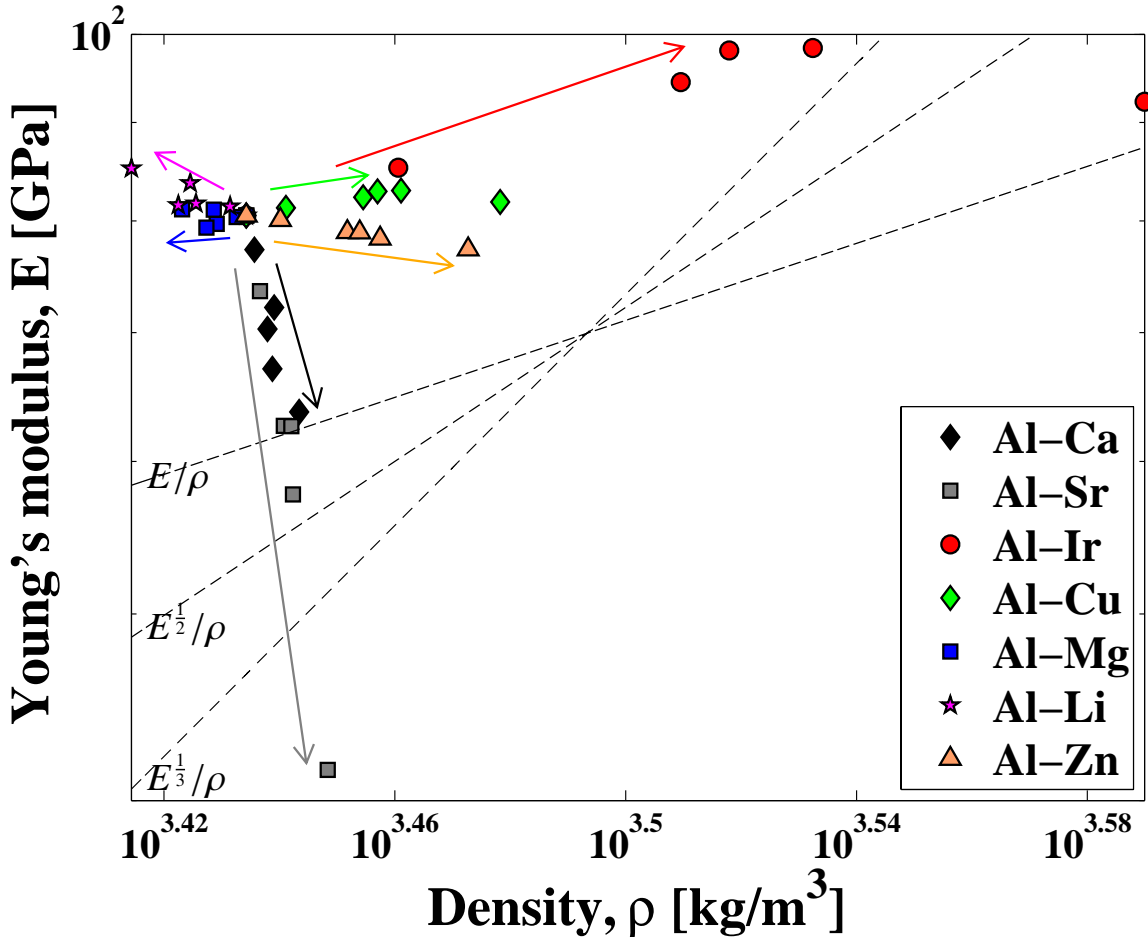
Figure 8.1: Young's modulus-density chart of the studied Al binary solid solutions. The arrows points the direction of the concentration increase. Straight dash lines are associated with material indices (see Table 3.4).

According to Table 3.4, the Young's modulus-density plot helps with the stiffness-limited design at the minimum mass and the vibration-limited design.

Still take the example of the aircraft wing spars in Section 3.6. At the minimum mass, the material should have enough stiffness. On the other hand, due to the turbulence of the air flow, the aircraft wings vibrate. In order to avoid resonance, the natural vibration frequency must be higher than the maximum operating frequency. Apparently in Figure 8.1, Al-Li solid solutions fulfill the above two conditions for the aircraft wing spars. And in fact, the aircraft construction is the main application of the Al-Li alloys (ASM Handbook, 1990).

8.2.2 |Elastic dipole| vs. density
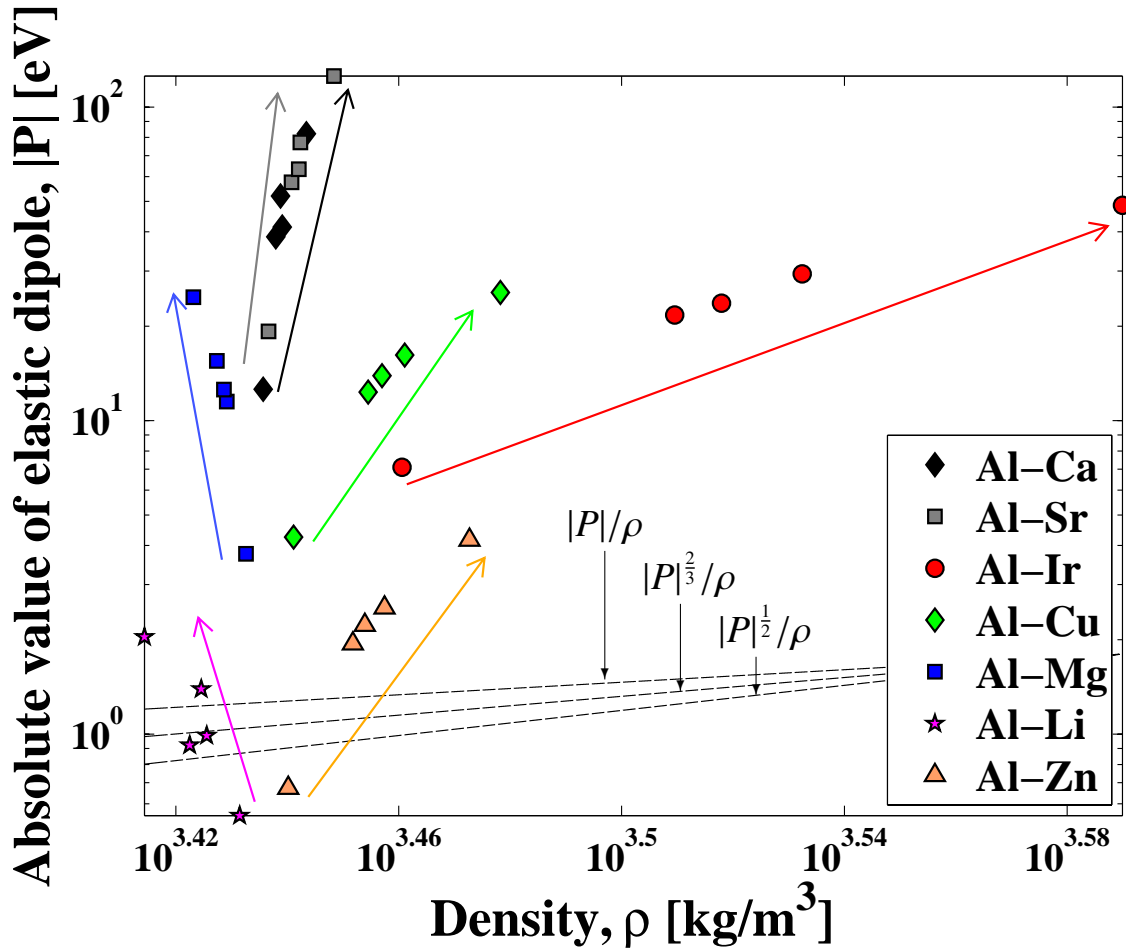
Figure 8.2: Absolute value of elastic dipole-density chart of the studied Al binary solid solutions. The arrows points the direction of the concentration increase. Straight dash lines are associated with material indices (see Table 3.4).

The absolute value of elastic dipole-density chart helps strength-limited design at minimum mass as described in Table 3.4.

In Figure 8.2, the obvious winner is the Al-Sr or Al-Ca solid solutions. But as shown in Section 4.3, Sr has no solubility in Al, and Ca has very low solubility in Al at high temperature (~1.9 at.% at 888K).

The next winner is the Al-Mg solid solutions. All three material indices in Figure 8.2 indicate the resistance against the internal pressure (Table 3.4). In practice, one of the applications of the Al-Mg is to make tubes, vessels, tanks, cans (ASM Handbook, 1990). These three material indices also indicate the performance of a beam loaded in bending. Another application of Al-Mg alloys is to make TV towers or drilling rigs (ASM Handbook, 1990) which should have enough strength against the strong wind encountered on the high ground or the off-shore.

Next to the Al-Mg solid solutions, the next winner is the Al-Cu solid solutions. In practice,

Al-Cu alloys are heat treatable alloys, namely the primary strengthening mechanism is precipitation strengthening. Assuming the density of Al-Cu alloys is not changed significantly by the precipitates, the tasks by the Al-Mg alloys should be fulfilled better by the precipitation strengthened Al-Cu alloys. Actually, some applications of the Al-Cu alloys are truck frames and wheels, and auto-body planet sheets (ASM Handbook, 1990). Apparently in these situations, the loading is more intensive than the TV towers or drilling rigs, therefore more strength is needed. On the other hand, the TV towers or drilling rigs are much larger and higher than trucks and autos, thus the weight, or the mass, of the material should be taken into account. Since the Al-Cu alloys are denser than Al-Mg alloys, the Al-Cu alloys are less favorable for the larger and higher structures.

8.2.3 Young's modulus vs. |elastic dipole|
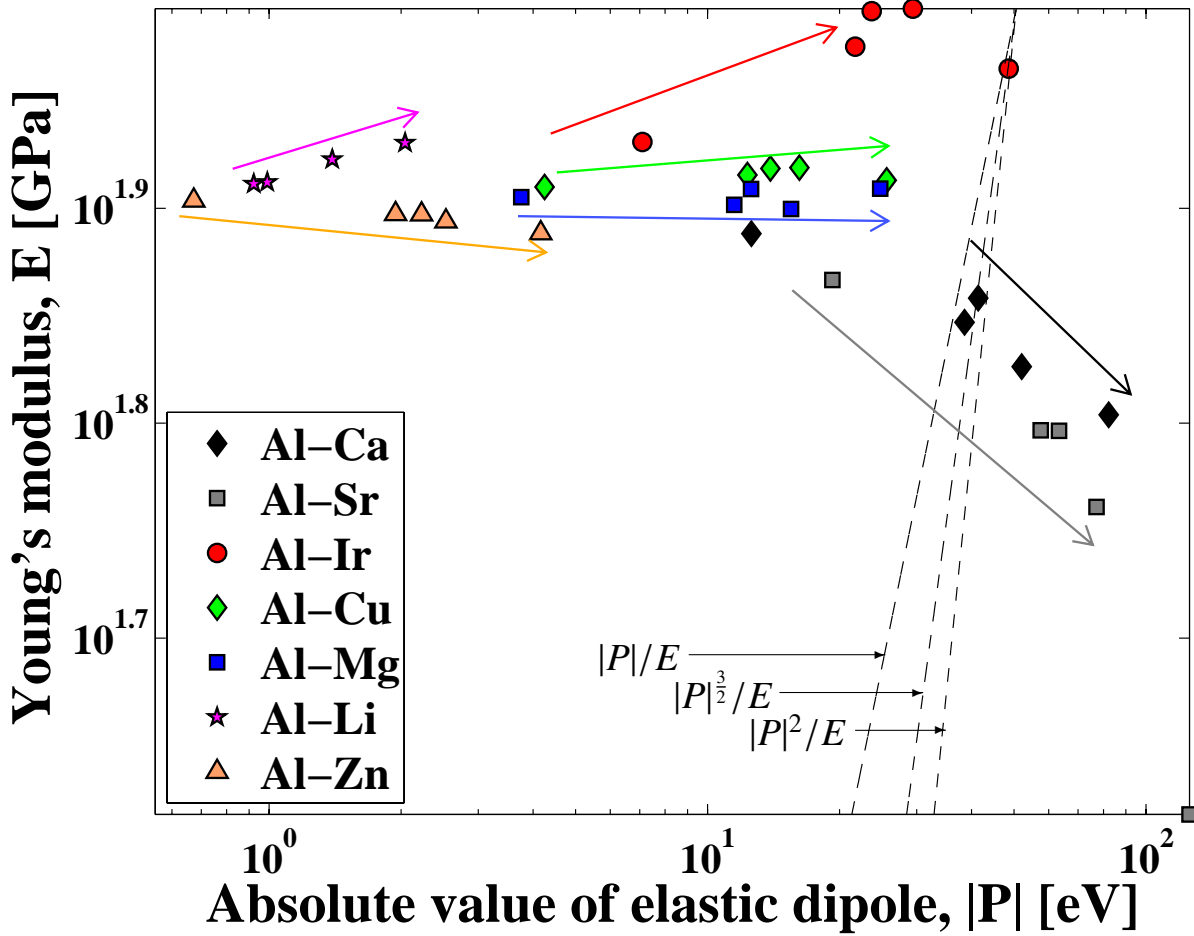
Figure 8.3: Young's modulus-absolute value of elastic dipole chart of the studied Al binary
solid solutions. The arrows points the direction of the concentration increase. Straight
dash lines are associated with material indices (see Table 3.4).

The Young's modulus-absolute value of elastic dipole chart helps strength-limited design for
the maximum performance.

Figure 8.3 clearly shows the Al-Li solid solutions perform the best among the studied solid solu-
tions, and the Al-Zn solid solutions are the second. According to Table 3.4, the material indices
in Figure 8.3 are for the applications of elastic hinges, knife edges, compression seals or gasket,
and springs. The Al-Li and Al-Zn alloys, however, are not usually used for these applications.
The main applications of the Al-Li and Al-Zn alloys are for the aircrafts (ASM Handbook,
1990). It is easy to imagine that an aircraft would encounter the loading, such as bending, bear-
ing, contact, even impact. The materials for the aircrafts should have the maximum flexibility,
conformability, and stored elastic energy without failure. Figure 8.3 indicates that the Al-Li and
Al-Zn solid solutions are the best choices among the studied Al solid solutions to fulfill these
requirements.

8.3 Ductility related design charts

8.3.1 Ductility measures: C_{12}/C_{44} and B/G

The ductility has been correlated with various materials properties, such as C_{12}/C_{44} and B/G:

1. C_{12}/C_{44}. This measure actually characterizes the angular character of the chemical bonding. If C_{12}/C_{44} is larger than 1, the bonding is more metallic. While if C_{12}/C_{44} is lower than 1, the bonding is more covalent (Pettifor, 1992). Therefore, the larger C_{12}/C_{44} is, the more ductile the material is.

2. B/G. This measure comes from the experimental observation (Pugh, 1954). The higher B/G (≥ 1.75), the more ductile the material is. The correlation of the ductility and Poisson ratio is also observed, especially in metallic glasses (Lewandowski et al., 2005). Since B/G and Poisson ratio are the isotropic elastic properties, and in isotropic elasticity only two modulus are sufficient, those two measures are essentially identical.

As shown in Figure 8.4, B/G ratios of the studied Al binary solid solutions roughly correlate with their C_{12}/C_{44}. This correlation is also found in pure metals (Gilman, 2003). More importantly, the ductility determined by those two measures should be consistent with each other. As shown in Figure 8.4, B/G ratios of the studied Al binary solid solutions are well above 1.75, while their C_{12}/C_{44} ratios are also well above 1.
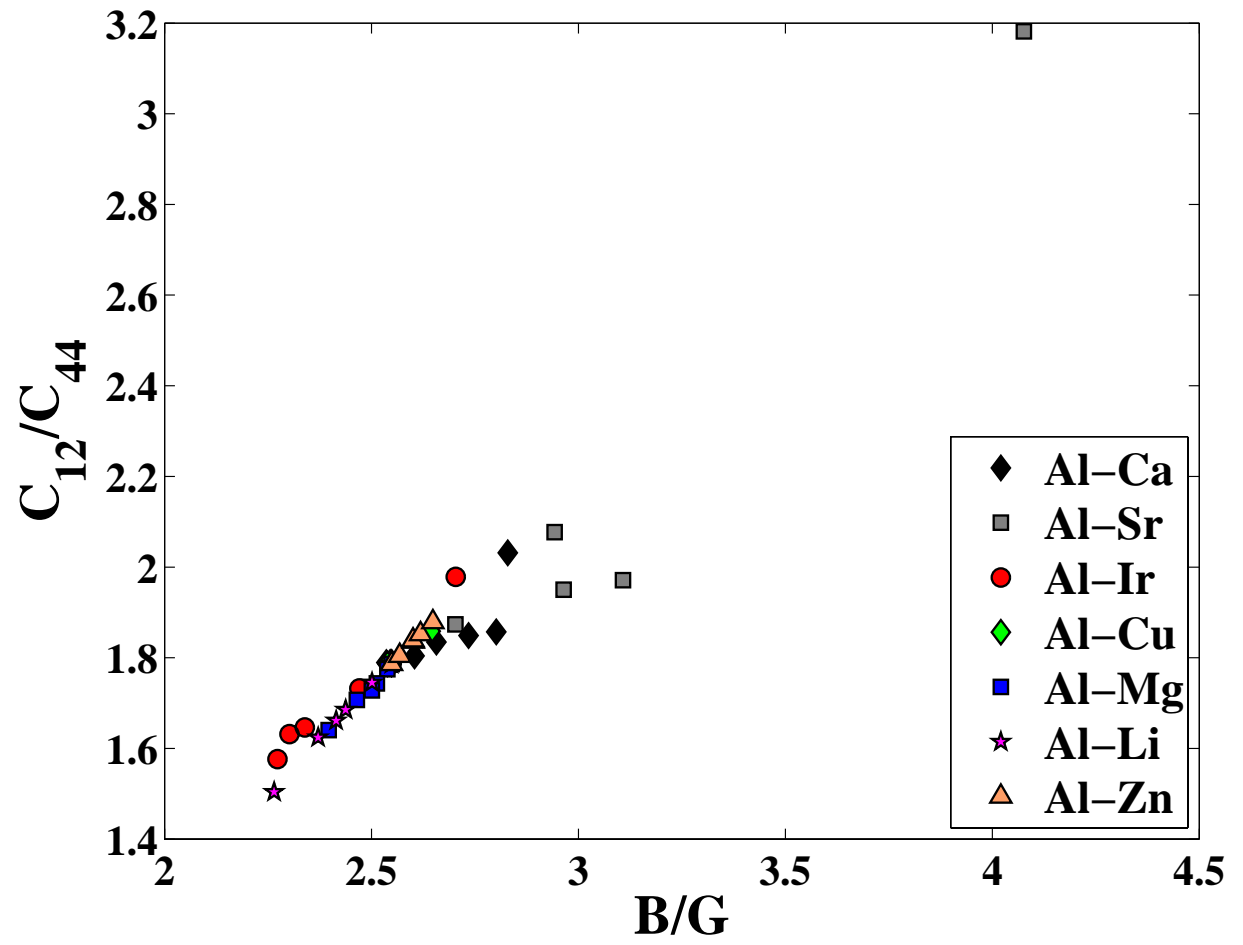
Figure 8.4: The correlation of B/G with C_{12}/C_{44}.

8.3.2   *B/G* vs. specific modulus and *B/G* vs. specific modulus
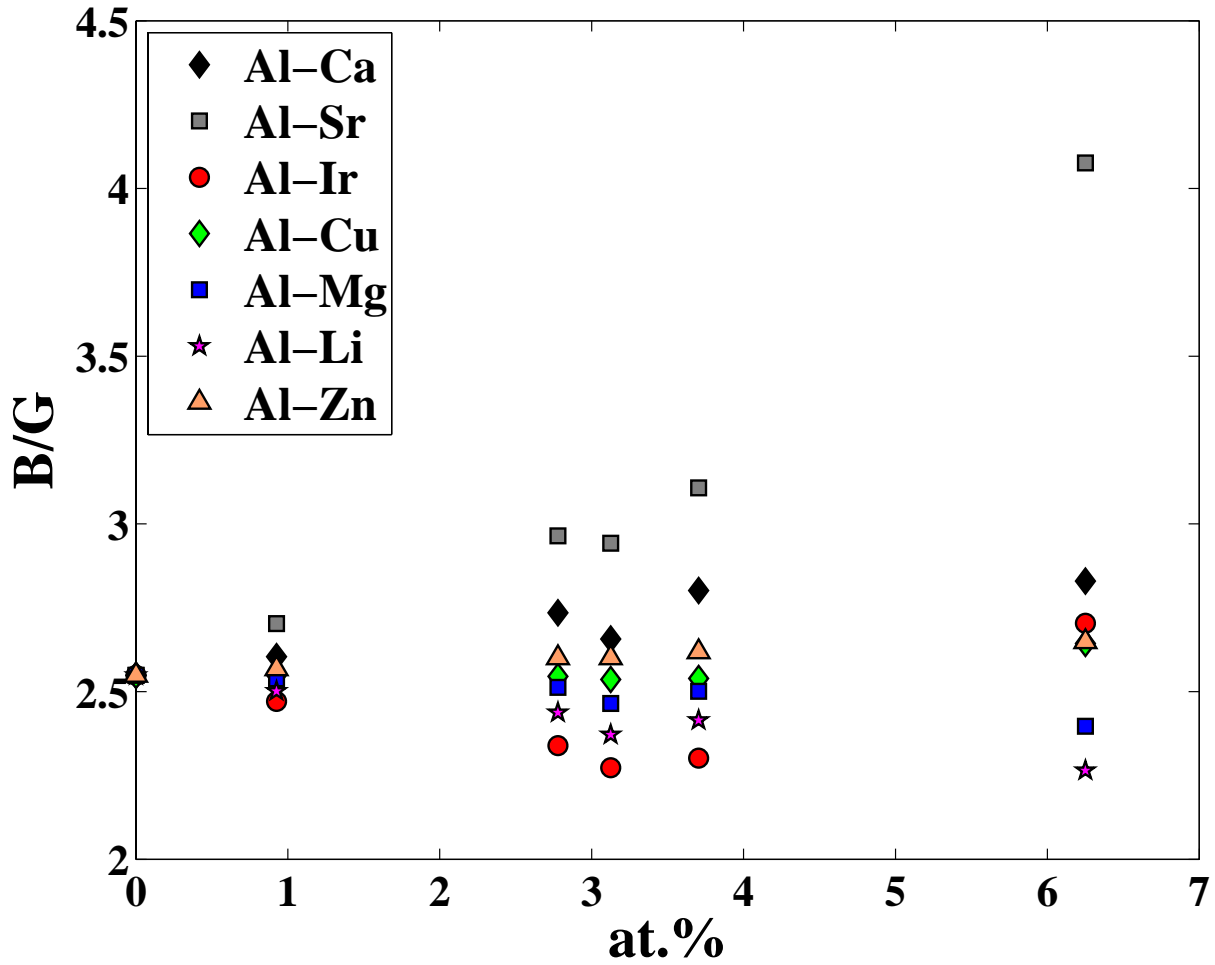
Figure 8.5: *B/G* ratios of the studied Al binary solid solutions.

As shown in Figure 8.5, The *B/G* ratios of the studied Al binary solid solutions are all above 1.75. There is a drawback of using *B/G* as the ductility measure. The global trend might be right, but the local trend might be wrong (Pugh, 1954; Yoo, 1981). It is sensible to use *B/G* to compare the ductility of certain materials, if their *B/G* ratios are far apart. It is also sensible to tell some materials are brittle or ductile, if their *B/G* ratios are below or above the ductility criterion. But it is not sensible to judge the ductility of the materials whose *B/G* ratios are close to each other and all above or below the criterion. Therefore, all the Al binary solid solutions can be considered to be very ductile revealed in this study, and in fact the ductility of the Al alloys is never an issue.

The *B/G*-specific modulus chart is shown on the top of Figure 8.6. The trend is very similar to the Mg-Li solid solutions (Counts et al., 2009). The data points lie in the southeast and the northwest. The desired trend, of course, is in the northeast. Since *B/G* ratios of the studied Al binary solid solutions are well above the ductile criterion (1.75), in this particular case, the

desired trend could just be to the east, namely to increase the specific modulus (E/ρ). This
information is already included in the Young's modulus-density chart (Figure 8.1).

The same argument about B/G also applies to B/G-specific strength chart on the bottom of
Figure 8.6. The information of the specific strength is also shown in Figure 8.2.
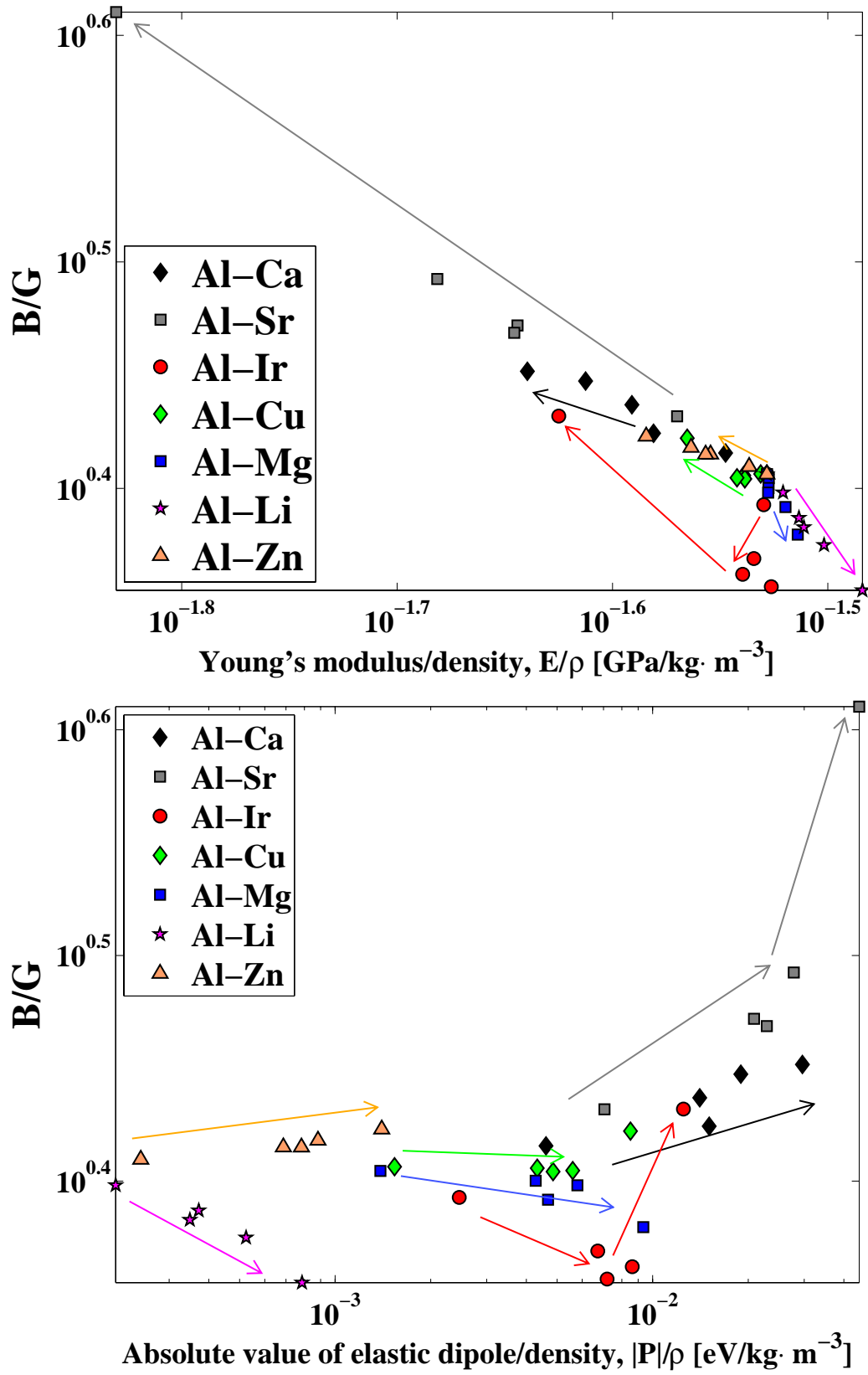
Figure 8.6: *B/G*-specific modulus (top) and *B/G*-specific absolute value of elastic dipole (bottom) chart of the studied Al binary solid solutions. The arrows points the direction of the concentration increase.

8.4 Fatigue-limited design charts

8.4.1 |Zener's ratio-1| vs. |elastic dipole|
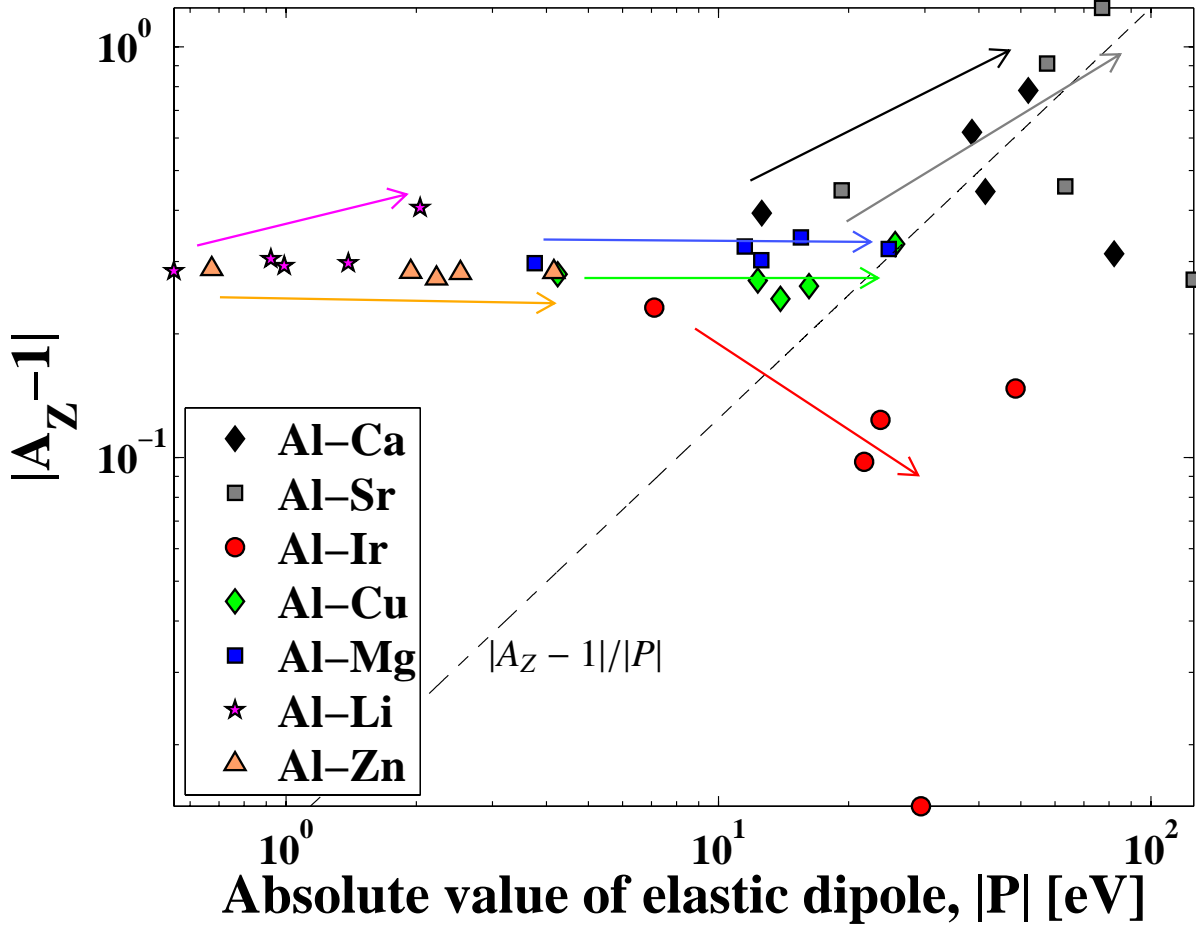
Figure 8.7: |Zener's ratio-1|-|elastic dipole| chart of the studied binary solid solutions. The arrows points the direction of the concentration increase.

As discussed in Section 8.1, $|A_Z - 1|$ is a measure of the range of the stress distribution when a polycrystalline material is "elastically" deformed. For a good fatigue property, $|A_Z - 1|$ should be minimized, and the strength should be maximized.

Figure 8.7 shows the $|A_Z - 1| - |P|$ chart in which the minimum $|A_Z - 1|/|P|$ means the best fatigue property. Apparently, the Al-Ir solid solutions have the best fatigue property among the studied Al binary solid solutions. Ir makes the A_Z of Al close to one and strengthens Al matrix. For the Al-Ca and Al-Sr solid solutions, the strength is significantly increased, but Ca and Sr make the solid solutions more elastically anisotropic. The change of A_Z in the Al-Cu, Al-Mg, Al-Li, and Al-Zn solid solutions is not pronounced. Therefore, in these four systems, the fatigue property is improved by the strengthening.

8.4.2 |Zener's ratio-1|/|elastic dipole| vs. Young's modulus/density
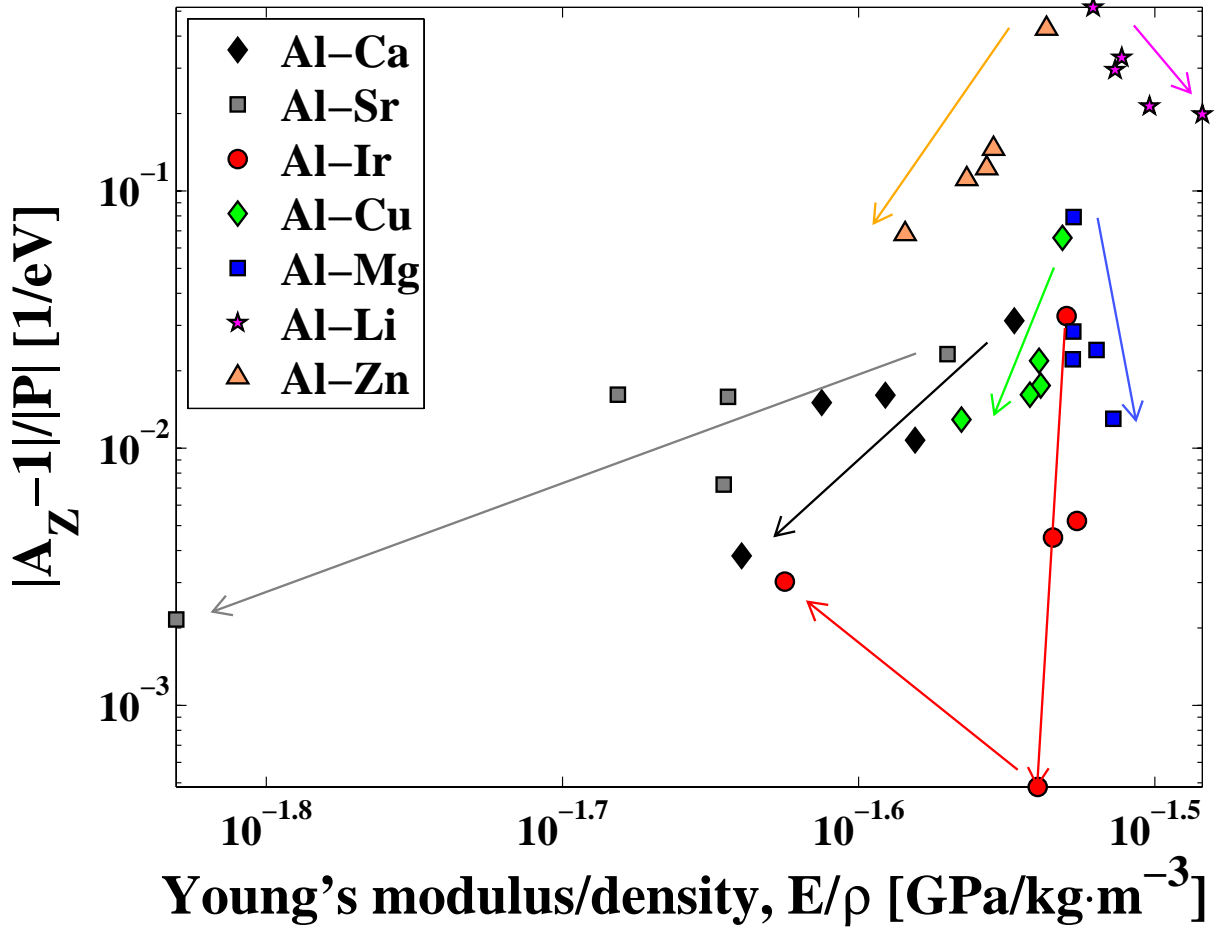
Figure 8.8: |Zener's ratio-1|/|elastic dipole|-Young's modulus/density chart of the studied binary solid solutions. The arrows points the direction of the concentration increase.

As discussed in Section 8.2.1, the specific modulus, E/ρ, is the material indice which describes the natural vibration frequency (Table 3.4). If a construction part vibrates, it not only needs to have maximum natural vibration frequency to avoid the resonance, but also a good fatigue property.

Figure 8.8 shows the $|A_Z - 1|/|P| - E/\rho$ chart which is the chart of fatigue property-natural vibration frequency. As discussed in Section 8.2.1, the Al-Li solid solutions have the highest natural vibration frequency. But the fatigue property is the worst. Because the solid solution strengthening alone is not enough to provide the sufficient strength. Fortunately, in Al-Li alloys, the metastable δ' phase provides precipitation hardening. Besides that, δ' phase is in $L1_2$ structure, its lattice parameter and elastic property can be roughly extrapolated from the dilute Al-Li solid solutions; experiments of the Young's modulus: Noble et al. (1982) shown in Figure 5.13) which keeps E/ρ almost the same as the dilute solid solutions.

Chapter 9

Summary and outlook

9.1 Summary

This thesis is summarized as the following:

Equation of state and elastic constants by DFT (Chapter 4 and Chapter 5)

1. DFT can accurately reproduce the lattice parameters, the bulk modulus and elastic constants of the pure bulk phase.

2. DFT can accurately reproduce the lattice parameters and the bulk modulus of the studied Al solid solutions.

3. In most studied systems, the general trend of the compositional dependence of the elastic constants can be reproduced by DFT, but not in good agreement with the experiments.

4. By using the ordered supercell, the compositional dependence of the elastic constants displays supercell size dependence. But the lattice parameter and the bulk modulus are not very sensitive to the supercell size.

Simplified approach to predict solid solution strengthening (Chapter 6)

1. The three strengthening measures (δ_b, ϵ_L and P/c) are in reasonable agreement with what is observed in the experiments and the direct DFT calculation.

2. Due to the uncertainties of the compositional dependence of the elastic constants by the ordered supercell, δ_b and P/c are the two measures which are more trustworthy than ϵ_L.

3. The lattice parameter of the studied Al binary solid solutions linear depends on the concentration up to 25% (Al_3X_1), which allows fast estimation of δ_b throughout the periodic table.

4. On the periodic table, there is a trend of the strengthening effect of the solute elements in a given matrix. Because the decisive parameters follow a trend. This kind of trend is found in Al (this thesis), Mg and Ni (re-analyzing previous studies) binary solid solutions.

5. $|\delta_b|$ of the studied solute elements in Al is correlated with their solubility enthalpies in Al by a power-law curve. By using this correlation, the optimal $|\delta_b|$ can be estimated to achieve the maximum strengthening effect.

Perturbation caused by solute atoms in Al matrix (Chapter 7)

1. The atomic volume, the amount of the charge transfer of the solute atoms in the studied Al binary solid solutions only depend on the immediate atomic environment, and nearly independent of the concentration.

2. Depending on the solute elements, the average electron density of each Al atoms are affected up to different ranges, which is the reason for the supercell size dependence observed in the calculated elastic constants.

3. The atomic relaxation has great contribution to the change in the average electron density of each Al atoms, except Al-Li and Al-Zn.

4. The atomic relaxation can be correlated with the strengthening effect, namely more relaxation higher strengthening effect.

DFT guided Ashby's material property and design chart (Chapter 8)

1. Various intrinsic materials properties can be extracted from DFT calculations and plotted into Ashby's material property and design charts.

2. The performance of the studied Al binary solid solutions revealed by the DFT guided material property and design charts guided reasonably coincides with their current applications.

3. Although Ca, Sr, and Ir has larger strengthening effect than the other studied solute elements (Cu, Mg, Li, and Zn), they do not always help Al perform better in some tasks.

9.2 Outlook

1. To characterize the di-elastic (modulus mismatch), a more reasonable parameter might be the slip mismatch parameter proposed by Yasi et al. (Yasi et al., 2010) (see Section 6.2). The explicit expression of combining the volume mismatch parameter and the slip mismatch parameter is still not known. In Yasi et al. (2010), it shows that this expression can be extracted by investigating the strain field of a dislocation in pure metals. Among the proposed methods of studying dislocations by DFT (see Table 1.2), the Peierls-Nabarro model+γ surface might be the most efficient one. And the shapes of the γ surfaces on (111) plane are the same in fcc metals. Therefore, the γ surface on (111) plane in fcc can be parametrized, and the strain field of the dislocations can be also parametrized. In this way, a parametrized expression of combining the volume and slip mismatch can be obtained for all fcc solid solutions.

2. Using the average electron density of each atoms alone is not adequate to study the perturbation caused by the solute elements, because the electrons are associated with certain energy levels. Therefore, the energetics on per atom basis in an alloy crystal should be investigated to gain further insight into the perturbation problem.

Part III

Appendix: Technical details

Appendix A

Convergence test

A.1 Purpose and procedures

Purpose of convergence test

As clarified in Section 3.1.3, to perform numerically convergent and physically meaningful DFT calculations, some input parameters should be set to sensible values. These input parameters include cut-off energy, k-point sampling, and σ value.

Convergence test procedure

The convergence test was conducted on pure elements in fcc structure and Al_3X_1 in $L1_2$ structure, and the procedure was:

1. At a constant cut-off energy, and varying the k-point sampling and the σ value, some material properties are calculated. Those properties include the lattice parameter, the bulk modulus, the total energy per atom, and the bulk modulus pressure derivative by using Murnaghan fit. This test aims at finding out the sufficient k-point sampling and the sensible σ value.

2. At a converged σ value from the previous test, and varying the cut-off energy, the same calculation was performed. In this test, the sufficiently high cut-off energy is determined.

3. EATOM of the isolated atoms was calculated, varying the cut-off energy. If the cut-off energy is sufficient, the difference between the calculated and the reference EATOM[1] should be within 10 meV.

In this Appendix, the convergence tests of Al, Cu, and Al_3Cu_1 are presented as examples. All the convergence tests are summarized in Section A.3.

---

[1] The reference EATOM is in the POTCAR file. The POTCAR file is one of the input files for performing DFT calculation on the platform of VASP. In POTCAR, one finds the information of the pseudopotential.

A.2 Convergence test examples of Al, Cu and Al$_3$Cu$_1$

A.2.1 Convergence test of Al

A.2.1.1 Convergence test of k-point sampling and σ value on fcc Al

At 240 eV cut-off energy, and varying the k-point sampling and the σ value, the lattice parameter, the bulk modulus, the total energy per atom, and the bulk modulus pressure derivative of fcc Al were calculated shwon in Figure A.1 and Figure A.2.

According to Figure A.1 and Figure A.2, the standard deviations of the calculated properties with respect to different k-point samplings are listed in Table A.1.

In Table A.1, at σ=1 eV, all the calculated properties are well converged, namely nearly independent of the k-point sampling. The sensible σ value depends on the density of states at the Fermi level. Since the density of states of fcc Al resembles the free electrons, the sensible σ value for fcc Al should be very high, such as 1 eV.

But σ=0.4 eV was chosen for the subsequent calculations for the following two reasons:

1. Other metals usually have low σ values. Such a high σ value might not be required for the calculations of the Al solid solutions. To be conservative, a lower σ value should be selected.

2. When dense k-point samplings are used, such as denser than 24×24×24, the convergence at σ=0.4 eV is still acceptable.

Table A.1: The standard deviations of the calculated properties of fcc Al with respect to different k-point samplings at σ=0.4, 0.6 and 1 eV and 240 eV cut-off energy.

Al			
	σ=0.4 eV	σ=0.6 eV	σ=1 eV
All tested k-point samplings			
Lattice parameter [Å]	0.000385	0.000121	9.39E-6
Bulk modulus [GPa]	0.0273	0.00648	0.00136
Equilibrium total energy per atom [meV]	0.256	9.01E-2	4.86E-13
Bulk modulus pressure derivative	0.0211	0.00381	0.000843
24×24×24 and denser k-point samplings			
Lattice parameter [Å]	6.29E-5	1.76E-5	8.28E-6
Bulk modulus [GPa]	0.00849	0.00155	0.000684
Equilibrium total energy per atom [meV]	6.85E-02	1.36E-02	0
Bulk modulus pressure derivative	0.00170	0.00122	0.000849
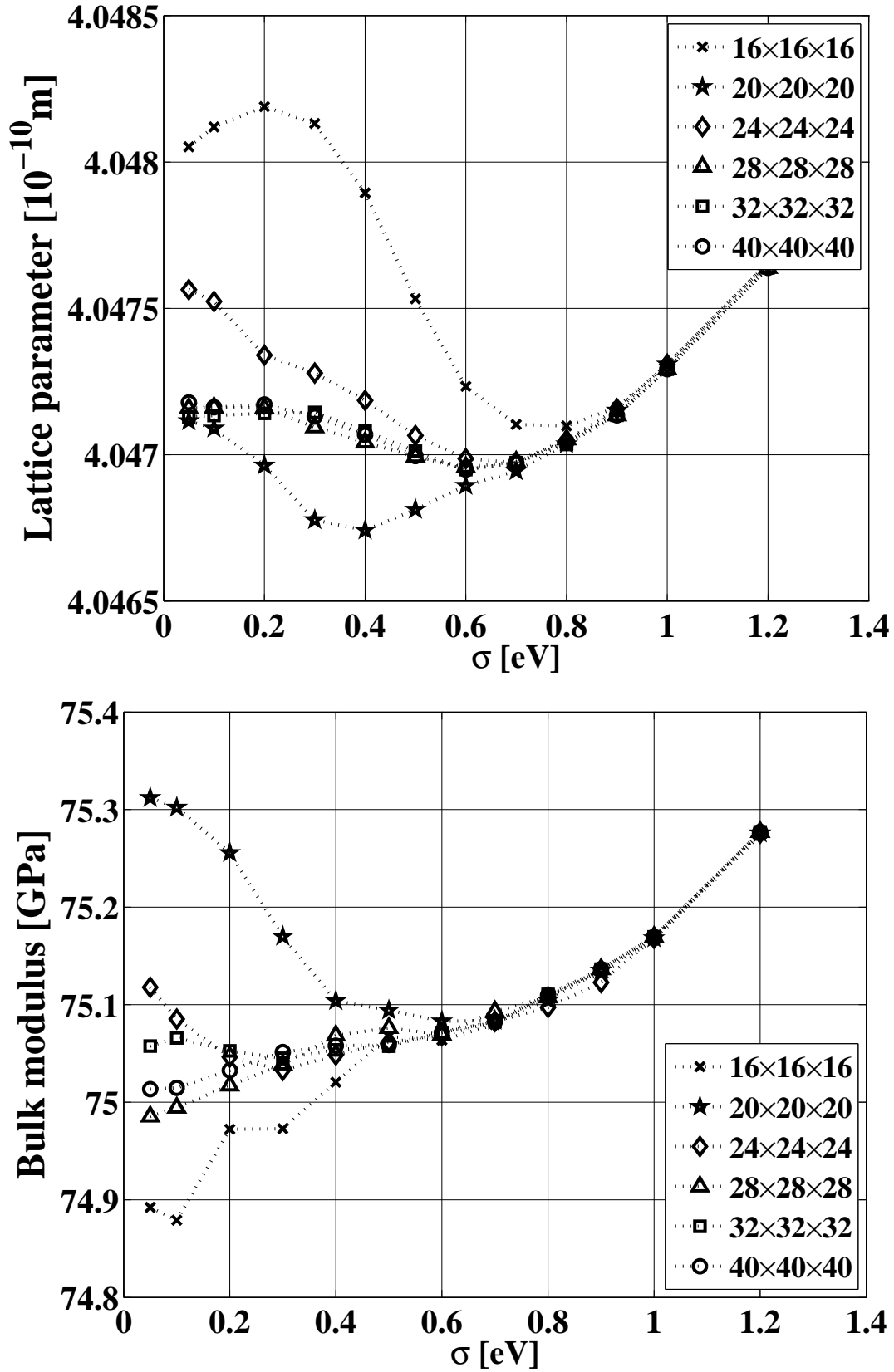
Figure A.1: Convergence test of the k-point sampling and the σ value on fcc Al at a constant cut-off energy of 240 eV. Top: the lattice parameter. Bottom: the bulk modulus. Legend: k-point sampling.
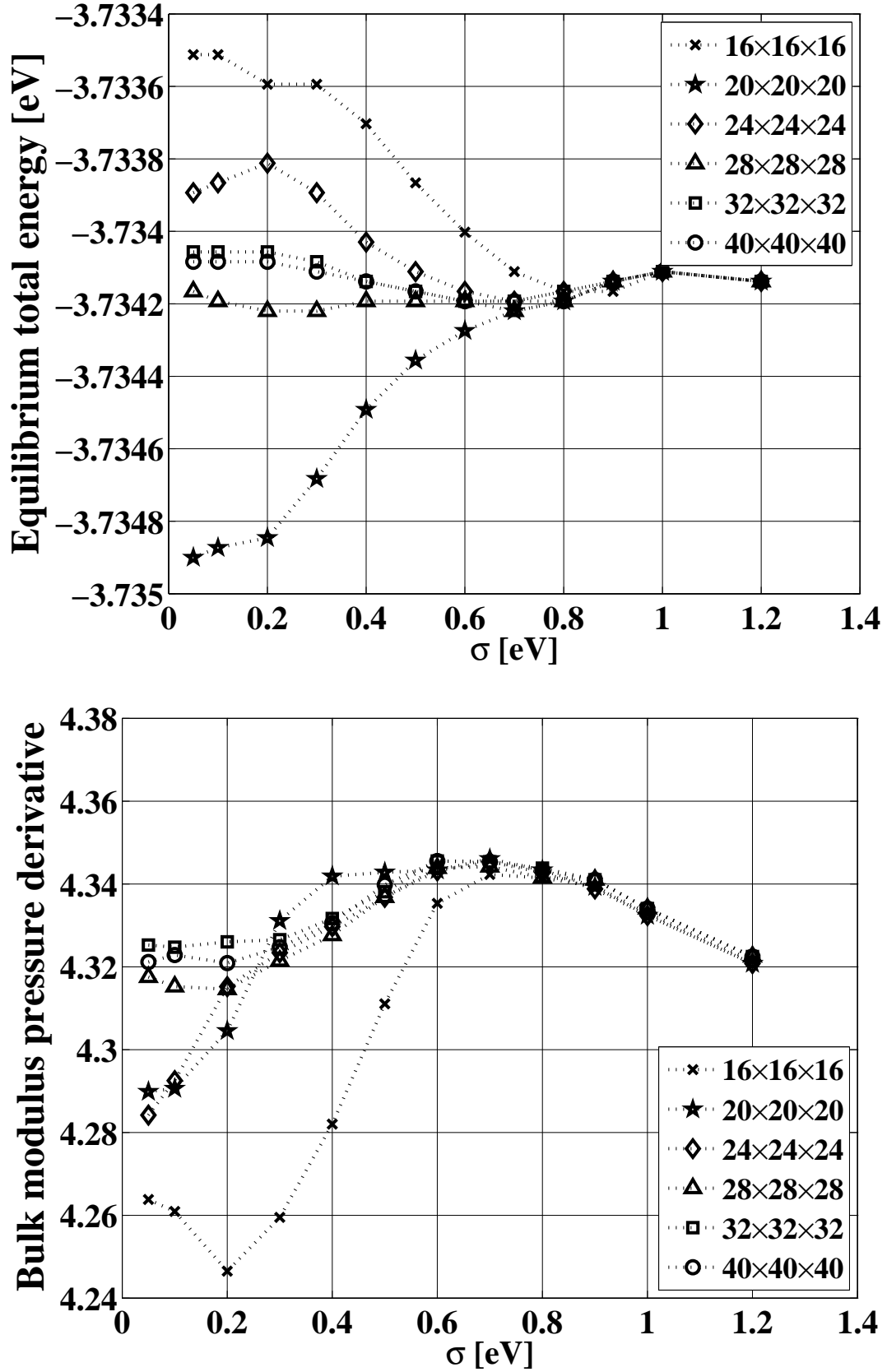
Figure A.2: Convergence test of the *k*-point sampling and the σ value on fcc Al at a constant cut-off energy of 240 eV. Top: the equilibrium total energy per atom. Bottom: the bulk modulus pressure derivative. Legend: *k*-point sampling.

A.2.1.2 Convergence test of cut-off energy on fcc Al

Figure A.3 and Figure A.4 show the calculated properties on the dependence of the cut-off energy at σ=0.4 eV. Above 420 eV cut-off energy, the calculated properties are almost independent of the cut-off energy.

The standard deviations of the properties calculated above 420 eV are listed in Table A.2. By using the k-point samplings of 24×24×24, 28×28×28 and 32×32×32, the standard deviations of the calculated properties are nearly identical. Thus, 420 eV cut-off energy and k-point sampling of 24×24×24 were chosen for the subsequent calculations.

Table A.2: The standard deviations of the calculated properties of fcc Al with respect to the cut-off energy from 420 to 500eV at the k-samplings of 24×24×24, 28×28×28 and 32×32×32 and σ=0.4eV.

Al			
k-point sampling	24×24×24	28×28×28	32×32×32
Lattice parameter [Å]	1.21E-5	1.22E-5	1.21E-5
Bulk modulus [GPa]	0.0180	0.0182	0.0181
Equilibrium total energy per atom [meV]	9.65E-2	9.68E-2	9.67E-2
Bulk modulus pressure derivative	0.00227	0.00225	0.00226
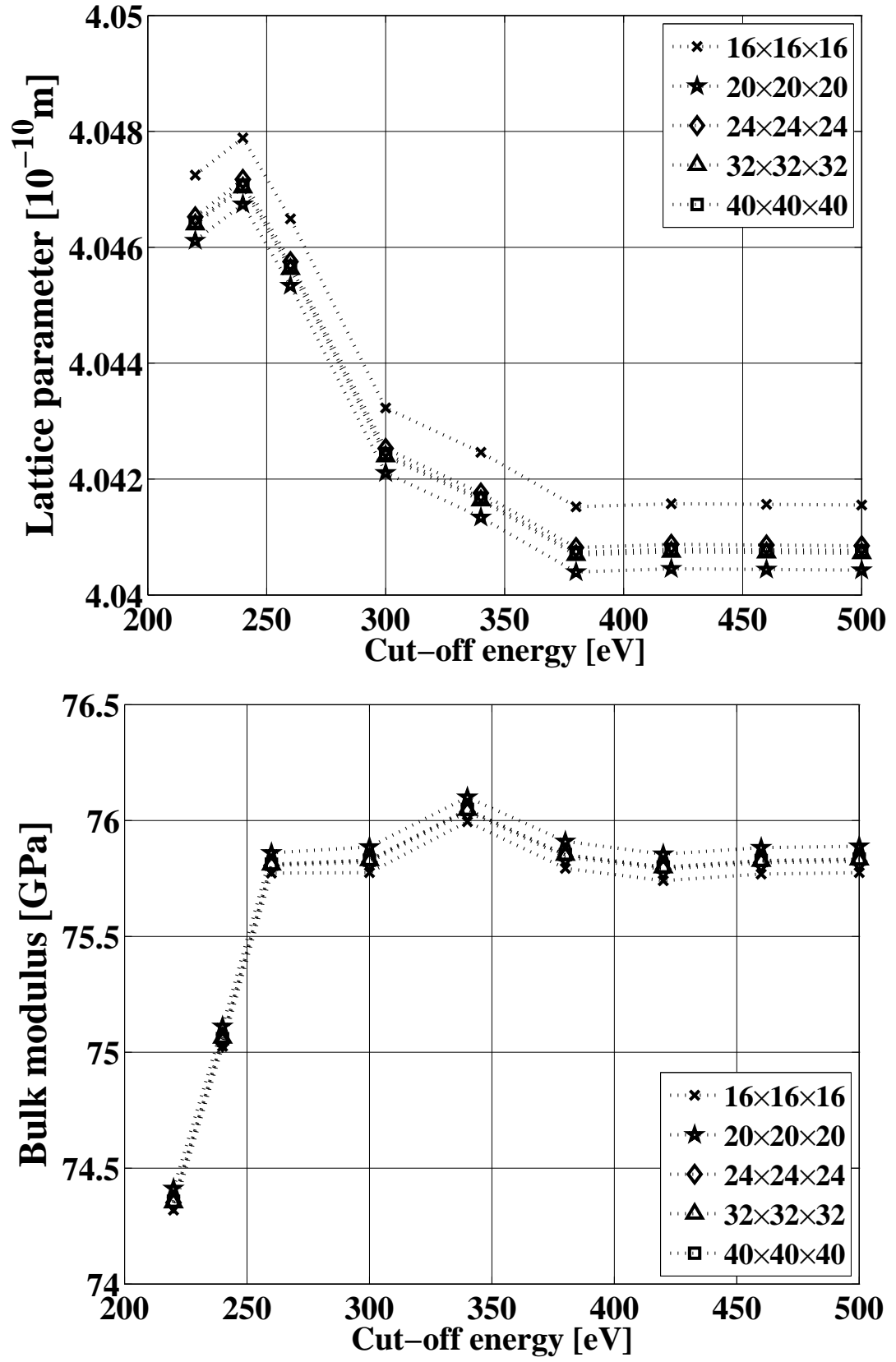
Figure A.3: Convergence test of Al on the cut-off energy at σ=0.4eV. Top: the lattice parameter. Bottom: the bulk modulus. Legend: k-point sampling.
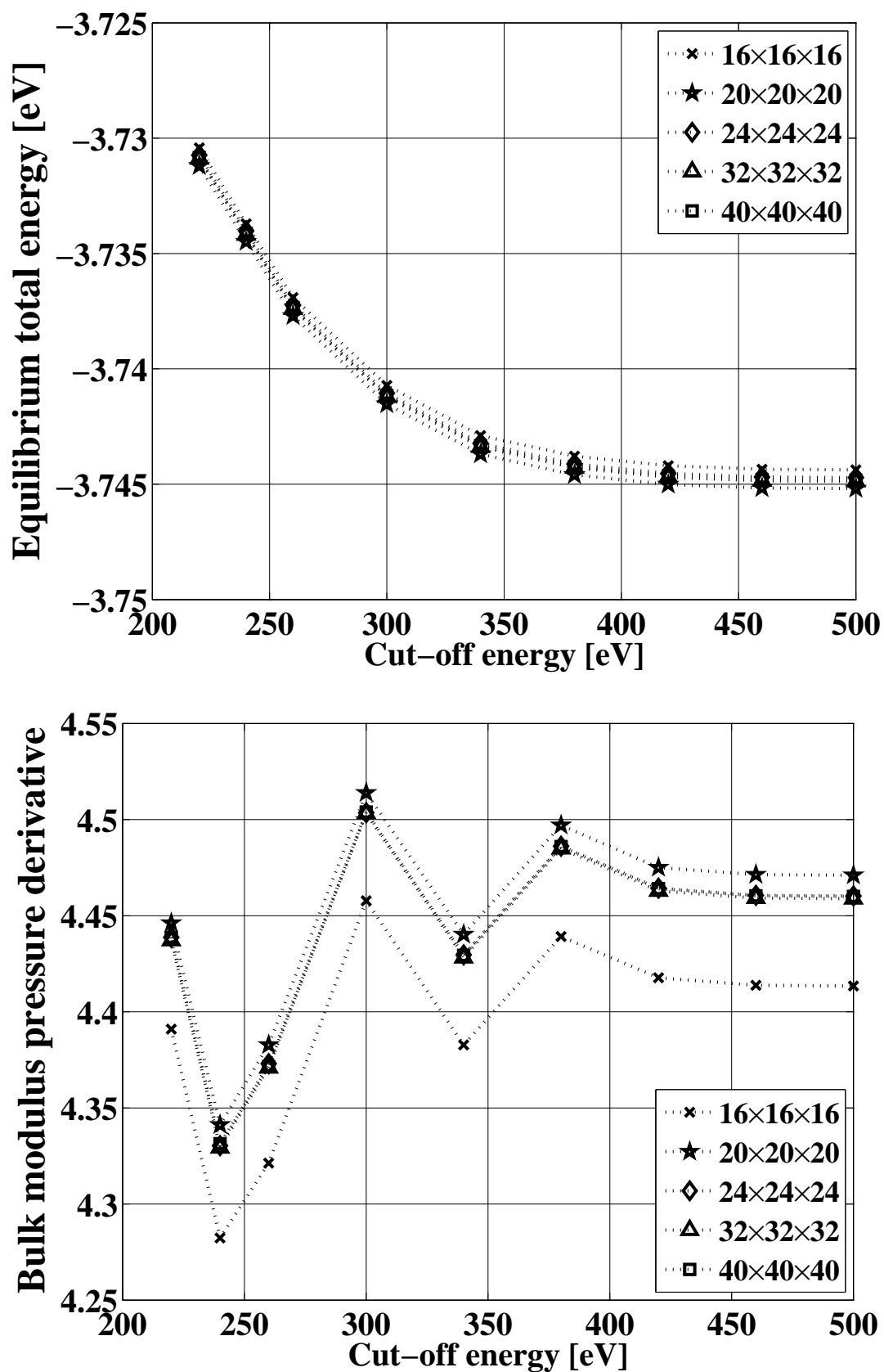
Figure A.4: Convergence test of Al on the cut-off energy at σ=0.4eV. Top: the equilibrium total energy per atom. Bottom: the bulk modulus pressure derivative. Legend: k-point sampling.

A.2.1.3 Convergence test on isolated Al atom

Figure A.5 shows, above the cut-off energy of 340eV, the difference between calculated and reference EATOM is less than 1 meV. This test ensures the cut-off energy from the previous test (420 eV) is safe.
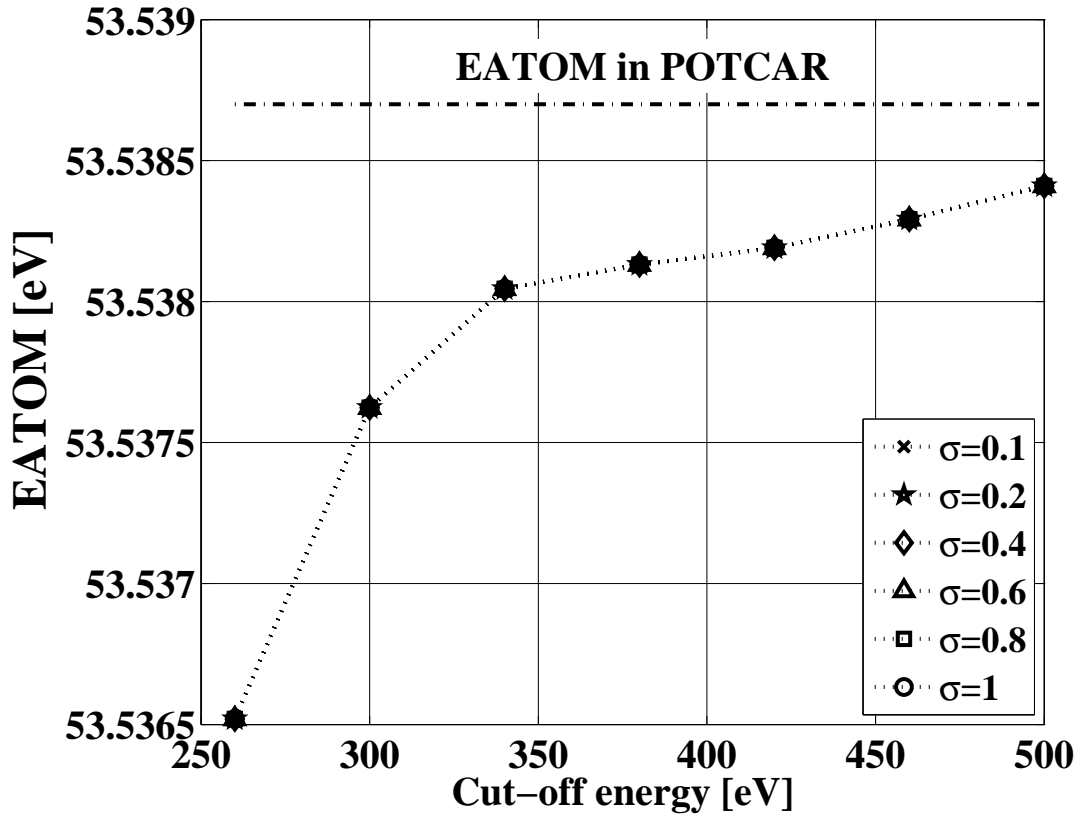
Figure A.5: Convergence test of the cut-off energy on the isolated Al atom. Legend: σ value in eV.

A.2.2 Convergence test of Cu

A.2.2.1 Convergence test of k-point sampling and σ value on fcc Cu

In Figure A.6 and Figure A.7, the calculated properties by different k-point samplings do not clearly converge to any σ value. But at a constant σ value, the difference of the calculated properties by different k-point samplings is almost constant. Thus, the convergent σ value can be considered to be very small.

The standard deviations of the calculated properties of Cu with respect to different k-point samplings are listed in Table A.3. By increasing the σ value, the standard deviations do not decrease.

Table A.3: The standard deviations of the calculated properties of fcc Cu with respect to different k-point samplings at σ=0.05, 0.1, 0.2 and 0.3 eV and 220 eV cut-off energy.

	Cu			
	σ=0.05 eV	σ=0.1 eV	σ=0.2 eV	σ=0.3 eV
Lattice parameter [Å]	0.000237	0.000241	0.000303	0.000421
Bulk modulus [GPa]	0.248	0.260	0.343	0.388
Equilibrium total energy per atom [meV]	0.346	0.349	0.407	0.463
Bulk modulus pressure derivative	0.0419	0.0411	0.0416	0.0478
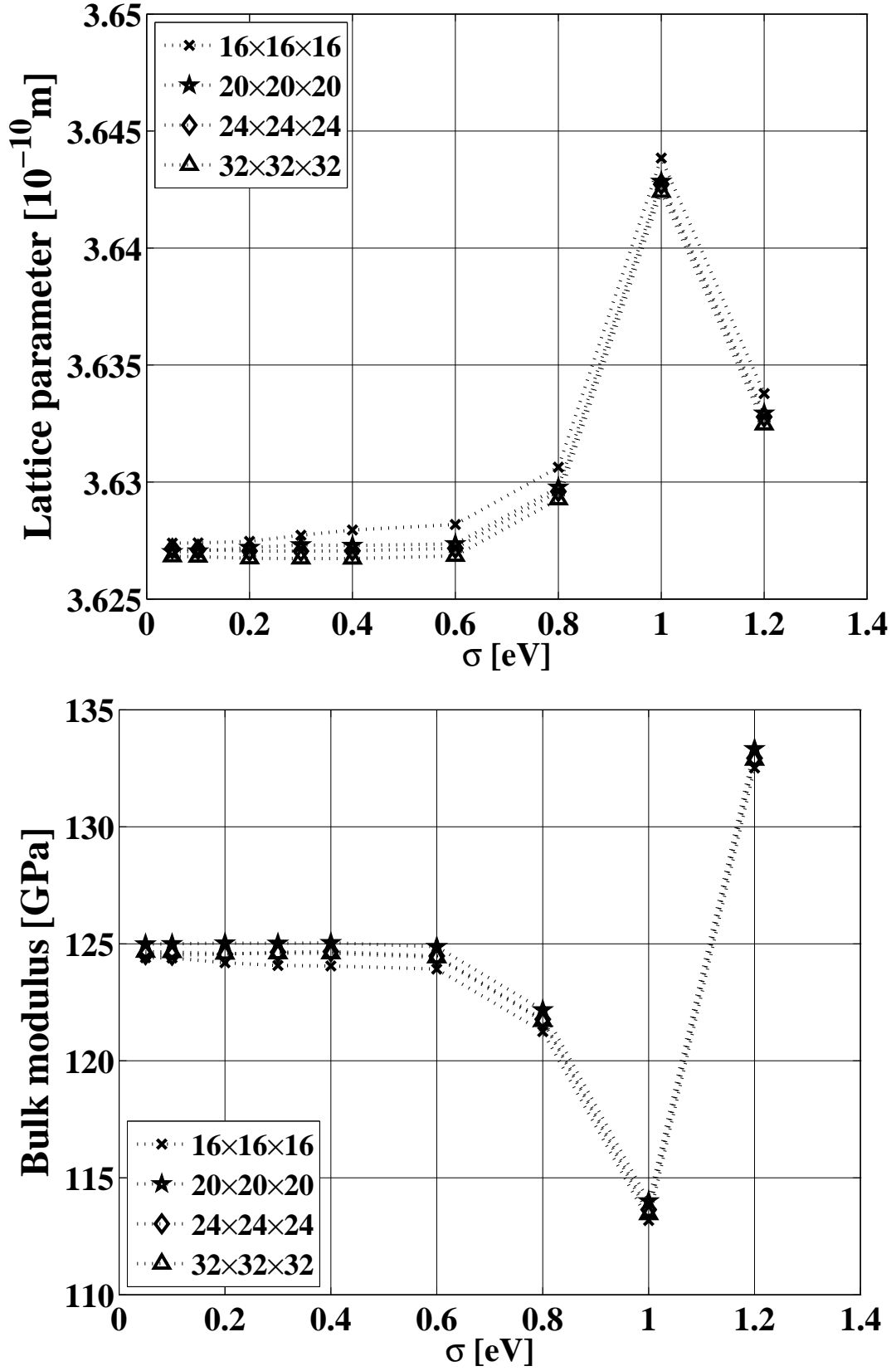
Figure A.6: Convergence test of Cu on the *k*-point samplings and the σ value at a constant cut-off energy of 220 eV. Top: the lattice parameter. Bottom: the bulk modulus. Legend: *k*-point sampling.
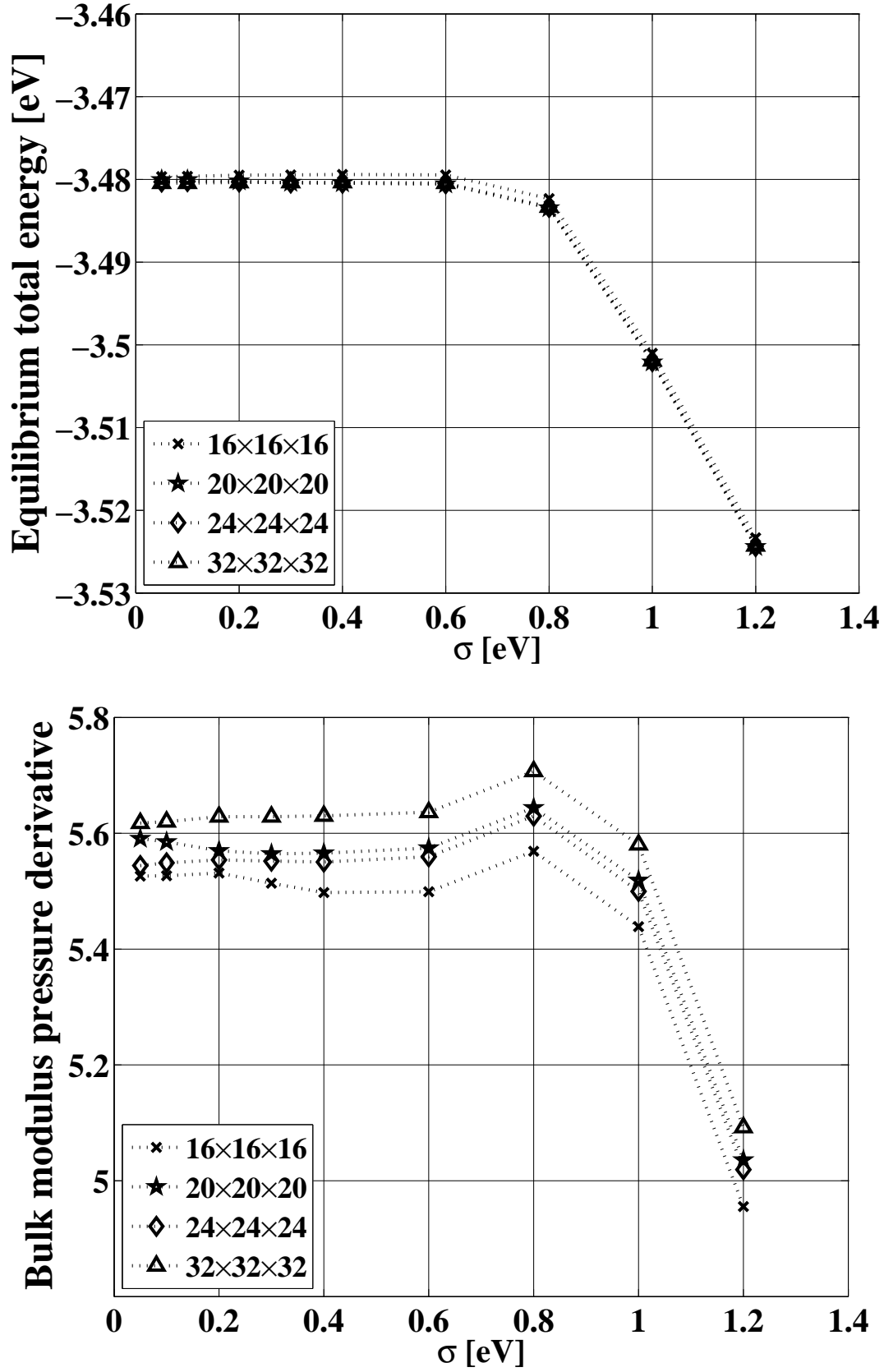
Figure A.7: Convergence test of Cu on the *k*-point samplings and the σ value at a constant cut-off energy of 220 eV. Top: the equilibrium total energy per atom. Bottom: the bulk modulus pressure derivative. Legend: *k*-point sampling.

A.2.2.2   Convergence test of cut-off energy on fcc Cu

Figure A.8 and Figure A.9 shows the convergence behavior of fcc Cu on the cut-off energy at σ=0.1eV. It seems above the cut-off energy of 300eV, the calculated properties are converged. Above the cut-off energy of 420eV, the standard deviations of the calculated properties of Cu are listed in A.4.

Table A.4: The standard deviations of the calculated properties of Cu with respect to the cut-off energy from 420 to 500 eV at k-samplings of 16×16×16, 20×20×20 and 32×32×32 and σ=0.1eV.

Cu			
k-point sampling	24×24×24	28×28×28	32×32×32
Lattice parameter [Å]	5.61E-5	5.53E-5	4.98E-5
Bulk modulus [GPa]	0.0721	0.0703	0.0715
Equilibrium total energy per atom [meV]	0.261	0.261	0.247
Bulk modulus pressure derivative	0.00164	0.00168	0.00119
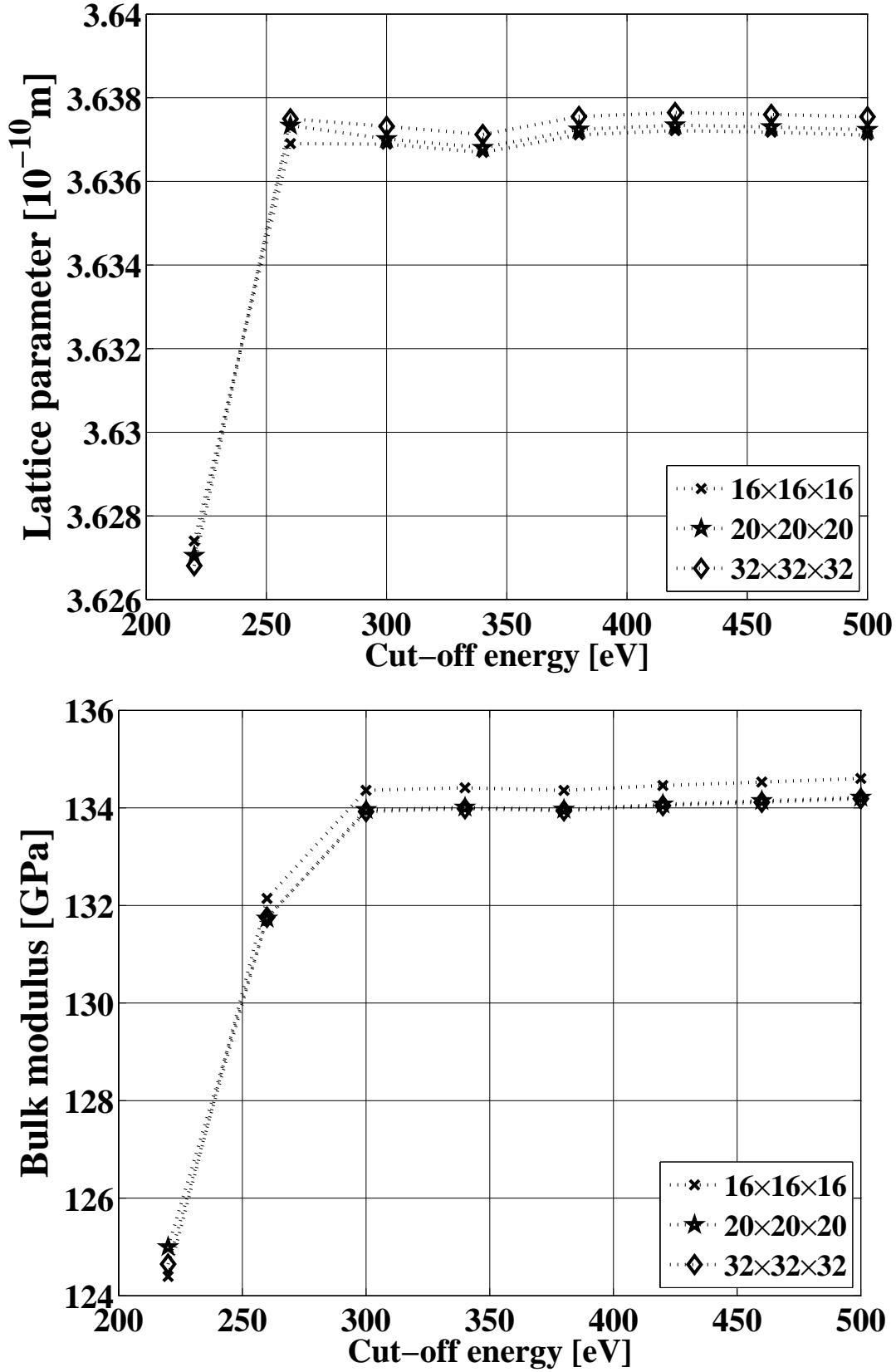
Figure A.8: Convergence test of Cu on the cut-off energy at σ=0.1eV. Top: the lattice parameter. Bottom: the bulk modulus. Legend: k-point sampling.
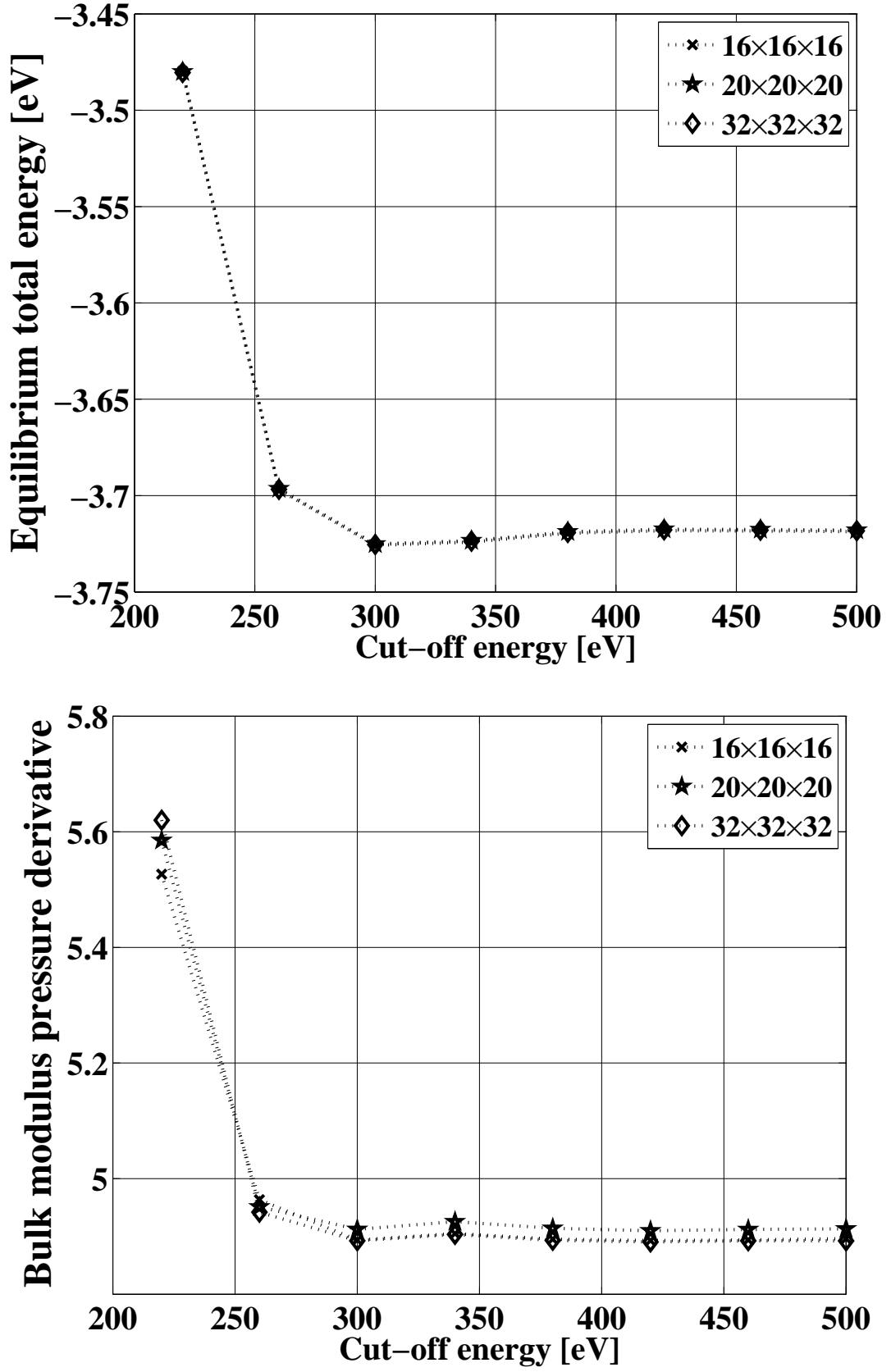
Figure A.9: Convergence test of Cu on the cut-off energy at σ=0.1eV. Top: the equilibrium total energy per atom. Bottom: the bulk modulus pressure derivative. Legend: k-point sampling.

A.2.2.3 Convergence test on isolated Cu atom

Above the cut-off energy of 420 eV, the difference between the calculated EATOM and the reference EATOM in POTCAR is less than 10 meV shown in Figure A.10.
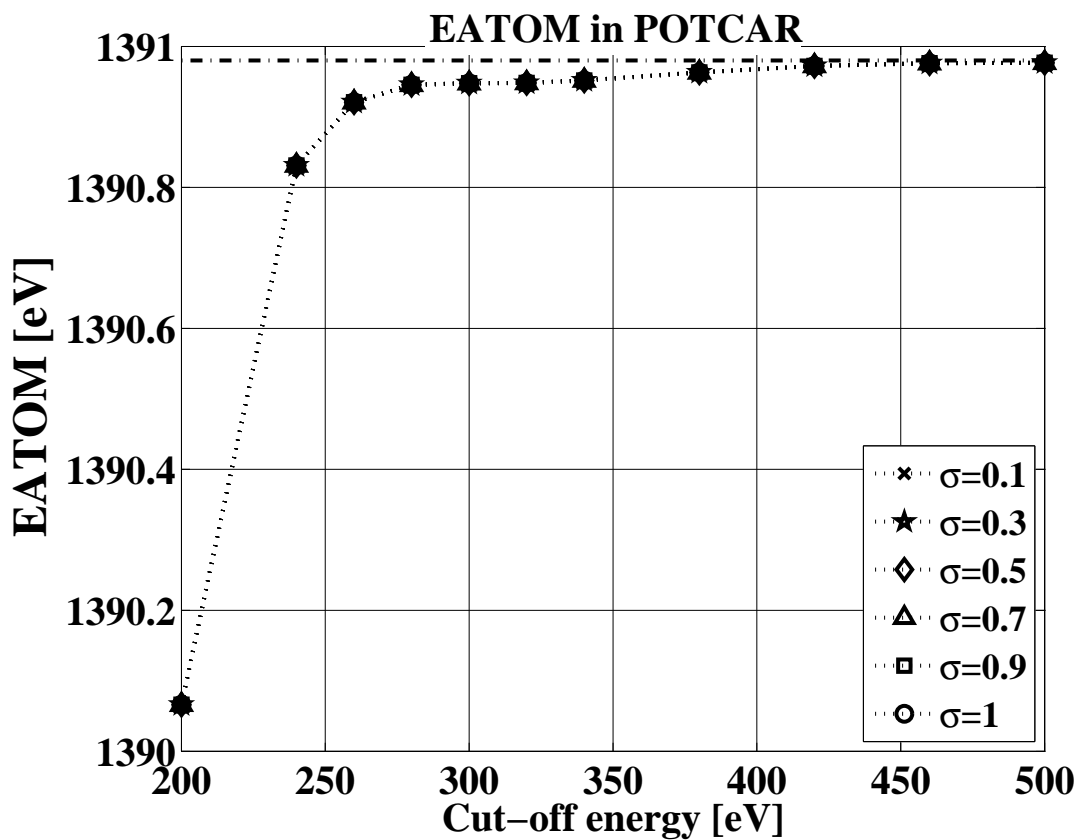
Figure A.10: Convergence test of the isolated Cu atom on the cut-off energy.

A.2.3 Convergence test of $L1_2$ **Al$_3$Cu$_1$**

A.2.3.1 Convergence test of k-**point sampling and** σ **value on** $L1_2$ **Al$_3$Cu$_1$**

The convergence test on the k-point sampling and the σ value of Al$_3$Cu$_1$ in $L1_2$ structure indicates that σ=0.4eV should be a reasonable convergent value shown Figure A.11, Figure A.12 and Table A.5.

Table A.5: The standard deviations of the calculated properties of Al$_1$Cu$_3$ with respect to different k-point samplings at σ=0.2, 0.3, 0.4 and 0.5eV and the cut-off energy of 240eV.

Al$_3$Cu$_1$				
	σ=0.2eV	σ=0.3eV	σ=0.4eV	σ=0.5eV
Lattice parameter [Å]	11.1E-5	7.44E-5	5.96E-5	6.09E-5
Bulk modulus [GPa]	0.0344	0.0193	0.00687	0.000997
Equilibrium total energy per atom [meV]	3.99E-2	4.80E-3	3.84E-3	4.52E-3
Bulk modulus pressure derivative	0.00846	0.00997	0.00991	0.00974
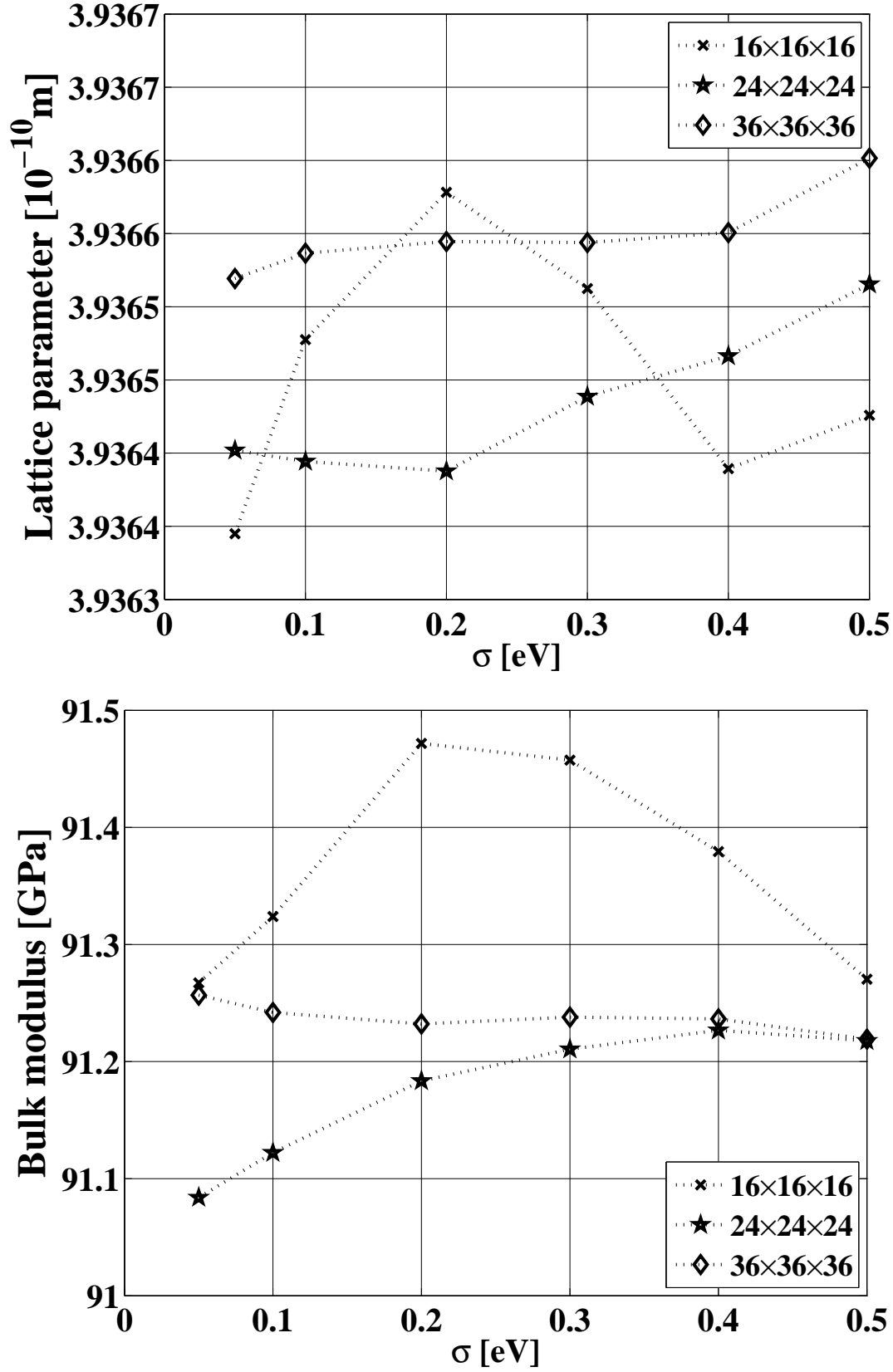
Figure A.11: Convergence test of Al₃Cu₁ on the *k*-point samplings and the σ value at a constant cut-off energy of 240 eV. Top: the lattice parameter. Bottom: the bulk modulus. Legend: *k*-point sampling.
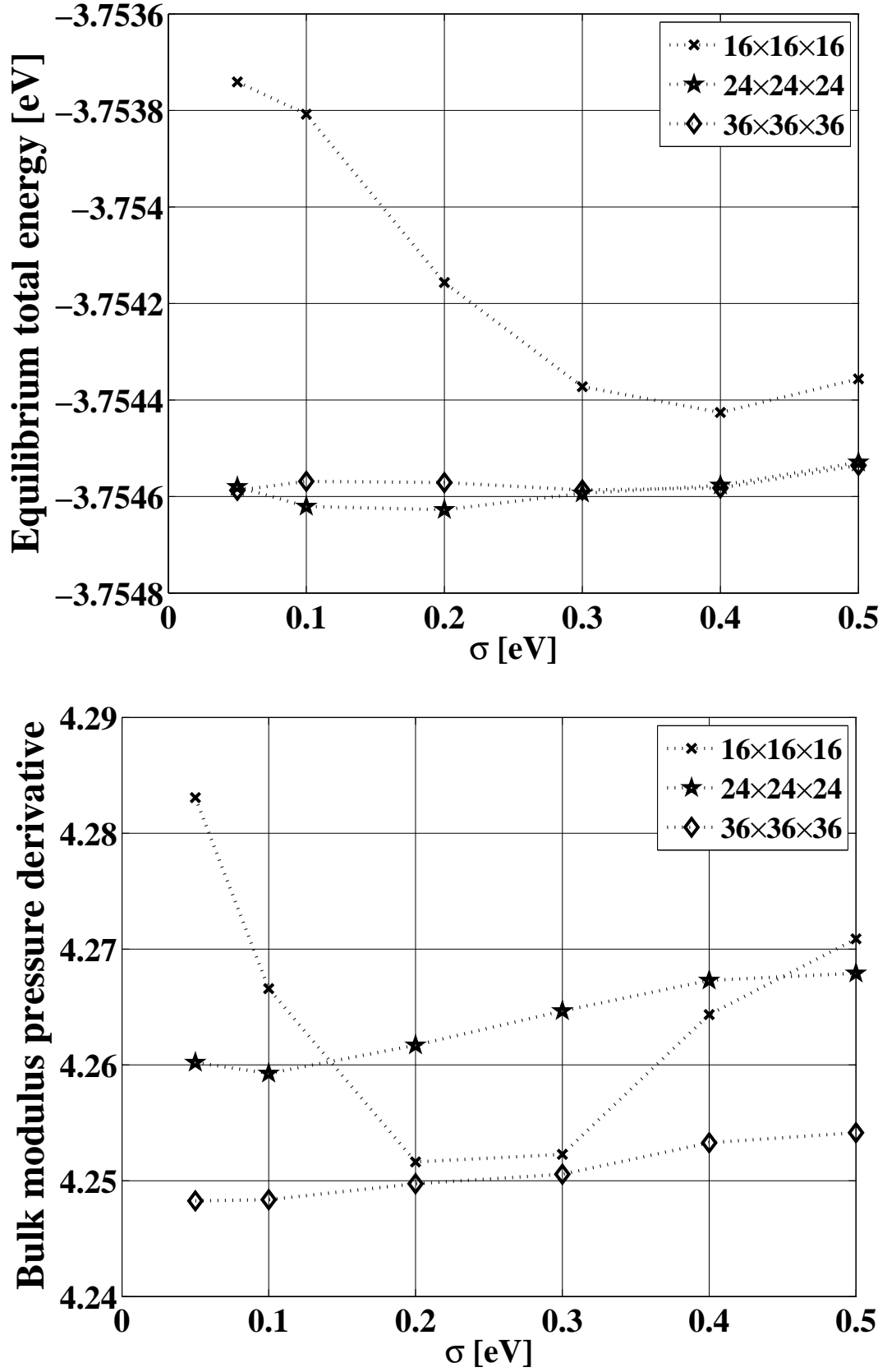
Figure A.12: Convergence test of Al$_3$Cu$_1$ on the k-point samplings and the σ value at a constant cut-off energy of 240 eV. Top: the equilibrium total energy per atom. Bottom: the bulk modulus pressure derivative. Legend: k-point sampling.

A.2.3.2 Convergence test of cut-off energy on $L1_2$ **Al$_3$Cu$_1$**

At the constant σ value of 0.4 eV, the convergence behavior of the calculated properties of Al$_3$Cu$_1$ on the cut-off energy is shown Figure A.13 and Figure A.14. Above the cut-off energy of 420 eV, the standard deviations of the calculated properties are listed in Table A.6.

Table A.6: The standard deviations of the calculated properties of Al$_3$Cu$_1$ with respect to the cut-off energy from 420 to 500 eV at k-samplings of 24×24×24 and 36×36×36 and σ=0.4 eV.

Al$_3$Cu$_1$		
	24×24×24	36×36×36
Lattice parameter [Å]	3.43E-5	3.43E-5
Bulk modulus [GPa]	0.0336	0.0335
Equilibrium total energy per atom [meV]	0.113	0.113
Bulk modulus pressure derivative	0.00215	0.00216
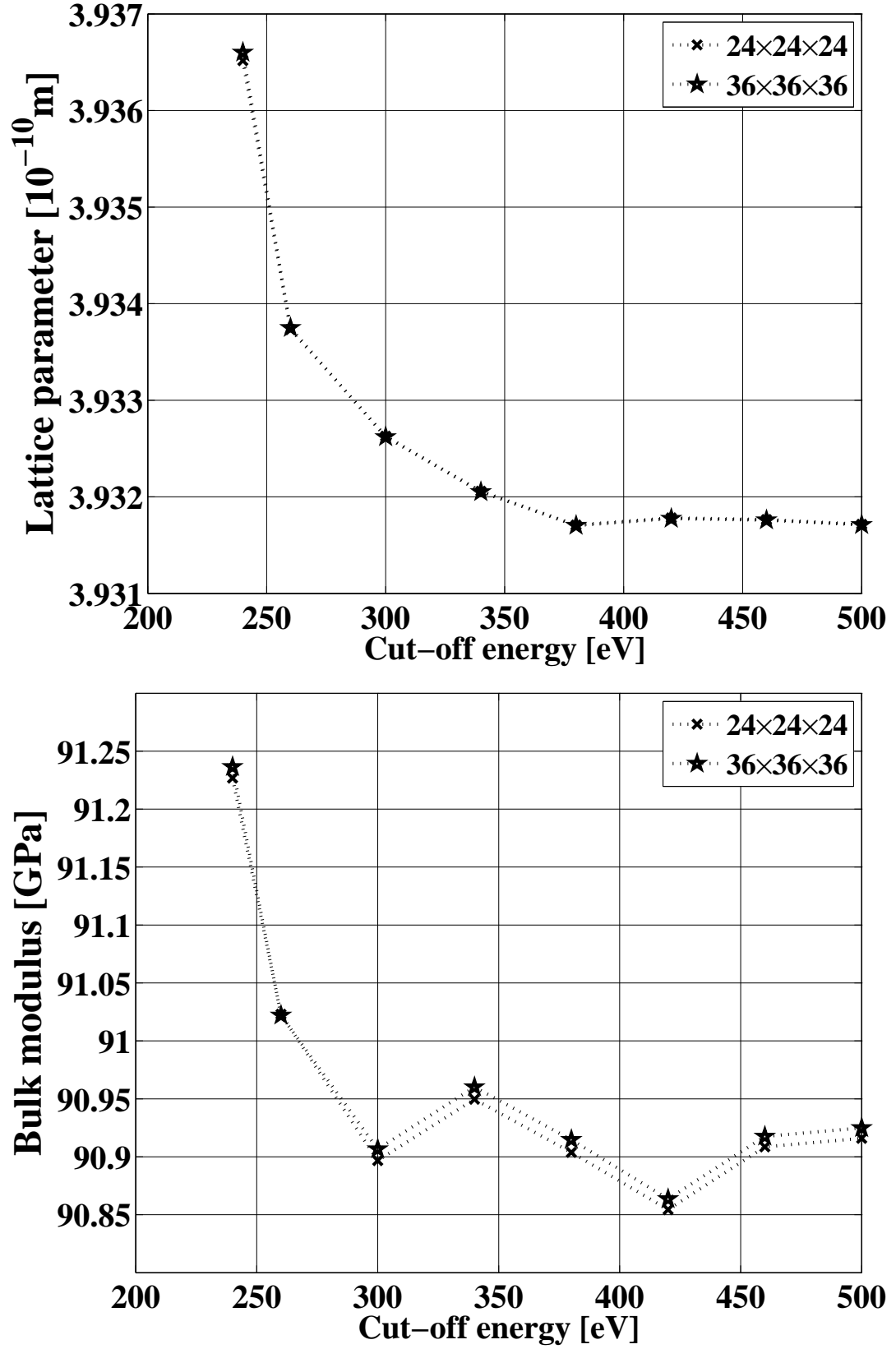
Figure A.13: Convergence test of Al_3Cu_1 on the cut-off energy at σ=0.4 eV. Top: the lattice parameter. Bottom: the bulk modulus. Legend: k-point sampling.
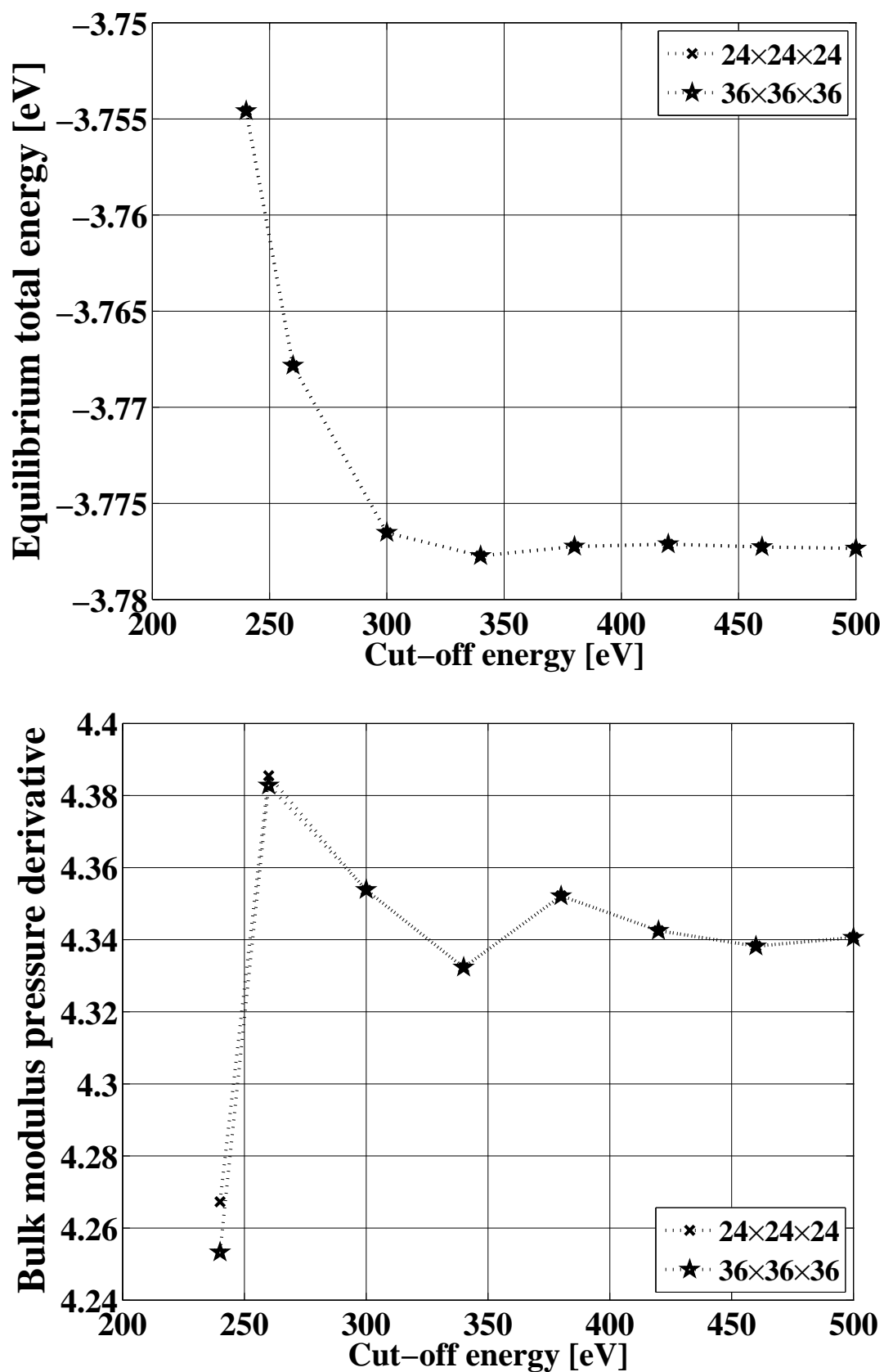
Figure A.14: Convergence test of Al_3Cu_1 on the cut-off energy at σ=0.4 eV. Top: the equilibrium total energy per atom. Bottom: the bulk modulus pressure derivative. Legend: *k*-point sampling.

A.3 Summary of convergence test

Table A.7: Summary of the convergence test of Al, Cu, Mg, Li, Zn, Ca, Sr and Ir. The description see text.

Element	Pure bulk phase (in fcc structure)		Isolated atom	Bulk Al₃X₁ (in L1₂ structure)	
Al	σ=0.4 eV 24×24×24 420~500 eV	1.21E-5 Å 0.0180 GPa 9.65E-2 meV 0.00227	420 eV 0.51 meV		
Cu	σ=0.1 eV 24×24×24 420~500 eV	5.61E-5 Å 0.0721 GPa 0.261 meV 0.00164	420 eV 10 meV	σ=0.4 eV 24×24×24 420~500 eV	3.43E-5 Å 0.0336 GPa 0.113 meV 0.00215
Mg	σ=0.4 eV 20×20×20 420~500 eV	0.000221 Å 0.0109 GPa 0.491 meV 0.000417	420 eV 6.45 meV	σ=0.4 eV 24×24×24 420~500 eV	7.91E-5 Å 0.0145 GPa 0.217 meV 0.000724
Li	σ=0.4 eV 20×20×20 420~500 eV	0.000196 Å 0.00576 GPa 0.235 meV 0.00393	420 eV 4.78 meV	σ=0.4 eV 24×24×24 420~500 eV	3.40E-5 Å 0.00448 GPa 0.134 meV 0.00153
Zn	σ=0.4 eV 20×20×20 420~500 eV	5.86E-5 Å 0.0253 GPa 0.347 meV 0.00203	420 eV 7 meV	σ=0.4 eV 24×24×24 420~500 eV	3.88E-5 Å 0.0169 GPa 0.146 meV 0.000681
Ca	σ=0.2 eV 24×24×24 420~500 eV	3.30E-5 Å 0.0107 GPa 0.181 meV 0.00125	420 eV 4.78 meV	σ=0.4 eV 24×24×24 420~500 eV	2.04E-5 Å 0.0335 GPa 7.37E-2 meV 0.00166
Sr	σ=0.1 eV 20×20×20 420~500 eV	0.000294 Å 0.00377 GPa 0.330 meV 0.00114	420 eV 2.13 meV	σ=0.4 eV 24×24×24 420~500 eV	9.96E-5 Å 0.00196 GPa 0.146 meV 0.00258
Ir	σ=0.4 eV 20×20×20 420~500 eV	2.04E-5 Å 0.0301 GPa 7.86E-2 meV 0.00214	420 eV 4 meV	σ=0.4 eV 24×24×24 420~500 eV	2.04E-5 Å 0.0335 GPa 7.37E-2 meV 0.00166

The convergence tests on the studied elements are summarized in Table A.7. The σ value, the k-point sampling, and the cut-off energy range are listed on the left column in the contents of the "Pure bulk phase" and "Bulk Al₃X₁". On the right column lists the standard deviations of the calculated properties (the lattice parameter, the bulk modulus, the equilibrium total energy

per atom and the bulk modulus pressure derivative) by the specified input parameters. In the content of "Isolated atom", the cut-off energy and the difference between the calculated and the reference EATOM by such a cut-off energy are listed.

Appendix B

Numerical tests of Equation of State

B.1 Purpose and procedures

B.1.1 Purpose of tests

The bulk modulus (B_0), the lattice parameter (a_0), the equilibrium total energy per atom (E_0), and the bulk modulus pressure derivative (B_0') can be obtained by fitting the calculated energy-volume curves by the equation of state (EOS) models.

In practice, the general procedure is: (1) calculate the total energies at a series volumes; (2) fit the energy-strain curve by the EOS models. There might be the following scenarios:

Scenario 1 Calculations are performed at expanded and compressed volumes to get the energy-volume curve. The question is how much the volume expansion and compression is appropriate.

Scenario 2 Due to unknown technical reasons, the computer crashes, and some calculations are not finished. The question is whether we can use the finished calculations to perform the curve fitting, or we still need to restart the crashed calculations.

Scenario 3 The EOS models are originally proposed for the experimentalists. In the experiments, it is almost impossible to expand the solids. The question is in the calculation whether it is better, if the amount of the volume compression is more than the volume expansion.

The above scenarios are all possible in the practical calculations. In order to minimize influence of these technical details on the final results, it is necessary to test these scenarios accordingly.

B.1.2 Test procedures

The tests were conducted mainly on pure fcc Al by using two EOS models (Murnaghan EOS and 3rd order Birch-Murnaghan fit[1], see Section 3.2). The tests were conducted according to the following procedures:

Test 1 A preliminary calculation was performed to obtain the an approximated equilibrium atomic volume (V_0). 9 total energies were calculated at $V_0 \pm dV_{max}$, $V_0 \pm 0.75dV_{max}$, $V_0 \pm 0.5dV_{max}$, $V_0 \pm 0.25dV_{max}$ and V_0. $\pm dV_{max}$ was varied from $\pm 1\%$ to $\pm 20\%$ of V_0.

Test 2 Among the 7 calculated total energies at $V_0 \pm 0.75dV_{max}$, $V_0 \pm 0.5dV_{max}$, $V_0 \pm 0.25dV_{max}$ and V_0, 1, 2, 3 and 4 total energies were omitted. The remaining total energies were used to fit the energy-volume curves, and compared with the results by fitting all the 9 data points.

---

[1]For simplicity, 3rd order Birch-Murnaghan fit is called Birch-Murnaghan fit onwards.

Test 3 From the 9 calculated total energies, some of them were selected. And among the se-
lected, there were more total energies at the compressed volumes than the expanded, or
another way round. The curve fitting was conducted on these selected total energies and
correspoinding volumes.

In order to quantify the quality of the curving fitting. Two measures of the goodness-of-fit
(GOF) were employed: SSE (sum of squares due to error) and R^2, and they are defined as:

$$SSE = \sum_{i=1}^{n} \left(E_i - \hat{E}_i \right)^2 \tag{B.1}$$

$$R^2 = \frac{\sum_{i=1}^{n} \left(\hat{E}_i - \overline{E}_i \right)^2}{\sum_{i=1}^{n} \left(E_i - \overline{E}_i \right)^2} \tag{B.2}$$

where n is the number of data points, E_i is the calculated energy, $\hat{E}_i$ is the fitted energy, $\overline{E}_i$ is the
average of the calculated energies. If the fit is perfect, SSE is 0. R^2 ranges from 0 to 1. If $R^2=1$,
it indicates a perfect fit. In this study, SSE is very close to 0 and R^2 is very close to 1, thus $1\text{-}R^2$
is used instead of R^2 so that those two measures of GOF can be put together for comparison.

B.2   Test 1
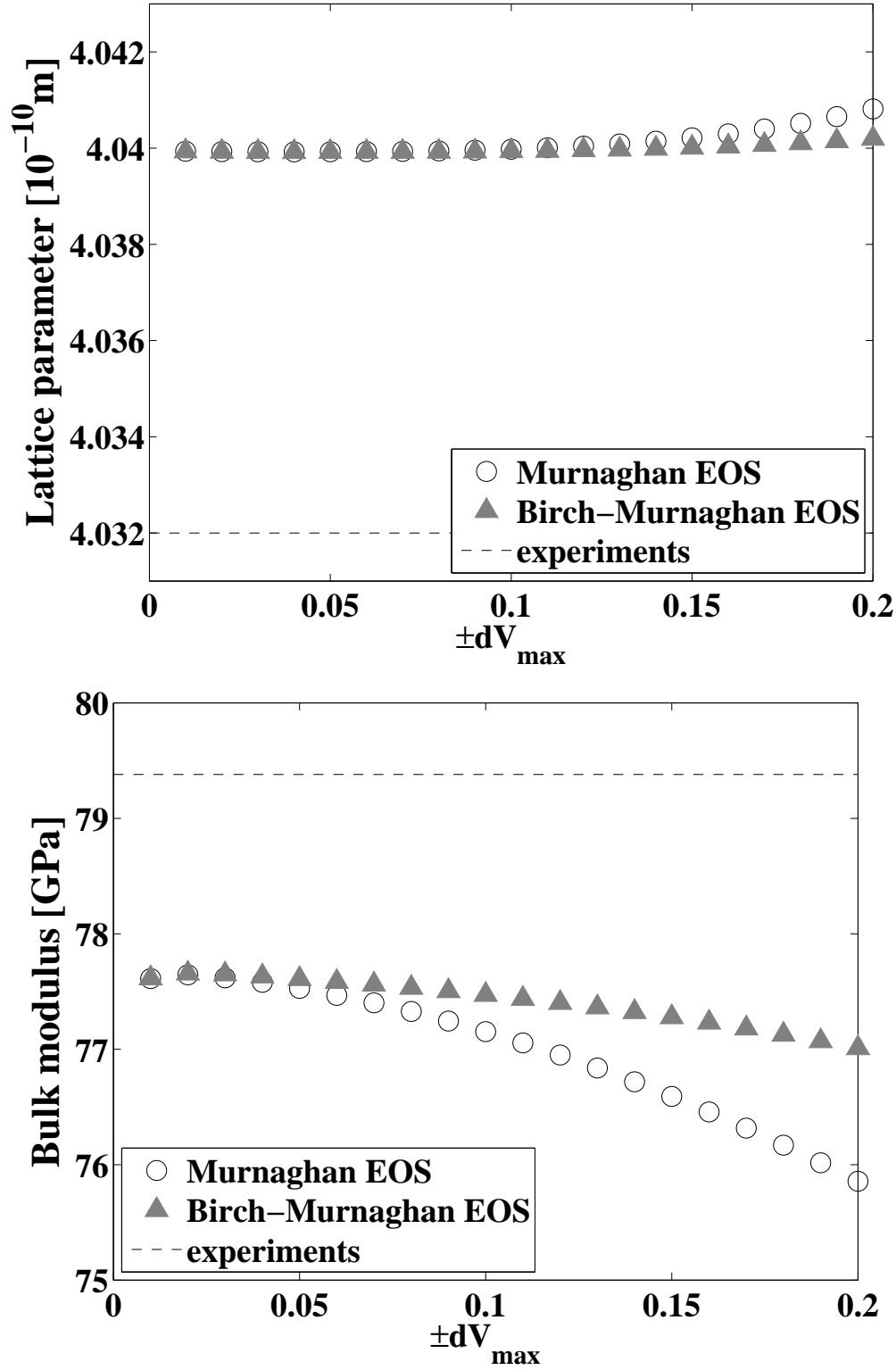
Figure B.1: The calculated lattice parameter (top) and bulk modulus (bottom) of fcc Al by using Murnaghan and Birch-Murnaghan fit. The horizontal dash lines are the experimental data from Grabowski et al. (2007).
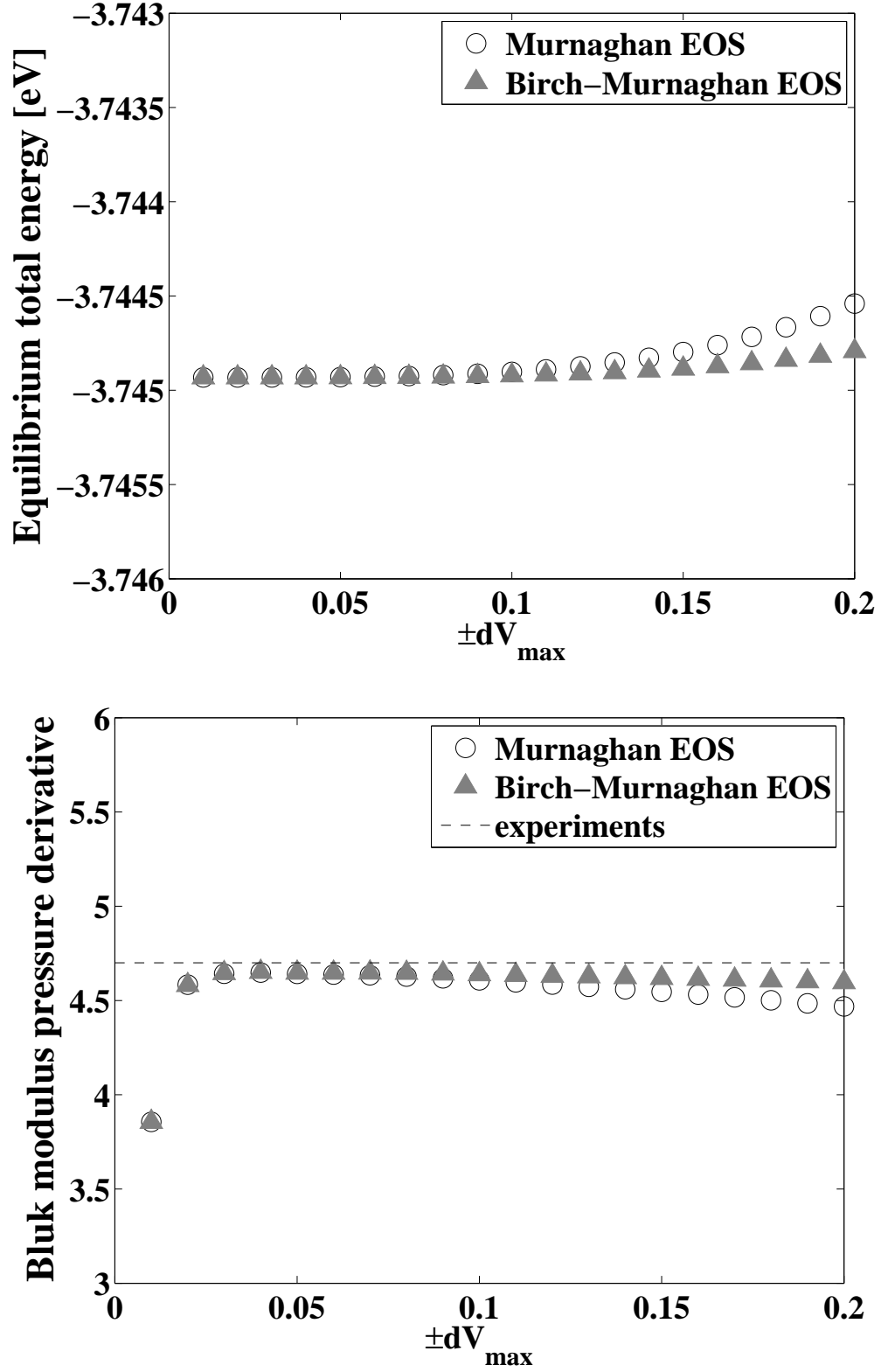
Figure B.2: The calculated equilibrium total energy per atom (top) and bulk modulus pressure derivative (bottom) of fcc Al by using Murnaghan and Birch-Murnaghan fit. The horizontal dash lines are the experimental data from Grabowski et al. (2007).

Figure B.1 and B.2 show the calculated properties on the dependence of the $\pm dV_{max}$. Obviously, Birch-Murnaghan fit is less dependent on the $\pm dV_{max}$ than Murnaghan fit. The predicted lattice parameter is always larger than the measured one, and the bulk modulus is always smaller than the measured one. Because in this study, PBE is used as the exchange-correlation functional and this is a general feature of PBE (see Section 3.1.2). In order to make the prediction close to the measured data, the $\pm dV_{max}$ should be as small as possible. However, the $\pm dV_{max}$ dependence of the predicted bulk modulus pressure derivative indicates that very small $\pm dV_{max}$ makes it deviated from the measurement.
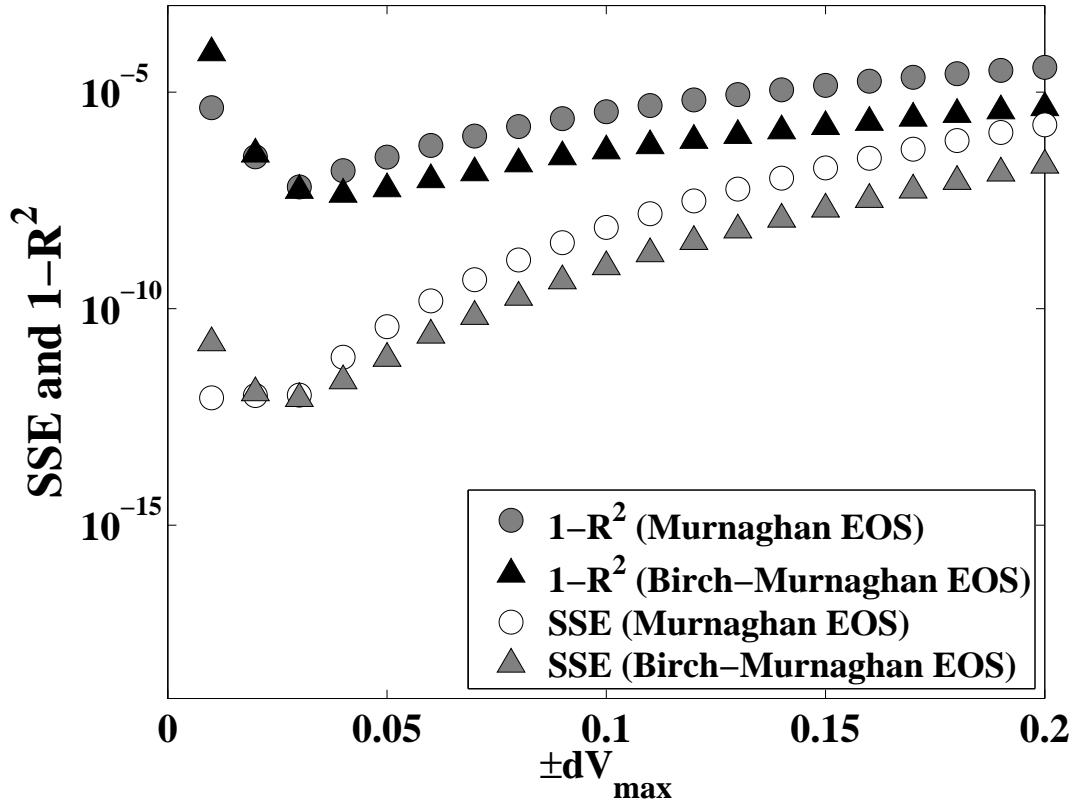
Figure B.3: SSE and $1 - R^2$ of Murnaghan fit and Birch-Murnaghan fit on the dependence of $\pm dV_{max}$ of fcc Al.

The GOF is shown in Figure B.3. As aforementioned, 0 for both SSE and $1 - R^2$ indicates perfect fit. In that sense, Birch-Murnaghan fit is better fitted than Murnaghan fit above $\pm dV_{max}$=3% of V_0, below that Murnaghan fit is better. Figure B.3 also indicates that 3% of V_0 Figure B.3 should be an optimal $\pm dV_{max}$. However, when $\pm dV_{max}$ is very small, the total energy difference between the data points is also very small, especially when the materials is soft. If the energy difference is comparable with the precision of the calculation, it is nearly impossible to make any meaningful curve fitting. Therefore, $\pm dV_{max}$=3% of V_0 might be optimal particularly for Al. Therefore, it is reasonable to believe that for hard materials, the optimal $\pm dV_{max}$ should be smaller, and it should be larger for soft materials.

Table B.1: The difference of the calculated properties between $\pm dV_{max} = 0.1$ and $\pm dV_{max} = 0.2$ by using Birch-Murnaghan fit.

Element	Structure	Deviation [%] (Y in Equation (B.3))			
		E_0	V_0	B_0	B_0'
Al	fcc	-0.0034	0.0191	-0.5953	-0.9065
Ca	fcc	-0.0018	0.0073	-0.2787	-0.3105
Cu	fcc	0.0004	0.0029	-0.0263	-0.2911
Ir	fcc	-0.0042	0.0157	-0.4357	-0.6849
Li	fcc	-0.0042	-0.0335	-1.4815	6.8171
	bcc	-0.0203	-0.1902	3.0631	48.4126
Mg	fcc	-0.0129	0.1193	-1.3621	-15.1268
	hcp	0.0015	0.0101	0.2351	-1.8054
Sr	fcc	-0.0004	-0.0089	-0.0854	1.3220
Zn	fcc	-0.0080	-0.0112	-0.5629	0.5473
	hcp	0.2164	-0.5342	38.3924	-58.1863

Some selected elements were also tested by using Birch-Murnaghan fit. In Table B.1, it lists the difference of the calculated properties between $\pm dV_{max}=0.1$ and $\pm dV_{max}=0.2$ defined as:

$$\frac{Y_{\pm dV_{max}=0.2} - Y_{\pm dV_{max}=0.1}}{Y_{\pm dV_{max}=0.1}} \times 100\% \tag{B.3}$$

where Y is the property predicted by fitting Birch-Murnaghan fit at the $\pm dV_{max} =10\%$ or 20% of V_0. The equilibrium total energy per atom is the least dependent on $\pm dV_{max}$. The second least one is the equilibrium atomic volume. The difference is within -0.02~0.22% and -0.52~0.12%, respectively. For the bulk modulus, most of the tested cases are within $\pm 3\%$. The disturbing case is the bulk modulus of hcp Zn in which the difference is almost 40%, while for fcc Zn the difference is less than 1%. The bulk modulus of Zn in hcp structure predicted at $\pm dV_{max}=10\%$ is 56.71 GPa, while 78.48 GPa at $\pm dV_{max}=20\%$. The measured one is 78.14 or 80.14 GPa (Garland and Dalven, 1958; Alers and Neighbours, 1958). However, it is doubtful to conclude that $\pm dV_{max}=20\%$ should be used instead of 10% for Zn in hcp structure, because larger $\pm dV_{max}$ leads to artifacts of the fit and the applicability issue of the model as shown in Figure B.1 and B.2. Thus, the more physically justified result is the one at $\pm dV_{max} =10\%$, not 20%, even it is closer to the experiments.

B.3 Test 2

The results of Test 2 are shown in Figure B.4 to Figure B.11.

In general, the scatter becomes larger when the $\pm dV_{max}$ becomes larger and more data points are omitted. The scatter by Birch-Murnaghan fit is less than Murnaghan fit. For the bulk modulus and the bulk modulus pressure derivative, when the $\pm dV_{max}$ range is very small (1% or 2% of V_0), the scatter is comparable with the scattering at very larger $\pm dV_{max}$.

The scatter bars of the calculated properties at certain $\pm dV_{max}$ are listed in Table B.2. The scatter bars of the lattice parameter and equilibrium total energy per atom are relatively smaller than the ones of the bulk modulus and the bulk modulus pressure derivative. Probably because the lattice parameter and the equilibrium total energy per atom are the first order quantities, while the other two are higher order quantities.

Table B.2: The scatter bars of the lattice parameter (a_0), the equilibrium total energy per atom (E_0), the bulk modulus (B_0), and the bulk modulus pressure derivative ($B_0^{'}$) at the $\pm dV_{max}$ =5%, 10%, and 20% by Murnaghan fit and Birch-Murnaghan fit.

Murnaghan fit				
$\pm dV_{max}$	a_0 [Å]	E_0 [meV]	B_0 [GPa]	$B_0^{'}$
0.05	0.000113	1.14E-2	0.0847	0.199
0.1	0.000778	0.147	0.300	0.343
0.2	0.00610	2.26	1.29	0.658
Birch-Murnaghan fit				
$\pm dV_{max}$	a_0 [Å]	E_0 [meV]	B_0 [GPa]	$B_0^{'}$
0.05	4.83E-5	5.23E-3	0.0412	0.0853
0.1	0.000267	5.23E-2	0.102	0.118
0.2	0.00200	0.000781	0.407	0.219

Figure B.12 and Figure B.13 show the standard deviations of the calculated properties at each $\pm dV_{max}$. Figure B.14 and Figure B.15 shows the GOF of the employed EOS models. In general Birch-Murnaghan fit fits better than Murnaghan fit, and the optimal $\pm dV_{max}$ is around 3~5% of V_0.
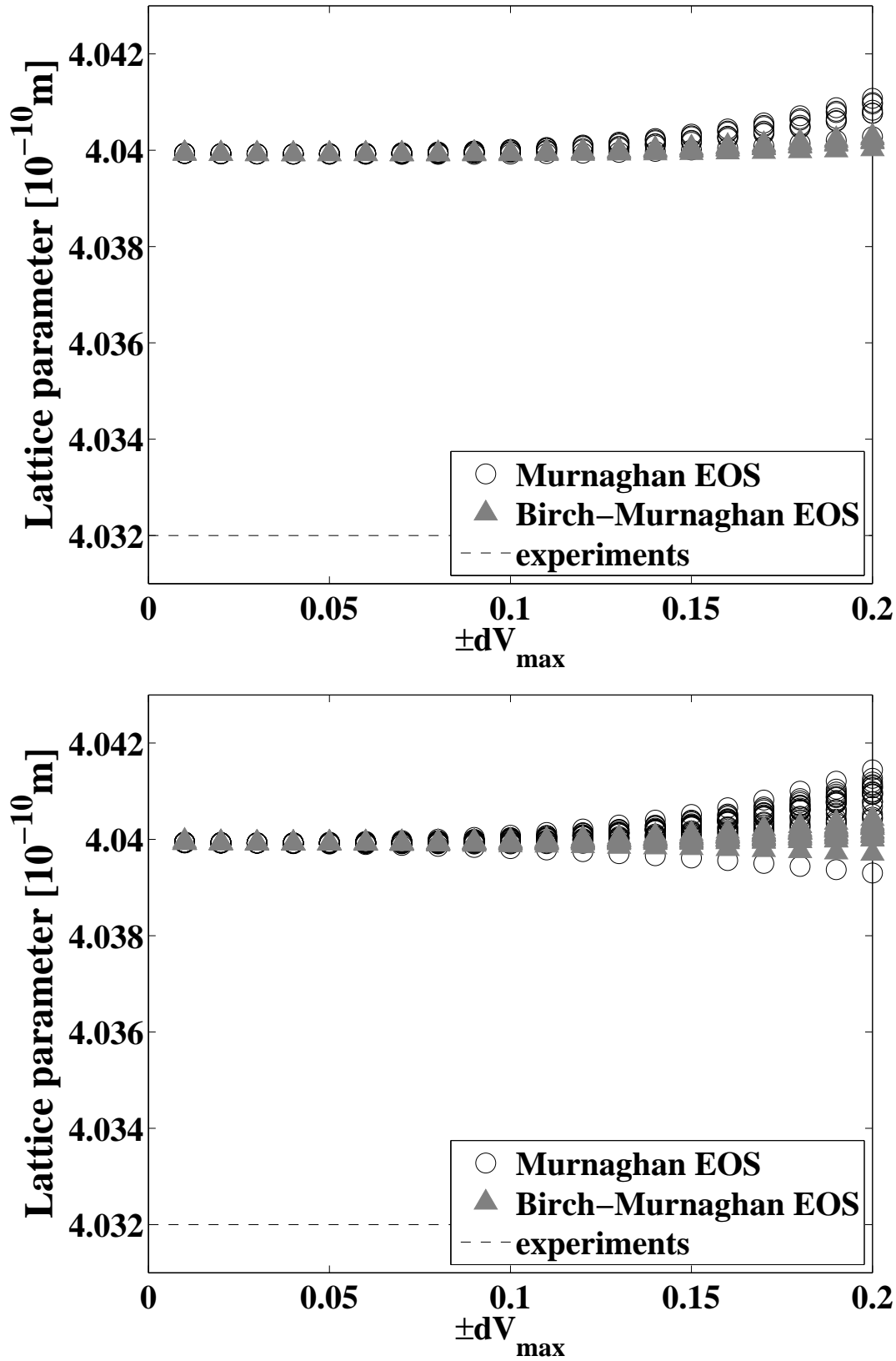
Figure B.4: The lattice parameter of fcc Al when 1 (top) and 2 (bottom) data points are omitted out of 9 data points. The horizontal dash lines are the experimental data from Grabowski et al. (2007).
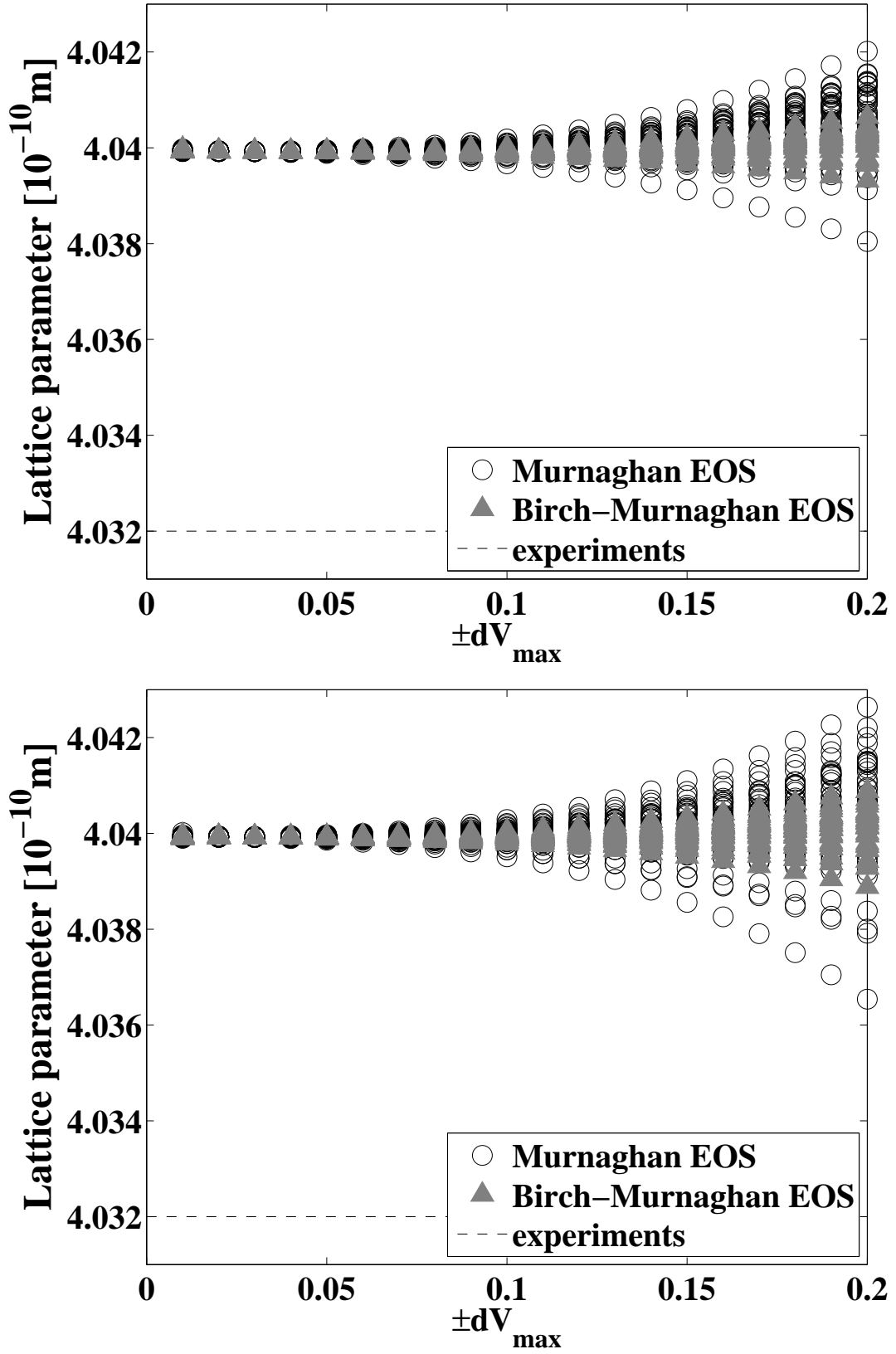
Figure B.5: The lattice parameter of fcc Al when 3 (top) and 4 (bottom) data points are omitted out of 9 data points. The horizontal dash lines are the experimental data from Grabowski et al. (2007).
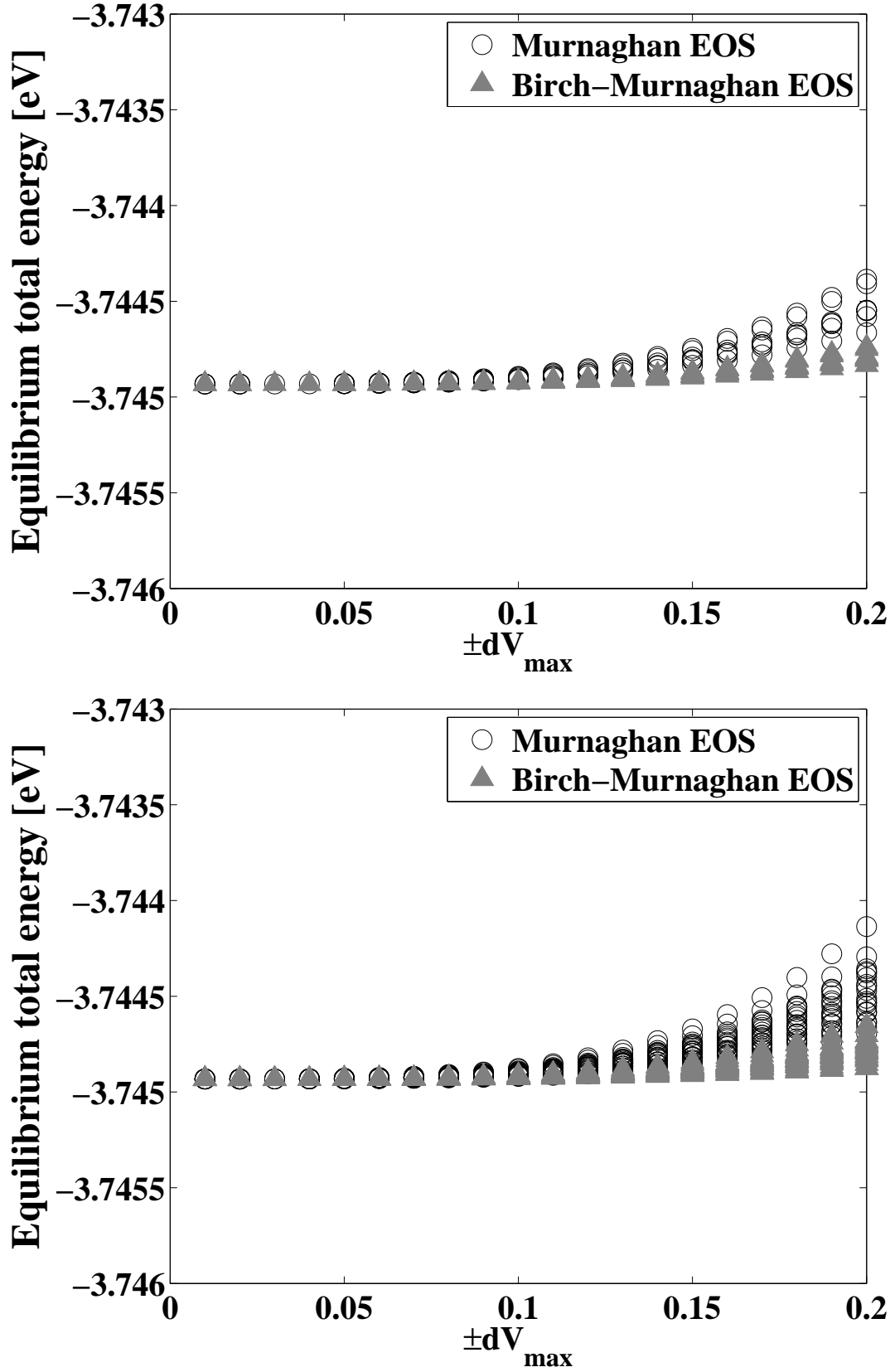
Figure B.6: The equilibrium total energy per atom of fcc Al when 1 (top) and 2 (bottom) data points are omitted out of 9 data points.
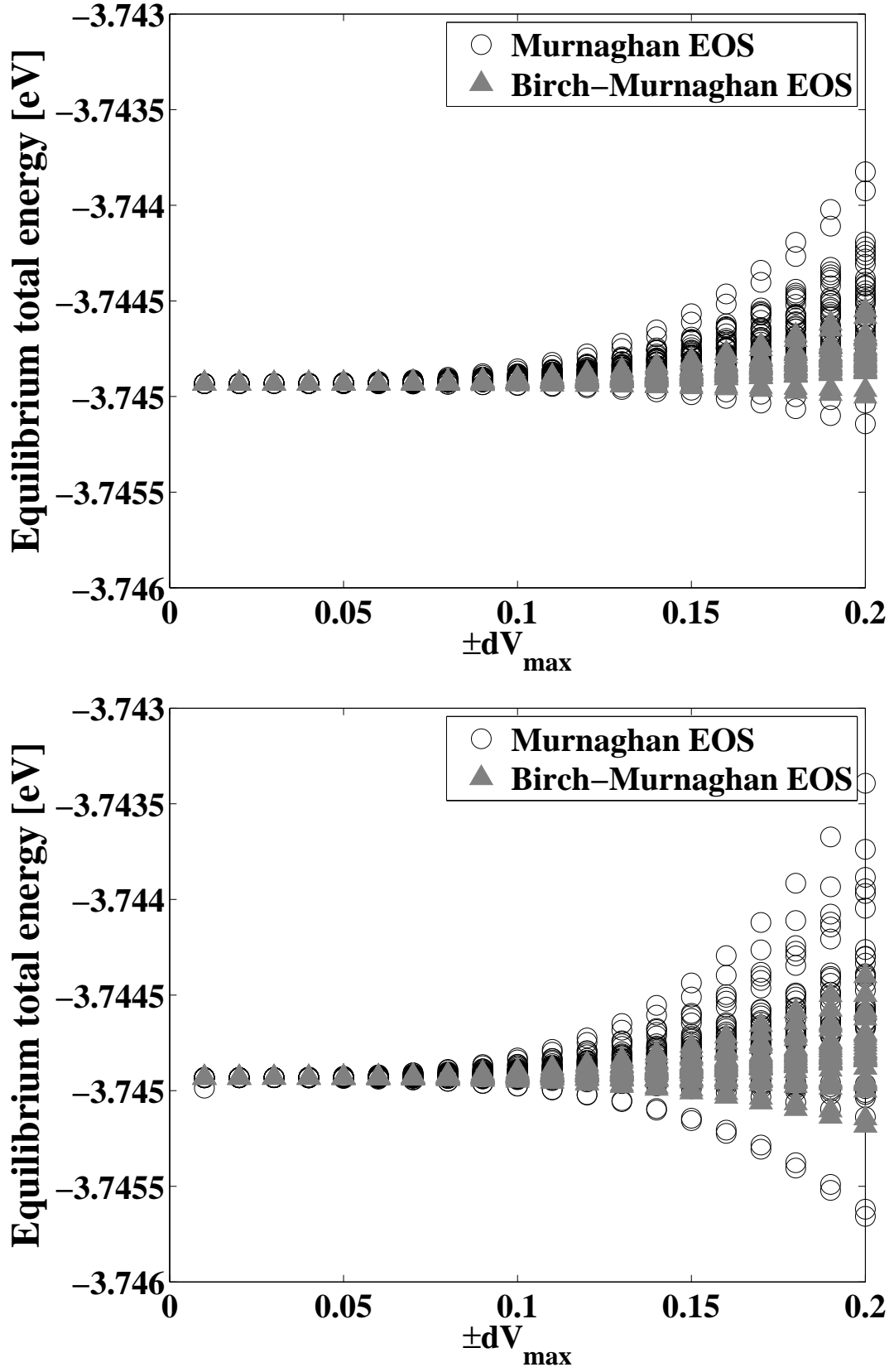
Figure B.7: The equilibrium total energy per atom of fcc Al when 3 (top) and 4 (bottom) data points are omitted out of 9 data points.
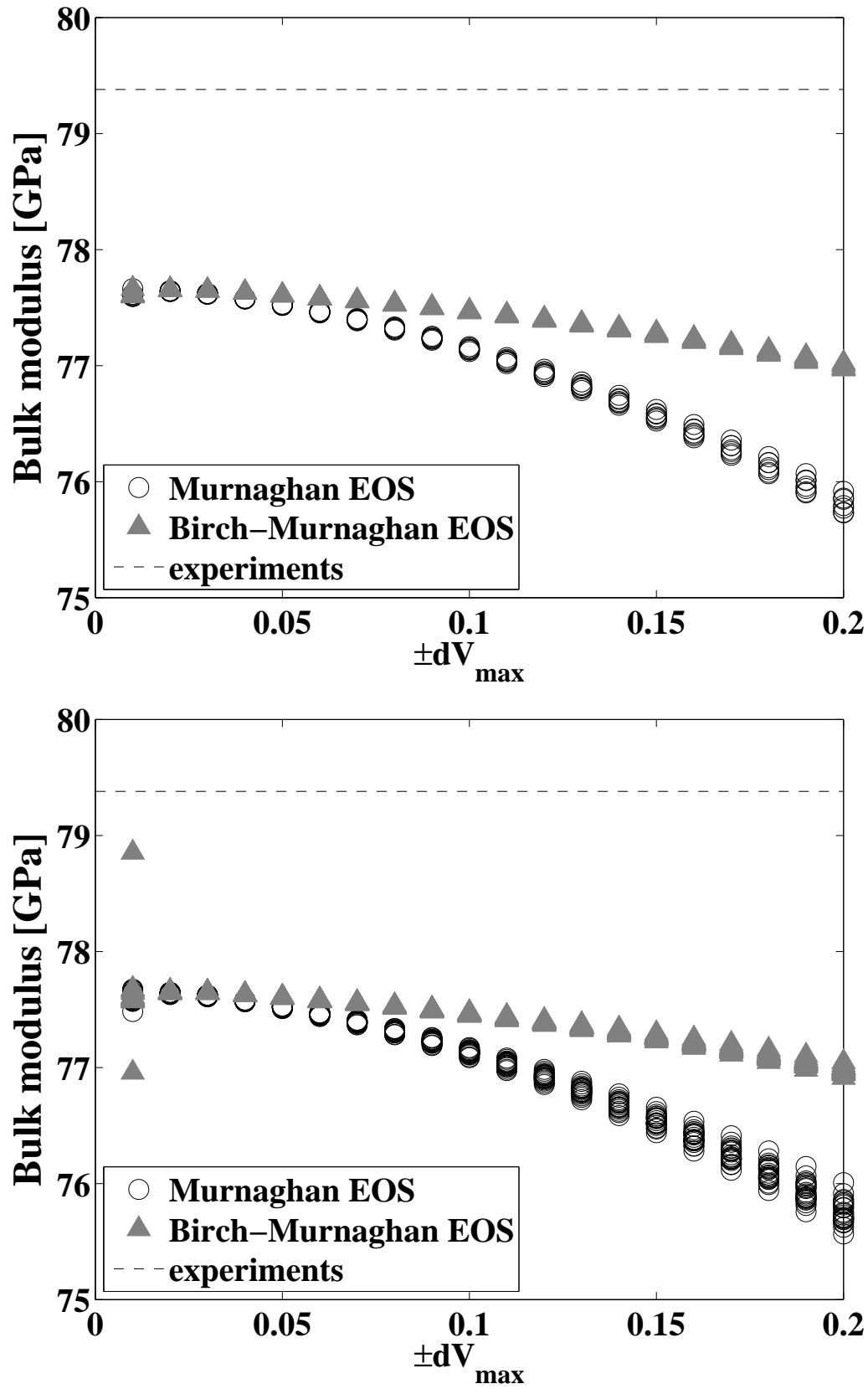
Figure B.8: The bulk modulus of fcc Al when 1 (top) and 2 (bottom) data points are omitted out of 9 data points. The horizontal dash lines are the experimental data from Grabowski et al. (2007).
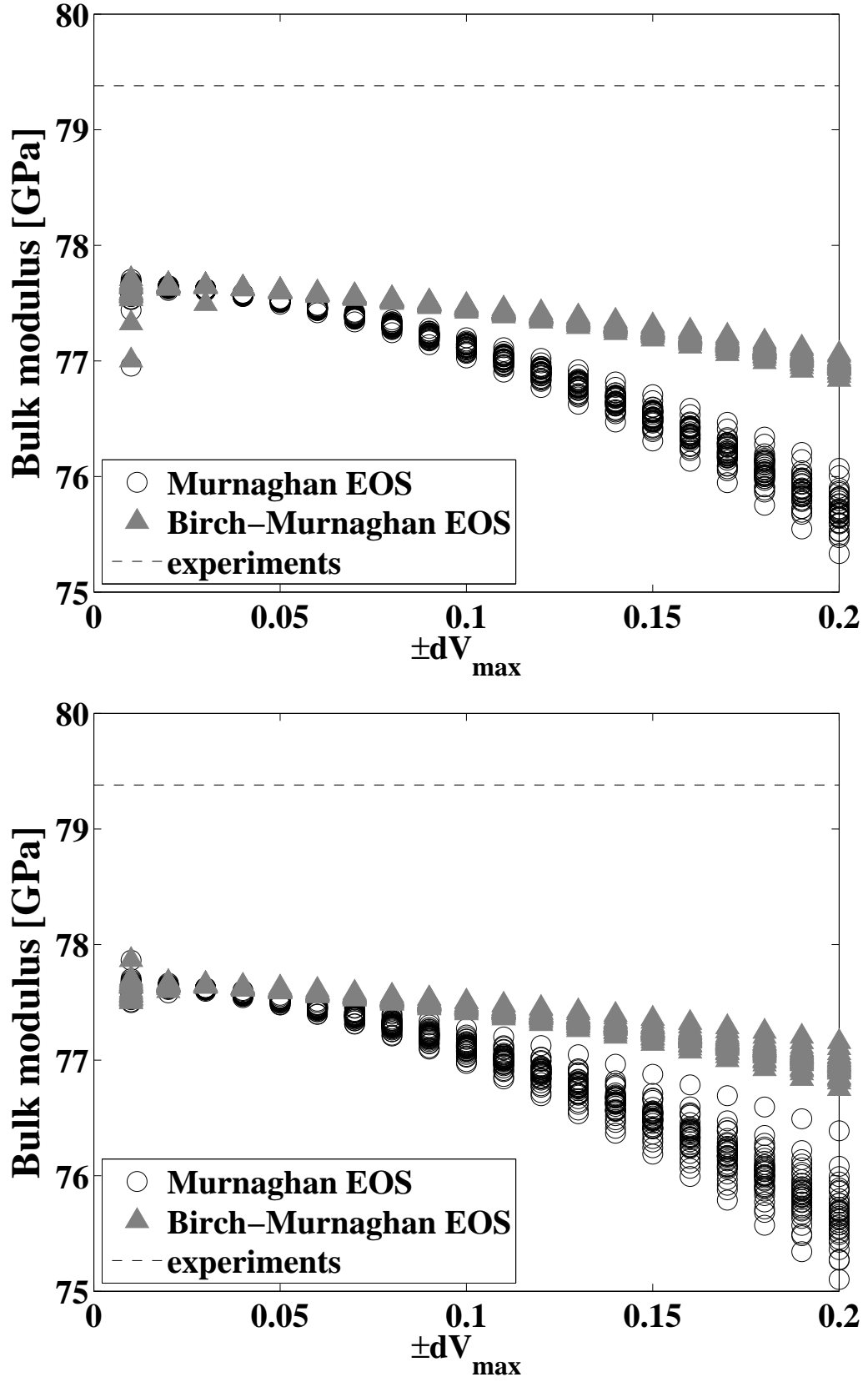
Figure B.9: The bulk modulus of fcc Al when 3 (top) and 4 (bottom) data points are omitted out of 9 data points. The horizontal dash lines are the experimental data from Grabowski et al. (2007).
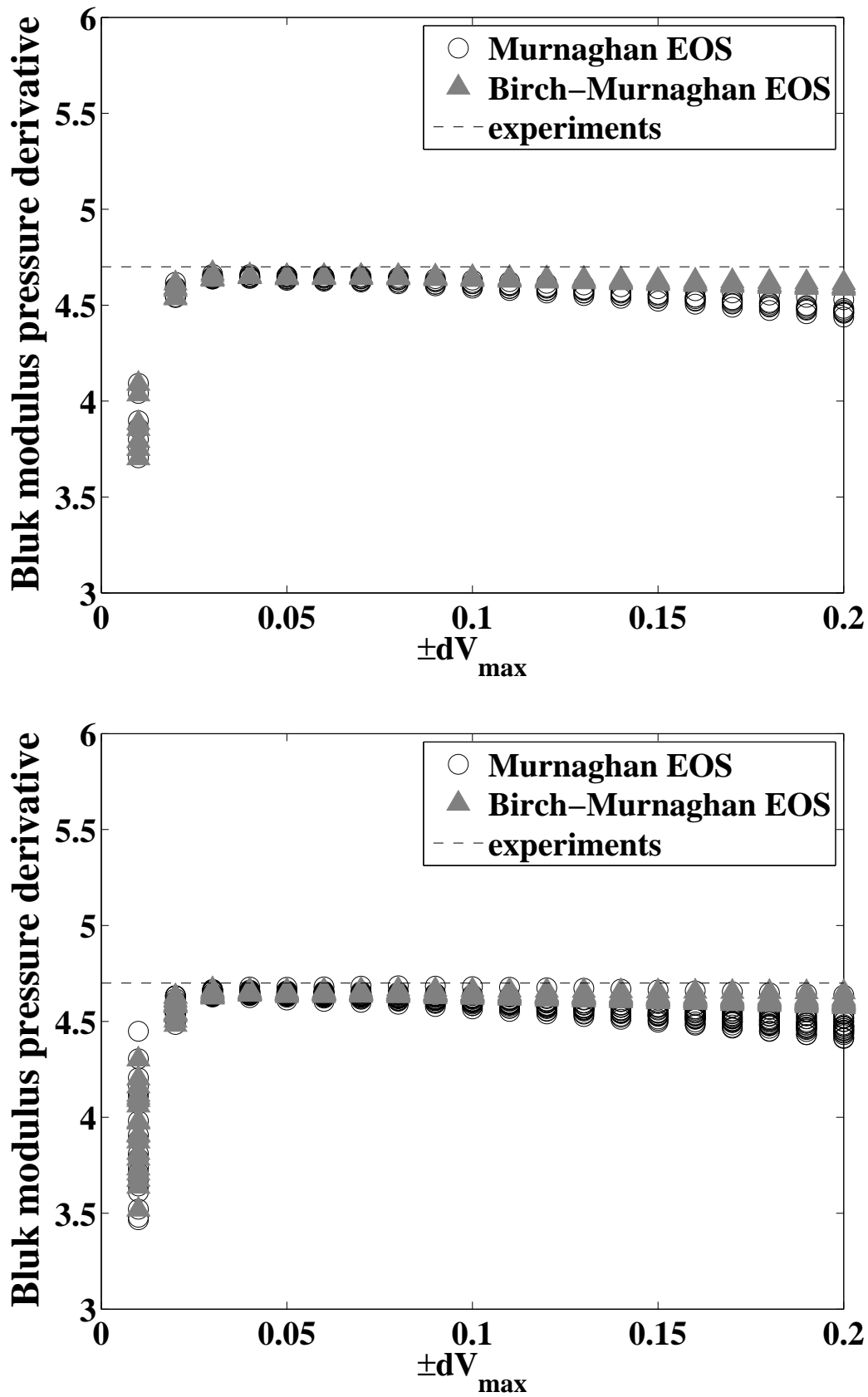
Figure B.10: The bulk modulus pressure derivative of fcc Al when 1 (top) and 2 (bottom) data points are omitted out of 9 data points. The horizontal dash lines are the experimental data from Grabowski et al. (2007).

220
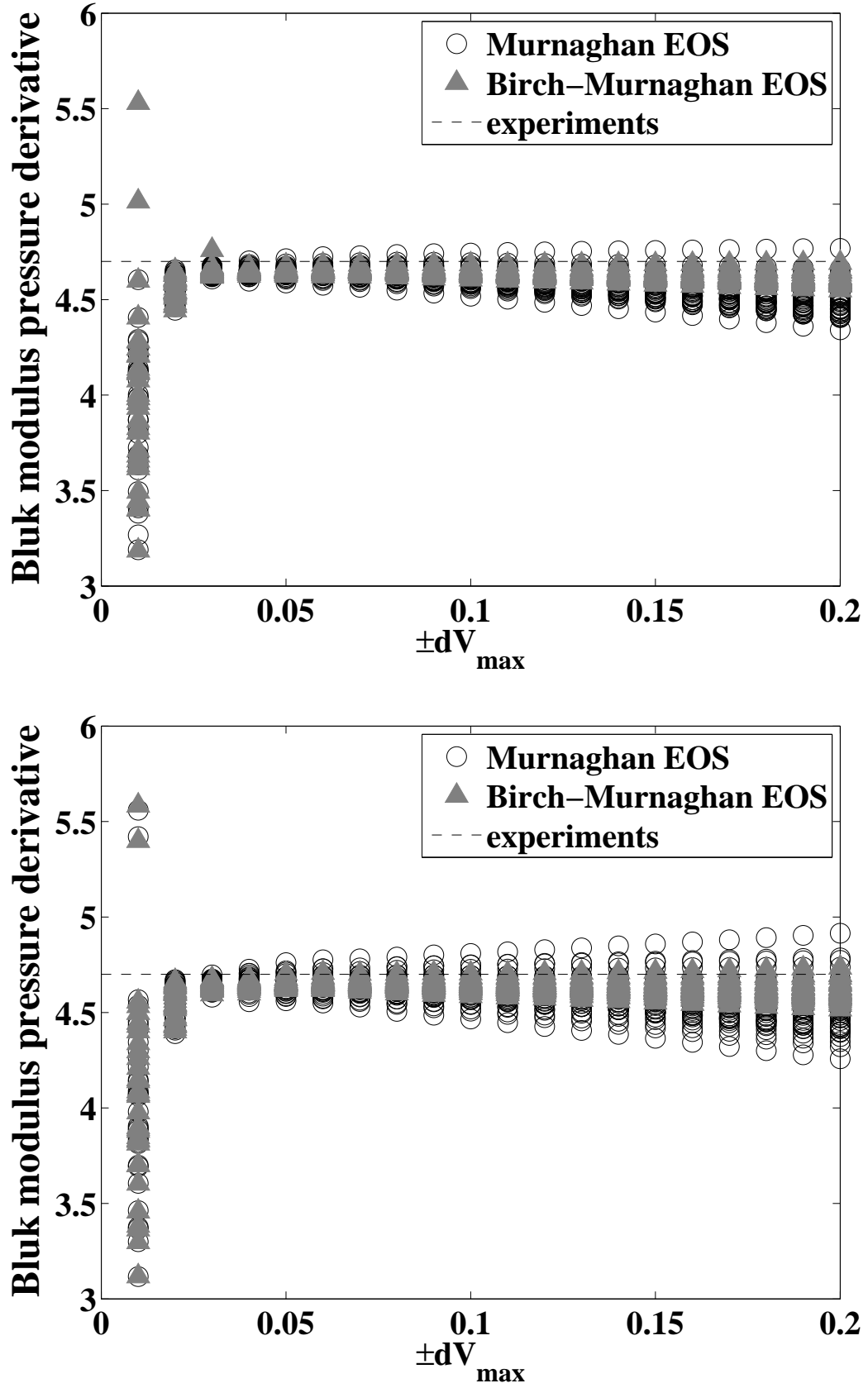
Figure B.11: The bulk modulus pressure derivative of fcc Al when 3 (top) and 4 (bottom) data points are omitted out of 9 data points. The horizontal dash lines are the experimental data from Grabowski et al. (2007).
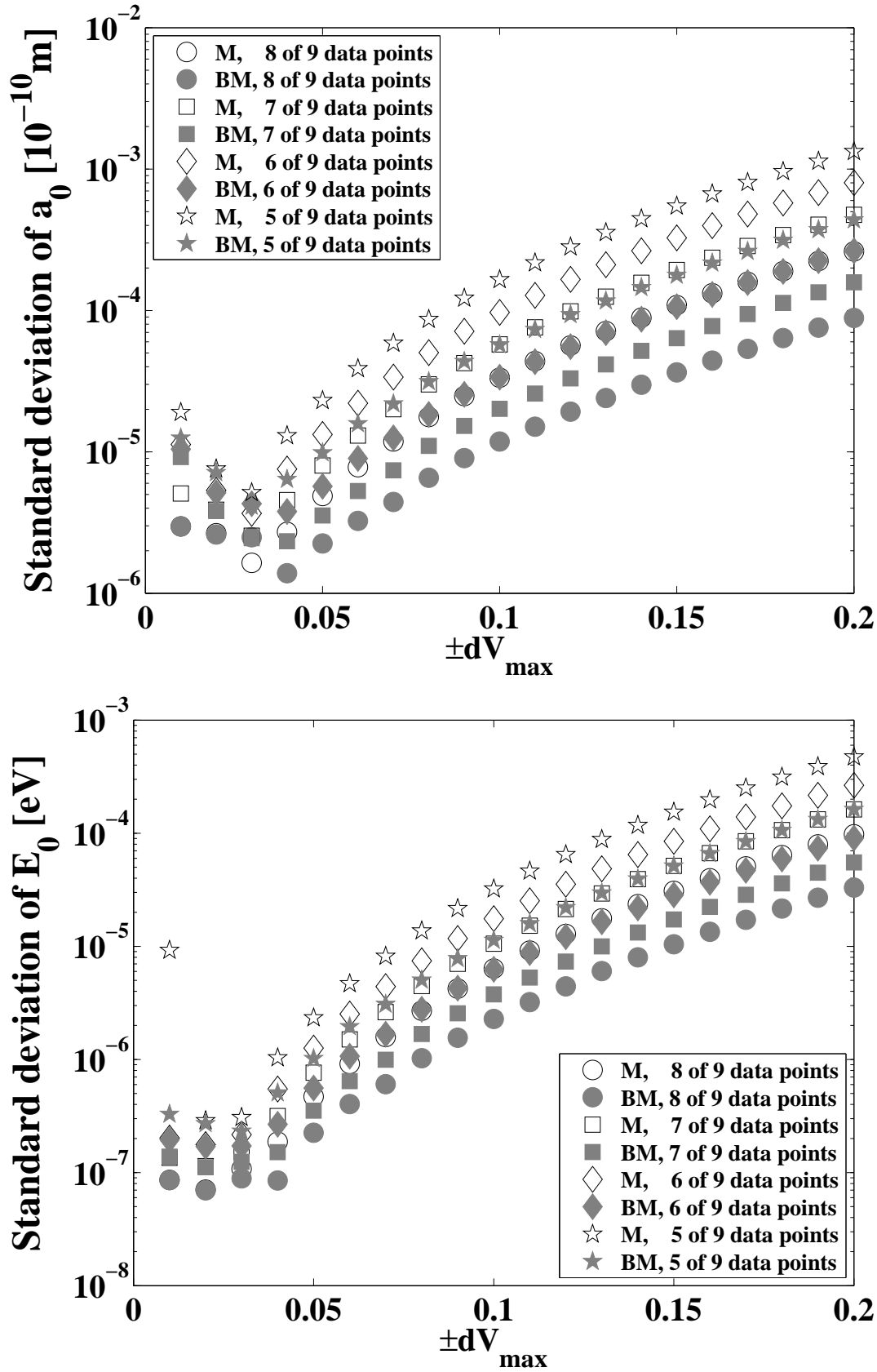
Figure B.12: The standard deviations of scattered the lattice parameter (top) and the equilibrium total energy per atom (bottom) of fcc Al.
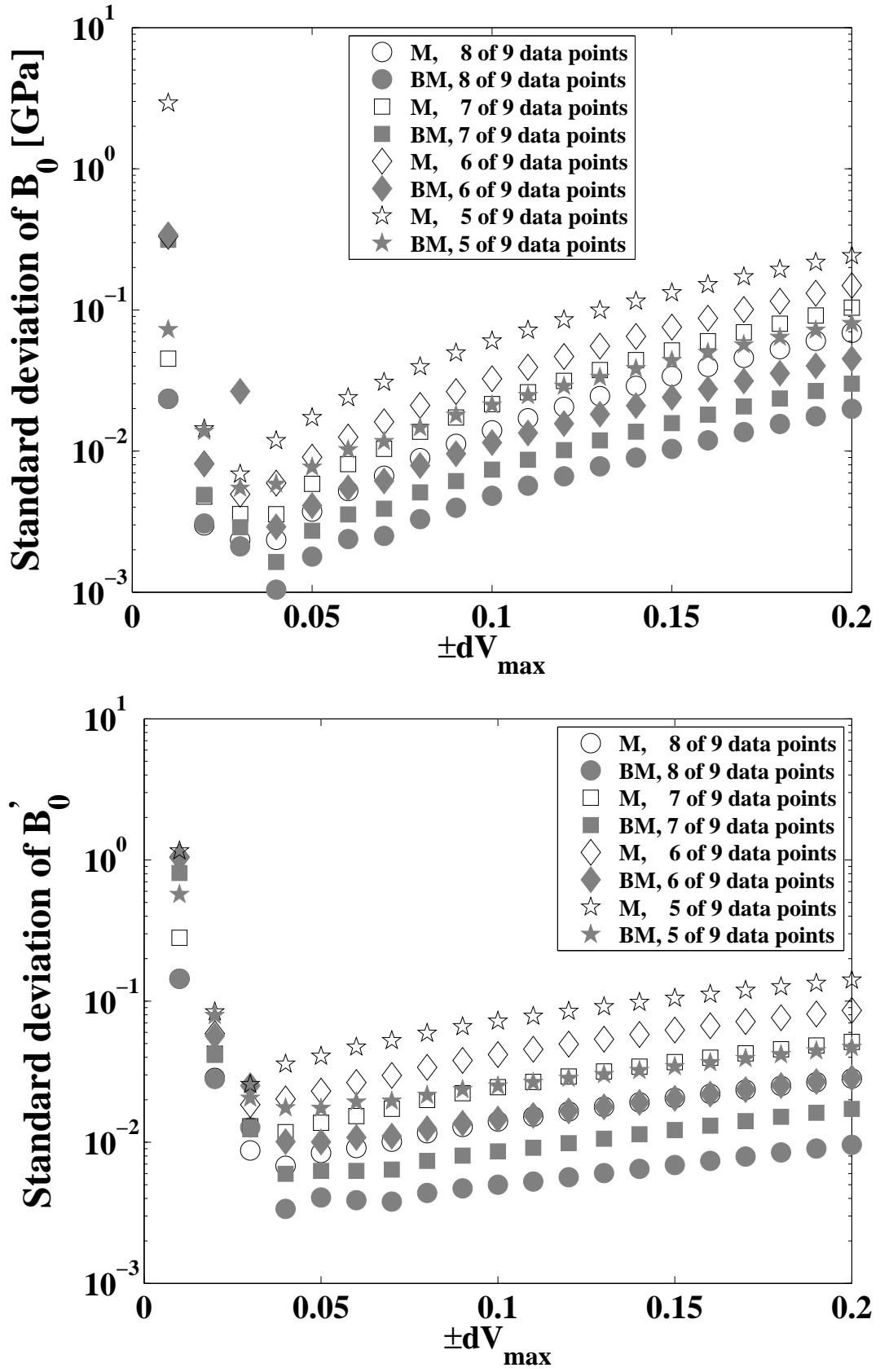
Figure B.13: The standard deviations of scattered the bulk modulus (top) and the bulk modulus pressure derivative (bottom) of fcc Al.
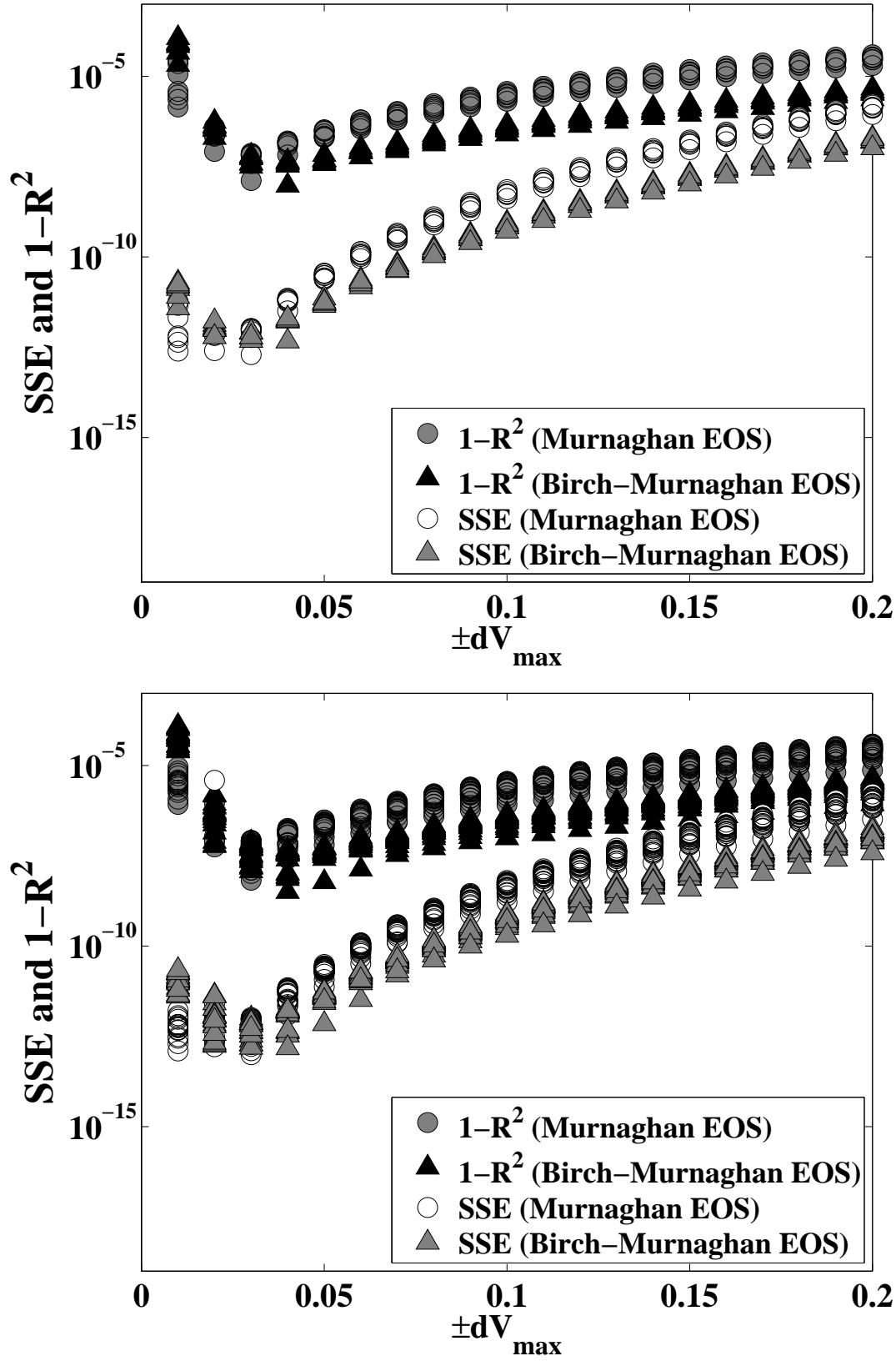
Figure B.14: SSE and $1 - R^2$ of Murnaghan and Birch-Murnaghan fit on the dependence of $\pm dV_{max}$ of fcc Al when 1 (top) and 2 (bottom) data points are omitted.
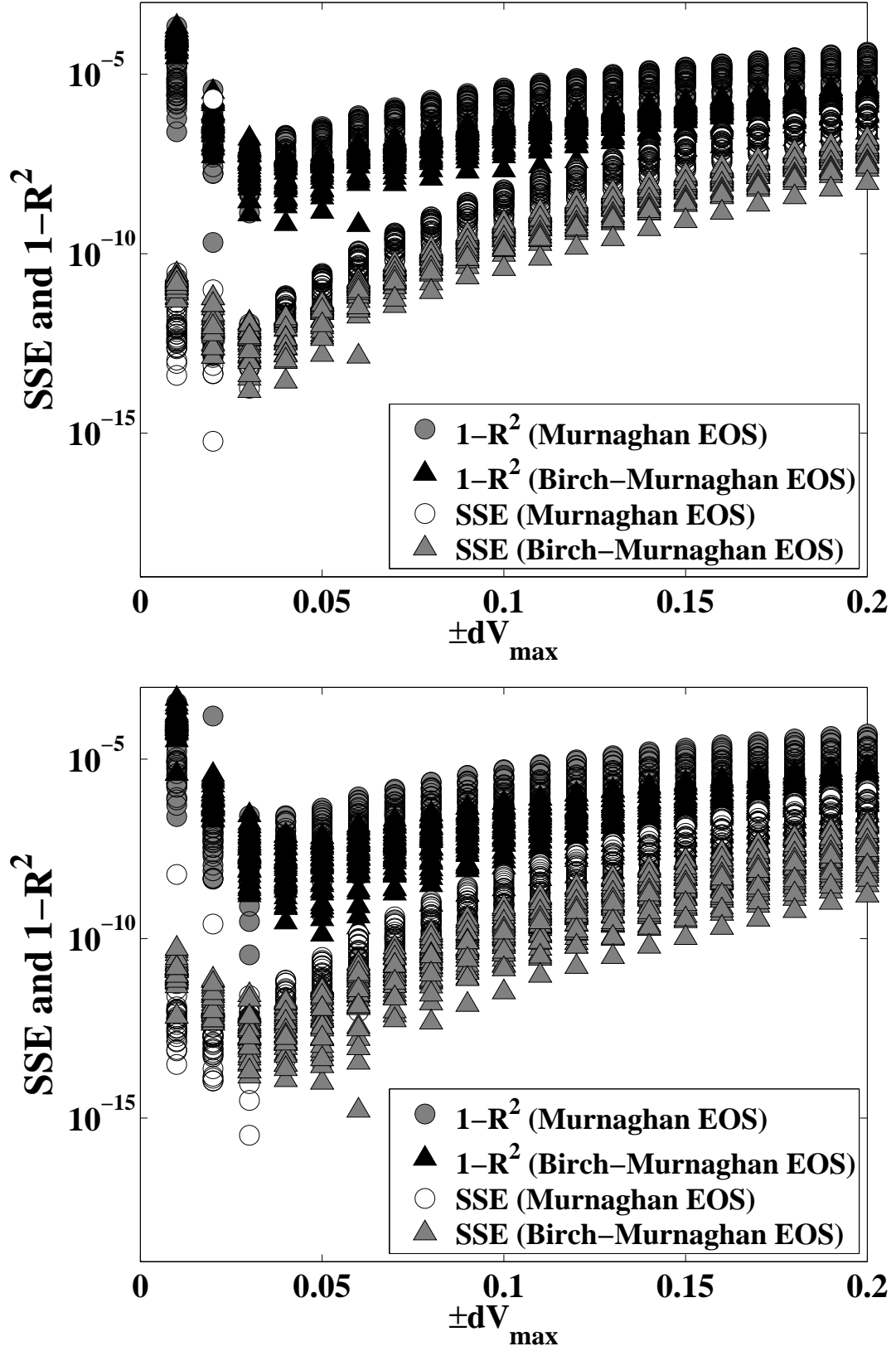
Figure B.15: SSE and $1 - R^2$ of Murnaghan and Birch-Murnaghan fit on the dependence of $\pm dV_{max}$ of fcc Al when 3 (top) and 4 (bottom) data points are omitted.

B.4 Test 3

The energy-volume curve is not an even function, and the energy increases is steeper on the compression side. The original models of Murnaghan or Birch-Murnagan fit are not meant to be used for expansion side, therefore when $\pm dV_{max}$ becomes larger SSE and $1 - R^2$ become larger indicating the fit gets worse (e.g. Figure B.3). 9 cases (Figure B.16) were tested to see the effect when more total energy data points are on the compression or expansion side. Case 1 to 4 have more energy data points on the compression side, while Case 6 to 9 have more on the expansion side. Case 1 and Case 9 are the extreme cases when all data points are on the compression or expansion side, respectively.
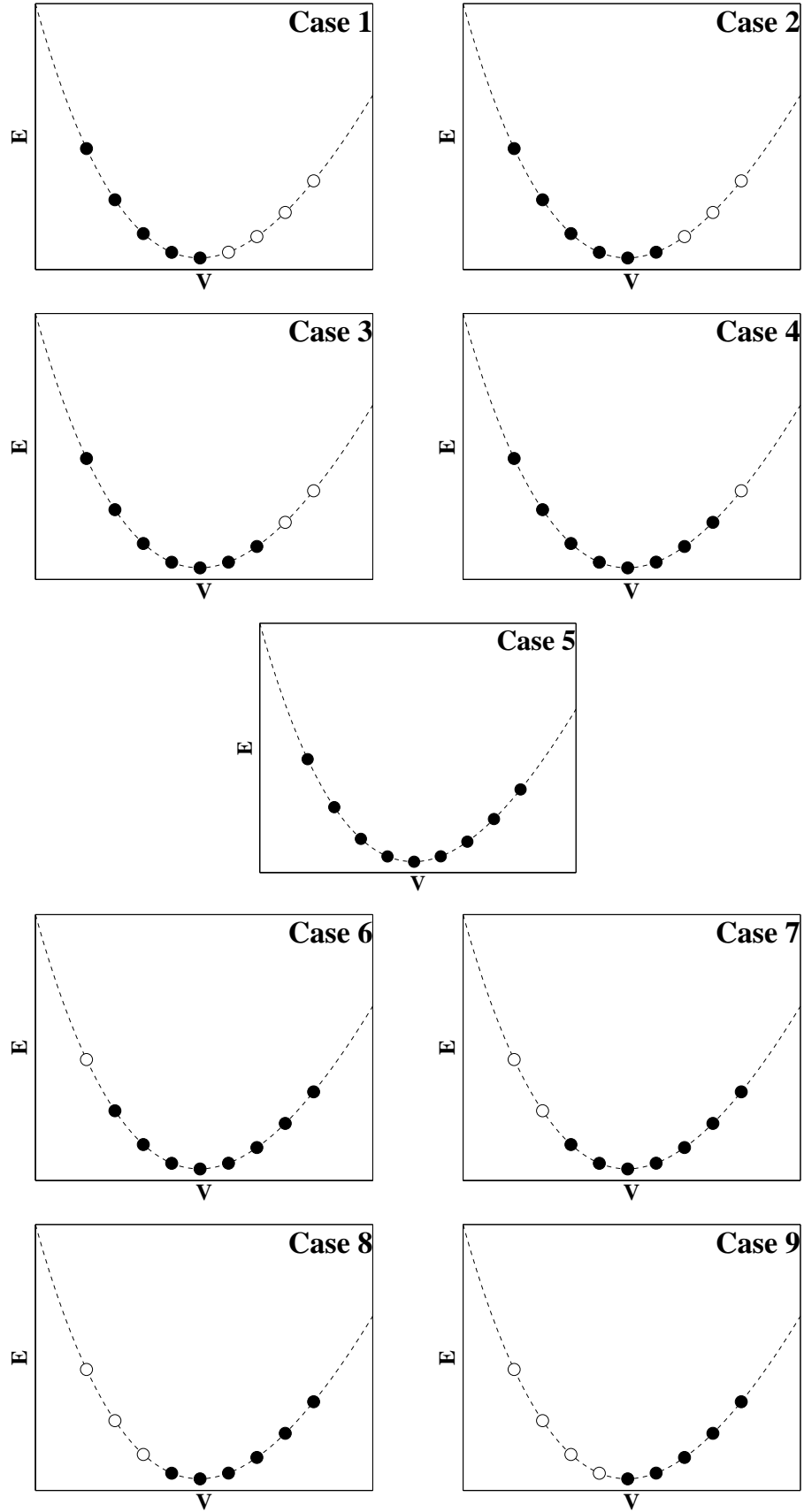
Figure B.16: Schematics of the 9 cases. Solid symbols are the energy data points are used to fit EOS, open symbols are the energy data points omitted.

From Figure B.17 to Figure B.20, it reveals a scattering feature when the $\pm dV_{max}$ becomes larger which is very similar to Figure B.6 to Figure B.10. The scatter of the calculated properties by Birch-Murnagahn fit is less than Murnaghan fit. The effect of more data points on either side can be seen clearer in the bottom of Figure B.17 to Figure B.20. The effect is the same for Murnaghan fit and Birch-Murnaghan fit, and only the magnitude is different.

The GOF is shown in Figure B.21 which reveals again that Birch-Murnaghan fit fits better than Murnaghan fit. More data points on either side make the fit better. But it is not very fair to draw such a general conclusion due to the fact that they were not fitted with the same number of data points.

In Figure B.17 and Figure B.18, the effect on the lattice parameter and the equilibrium total energy is not very large, the largest difference (by Murnaghan fit at $\pm dV_{max}$=20%) is less than 0.002 Åand 0.6 meV. The effect on the bulk modulus and the bulk modulus derivative is not negligible. A general belief is if the energy-volume curve is more extended into the expansion side, the fitted bulk modulus will be lower. But the bulk modulus and the bulk modulus pressure derivative both increases when more data points in the expansion side, and the largest increase is about 4 GPa and 1.2 respectively.
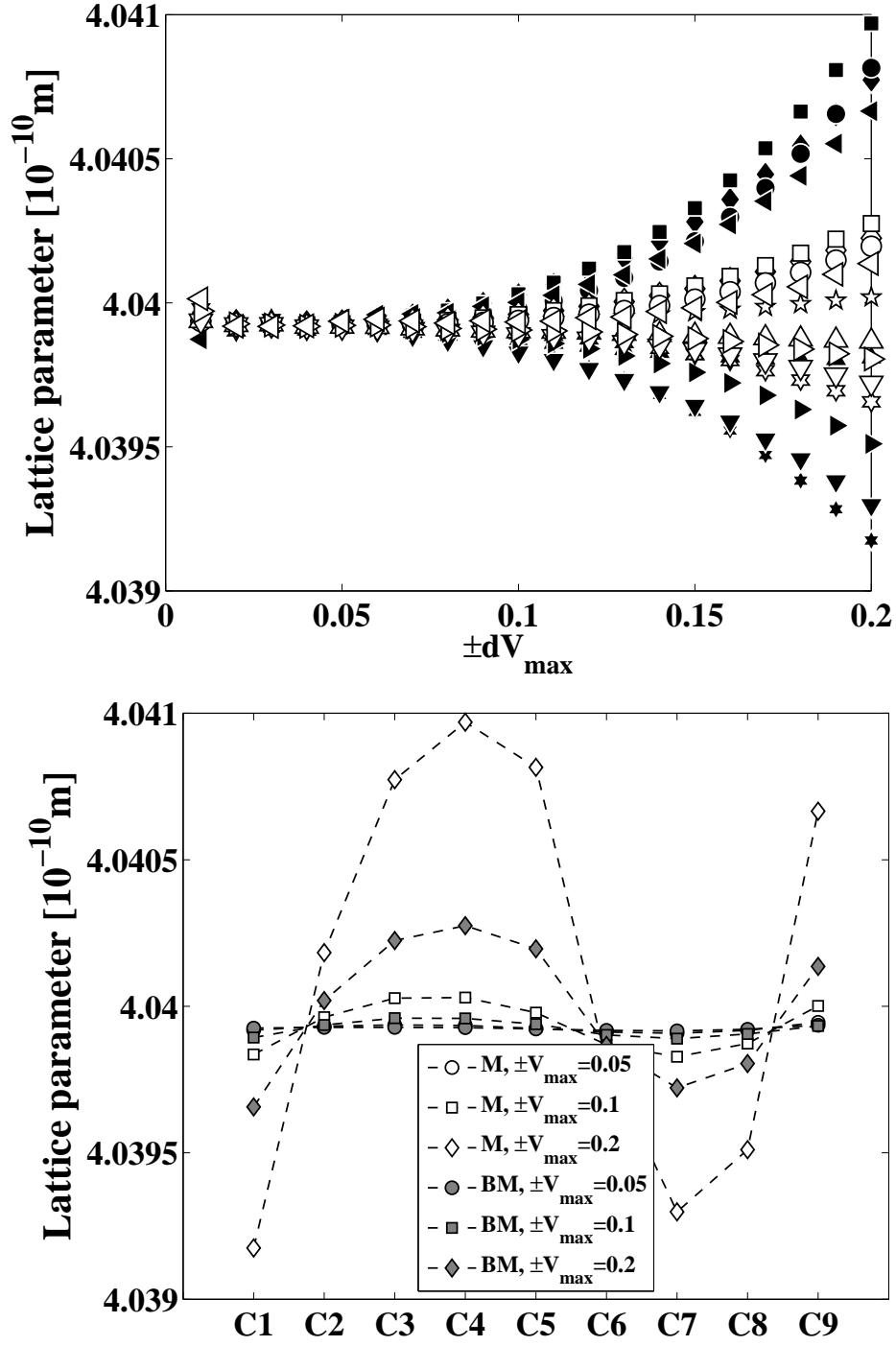
Figure B.17: Top: The calculated lattice parameter of fcc Al by Murnaghan fit (solid symbol) and Birch-Murnaghan (open symbol) fit according to the cases in Figure B.16. Right: The calculated lattice parameters of fcc Al by Murnaghan fit (M, open symbol) and Birch-Murnaghan (BM, solid symbol) fit according to the cases in Figure B.16 at the $\pm dV_{max}$ of 0.05 (circle), 0.1 (square), and 0.2 (diamond). C1 (hexagram), C2 (pentagram), C3 (diamond), C4 (Square), C5 (circle), C6 (upward-pointing triangle), C7 (downward-pointing triangle), C8 (left-pointing triangle), C9 (right-pointing triangle). C*i*, case *i* in Figure B.16.
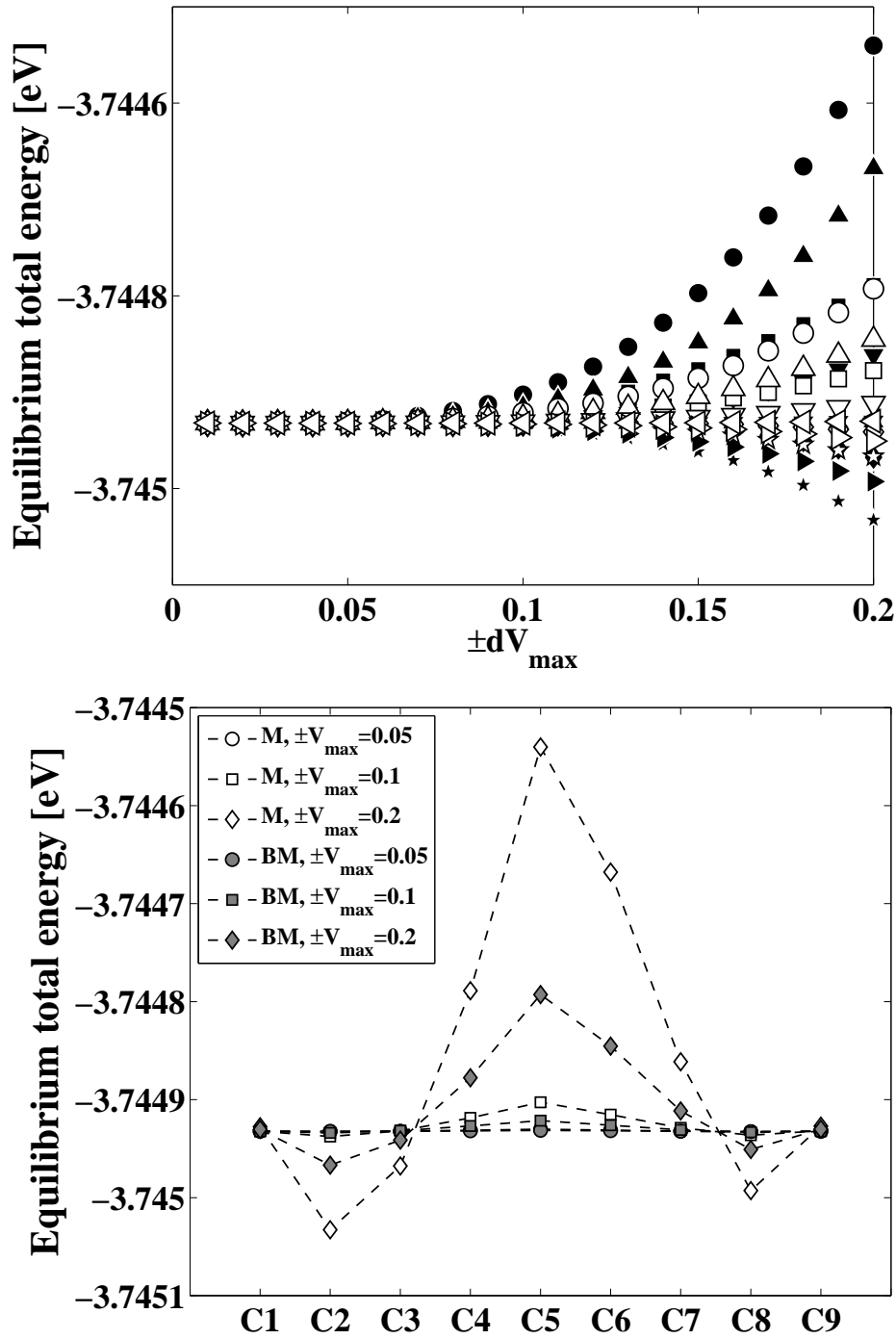
Figure B.18: Top: The calculated equilibrium total energy per atom of fcc Al by Murnaghan fit (solid symbol) and Birch-Murnaghan (open symbol) fit according to the cases in Figure B.16. Bottom: The calculated equilibrium total energy per atom of fcc Al by Murnaghan fit (M, open symbol) and Birch-Murnaghan (BM, solid symbol) fit according to the cases in Figure B.16 at the $\pm dV_{max}$ of 0.05 (circle), 0.1 (square), and 0.2 (diamond). C1 (hexagram), C2 (pentagram), C3 (diamond), C4 (Square), C5 (circle), C6 (upward-pointing triangle), C7 (downward-pointing triangle), C8 (left-pointing triangle), C9 (right-pointing triangle). Ci, Case i in Figure B.16.
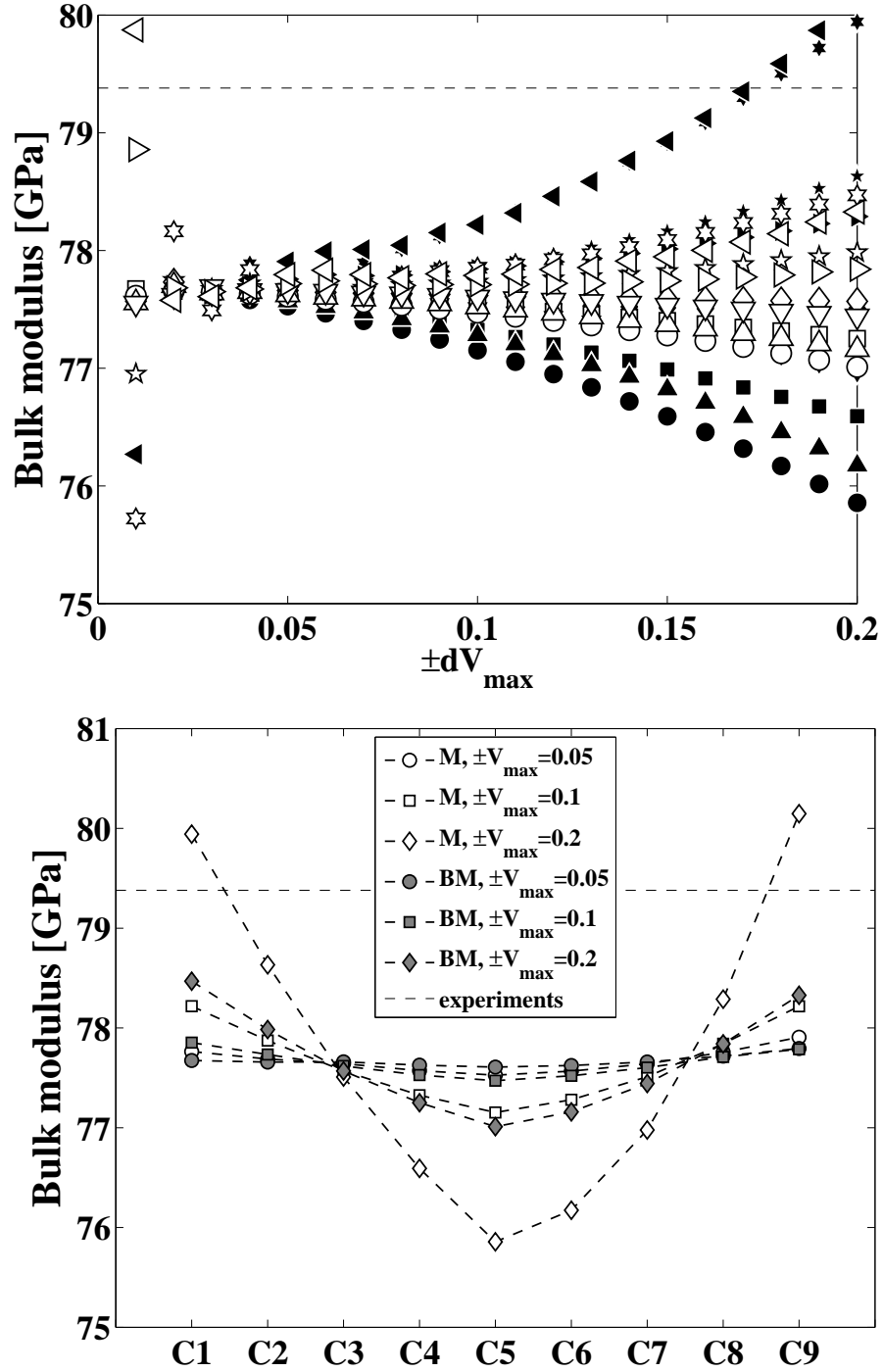
Figure B.19: Top: The calculated bulk modulus of fcc Al by Murnaghan fit (solid symbol) and Birch-Murnaghan (open symbol) fit according to the cases in Figure B.16. Bottom: The calculated bulk modulus of fcc Al by Murnaghan fit (M, open symbol) and Birch-Murnaghan (BM, solid symbol) fit according to the cases in Figure B.16 at the $\pm dV_{max}$ of 0.05 (circle), 0.1 (square), and 0.2 (diamond). C1 (hexagram), C2 (pentagram), C3 (diamond), C4 (Square), C5 (circle), C6 (upward-pointing triangle), C7 (downward-pointing triangle), C8 (left-pointing triangle), C9 (right-pointing triangle). Ci, Case i in Figure B.16. The horizontal dash lines are the experimental data from Grabowski et al. (2007).

Figure B.20: Top: The calculated bulk modulus pressure derivative of fcc Al by Murnaghan fit (solid symbol) and Birch-Murnaghan (open symbol) fit according to the cases in Figure B.16. Bottom: The calculated bulk modulus pressure derivative of fcc Al by Murnaghan fit (M, open symbol) and Birch-Murnaghan (BM, solid symbol) fit according to the cases in Figure B.16 at the $\pm dV_{max}$ of 0.05 (circle), 0.1 (square), and 0.2 (diamond). C1 (hexagram), C2 (pentagram), C3 (diamond), C4 (Square), C5 (circle), C6 (upward-pointing triangle), C7 (downward-pointing triangle), C8 (left-pointing triangle), C9 (right-pointing triangle). Ci, Case i in Figure B.16. The horizontal dash lines are the experimental data from Grabowski et al. (2007).

Figure B.21: SSE and $1 - R^2$ of the fit by Murnaghan (solid symbol) and Birch-Murnaghan (open symbol) fit according to the cases in Figure B.16. C1 (hexagram), C2 (pentagram), C3 (diamond), C4 (square), C5 (circle), C6 (upward-pointing triangle), C7 (downward-pointing triangle), C8 (left-pointing triangle), C9 (right-pointing triangle). Ci, Case i in Figure B.16.

B.5 Summary of numerical tests of Equation of State

According to the tests, the questions proposed at the beginning (see Section B.1) still cannot be answered explicitly. There are only some general conclusions: (1) the Birch-Murnaghan fit is not very sensitive to proposed scenarios (see Section B.1); (2) there is an optimal $\pm dV_{max}$, e.g $\sim 3\%$ for fcc Al. This optimal $\pm dV_{max}$, however, might not be shared by studied Al binary solid solutions. As stated in Section B.2, the optimal $\pm dV_{max}$ should be small for the matter with the high bulk modulus, and large for the low bulk modulus. In order to be equal-footing, $\pm dV_{max}=10\%$ of V_0 was used for all the studied Al binary solid solutions, where V_0 is the equilibrium atomic volume of studied Al binary solid solutions from a preliminary calculation.

Appendix C

Calculating elastic constants from energy-strain curves

C.1 Purpose and procedures

C.1.1 Purpose of tests

In first-principles, a series of strains are applied to the supercell, and the corresponding total energies are calculated. The energy-strain curve is fitted by a polynomial function. The fitted coefficients are certain combinations of the elastic constants (see Section 3.3). Three technical questions of using such a method should be answered:

1. which order polynomial function should be used to fit the energy-strain curve? 2nd order or higher?

2. how much strain should be applied?

3. how many data points are sufficient?

C.1.2 Test procedures

The above questions were investigated in the following ways:

Test 1 The energy-strain curves were calculated by using known elastic constants. The applied strains are equally spaced. The curves were fitted by 2nd, 3rd and 4th order polynomial functions, in order to see whether the fitting parameters are consistent with the input known elastic constants.

Test 2 The energy-strain curves of selected pure fcc metals were calculated by using DFT, and fitted by 2nd, 3rd and 4th order polynomial functions.

Test 3 The energy-strain curves of studied Al solid solutions were calculated by using DFT, and fitted by 2nd and 4th order polynomial functions.

C.2   Test 1

The energy-strain curves were calculated using Equation (3.50), (3.51), (3.52), and (3.53) by inputting the known elastic constants of Al and Cu listed in Table C.1.

Table C.1: Known elastic constants [GPa] of Al and Cu (Wang and Li, 2009).

	C_{11}		C_{12}		C_{44}	
Al	108		62		28.3	
Cu	169		122		75.3	

	C_{111}	C_{112}	C_{123}	C_{144}	C_{155}	C_{456}
Al	-1427	-408	32	-85	-396	-42
Cu	-2000	-1220	-500	-132	-705	25

	C_{1111}	C_{1112}	C_{1122}	C_{1123}	C_{1144}	C_{1155}	C_{1255}	C_{1266}	C_{1456}	C_{4444}	C_{4455}
Al	3900	2173	2471	-146	-146	2173	-146	2471	-146	2471	-146
Cu	7449	4233	4756	-262	-262	4233	-262	4756	-262	4756	-262

The energy-strain curves are shown in Figure C.1 and Figure C.2. Up to the strain of 0.06, the most of the elastic energy comes from the second order effect. Upon the tetragonal shear, the elastic energy becomes asymmetric when the higher order effect is included. The asymmetry is more pronounced in Cu than Al. Upon the trigonal shear, the symmetry of the energy-strain is not affected even the higher order effect are taken into account. The asymmetry or symmetry comes from the nature of the deformation mode. The positive strain in the tetragonal shear is tension and negative is compression. While in the case trigonal shear, due the cubic symmetry, the positive and the negative strain are essentially the same.
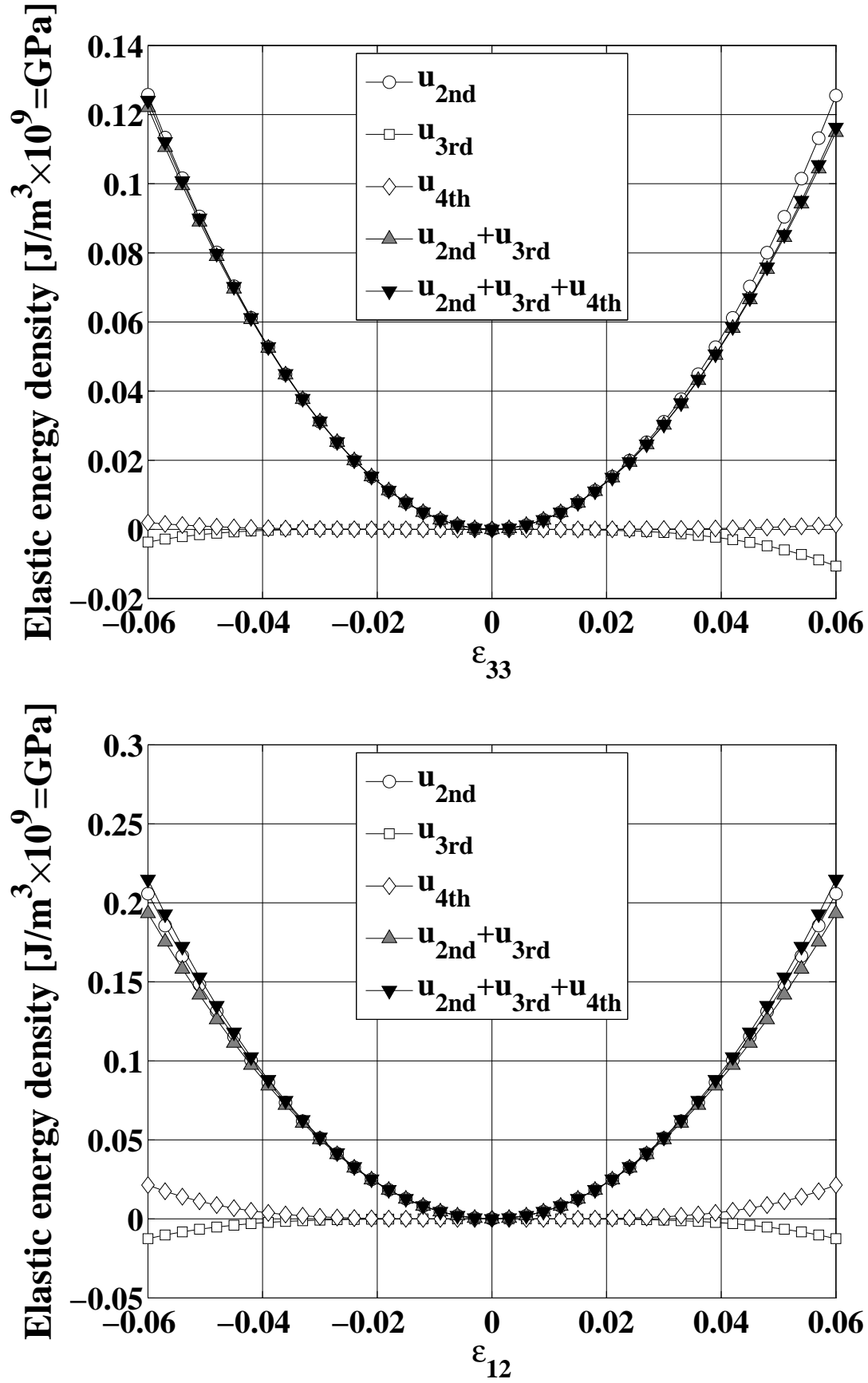
Figure C.1: Energy-strain curves of Al upon tetragonal (top) and trigonal (bottom) shear calculated by using known elastic constants.
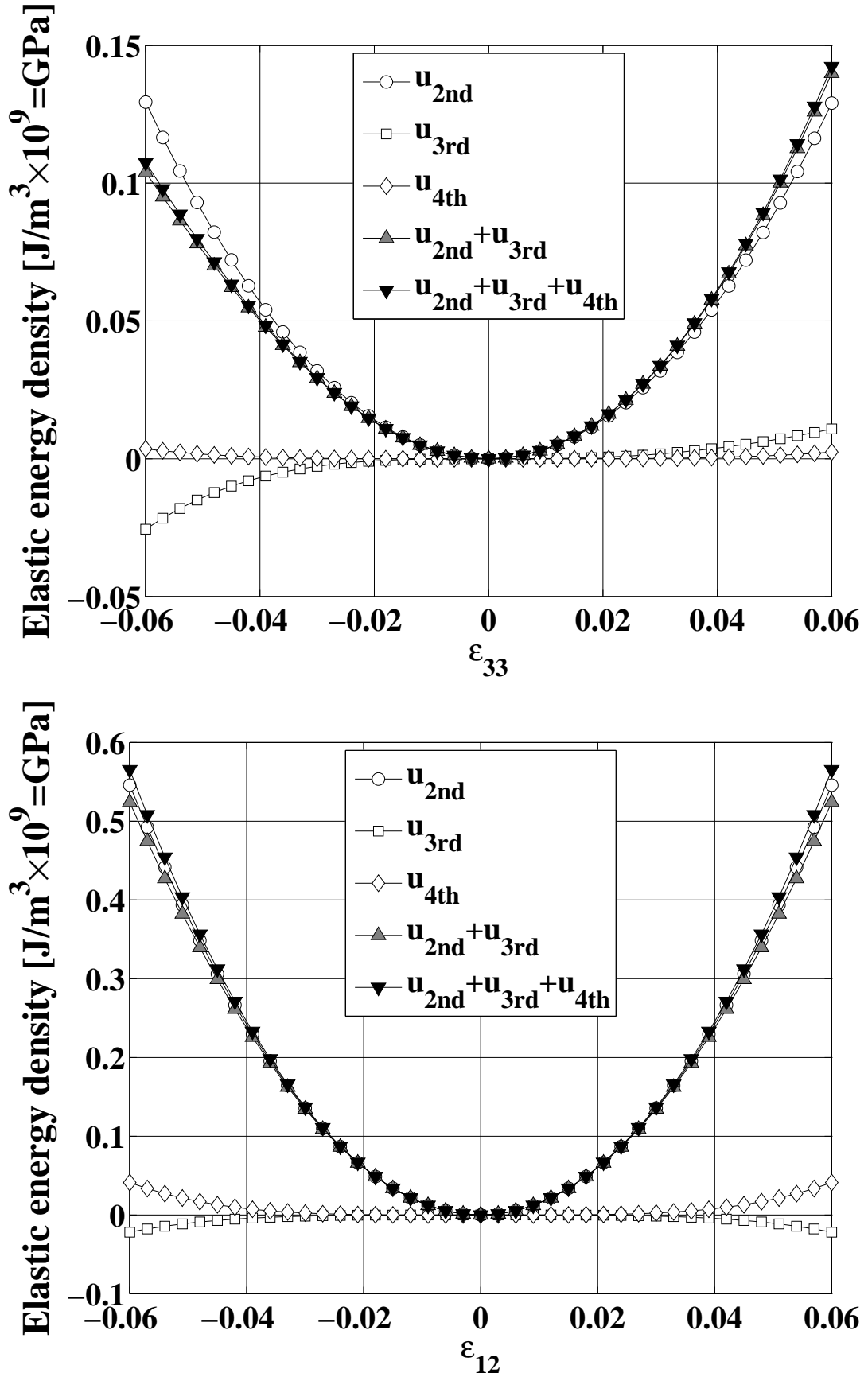
Figure C.2: Energy-strain curves of Cu upon tetragonal (top) and trigonal (bottom) shear calculated by using known elastic constants.
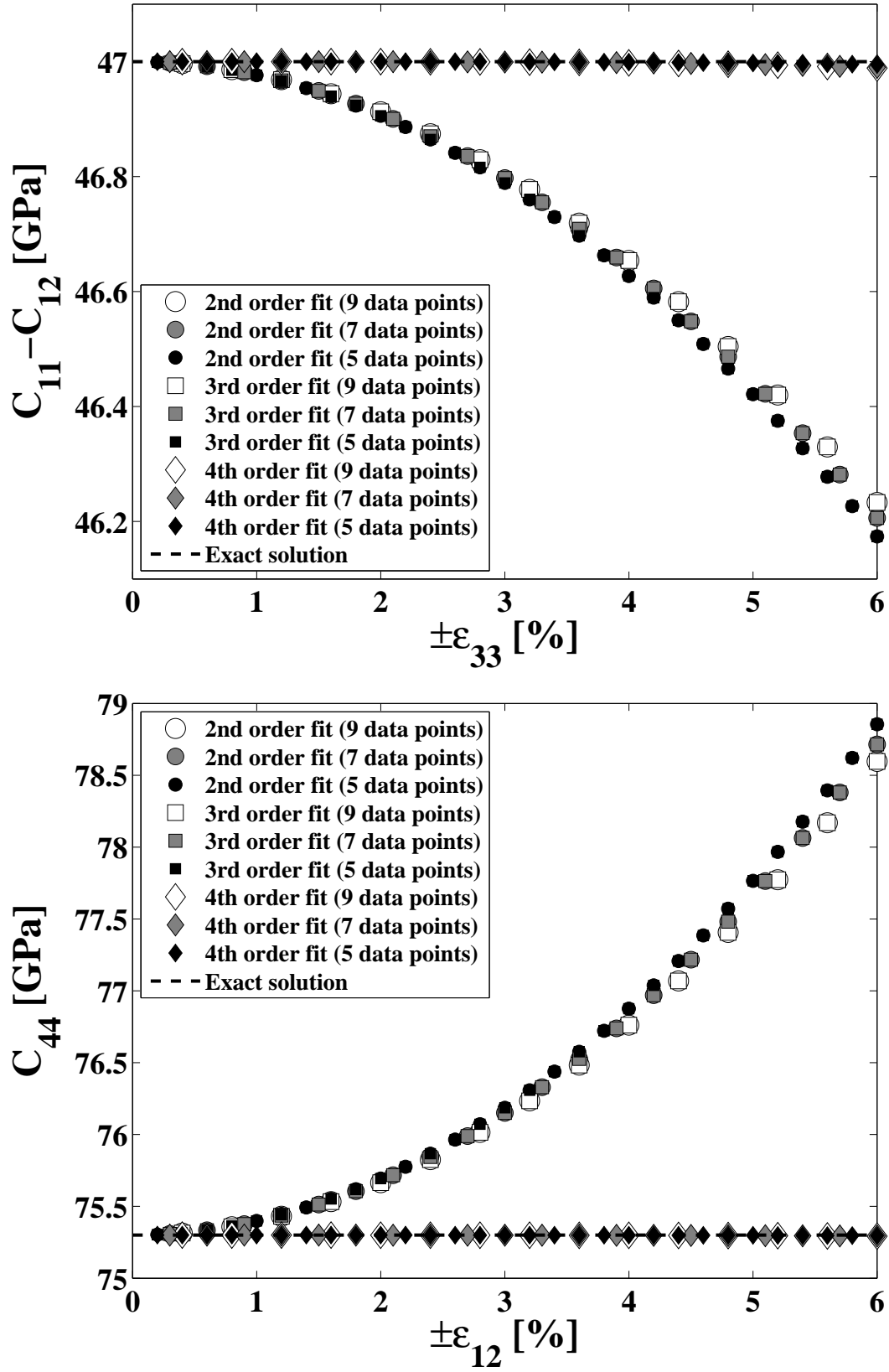
Figure C.3: $C_{11} - C_{12}$ (top) and C_{44} (bottom) of Cu calculated by fit the energy-strain curves ($u_{2nd} + u_{3rd} + u_{4th}$ in Figure C.1) using 2nd ($\bigcirc$), 3rd ($\square$), and 4th ($\diamond$) order polynomial with 5 (white), 7 (gray), and 9 (black) data points.
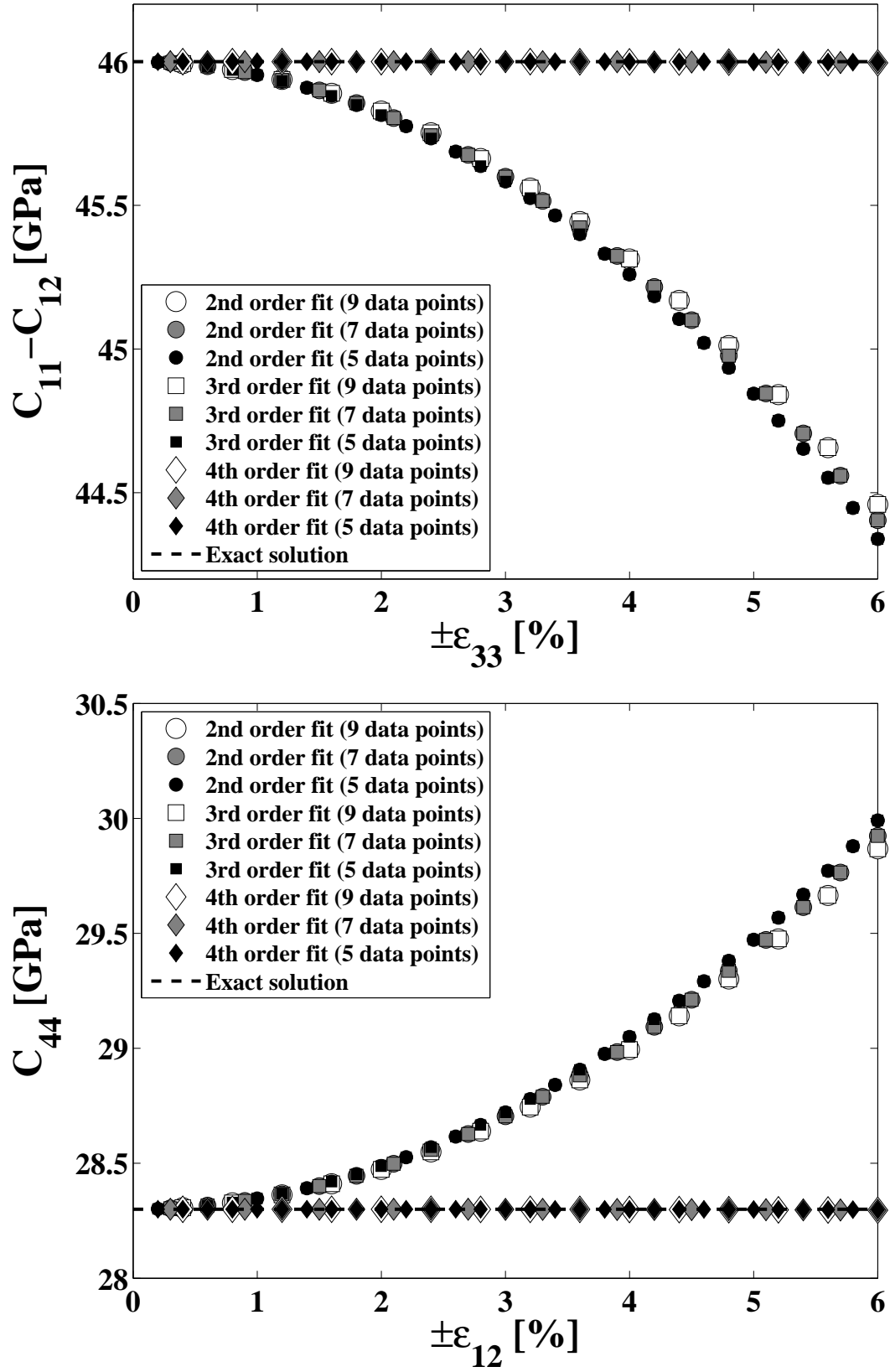
Figure C.4: $C_{11} - C_{12}$ (top) and C_{44} (bottom) of Al calculated by fit the energy-strain curves ($u_{2nd} + u_{3rd} + u_{4th}$ in Figure C.2) using 2nd ($\bigcirc$), 3rd ($\square$), and 4th ($\diamond$) order polynomial with 5 (white), 7 (gray), and 9 (black) data points.

The energy-strain curves are fitted by 2nd, 3rd and 4th order polynomial functions and the resulting elastic constants are shown in Figure C.3 and Figure C.4. And they are compared with the exact solution. The 3rd order fit does not bring any difference from the 2nd order fit. For trigonal shear, analytically, the 3rd order coefficient is zero. For tetragonal shear, the 3rd order coefficient is not zero but in the order of magnitude of 10^2. Within the strain range, the contribution from the 3rd order term is roughly 1/10 of the 2nd order term. Therefore, if the 3rd order coefficient is much larger than the 2nd one, the 3rd order fit may bring some difference in the fitting results. The number of the data points also does not have any significant effect on the calculated elastic constants. The 4th order fit gives the exact solution at any strain range which is expected. The 2nd and 3rd order fit give the exact solution when the strain range is extremely small. When the strain range becomes larger the results deviate from the exact solution. In case of $C_{11} - C_{12}$, the results decrease away from the exact solution, and in case of C_{44}, it increases.

C.3   Test 2

C.3.1   Test 2: fcc Cu, Ir and Li

Figure C.5 shows the calculated elastic constants of Cu on the dependence of the applied strain. For $C_{11} - C_{12}$ of Cu, the applied strain dependence is inconsistent with the observation in the previous section (Figure C.3 and Figure C.4). When the applied strain range is small ($2\sim3\%$), the results are scattered in the range of $6\sim8$ GPa ($\sim14\%$ of the measured value). At larger strain, the calculated $C_{11} - C_{12}$ tends to converge and close to the experimental value.

Figure C.6 shows the calculated elastic constants of Ir on the dependence of the applied strain. The scatter at the small applied strain range is less pronounced than Cu. The magnitude of the scatter at small strain range is related to the elastic stiffness of the studied substance. In the case of Ir, the elastic modulus is very high. Even at small applied strain range, the elastic energy could be much higher than the precision of DFT. Most of the scattered results at the small applied strain range are from the 4th order fit. The GOF of the 4th order fit is always better than 2nd or 3rd. But the 4th order fit also fits some unreasonable local minima or maxima, in which case the unreasonable or unphysical trend is included in the fitting. On the other hand, 2nd or 3rd keeps the general trend of the energy-strain curves.

Figure C.7 shows that the applied strain dependence of the calculated elastic constants of Li is similar to Figure C.3 and Figure C.4. Again, the 4th order fit gives a large scatter at small applied strains.
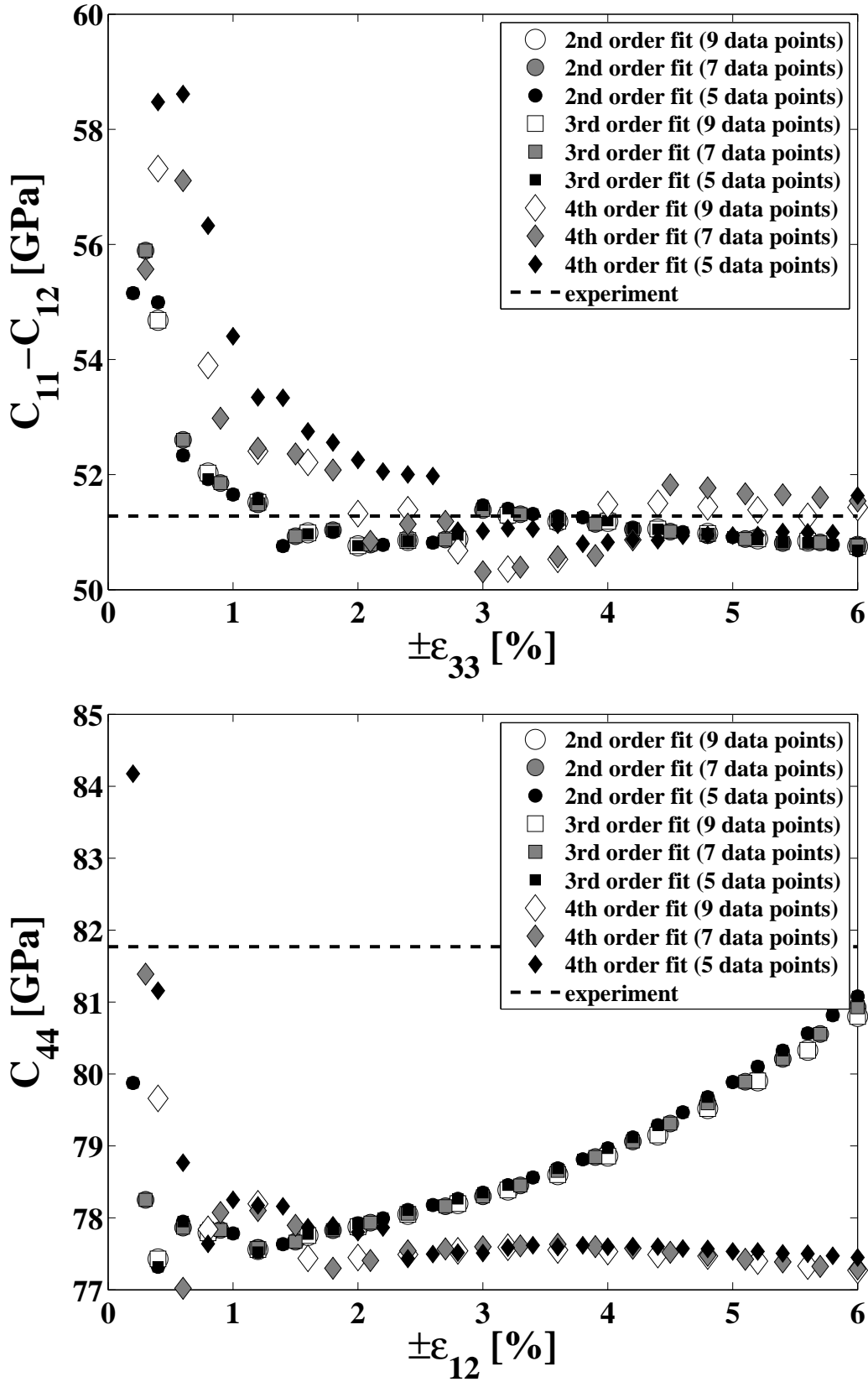
Figure C.5: $C_{11} - C_{12}$ (top) and C_{44} (bottom) of fcc Cu calculated by fitting the energy-strain curves DFT using 2nd (circle), 3rd (square), and 4th (diamond) order polynomial with 5 (white), 7 (gray), and 9 (black) data points. The horizontal dash lines are the experimental values close to 0 K (Overton and Gaffney, 1955).
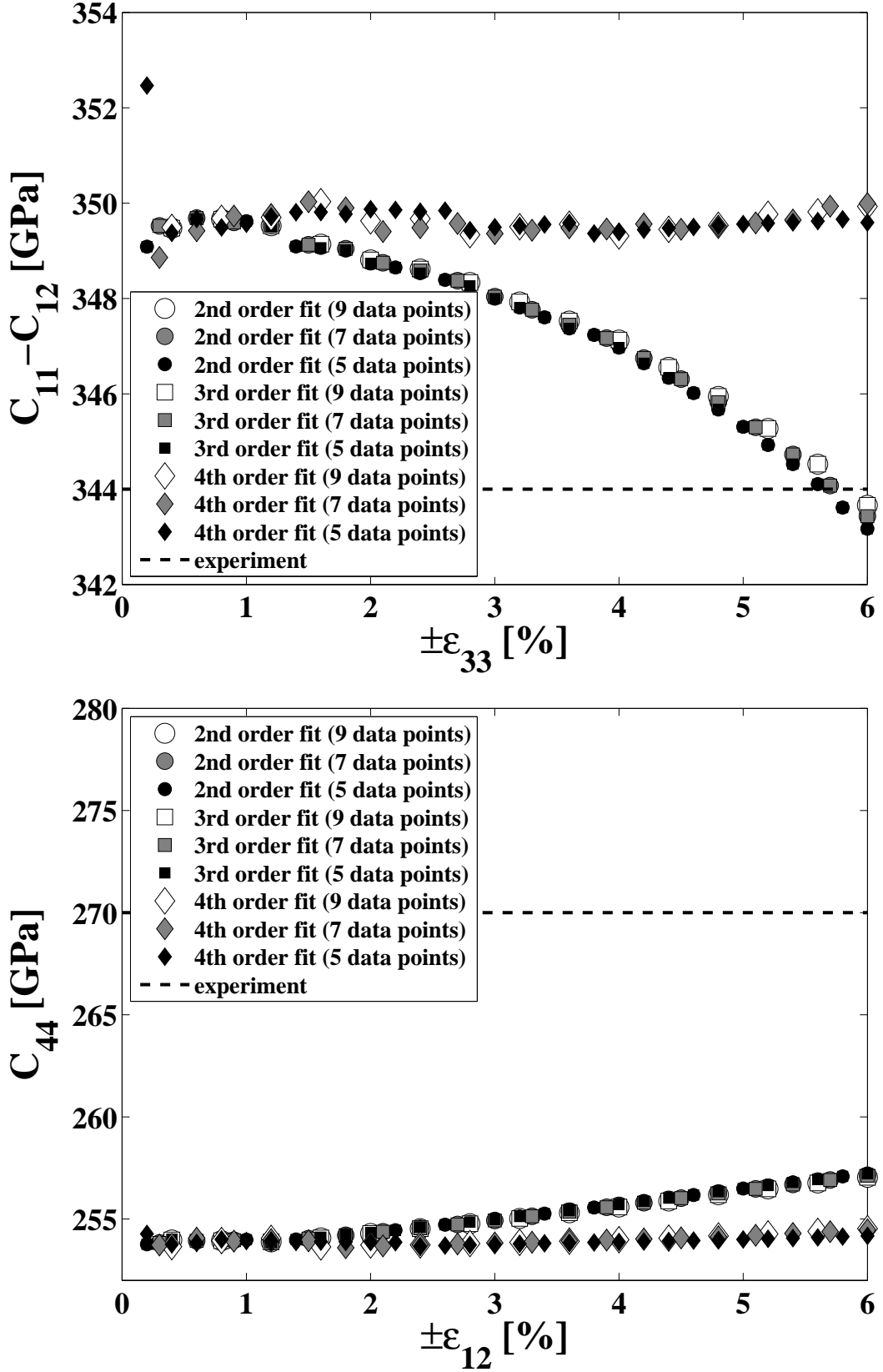
Figure C.6: $C_{11} - C_{12}$ (top) and C_{44} (bottom) of fcc Ir (left column) and Ir (right column) calculated by fitting the energy-strain curves DFT using 2nd (circle), 3rd (square), and 4th (diamond) order polynomial with 5 (white), 7 (gray), and 9 (black) data points. The horizontal dash lines are the experimental values close to 0 K (MacFarlane et al., 1966).
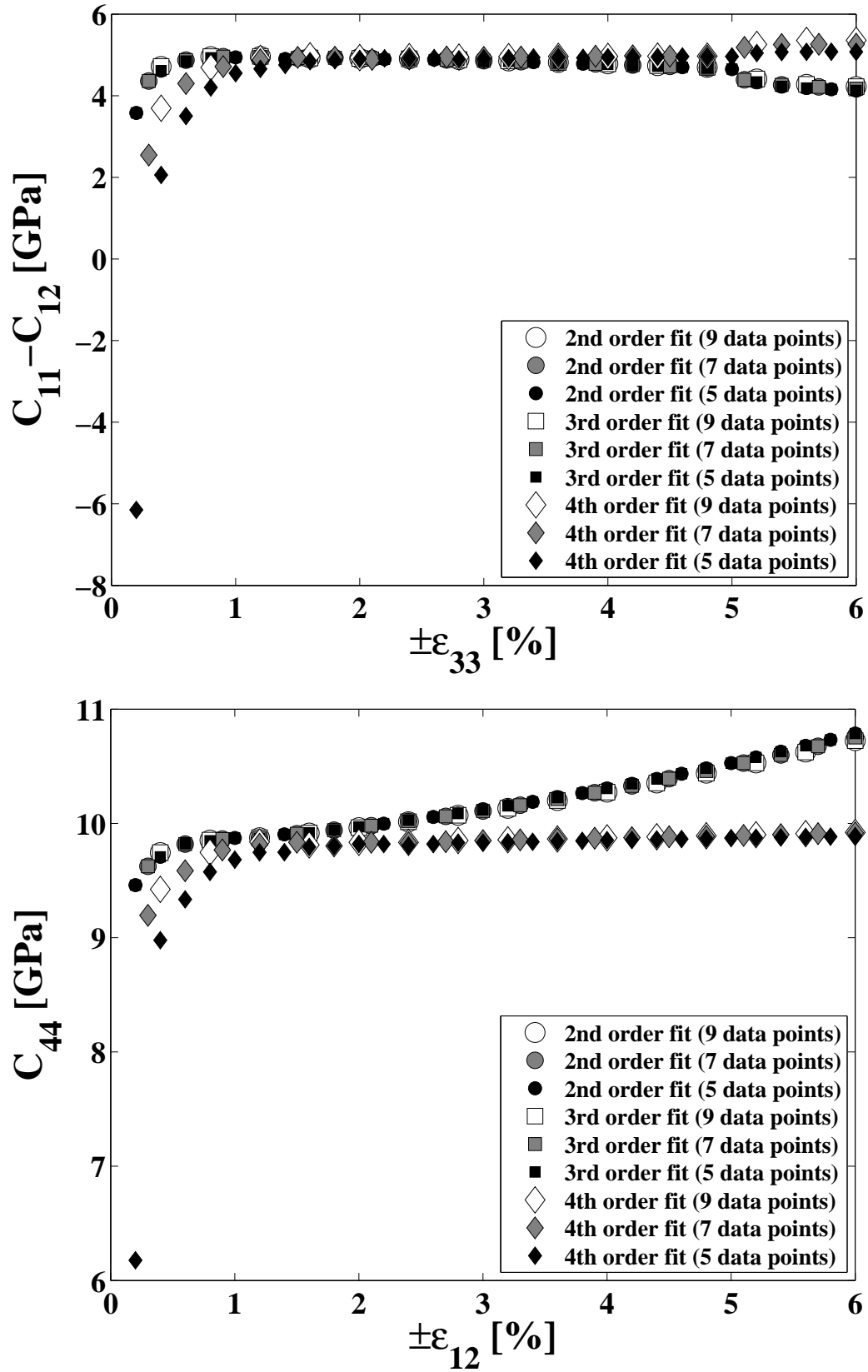
Figure C.7: $C_{11} - C_{12}$ (top) and C_{44} (bottom) of fcc Li calculated by fitting the energy-strain curves DFT using 2nd (circle), 3rd (square), and 4th (diamond) order polynomial with 5 (white), 7 (gray), and 9 (black) data points.

C.3.2   Test 2: fcc Al

The elastic constants of fcc by fitting the energy-strain curves from DFT are shown in Figure C.8 (2nd order fit) and Figure C.9 (4th order fit). Since the elastic constants by 3rd order fit are very similar to 2nd order fit, the results of 3rd order fit are not shown.

The elastic constants strongly depend on the σ value. Especially for $C_{11} - C_{12}$, at the small applied strains, the difference can be almost 30 GPa which is 58% of the experimental value. At higher σ values (0.6 eV, 0.8 eV, and 1 eV), the results are much less dependent on the applied strain than the lower σ values.

At higher strain, the calculated elastic constants tend to converge, by using different σ values.
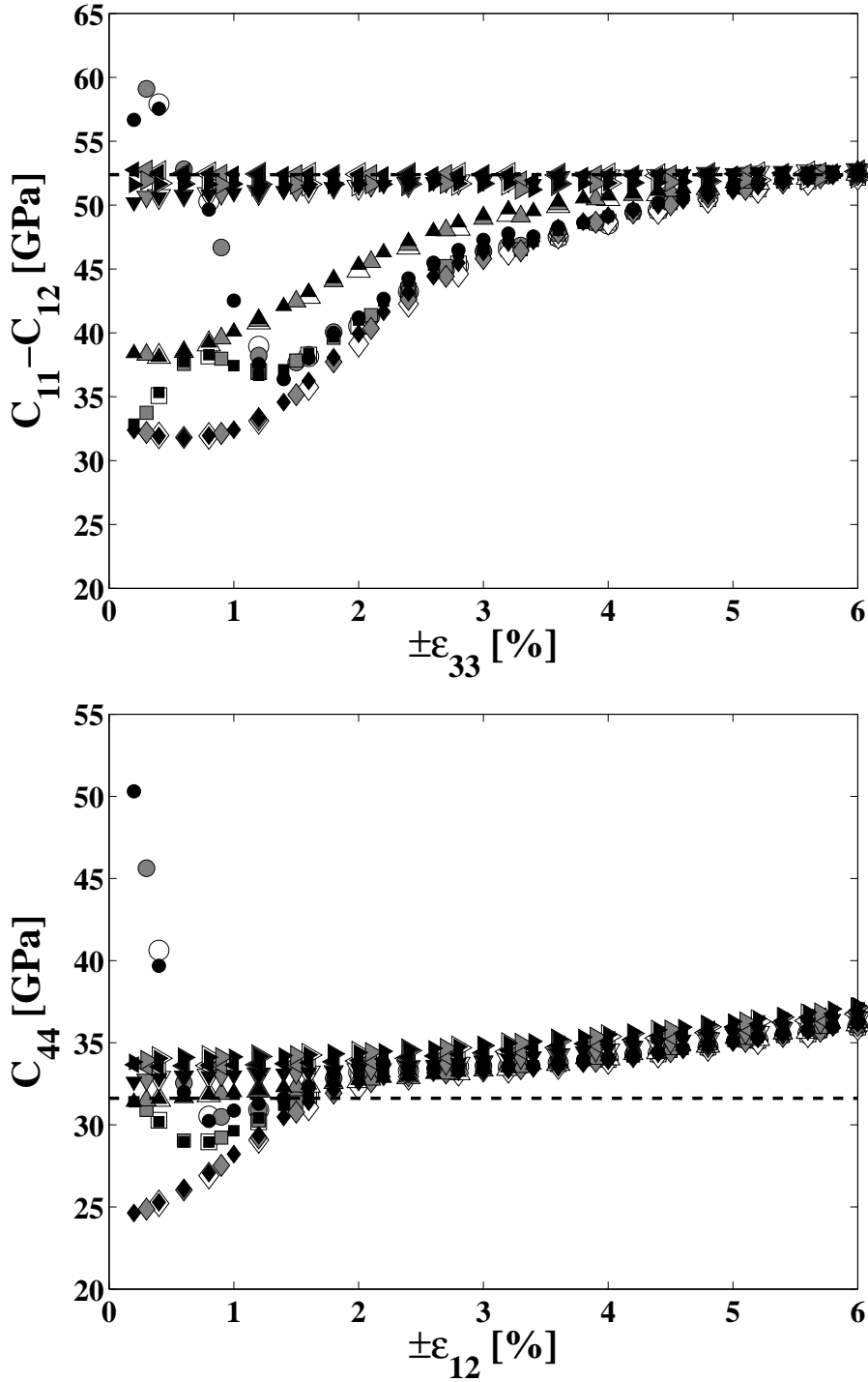
Figure C.8: 2nd order fit. $C_{11} - C_{12}$ (top) and C_{44} (bottom) of fcc Al calculated by fitting the energy-strain curves calculated by DFT calculated by using different σ values: 0.05 eV (circle), 0.1 eV (square), 0.2 eV (diamond), 0.4 eV (upward-pointing triangle), 0.6 eV (downward-pointing triangle), 0.8 eV (left-pointing triangle), and 1.0 eV (right-pointing triangleright) using 2nd order polynomial with 5 (white), 7 (gray), and 9 (black) data points equally spaced within the strain range of ε_{33} or ε_{12}. The horizontal dash lines are at the experimental values at 0K (Kamm and Alers, 1964). Calculation setup: cut-off energy, 420 eV; k-point sampling, 24×24×24.
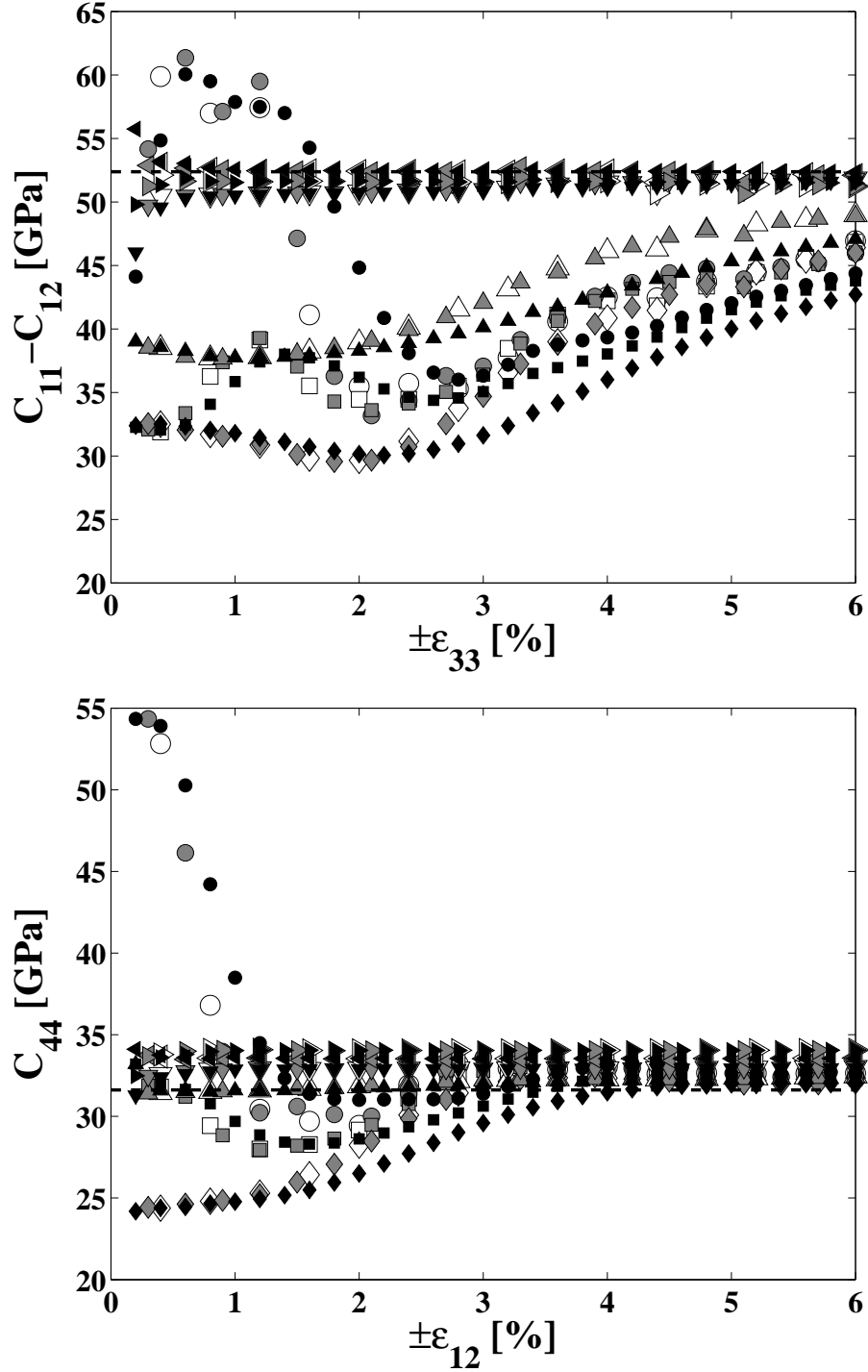
Figure C.9: 4th order fit. $C_{11} - C_{12}$ (top) and C_{44} (bottom) of fcc Al calculated by fitting the energy-strain curves calculated by DFT calculated by using different σ values: 0.05 eV (circle), 0.1 eV (square), 0.2 eV (diamond), 0.4 eV (upward-pointing triangle), 0.6 eV (downward-pointing triangle), 0.8 eV (left-pointing triangle), and 1.0 eV (right-pointing triangleright) using 4th order polynomial with 5 (white), 7 (gray), and 9 (black) data points equally spaced within the strain range of ε_{33} or ε_{12}. The horizontal dash lines are at the experimental values at 0K (Kamm and Alers, 1964). Calculation setup: cut-off energy, 420 eV; k-point sampling, 24×24×24.

C.4 Test 3

In last section, it shows that the σ value has great effect on the calculated the elastic constants of fcc Al. In this section, it shows the effect of the σ value and the order of fitting function on the compositional dependence of studied Al binary solid solutions.

The comparison of the calculated elastic constants with σ=0.4 and 0.8eV by fitting 2nd and 4th order polynomial function are shown in Figure C.10 to Figure C.16.

In most cases, the σ value and the order of the fitting function only influence the calculated values of the elastic constants, and the compositional dependence is not significantly affected by the σ value and the order of the fitting function.

There two disturbing cases which are $C_{11} - C_{12}$ of the Al-Mg and Al-Zn solid solutions. In these two cases, by using σ=0.4 eV and the 4th order fit, the compositional dependence is different from those under other calculation conditions.
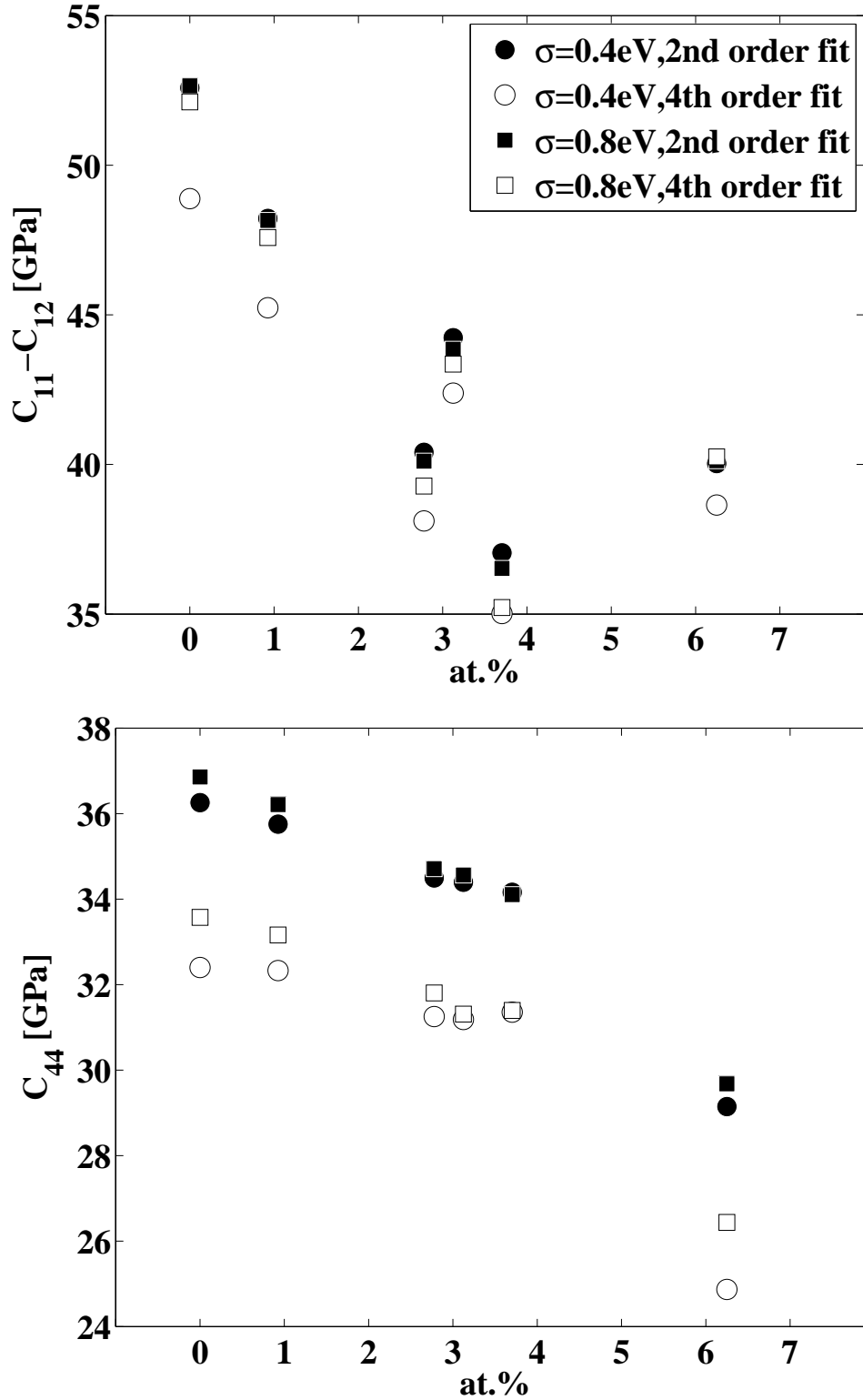
Figure C.10: $C_{11} - C_{12}$ (top) and C_{44} (bottom) of Al-Ca solid solutions calculated by fitting the energy-strain curves using 2nd order (solid symbols) and 4th order (open symbols) polynomial function at $\sigma=0.4$ eV (circle) and 0.8 eV (square). The fitting is done on 7 strains equally spaced within ±0.06. Calculation setup: cut-off energy, 420 eV; equilibrium k-point sampling, 24×24×24.
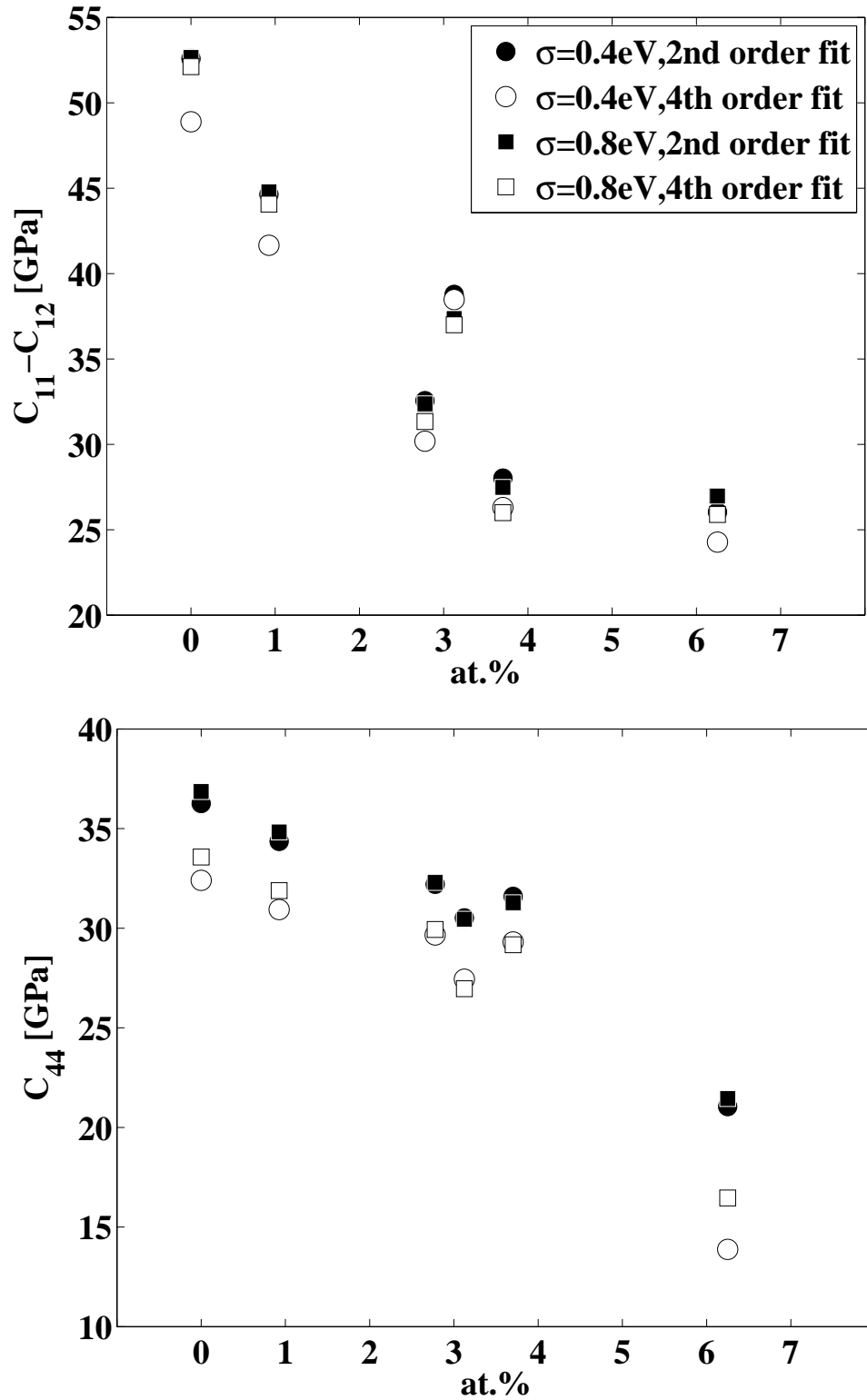
Figure C.11: $C_{11} - C_{12}$ (top) and C_{44} (bottom) of Al-Ca solid solutions calculated by fitting the energy-strain curves using 2nd order (solid symbols) and 4th order (open symbols) polynomial function at σ=0.4 eV (circle) and 0.8 eV (square). The fitting is done on 7 strains equally spaced within ±0.06. Calculation setup: cut-off energy, 420 eV; equilibrium k-point sampling, 24×24×24.
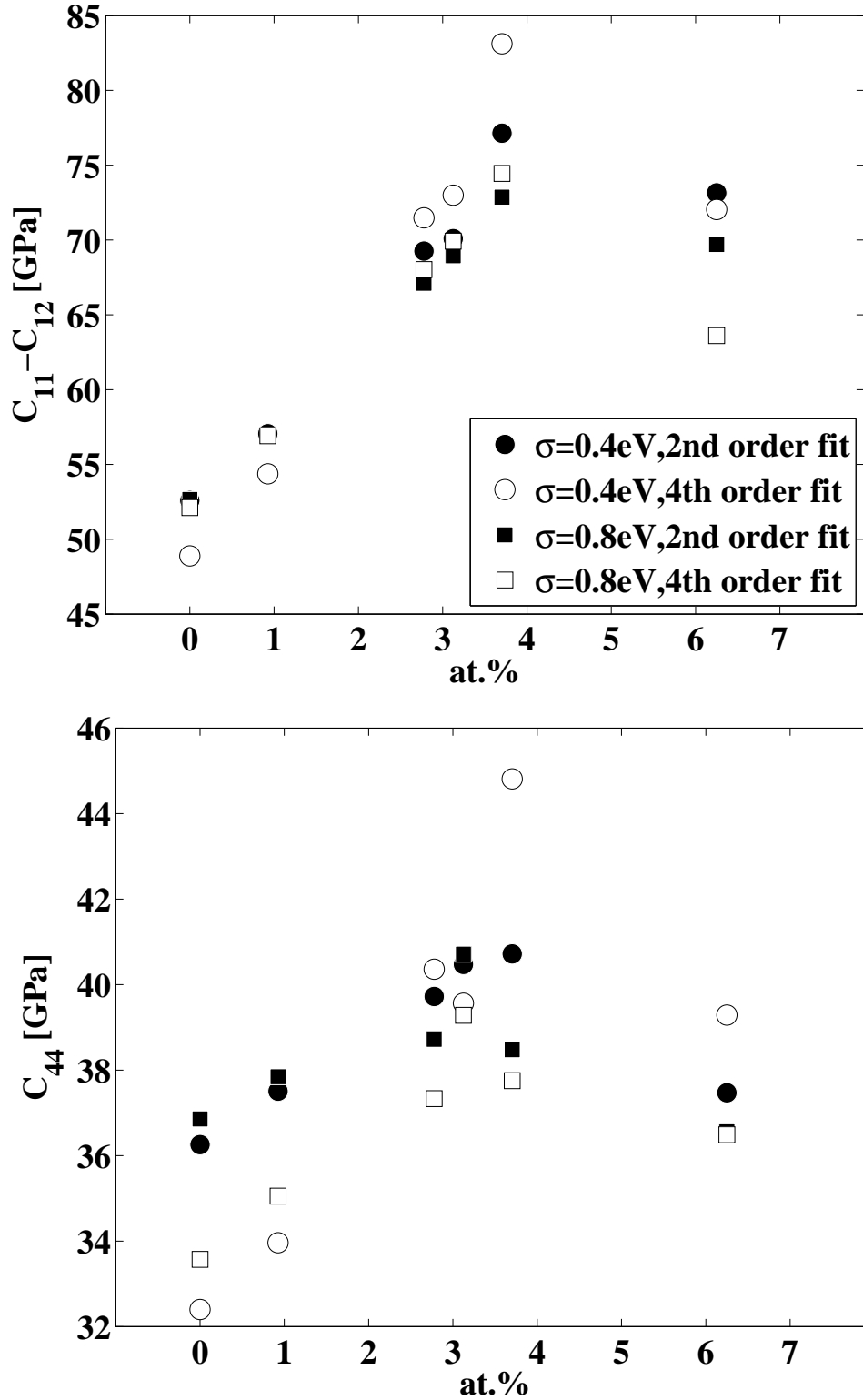
Figure C.12: $C_{11} - C_{12}$ (top) and C_{44} (bottom) of Al-Ir solid solutions calculated by fitting the energy-strain curves using 2nd order (solid symbols) and 4th order (open symbols) polynomial function at σ=0.4 eV (circle) and 0.8 eV (square). The fitting is done on 7 strains equally spaced within ±0.06. Calculation setup: cut-off energy, 420 eV; equilibrium k-point sampling, 24×24×24.

Figure C.13: $C_{11} - C_{12}$ (top) and C_{44} (bottom) of Al-Cu solid solutions calculated by fitting the energy-strain curves using 2nd order (solid symbols) and 4th order (open symbols) polynomial function at σ=0.4 eV (circle) and 0.8 eV (square). The fitting is done on 7 strains equally spaced within ±0.06. Calculation setup: cut-off energy, 420 eV; equilibrium k-point sampling, 24×24×24.

Figure C.14: $C_{11} - C_{12}$ (top) and C_{44} (bottom) of Al-Mg solid solutions calculated by fitting the energy-strain curves using 2nd order (solid symbols) and 4th order (open symbols) polynomial function at σ=0.4 eV (circle) and 0.8 eV (square). The fitting is done on 7 strains equally spaced within ±0.06. Calculation setup: cut-off energy, 420 eV; equilibrium k-point sampling, 24×24×24.

Figure C.15: $C_{11} - C_{12}$ (top) and C_{44} (bottom) of Al-Li solid solutions calculated by fitting the energy-strain curves using 2nd order (solid symbols) and 4th order (open symbols) polynomial function at σ=0.4 eV (circle) and 0.8 eV (square). The fitting is done on 7 strains equally spaced within ±0.06. Calculation setup: cut-off energy, 420 eV; equilibrium k-point sampling, 24×24×24.
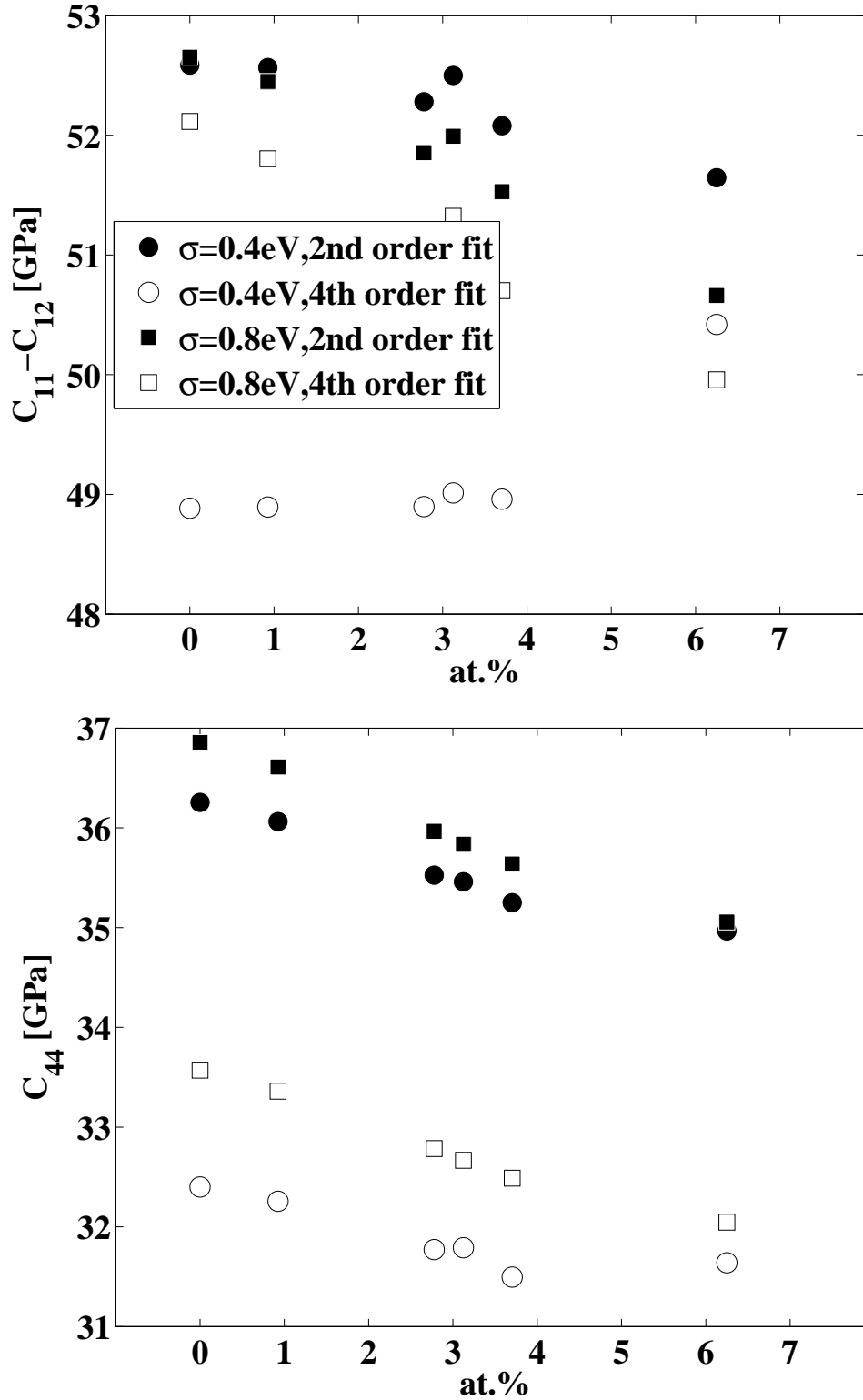
Figure C.16: $C_{11} - C_{12}$ (top) and C_{44} (bottom) of Al-Zn solid solutions calculated by fitting the energy-strain curves using 2nd order (solid symbols) and 4th order (open symbols) polynomial function at σ=0.4 eV (circle) and 0.8 eV (square). The fitting is done on 7 strains equally spaced within ±0.06. Calculation setup: cut-off energy, 420 eV; equilibrium k-point sampling, 24×24×24.

C.5   Summary of calculating elastic constants from energy-strain curves

In the light of the above analysis, the questions proposed at the beginning of this appendix can be tentatively answered:

1. Which order polynomial function should be used to fit the energy-strain curve?
   According to the analysis of fitting the energy-strain curves from the known elastic constants and DFT, the 2nd and 3rd give almost identical results, but 2nd and 3rd fit depends on the applied strain. 4th order fit less depends on the applied strain.

2. how much strain should be applied?
   If the elastic stiffness and the applied strain are both small, the calculated elastic energy is close or even within the system error. In such a case, the calculated elastic constants may scatter. The optimal applied strain range is should depend on the system. In this analysis, the applied strain ±0.06 seems to be a reasonable for Al.

3. how many data points are sufficient?
   The number of the data points has no significant effect on the results. From the curve fitting point of view, it is better to make the fitting problem redundant system, namely more data points than unknown parameters.

Appendix D

Calculation setup

D.1 Basic setup

In this study, VASP (Kresse and Furthmüller, 1996; Kresse and Joubert, 1999) is used for all the DFT calculations. PBE is used as the exchange-correlation functional (Perdew et al., 1996). The basic information of the employed pseudopotentials is listed in Table D.1.

Table D.1: Basic information in POTCAR files of the tested elements

Element	Designation in VASP	Valence electrons[a]	ENMIN ~ ENMAX[b][eV]
Al	Al	$3s^2 3p^1$	180.225 ~ 240.300
Ca	Ca_sv	$3s^2 3p^6 4s^2$	199.939 ~ 266.586
Sr	Sr_sv	$4s^2 4p^6 5s^2$	171.961 ~ 229.282
Ir	Ir	$5d^8 6s^1$	158.153 ~ 210.870
Cu	Cu	$3d^{10} 4p^1$	204.910 ~ 273.214
Mg	Mg_pv	$2p^6 3s^2$	199.180 ~ 265.574
Li	Li_sv	$1s^1 2s^1 2p^1$	203.737 ~ 271.649
Zn	Zn	$3d^{10} 4p^2$	207.545 ~ 276.727

[a] The electronic configuration of the valence electrons is obtained from the groundstate of bulk phase, not the free atom.

[b] ENMIN~ENMAX is the recommended cut-off energy range in POTCAR, above ENMIN it is supposed to be safe.

The basic input parameters are summarized in Table D.2 according to the tests in Appendix A, B, and C.

The atoms are arranged in fcc structure. Certain Al atoms are substituted by solute atoms in the supercell to mimic the solid solutions. The positions of solute atoms in the supercell are listed in Table D.3. The atomic positions of the solute atoms are selected to maintain the cubic symmetry of the supercell.

Table D.2: The basic input parameters of the calculations in this study.

σ value	Cut-off energy	k-point sampling	Supercell size	Number of atoms
0.4eV (EOS)		24×24×24	1×1×1	4
	420 eV	12×12×12	2×2×2	32
0.8eV (elastic constants)		8×8×8	3×3×3	108

Table D.3: The concentrations of the solid solutions in this study, the corresponding supercells and the positions of the solute atoms in the supercells.

	Concentration [at.%]	Atomic positions of the solute atoms
$Al_{107}X_1$	0.926	(0, 0, 0)
$Al_{105}X_3$	2.778	(0, 0.5, 0.5) (0.5, 0, 0.5) (0.5, 0.5, 0)
$Al_{31}X_1$	3.125	(0.5, 0.5, 0.5)
$Al_{104}X_4$	3.704	(0, 0, 0) (0, 0.5, 0.5) (0.5, 0, 0.5) (0.5, 0.5, 0)
$Al_{30}X_2$	6.25	(0, 0, 0) (0.5, 0.5, 0.5)
Al_3X_1	25	(0, 0, 0)

D.2   Additional setup for Equation of State (EOS)

According to the tests in Appendix B, the energy-volume curves of the selected pure bulk phases and the studied Al binary solid solutions are calculated in the following way:

1. A preliminary calculation is conducted obtain an approximated equilibrium atomic volume (V_0).

2. 9 energy data points are calculated at the volumes of $V_0 \pm dV_{max}$, $V_0 \pm 0.75dV_{max}$, $V_0 \pm 0.5dV_{max}$, $V_0 \pm 0.25dV_{max}$ and V_0, where $\pm dV_{max}$ is $\pm 10\%$ of V_0.

3. The calculated energy-volume curves are fitted by Birch-Murnaghan fit. Murnaghan fit and Birch-Murnaghan fit are used on the selected pure bulk phases for the sake of comparison.

D.3   Additional setup for elastic constants

According to the tests in Appendix C, the energy-strain curves of the studied Al binary alloys are calculated in the following way:

1. 7 energies are calculated at strains of $\pm 0.06\epsilon_{ij}$, $\pm 0.04\epsilon_{ij}$, $\pm 0.02\epsilon_{ij}$ and 0, where ϵ_{ij} is ϵ_{33} for tetragonal shear, and ϵ_{12} for trigonal shear.

2. The calculated data are fitted by the 4th order polynomial function. Then the second order coefficients are taken to calculated $C_{11} - C_{12}$ and C_{44} (see Section 3.3).

D.4   Additional setup for Bader analysis

For Bader analysis, the electron density is output on each FFT grid. The sizes of the FFT grid for the electron density output for each supercell is listed in Table D.4.

Table D.4: FFT grid of each supercell for the electron density output.

Supercell size	FFT grid size	Number of atoms
1×1×1	140×140×140	4
2×2×2	280×280×280	32
3×3×3	400×400×400	108

Bibliography

Abrikosov, I. A., Ruban, A. V., Johansson, B., and Skriver, H. L. (1998). Total energy calculations of random alloys: Supercell, Connolly-Williams, and CPA methods. *Computational Materials Science*, 10(1-4):302–305. Computational Modelling of Issues in Materials Science. (Cited on page 6.)

Agnew, S. R., Yoo, M. H., and Tomé, C. N. (2001). Application of texture simulation to understanding mechanical behavior of Mg and solid solution alloys containing Li or Y. *Acta Materialia*, 49(20):4277–4289. (Cited on page 13.)

Akhtar, A. and Teghtsoonian, E. (1971). Plastic deformation of Ni-Cr single crystals. *Metallurgical and Materials Transactions B*, 2(10):2757–2763. (Cited on page 11.)

Akhtar, A. and Teghtsoonian, E. (1972). Substitutional solution hardening of magnesium single crystals. *Philosophical Magazine*, 25(4):897–916. (Cited on page 13.)

Alers, G. and Neighbours, J. (1958). The elastic constants of zinc between 4.2 and 670 K. *Journal of Physics and Chemistry of Solids*, 7(1):58–64. (Cited on pages 51 and 212.)

Allen, N. P., Schofield, T. H., and Tate, A. E. L. (1951). Mechanical properties of α-solid solutions of copper, with zinc, gallium, germanium and arsenic. *Nature*, 168(4270):378–379. (Cited on page 20.)

Anderson, M. S., Swenson, C. A., and Peterson, D. T. (1990). Experimental equations of state for calcium, strontium, and barium metals to 20 kbar from 4 to 295 K. *Physical Review B*, 41(6):3329–3338. (Cited on page 50.)

Ando, S. and Tonda, H. (2000). Non-basal slip in magnesium-lithium alloy single crystals. *Materials Transactions JIM*, 41(9):1188–1191. (Cited on pages 13 and 285.)

Arblaster, J. W. (2010). Crystallographic properties of iridium, assessment of properties from absolute zero to the melting point. *Platinum Metals Review*, 54(2):93–102. (Cited on page 50.)

Asada, H., Horiuchi, R., Yoshinaga, H., and Nakamoto, S. (1967). Flow stress in Al-Mg alloy single crystals. *Transactions of the Japan Institute of Metals*, 8(3):159–167. (Cited on page 96.)

Ashby, M., Shercliff, H., and Cebon, D. (2007). *Materials Engineering, Science, Processing and Design*. Elsevier Ltd. (Cited on pages 43 and 285.)

Ashby, M. F. (2005). *Materials Selection in Mechanical Design, 3rd Edition*. Butterworth-Heinemann. (Cited on pages 42, 43, 44, 285, and 297.)

ASM Handbook (1990). *ASM Handbook Vol. 2: Properties and Selection : Nonferrous Alloys and Special-Purpose Materials*. ASM International, 10th edition. (Cited on pages 95, 96, 164, 165, 166, and 167.)

Auer, H., Gerold, V., Haberkorn, H., and Zürn, W. (1964). Die mechanischen Eigenschaften von Aluminium-Zink-und Aluminium-Silber-Legierungen. *physica status solidi (b)*, 6(2):K91–K94. (Cited on page 96.)

Axler, K., Foltyn, E., Peterson, D., and Hutchinson, W. (1989). Phase investigations of the Al-Ir system. *Journal of the Less Common Metals*, 156(1-2):213–219. (Cited on page 66.)

Bacon, D. J., Barnett, D. M., and Scattergood, R. O. (1980). Anisotropic continuum theory of lattice defects. *Progress in Materials Science*, 23(2-4):51–262. (Cited on page 14.)

Bader, R. F. W. (1994). *Atoms in Molecules. A Quantum Theory*. Oxford University Press, USA. (Cited on pages 41 and 285.)

Barrett, C. S. (1956). X-ray study of the alkali metals at low temperatures. *Acta Crystallographica*, 9(8):671–677. (Cited on page 51.)

Berliner, R., Fajen, O., Smith, H. G., and Hitterman, R. L. (1989). Neutron powder-diffraction studies of lithium, sodium, and potassium metal. *Physical Review B*, 40(18):12086–12097. (Cited on page 51.)

Birch, F. (1938). The effect of pressure upon the elastic parameters of isotropic solids, according to murnaghan's theory of finite strain. *Journal of Applied Physics*, 9(4):279–288. (Cited on pages 32 and 33.)

Birch, F. (1947). Finite elastic strain of cubic crystals. *Physical Review*, 71(11):809–824. (Cited on pages 16, 32, 35, 36, and 37.)

Blanter, M. S., Golovin, I. S., Neuhäuser, H., and Sinning, H.-R. (2010). *Internal Friction in Metallic Materials: A Handbook*. Springer. (Cited on page 20.)

Blöchl, P. E. (1994). Projector augmented-wave method. *Physical Review B*, 50(24):17953–17979. (Cited on page 31.)

Blöchl, P. E., Jepsen, O., and Andersen, O. K. (1994). Improved tetrahedron method for brillouin-zone integrations. *Physical Review B*, 49(23):16223–16233. (Cited on pages 30 and 285.)

Borchers, H. and Dropmann, P. (1972). Mischkristallhärtung von Aluminium-Einkristallen durch Gallium. *Zeitschrif für Metallkunde*, 63(3):137–140. (Cited on page 109.)

Brandl, C., Derlet, P. M., and Swygenhoven, H. V. (2007). General-stacking-fault energies in highly strained metallic environments: Ab initio calculations. *Physical Review B*, 76(5):054124. (Cited on pages 4 and 98.)

Buchenau, U., Heiroth, M., Schober, H. R., Evers, J., and Oehlinger, G. (1984). Lattice dynamics of strontium and barium. *Physical Review B*, 30(6):3502–3505. (Cited on page 68.)

Buchenau, U., Schober, H., and Wagner, R. (1981). Coherent neutron-scattering from polycrystals. *Journal de Physique*, 42(NC6):395–397. (Cited on page 68.)

Bullough, R. and Newman, R. C. (1970). The kinetics of migration of point defects to dislocations. *Reports on Progress in Physics*, 33(1):101–148. (Cited on page 14.)

Butt, M. Z., Feltham, P., and Ghauri, I. M. (1983). Stress-equivalence of solid-solution hardening in concentrated Ag-Al and ag-zn alloys. *physica status solidi (a)*, 80(2):K125–K128. (Cited on page 11.)

Butt, M. Z., Rafi, Z., and Khan, M. A. (1990). Low-temperature anomaly in the strength of copper-manganese alloy single crystals. *physica status solidi (a)*, 120(2):K149–K154. (Cited on page 11.)

Cai, W., Arsenlis, A., Weinberger, C. R., and Bulatov, V. V. (2006). A non-singular continuum theory of dislocations. *Journal of the Mechanics and Physics of Solids*, 54(3):561–587. (Cited on page 15.)

Caillard, D. and Martin, J. (2003). *Thermally Activated Mechanisms in Crystal Plasticity*, volume 8 of *Pergamon Materials Series*, chapter 3 Interaction between dislocations and small-size obstacles, page 75. Elsevier Science. (Cited on pages 10 and 285.)

Capelle, K. (2006). A bird's-eye view of density-functional theory. *Brazilian Journal of Physics*, 36(4a):1318–1343. (Cited on page 22.)

Carlsen, K. M. and Honeycombe, R. W. K. (1954-1955). Plastic deformation of aluminium-3.5% copper alloy single crystals. *Journal of the Institute of Metals*, 83(10):449–454. (Cited on page 96.)

Castleton, C. W. M., Höglund, A., and Mirbt, S. (2009). Density functional theory calculations of defect energies using supercells. *Modelling and Simulation in Materials Science and Engineering*, 17(8):084003. (Cited on page 134.)

Ceder, G., Chiang, Y.-M., Sadoway, D. R., Aydinol, M. K., Jang, Y.-I., and Huang, B. (1998). Identification of cathode materials for lithium batteries guided by first-principles calculations. *Nature*, 392(6677):694–696. (Cited on page 4.)

Ceperley, D. M. and Alder, B. J. (1980). Ground state of the electron gas by a stochastic method. *Physical Review Letter*, 45(7):566–569. (Cited on page 26.)

Chiarotti, G. (1993). *Landolt-Börnstein Numberical Data and Functional Relationships in Science and Technology Group III (Condensed Matter)*, volume Volume 24a Crystallography, Structure and Morphology, Physics of Solid Surfaces, Structure, chapter General introduction, page 23. Springer-Verlag. (Cited on page 51.)

Choi, G., Shinoda, T., Mishima, Y., and Suzuki, T. (1990). Solid-solution hardening in the Ni-40at%Co-x ternary alloys. *ISIJ International*, 30(3):248–254. (Cited on pages 17, 115, 116, and 288.)

Churyumov, A., Solonin, A., and Zolotorevskii, V. (2007a). Simulation of the flow stress of recrystallized single-phase alloys of the Al-Mg and Al-Cu systems. *Russian Journal of Non-Ferrous Metals*, 48(4):286–290. (Cited on page 96.)

Churyumov, A., Zolotorevskii, N., Solonin, A., and Zolotorevskii, V. (2007b). Simulation of flow stress in Al-Mg alloys quenched after casting. *Russian Journal of Non-Ferrous Metals*, 48(3):208–213. (Cited on page 96.)

Clouet, E. (2006). The vacancy-edge dislocation interaction in fcc metals: A comparison between atomic simulations and elasticity theory. *Acta Materialia*, 54(13):3543–3552. Selected Papers from the Meeting "Micromechanics and Microstructure Evolution: Modeling, Simulation and Experiments" held in Madrid/Spain, 11-16 September 2005. (Cited on pages 15 and 16.)

Clouet, E., Garruchet, S., Nguyen, H., Perez, M., and Becquart, C. S. (2008). Dislocation interaction with C in α-Fe: A comparison between atomic simulations and elasticity theory. *Acta Materialia*, 56(14):3450–3460. (Cited on page 15.)

Collings, E. and Gegel, H. (1973). A physical basis for solid-solution strengthening and phase stability in alloys of titanium. *Scripta Metallurgica*, 7(5):437–443. (Cited on pages 20 and 150.)

Collings, E. W. (1975). Physical principles of solid solution strengthening in alloys. In Collings, E. W. and Gegel, H. L., editors, *Physics of solid solution strengthening*, pages 147–182. Plenum press. New York and London. (Cited on pages 20 and 150.)

Cottrell, A. (1948). Effect of solute atoms on the behaviour of dislocations. In *Report on Conference of the Strength of Solids*, pages 30–37, London, UK. Physical Society. Conference on the Strength of Solids, 1947, London, UK. (Cited on pages 5 and 14.)

Cottrell, A. H., Hunter, S. C., and Nabarro, F. R. N. (1953). CXI. Electrical interaction of a dislocation and a solute atom. *Philosophical Magazine Series 7*, 44(357):1064–1067. (Cited on page 17.)

Counts, W., Friák, M., Raabe, D., and Neugebauer, J. (2009). Using ab initio calculations in designing bcc Mg-Li alloys for ultra-lightweight applications. *Acta Materialia*, 57(1):69–76. (Cited on pages 6 and 170.)

Csonka, G. I., Perdew, J. P., Ruzsinszky, A., Philipsen, P. H. T., Lebègue, S., Paier, J., Vydrov, O. A., and Ángyán, J. G. (2009). Assessing the performance of recent density functionals for bulk solids. *Physical Review B*, 79(15):155107. (Cited on pages 26 and 27.)

Dash, J. and Fine, M. (1961). Temperature and composition dependence of the strength of aluminum base zinc alloy single crystals. *Acta Metallurgica*, 9(2):149–154. (Cited on pages 95 and 96.)

Day, J. P. and Ruoff, A. L. (1974). The variation of the elastic constants of lithium with temperature and pressure. *physica status solidi (a)*, 25(1):205–213. (Cited on page 51.)

Delczeg, L., Delczeg-Czirjak, E. K., Johansson, B., and Vitos, L. (2009). Assessing common density functional approximations for the ab initio description of monovacancies in metals. *Physical Review B*, 80(20):205121. (Cited on page 27.)

Deschamps, A., Bréchet, Y., Necker, C. J., Saimoto, S., and Embury, J. D. (1996). Study of large strain deformation of dilute solid solutions of Al-Cu using channel-die compression. *Materials Science and Engineering A*, 207(2):143–152. (Cited on page 96.)

Dew-Hughes, D. and Robertson, W. (1960). The mechanism of hardening in aged aluminum-copper alloys. *Acta Metallurgica*, 8(3):156–167. (Cited on page 96.)

Dorn, J., Pietrokowsky, P., and Tietz, T. E. (1950). the effect of alloying elements on the plastic properties of aluminum alloys. *Transactions of the American Institute of Mining and Metallurgical Engineers*, 188(7):933–943. (Cited on page 109.)

Dudiy, S. V. and Zunger, A. (2006). Searching for alloy configurations with target physical properties: Impurity design via a genetic algorithm inverse band structure approach. *Physical Review Letter*, 97(4):046401. (Cited on page 4.)

Eberhart, M. E. and Clougherty, D. P. (2004). Looking for design in materials design. *Nature Materials*, 3(10):659–661. (Cited on page 4.)

Eringen, A. C. (2002). *Nonlocal Continuum Field Theories*. Springer. (Cited on page 15.)

Eshelby, J. (1956). The continuum theory of lattice defects. In Seitz, F. and Turnbull, D., editors, *Solid State Physics-Advances in Research and Applications*, volume 3 of *Solid State Physics*, pages 79–144. Academic Press. (Cited on page 14.)

Felice, R. A., Trivisonno, J., and Schuele, D. E. (1977). Temperature and pressure dependence of the single-crystal elastic constants of ^{6}Li and natural lithium. *Physical Review B*, 16(12):5173–5184. (Cited on page 51.)

Fiore, N. and Bauer, C. (1964). Solute atom-dislocation binding energy in dilute Cu-Ge alloys. *Acta Metallurgica*, 12(12):1329–1336. (Cited on page 20.)

Fiore, N. F. and Bauer, C. L. (1968). Binding of solute atoms to dislocations. *Progress in Materials Science*, 13:85–134. (Cited on pages 14, 17, and 20.)

Fisher, J. (1954). On the strength of solid solution alloys. *Acta Metallurgica*, 2(1):9–10. (Cited on page 17.)

Fleischer, R. L. (1961). Solution hardening. *Acta Metallurgica*, 9(11):996–1000. (Cited on pages 5 and 15.)

Fleischer, R. L. (1963). Substitutional solution hardening. *Acta Metallurgica*, 11(3):203–209. (Cited on pages 5, 15, and 97.)

Fleischer, R. L. (1964). Chapter 3 solid-solution hardening. In Peckner, D., editor, *The strengthening in metals*, pages 93–140. Reinhold Press, New York. (Cited on page 18.)

Flinn, P. (1958). Solute hardening of close-packed solid solutions. *Acta Metallurgica*, 6(10):631–635. (Cited on pages 16 and 17.)

Flinn, P. A. (1962). Chapter 2 solid solution strengthening. In *Strengthening Mechanisms in Solids*, pages 17–50. American Society for Metals, Metals Park, Ohio. Papers presented at a Seminar of the American Society for Metals on October 13 and 14, 1960. (Cited on pages 16 and 17.)

Fomenko, V. S., Isaev, N. V., and Pustovalov, V. V. (1993). Low-temperature plastic deformation of Al-Li solid solutions. *Low Temperature Physics*, 19(4):301–304. (Cited on page 96.)

Franceschetti, A. and Zunger, A. (1999). The inverse band-structure problem of finding an atomic configuration with given electronic properties. *Nature*, 402(6757):60–63. (Cited on page 4.)

Friák, M., Šob, M., and Vitek, V. (2001). Ab initio calculation of tensile strength in iron. *Philosophical Magazine*, 83(31):3529–3537. (Cited on page 4.)

Friák, M., Šob, M., and Vitek, V. (2003). Ab initio study of the ideal tensile strength and mechanical stability of transition-metal disilicides. *Physical Review B*, 68(18):184101. (Cited on page 4.)

Friedel, J. (1964). *Dislocations*. Oxford : Pergamon. (Cited on pages 17 and 18.)

Furukawa, M., Miura, Y., and Nemoto, M. (1985). The effect of temperature on the yield stress of Al-Li alloy. *Transactions of the Japan Institute of Metals*, 26(6):414–422. (Cited on pages 95 and 107.)

Gandin, C.-A., Brechet, Y., Rappaz, M., Canova, G., Ashby, M., and Shercliff, H. (2002). Modelling of solidification and heat treatment for the prediction of yield stress of cast alloys. *Acta Materialia*, 50(5):901–927. (Cited on page 96.)

Ganeshan, S., Shang, S., Wang, Y., and Liu, Z.-K. (2009). Effect of alloying elements on the elastic properties of Mg from first-principles calculations. *Acta Materialia*, 57(13):3876–3884. (Cited on page 6.)

Garland, C. W. and Dalven, R. (1958). Elastic constants of zinc from 4.2°K to 77.6°K. *Physical Review*, 111(5):1232–1234. (Cited on pages 51 and 212.)

Gastberger, L., Vöhringer, O., and Macherauch, E. (1974a). Der Einflußvon Verformungstemperatur und Verformungsgeschwindigkeit auf 0,2-Dehngrenzen homogener Kupfer-Aluminium-, Kupfer-Gallium- und Kupfer-Germanium-Legierungen. *Zeitschrif für Metallkunde*, 65(1):17–26. (Cited on page 11.)

Gastberger, L., Vöhringer, O., and Macherauch, E. (1974b). Der Einflußvon Verformungstemperatur und Verformungsgeschwindigkeit auf 0,2-Dehngrenzen homogener Kupfer-Arsen-, Kupfer-Indium- und Kupfer-Germanium-Legierungen. *Zeitschrif für Metallkunde*, 65(1):26–31. (Cited on page 11.)

Gault, C., Dauger, A., and Boch, P. (1977). Variations of the elastic constants of aluminium-magnesium single crystals with Guinier-Preston zones. *physica status solidi (a)*, 43(2):625–632. (Cited on pages 54, 55, 75, 76, 77, 88, 89, 90, 94, and 286.)

Ghate, P. B. (1964). Fourth-order elastic coefficients. *Journal of Applied Physics*, 35(2):337–339. (Cited on page 37.)

Ghauri, I. M., Feltham, P., and Butt, M. Z. (1986). Solid-solution hardening in α -brasses at low temperatures. *physica status solidi (a)*, 96(1):K43–K47. (Cited on page 11.)

Ghosh, G., van de Walle, A., and Asta, M. (2008). First-principles calculations of the structural and thermodynamic properties of bcc, fcc and hcp solid solutions in the Al-TM (TM = Ti, Zr and Hf) systems: A comparison of cluster expansion and supercell methods. *Acta Materialia*, 56(13):3202–3221. (Cited on page 6.)

Gilman, J. (2003). *Electronic basis of the strength of materials*, chapter 13 Shear modulus, page 152. Cambridge University Press. (Cited on page 168.)

Grabowski, B., Hickel, T., and Neugebauer, J. (2007). Ab initio study of the thermodynamic properties of nonmagnetic elementary fcc metals: Exchange-correlation-related error bars and chemical trends. *Physical Review B*, 76(2):024309. (Cited on pages 4, 27, 50, 208, 209, 214, 215, 218, 219, 220, 221, 231, 232, 291, 292, and 293.)

Grabowski, B., Ismer, L., Hickel, T., and Neugebauer, J. (2009). Ab initio up to the melting point: Anharmonicity and vacancies in aluminum. *Physical Review B*, 79(13):134106. (Cited on pages 4 and 27.)

Granato, A. and Lücke, K. (1956). Theory of mechanical damping due to dislocations. *Journal of Applied Physics*, 27(6):583–593. (Cited on page 20.)

Gschneidner Jr., K. A. (1964). Physical properties and interrelationships of metallic and semimetallic elements. In Seitz, F. and Turnbull, D., editors, *Solid State Physics: Advances in Research and Applications*, volume 16, pages 275–426. Academic Press. (Cited on pages 102 and 118.)

Gyorffy, B. L. (1972). Coherent-potential approximation for a nonoverlapping-muffin-tin-potential model of random substitutional alloys. *Physical Review B*, 5(6):2382–2384. (Cited on page 5.)

Gypen, L. and Deruyttere, A. (1981). The combination of atomic size and elastic modulus misfit interactions in solid solution hardening. *Scripta Metallurgica*, 15(8):815–820. (Cited on page 15.)

Gypen, L. A. and Deruyttere, A. (1977b). Multi-component solid solution hardening-proposed model. *Journal of Materials Science*, 12(5):1028–1033. (Cited on page 18.)

Gypen, L. A. and Deruyttere, A. (1977a). Multi-component solid solution hardening-agreement with experimental results. *Journal of Materials Science*, 12(5):1034–1038. (Cited on page 18.)

Haas, P., Tran, F., and Blaha, P. (2009). Calculation of the lattice constant of solids with semilocal functionals. *Physical Review B*, 79(8):085104. (Cited on pages 26 and 27.)

Haas, P., Tran, F., Blaha, P., Pedroza, L. S., da Silva, A. J. R., Odashima, M. M., and Capelle, K. (2010). Systematic investigation of a family of gradient-dependent functionals for solids. *Physical Review B*, 81(12):125136. (Cited on pages 26 and 27.)

Haasen, P. (1979). Chapter 15 part 1 solution hardening in f.c.c. metals. In Nabarro, F. R. N., editor, *Dislocations in solids, Volumn IV. Dislocations in metallurgy*, pages 155–189. North-Holland, Amsterdam, Netherlands. (Cited on pages 14, 18, and 20.)

Haasen, P. (1996). Chapter 23 mechanical properties of solid solutions. In Cahn, R. W. and Haasen, P., editors, *Physical Metallurgy 4th Edition*, pages 2009–2074. North-Holland, Amsterdam, Netherlands. (Cited on pages 14 and 18.)

Haasen, P. and King, A. (1960). Verfestigung und Stapelfehlerenergie von Kupfer-Liegierungskristallen. *Zeitschrif für Metallkunde*, 51(12):722–736. (Cited on page 11.)

Haberkorn, H. and Gerold, V. (1966). Die Plastizität von Aluminium-Zink-Legierungen II Zur Strukturabhängigkeit einiger verfestigungsparameter. *physica status solidi (b)*, 15(1):167–180. (Cited on page 96.)

Hafner, J. (2000). Atomic-scale computational materials science. *Acta Materialia*, 48(1):71–92. (Cited on page 4.)

Hanlumyuang, Y., Gordon, P., Neeraj, T., and Chrzan, D. (2010). Interactions between carbon solutes and dislocations in bcc iron. *Acta Materialia*, 58(16):5481–5490. (Cited on page 15.)

Heiroth, M., Buchenau, U., Schober, H. R., and Evers, J. (1986). Lattice dynamics of fcc and bcc calcium. *Physical Review B*, 34(10):6681–6689. (Cited on page 68.)

Hendrickson, A. A. and Fine, M. E. (1961). Solid solution strengthening of Ag by Al. *Transactions of the Metallurgical Society of AIME*, 221(5):967–974. (Cited on page 11.)

Henkelman, G., Arnaldsson, A., and Jónsson, H. (2006). A fast and robust algorithm for bader decomposition of charge density. *Computational Materials Science*, 36(3):354–360. (Cited on page 41.)

Hershey, A. (1954). The elasticity of an isotropic aggregate of anisotropic cubic crystals. *Journal of Applied Mechanics-Transactions of the ASME*, 21(3):236–240. (Cited on pages 39, 82, and 94.)

Hibbard, W. (1958). Solid solution hardening. *Transactions of the American Institute of Mining and Metallurgical Engineers*, 212:1–5. (Cited on page 20.)

Hiki, Y. (1981). Higher order elastic constants of solids. *Annual Review of Materials Science*, 11(1):51–73. (Cited on pages 35 and 36.)

Hill, P. J., Cornish, L. A., and Witcomb, M. J. (1998). Constitution and hardnesses of the Al-Ir system. *Journal of Alloys and Compounds*, 280(1-2):240–250. (Cited on page 66.)

Hill, R. (1952). The elastic behaviour of a crystalline aggregate. *Proceedings of the Physical Society. Section A*, 65(5):349–354. (Cited on page 39.)

Hirano, K. (1969). Metastable state in aluminum-silver alloys formed during quenching. *Transactions of the Japan Institute of Metals*, 10(2):132–139. (Cited on page 107.)

Hohenberg, P. and Kohn, W. (1964). Inhomogeneous electron gas. *Physical Review*, 136(3B):B864–B871. (Cited on page 22.)

Ide, N., Yamashita, M., and Asano, S. (1999). Solid solution hardening evaluated from amplitude-dependent internal friction in polycrystalline copper alloys. *Scripta Materialia*, 41(2):181–185. (Cited on page 20.)

Isaev, N. V., Pustovalov, V. V., Fomenko, V. S., and Shumilin, S. E. (1994). Plasticity of Al-Li alloys in the temperature range 0.5-300 K: Low-temperature anomalies, deformation instability and the effect of superconducting transition. *Low Temperature Physics*, 20(8):653–659. (Cited on page 96.)

Isaev, N. V., Pustovalov, V. V., Fomenko, V. S., and Shumilin, S. E. (1996). About yield stress of Al-Li alloys at 0.5 to 295 K. *physica status solidi (a)*, 157(2):249–254. (Cited on page 96.)

Jahnátek, M., Hafner, J., and Krajčí, M. (2009). Shear deformation, ideal strength, and stacking fault formation of fcc metals: A density-functional study of Al and Cu. *Phys. Rev. B*, 79(22):224103. (Cited on page 98.)

Jaoul, B. (1955). Influence des impuretes sur la forme des courbes de tranction de monocristaux d'aluminium. *Comptes Rendus Hebdomadaires des Seances de L Academie des Sciences*, 240:2532–2534. (Cited on page 96.)

Jax, P., Kratochvil, P., and Haasen, P. (1970). Solid solution hardening of gold and other f.c.c. single crystals. *Acta Metallurgica*, 18(2):237–245. (Cited on pages 11 and 120.)

Jiang, C. and Gleeson, B. (2006). A combined first-principles/CALPHAD modeling of the Al-Ir system. *Acta Materialia*, 54(15):4101–4110. (Cited on pages 60, 62, and 63.)

Jones, W. R. D. and Das, P. P. (1960). The mechanical properties of aluminium-lithium alloys. *Journal of the Institute of Metals*, 88(10):435–443. (Cited on page 96.)

Kalk, A. and Schwink, C. (1995). On dynamic strain ageing and the boundaries of stable plastic deformation studied on Cu-Mn polycrystals. *Philosophical Magazine A*, 72(2):315–339. (Cited on page 11.)

Kamm, G. N. and Alers, G. A. (1964). Low-temperature elastic moduli of aluminum. *Journal of Applied Physics*, 35(2):327–330. (Cited on pages 50, 68, 248, 249, and 294.)

Kardashe, B. K., Nikanoro, S. P., and Lashek, I. (1968). Temperature dependence of Young's modulus of Al-Zn alloys and its influence upon metastable coherent phase diagram. *Czechoslovak Journal of Physics*, 18(2):275–283. (Cited on pages 91 and 92.)

Kaxiras, E. (2003). *Atomic and Electronic Structure of Solids*, chapter 2 The single-particle approximation, page 76. Cambridge University Press. (Cited on pages 31 and 285.)

Kibey, S., Liu, J., Curtis, M., Johnson, D., and Sehitoglu, H. (2006). Effect of nitrogen on generalized stacking fault energy and stacking fault widths in high nitrogen steels. *Acta Materialia*, 54(11):2991–3001. (Cited on page 4.)

Kibey, S., Liu, J., Johnson, D., and Sehitoglu, H. (2007a). Predicting twinning stress in fcc metals: Linking twin-energy pathways to twin nucleation. *Acta Materialia*, 55(20):6843–6851. (Cited on page 4.)

Kibey, S., Liu, J. B., Johnson, D. D., and Sehitoglu, H. (2007b). Energy pathways and directionality in deformation twinning. *Applied Physics Letters*, 91(18):181916. (Cited on page 4.)

Kim, D., Shang, S.-L., and Liu, Z.-K. (2009). Effects of alloying elements on elastic properties of Ni by first-principles calculations. *Computational Materials Science*, 47(1):254–260. (Cited on pages 6, 117, and 288.)

van't Klooster, P., Trappeniers, N. J., and Biswas, S. N. (1979). Effect of pressure on the elastic constants of noble metals from -196 to +25 °Cand up to 2500 bar: I. copper. *Physica B+C*, 97(1):65–75. (Cited on page 50.)

Kloske, R. and Fine, M. (1969). Solid-solution strengthening and yield drop effects in Au-Ag alloy single crystals containning 1 to 5 and 95 to 99 at pct Ag. *Transactions of the Metallurgical Society of AIME*, 245(2):217. (Cited on page 11.)

Kocks, U. (1979). Superposition of alloy hardening, strain hardening, and dynamic recovery. In Haasen, P., Gerold, V., and Kostorz, G., editors, *Strength of Metals and Alloys. Proceedings of the 5th International Conference*, pages (III)1661–1680. Pergamon, New York, NY, USA. Strength of Metals and Alloys. Proceedings of the 5th International Conference, 27-31 August 1979, Aachen, West Germany. (Cited on page 10.)

Kocks, U. (1985). Kinetics of solution hardening. *Metallurgical and Materials Transactions A*, 16(12):2109–2129. This paper is based on a presentation made at the symposium "50th Anniversary of the Introduction of Dislocations" held at the fall meeting of the TMS-AIME in Detroit, Michigan in October 1984 under the TMS-AIME Mechanical Metallurgy and Physical Metallurgy Committees. (Cited on page 10.)

Kohn, W. and Sham, L. J. (1965). Self-consistent equations including exchange and correlation effects. *Physical Review*, 140(4A):A1133–A1138. (Cited on page 23.)

Körmann, F., Dick, A., Grabowski, B., Hallstedt, B., Hickel, T., and Neugebauer, J. (2008). Free energy of bcc iron: Integrated ab initio derivation of vibrational, electronic, and magnetic contributions. *Physical Review B*, 78(3):033102. (Cited on page 4.)

Köster, W. and Speidel, M. (1965). Der Einflußder Temperatur und der Korngrosse auf die ausgepragte Streckgrenze von Kupferlegierungen. *Zeitschrif für Metallkunde*, 56(9):585–598. (Cited on page 11.)

Kostorz, G. and Haasen, P. (1969). Mischkristallhärtung von Kupfer. *Zeitschrif für Metallkunde*, 60(1):26–28. (Cited on page 11.)

Kosugi, T. and Kino, T. (1993). Ultrasonic study of the interaction potential between a dislocation and a single solute atom. *Materials Science and Engineering: A*, 164(1-2):316–321. European Research Conference on Plasticity of Materials-Fundamental Aspects of Dislocation Interactions: Low-energy Dislocation Structures III. (Cited on pages 20, 95, and 96.)

Kratochvil, P. (1970). On the effect of electron concentration on solid solution hardening in f.c.c. metals. *Scripta Metallurgica*, 4(5):333–335. (Cited on page 20.)

Kratochvíl, P. and Neradová, E. (1971). Solid solution hardening in some copper base alloys. *Czechoslovak Journal of Physics*, 21(12):1273–1278. (Cited on page 15.)

Kresse, G. and Furthmüller, J. (1996). Efficiency of ab-initio total energy calculations for metals and semiconductors using a plane-wave basis set. *Computational Materials Science*, 6(1):15–50. (Cited on pages 29, 260, and 285.)

Kresse, G. and Joubert, D. (1999). From ultrasoft pseudopotentials to the projector augmented-wave method. *Physical Review B*, 59(3):1758–1775. (Cited on pages 31 and 260.)

Kröner, E. (1958). Berechnung der elastischen Konstanten des Vielkristalls aus den Konstanten des Einkristalls. *Zeitschrift für Physik A Hadrons and Nuclei*, 151(4):504–518. (Cited on page 39.)

Kuehmann, C. J. and Olson, G. B. (2009). Computational materials design and engineering. *Materials Science and Technology*, 25(4):472–478. (Cited on page 4.)

Kurth, S., Perdew, J. P., and Blaha, P. (1999). Molecular and solid-state tests of density functional approximations: LSD, GGAs, and meta-GGAs. *International Journal of Quantum Chemistry*, 75(4-5):889–909. (Cited on page 26.)

Labusch, R. (1970). A statistical theory of solid solution hardening. *physica status solidi (b)*, 41(2):659–669. (Cited on pages 15, 18, and 124.)

Labusch, R. (1972). Statistische Theorien der Mischkristallhärtung. *Acta Metallurgica*, 20(7):917–927. (Cited on pages 18 and 124.)

Ledbetter, H. M. (1981). Elastic constants of polycrystalline copper at low temperatures. relationship to single-crystal elastic constants. *physica status solidi (a)*, 66(2):477–484. (Cited on page 50.)

Leslie, W. (1972). Iron and its dilute substitutional solid solutions. *Metallurgical and Materials Transactions B*, 3:5–26. (Cited on page 12.)

Lewandowski, J. J., Wang, W. H., and Greer, A. L. (2005). Intrinsic plasticity or brittleness of metallic glasses. *Philosophical Magazine Letters*, 85(2):77–87. (Cited on page 168.)

Leyson, G. P. M., Curtin, W. A., Hector Jr, L. G., and Woodward, C. F. (2010). Quantitative prediction of solute strengthening in aluminium alloys. *Nature Materials*, 9(9):750–755. (Cited on pages 16, 95, 96, 97, 109, 124, 125, and 288.)

Liu, X.-Y., Wang, J., and Biner, S. B. (2008). Hydrogen and self-interstitial interactions with edge dislocations in Ni: atomistic and elasticity comparisons. *Modelling and Simulation in Materials Science and Engineering*, 16(4):045002. (Cited on pages 15 and 16.)

Liu, Z.-K. (2009). First-principles calculations and CALPHAD modeling of thermodynamics. *Journal of Phase Equilibria and Diffusion*, 30:517–534. (Cited on page 4.)

Ma, A., Roters, F., and Raabe, D. (2006). On the consideration of interactions between dislocations and grain boundaries in crystal plasticity finite element modeling - theory, experiments, and simulations. *Acta Materialia*, 54(8):2181–2194. (Cited on page 163.)

MacFarlane, R., Rayne, J., and Jones, C. (1966). Temperature dependence of elastic moduli of iridium. *Physics Letters*, 20(3):234–235. (Cited on pages 50, 68, 245, and 294.)

Masafumi, S. and Takefumi, H. (1988). Elastic constants of Al-Cu solid-solution alloys and their variations by aging treatments. *JSME international journal. Ser. 1, Solid mechanics, strength of materials*, 31(4):664–670. (Cited on pages 54, 55, 86, 87, 94, and 286.)

Matsubara, M., Godet, J., and Pizzagalli, L. (2010). Theoretical study of hydrogen stability and aggregation in dislocation cores in silicon. *Physical Review B*, 82(2):024107. (Cited on page 4.)

McAlister, A. (1982). The Al-Li (aluminum-lithium) system. *Journal of Phase Equilibria*, 3(2):177–183. (Cited on pages 55, 66, 94, and 286.)

McDowell, D. and Olson, G. (2008). Concurrent design of hierarchical materials and structures. *Scientific Modeling and Simulation*, 15(1):207–240. (Cited on page 4.)

Medvedeva, N. I., Gornostyrev, Y. N., and Freeman, A. J. (2005). Solid solution softening in bcc Mo alloys: Effect of transition-metal additions on dislocation structure and mobility. *Physical Review B*, 72(13):134107. (Cited on page 12.)

Medvedeva, N. I., Gornostyrev, Y. N., and Freeman, A. J. (2007). Solid solution softening and hardening in the group-V and group-VI bcc transition metals alloys: First principles calculations and atomistic modeling. *Physical Review B*, 76(21):212104. (Cited on page 12.)

Methfessel, M. and Paxton, A. T. (1989). High-precision sampling for Brillouin-zone integration in metals. *Physical Review B*, 40(6):3616–3621. (Cited on pages 29 and 285.)

Meyerhoff, R. W. and Smith, J. F. (1962). Anisotropic thermal expansion of single crystals of thallium, yttrium, beryllium, and zinc at low temperatures. *Journal of Applied Physics*, 33(1):219–224. (Cited on page 51.)

Mishima, Y., Ochiai, S., Hamao, N., Yodogawa, M., and Suzuki, T. (1986). Solid solution hardening of nickel-role of transition metal and B-subgroup solutes. *Transactions of the Japan Institute of Metals*, 27(9):656–664. (Cited on pages 15, 17, 115, 116, and 288.)

Mishin, Y., Asta, M., and Li, J. (2010). Atomistic modeling of interfaces and their impact on microstructure and properties. *Acta Materialia*, 58(4):1117–1151. (Cited on page 4.)

Mitchell, T. E. and Thornton, P. R. (1963). The work-hardening characteristics of Cu and α-brass single crystals between 4.2 and 500 K. *Philosophical Magazine*, 8(91):1127–1159. (Cited on page 11.)

Miura, Y., Nishitani, S., Furukawa, M., and Nemoto, M. (1988). Yield strength of Al-Li solid solution alloys at high temperatures. In Kettunen, P. O., Lepisto, T. K., and Lehtonen, M. E., editors, *Strength of Metals and Alloys. Proceedings of the 8th International Conference*, pages (II)995–1000. Pergamon, Oxford, UK. Strength of Metals and Alloys (ICSMA 8) Proceedings of the 8th International Conference, Tampere, Finland, 22-26 August 1988. (Cited on page 96.)

Miura, Y., Yusu, K., Furukawa, M., and Nemoto, M. (1987). Temperature-dependence of yield strength of Al-Li single crystals. *Journal de Physique*, 48(C3):549–555. (Cited on page 96.)

Mohri, T. and Suzuki, T. (1999). Chapter 9 solid solution hardening by impurities. In Briant, C., editor, *Impurities in Engineering Materials: Impact, Reliability, and Control*, pages 259–299. CRC Press. (Cited on page 14.)

Monchoux, F. and Neuhäuser, H. (1987). An in situ transmission electron microscope study of dislocation glide in Cu-Ge alloys. *Journal of Materials Science*, 22(4):1443–1449. (Cited on page 11.)

Monkhorst, H. J. and Pack, J. D. (1976). Special points for Brillouin-zone integrations. *Physical Review B*, 13(12):5188–5192. (Cited on page 28.)

Mott, N. F. and Nabarro, F. R. N. (1940). An attempt to estimate the degree of precipitation hardening, with a simple model. *Proceedings of the Physical Society*, 52(1):86–89. (Cited on page 14.)

Müller, W., Bubeck, E., and Gerold, V. (1986). Elastic constants of Al-Li solid solutions and δ' precipitates. In Baker, C., Gregson, P. J., Harris, S. J., and Peel, C. J., editors, *Aluminium-Lithium Alloys III*, pages 435–441. Proceedings of the 3rd International Aluminium-Lithium Conference Sponsored and Organized by the Institute of Metals. (Cited on pages 54, 55, 75, 76, 77, 78, 79, 89, 90, 92, 94, and 286.)

Murnaghan, F. D. (1937). Finite deformations of an elastic solid. *American Journal of Mathematics*, 59(2):235–260. (Cited on pages 32 and 33.)

Murnaghan, F. D. (1944). The compressibility of media under extreme pressures. *Proceedings of the National Academy of Sciences of the United States of America*, 30(9):244–247. (Cited on page 32.)

Murray, J. (1982). The Al-Mg (aluminum-magnesium) system. *Journal of Phase Equilibria*, 3(1):60–74. 10.1007/BF02873413. (Cited on pages 55, 66, 94, and 286.)

Murray, J. (1983). The Al-Zn (aluminum-zinc) system. *Journal of Phase Equilibria*, 4(1):55–73. (Cited on pages 55, 66, 94, and 286.)

Murray, J. L. (1985). The aluminium-copper system. *International Metals Reviews*, 30:211–234. (Cited on pages 55, 66, 94, and 286.)

Nabarro, F. R. N. (1947). Dislocations in a simple cubic lattice. *Proceedings of the Physcial Society of London*, 59(332):256–272. (Cited on page 16.)

Nabarro, F. R. N. (1977). The theory of solution hardening. *Philosophical Magazine*, 35(3):613–622. (Cited on pages 18, 19, and 285.)

Nagarjuna, S., Srinivas, M., Balasubramanian, K., and Sarma, D. S. (1999). On the variation of mechanical properties with solute content in Cu-Ti alloys. *Materials Science and Engineering A*, 259(1):34–42. (Cited on page 20.)

Nagata, N. and Yoshida, S. (1972). Strain rate and temperature dependence of the flow stress of copper-manganese dilute alloy single crystals. *Transactions of the Japan Institute of Metals*, 13(5):339–334. (Cited on page 11.)

Nakada, Y. and Keh, A. (1971). Solid-solution strengthening in Ni-C alloys. *Metallurgical and Materials Transactions B*, 2(2):441–447. (Cited on page 11.)

Nakagawa, Y. and Hirano, K. (1968). Correlation of solution hardening of bcc Fe-alloys with size factor and solid solubility. *Transactions of the Japan Institute of Metals*, S9(Suppl. S):702–707. (Cited on pages 20 and 122.)

Nash, H. C. and Smith, C. S. (1959). Single-crystal elastic constants of lithium. *Journal of Physics and Chemistry of Solids*, 9(2):113–118. (Cited on page 51.)

Noble, B., Harris, S. J., and Dinsdale, K. (1982). The elastic modulus of aluminium-lithium alloys. *Journal of Materials Science*, 17(2):461–468. (Cited on pages 90, 96, 109, and 174.)

Nogueira, F., Castro, A., and Marques, M. A. L. (2003). Chapter 6 a tutorial on density functional theory. In Carlos Fiolhais, Miguel A. L. Marques, F. N., editor, *A primer in density functional theoy*, pages 218–256. Springer-Verlag Berlin Heidelberg New York. (Cited on page 28.)

Nowotny, H., Wormes, E., and Mohrnheim, A. (1940). Untersuchungen in den Systemen Aluminium -Kalzium, Magnesium-Kalzium und Magnesium-Zirkon. *Zeitschrif für Metallkunde*, 32(2):39–42. (Cited on pages 66 and 94.)

Ogata, S., Li, J., and Yip, S. (2002). Ideal pure shear strength of aluminum and copper. *Science*, 298(5594):807–811. (Cited on page 98.)

Ogata, S., Li, J., and Yip, S. (2005). Energy landscape of deformation twinning in bcc and fcc metals. *Physical Review B*, 71(22):224102. (Cited on page 4.)

Ogata, S., Umeno, Y., and Kohyama, M. (2009). First-principles approaches to intrinsic strength and deformation of materials: perfect crystals, nano-structures, surfaces and interfaces. *Modelling and Simulation in Materials Science and Engineering*, 17(1):013001. (Cited on page 4.)

Olmsted, D. L., Hector, L. G., Jr., and Curtin, W. (2006). Molecular dynamics study of solute strengthening in Al/Mg alloys. *Journal of the Mechanics and Physics of Solids*, 54(8):1763–1788. (Cited on page 16.)

Overton, W. C. and Gaffney, J. (1955). Temperature variation of the elastic constants of cubic elements. I. copper. *Physical Review*, 98(4):969–977. (Cited on pages 50, 68, 244, and 294.)

Owen, E. A. and Yates, E. L. (1934). IX. The thermal expansion of the crystal lattices of silver, platinum, and zinc. *Philosophical Magazine Series 7*, 17(110):113–131. (Cited on page 51.)

Ozoliņš, V., Sadigh, B., and Asta, M. (2005). Effects of vibrational entropy on the Al-Si phase diagram. *Journal of Physics: Condensed Matter*, 17(13):2197. (Cited on page 126.)

Ozoliņš, V. and Asta, M. (2001). Large vibrational effects upon calculated phase boundaries in Al-Sc. *Physical Review Letters*, 86(3):448–451. (Cited on page 126.)

Page, Y. L. and Saxe, P. (2001). Symmetry-general least-squares extraction of elastic coefficients from ab initio total energy calculations. *Physical Review B*, 63(17):174103. (Cited on page 4.)

Page, Y. L. and Saxe, P. (2002). Symmetry-general least-squares extraction of elastic data for strained materials from ab initio calculations of stress. *Physical Review B*, 65(10):104104. (Cited on page 4.)

Pearson, W. (1964). *Handbook of Lattice Spacings & Structures of Metals & Alloys*, volume 411 of *International Series of Monographs on Metals Physics & Physical Metallurgy*. Franklin Book Co. (Cited on pages 117 and 288.)

Pedroza, L. S., da Silva, A. J. R., and Capelle, K. (2009). Gradient-dependent density functionals of the Perdew-Burke-Ernzerhof type for atoms, molecules, and solids. *Physical Review B*, 79(20):201106. (Cited on pages 26 and 27.)

Peierls, R. (1940). The size of a dislocation. *Proceedings of the Physical Society*, 52(1):34–37. (Cited on page 16.)

Perdew, J. P., Burke, K., and Ernzerhof, M. (1996). Generalized gradient approximation made simple. *Physical Review Letter*, 77(18):3865–3868. (Cited on pages 26 and 260.)

Perdew, J. P., Ruzsinszky, A., Csonka, G. I., Vydrov, O. A., Scuseria, G. E., Constantin, L. A., Zhou, X., and Burke, K. (2008). Restoring the density-gradient expansion for exchange in solids and surfaces. *Physical Review Letter*, 100(13):136406. (Cited on page 27.)

Perdew, J. P., Ruzsinszky, A., Tao, J., Staroverov, V. N., Scuseria, G. E., and Csonka, G. I. (2005). Prescription for the design and selection of density functional approximations: More constraint satisfaction with fewer fits. *The Journal of Chemical Physics*, 123(6):062201. (Cited on pages 25 and 285.)

Perdew, J. P. and Wang, Y. (1992). Accurate and simple analytic representation of the electron-gas correlation energy. *Physical Review B*, 45(23):13244–13249. (Cited on page 26.)

Perdew, J. P. and Yue, W. (1986). Accurate and simple density functional for the electronic exchange energy: Generalized gradient approximation. *Physical Review B*, 33(12):8800–8802. (Cited on page 26.)

Perdew, J. P. and Zunger, A. (1981). Self-interaction correction to density-functional approximations for many-electron systems. *Physical Review B*, 23(10):5048–5079. (Cited on page 26.)

Peterson, D. and Mclachlan, D. (1975). Effect of nitrogen on the strength of thorium. *Metallurgical and Materials Transactions A*, 6(7):1359–1366. (Cited on page 11.)

Peterson, D. T. and Skaggs, R. L. (1968). Effect of carbon on strength of thorium. *Transactions of the Metallurgical Society of AIME*, 242(5):922–929. (Cited on page 11.)

Pettifor, D. G. (1992). Theoretical prediction of structure and related properties of intermetallics. *Materials Science and Technology*, 8:345. (Cited on page 168.)

von Pezold, J., Dick, A., Friák, M., and Neugebauer, J. (2010). Generation and performance of special quasirandom structures for studying the elastic properties of random alloys: Application to Al-Ti. *Physical Review B*, 81(9):094203. (Cited on page 80.)

Pink, E. and Arsenault, R. J. (1980). Low-temperature softening in body-centered cubic alloys. *Progress in Materials Science*, 24:1–50. (Cited on pages 12 and 285.)

Piquini, P., Graf, P. A., and Zunger, A. (2008). Band-gap design of quaternary (In,Ga)(As,Sb) semiconductors via the inverse-band-structure approach. *Physical Review Letter*, 100(18):186403. (Cited on page 4.)

Podkuiko, V. P., Pustovalov, V. V., Roitman, L. U., and Startsev, V. I. (1972). Critical shear stress temperature dependence in Al-Mg single crystal alloys of various concentrations in the range 1.6-300 K. *Strength of Materials*, 4(8):963–967. (Cited on page 96.)

Podkuyko, V. P. and Pustovalov, V. V. (1975). Low-temperature strengthening of aluminium-magnesium single crystals. *Fizika metallov i metallovedenie*, 39(4):852–860. (Cited on page 96.)

Poirier, J.-P. (2000). *Introduction to the Physics of the Earth's Interior, Second Edition (Cambridge Topics in Mineral Physics & Chemistry)*. Cambridge University Press, 2 edition. (Cited on page 32.)

Pugh, S. F. (1954). Relations between the elastic moduli and the plastic properties of polycrystalline pure metals. *Philosophical Magazine Series 7*, 45(367):823–843. (Cited on pages 163, 168, and 170.)

Qi, Y. and Mishra, R. K. (2007). Ab initio study of the effect of solute atoms on the stacking fault energy in aluminum. *Physical Review B*, 75(22):224105. (Cited on pages 111 and 287.)

Raju, K. and Reddy, J. (1980). Elastic properties of polycrystalline Al-Mg and Al-Cu alloys. *Journal of the Acoustical Society of India*, 8(3):29–31. (Cited on pages 88, 89, and 90.)

Ravi, C., Wolverton, C., and Ozoliņš, V. (2006). Predicting metastable phase boundaries in aluminium-copper alloys from first-principles calculations of free energies: The role of atomic vibrations. *Europhysics Letters*, 73(5):719–725. (Cited on page 126.)

Rayne, J. A. (1959). Elastic constants of α-brasses: Variation with solute concentration from 4.2-300°k. *Physical Review*, 115(1):63–66. (Cited on pages 50 and 68.)

Reuss, A. (1929). Berechnung der Fließgrenze von Mischkristallen auf Grund der Plastizitätsbedingung für Einkristalle . *Zeitschrift für Angewandte Mathematik und Mechanik*, 9(1):49–58. (Cited on page 39.)

Riddhagni, B. R. and Asimow, R. M. (1968). Solid-solution hardening in concentrated solutions. *Journal of Applied Physics*, 39(9):4144–4151. (Cited on page 18.)

Roberge, R. and Herman, H. (1973). Precipitation in liquid-quenched Al-base Ag alloys. *Journal of Materials Science*, 8(10):1482–1494. (Cited on page 107.)

Ropo, M., Kokko, K., and Vitos, L. (2008). Assessing the Perdew-Burke-Ernzerhof exchange-correlation density functional revised for metallic bulk and surface systems. *Physical Review B*, 77(19):195445. (Cited on pages 26 and 27.)

Rose, J. H., Smith, J. R., Guinea, F., and Ferrante, J. (1984). Universal features of the equation of state of metals. *Physical Review B*, 29(6):2963–2969. (Cited on page 50.)

Rossouw, C. and Venkatesan, K. (2001). Holz line analysis of lattice parameters in magnesium alloys. *Journal of Electron Microscopy*, 50(5):391–404. (Cited on page 51.)

Roters, F., Eisenlohr, P., Hantcherli, L., Tjahjanto, D., Bieler, T., and Raabe, D. (2010). Overview of constitutive laws, kinematics, homogenization and multiscale methods in crystal plasticity finite-element modeling: Theory, experiments, applications. *Acta Materialia*, 58(4):1152–1211. (Cited on pages 40 and 163.)

Roth, H., Davis, C., and Thomson, R. (1997). Modeling solid solution strengthening in nickel alloys. *Metallurgical and Materials Transactions A*, 28(6):1329–1335. (Cited on page 11.)

Ryen, Ø., Nijs, O., Sjölander, E., Holmedal, B., Ekström, H., and Nes, E. (2006). Strengthening mechanisms in solid solution aluminum alloys. *Metallurgical and Materials Transactions A*, 37(6):1999–2006. (Cited on page 96.)

Sanchez, J. M. (2010). Cluster expansion and the configurational theory of alloys. *Physical Review B*, 81(22):224202. (Cited on page 5.)

Sanders, R. E. J., Baumann, S. F., and Stumpf, H. C. (1986). Non-heat-treatable aluminum alloys. In Starke Jr., E. A. and Sanders Jr., T. H., editors, *Aluminum alloys-physical and mechanical properties*, volume 3, pages 1441–1484. Engineering Materials Advisory Services. (Cited on page 96.)

Sanville, E., Kenny, S. D., Smith, R., and Henkelman, G. (2007). An improved grid-based algorithm for bader charge allocation. *Journal of Computational Chemistry*, 28(5):899–908. (Cited on page 41.)

Saxl, I. (1964). Elastic interaction of point defects with dislocations. *Czechoslovak Journal of Physics*, 14(6):381–392. (Cited on page 15.)

Schoeck, G. (2005). The Peierls model: Progress and limitations. *Materials Science and Engineering: A*, 400-401(0):7–17. (Cited on page 16.)

Seeger, A. (1957). The mechanism of glide and work hardening in face-centered cubic and hexagonal close-packed metals. In Fisher, J., Johnston, W., Thomson, R., and Vreeland Jr., T., editors, *Dislocations and mechanical properties of crystals*, pages 243–332. John Wiley And Sons Inc. (Cited on page 16.)

Seeger, A. and Haasen, P. (1958). Density changes of crystals containing dislocations. *Philosophical Magazine*, 3(29):470–475. (Cited on page 16.)

Shang, S., Saengdeejing, A., Mei, Z., Kim, D., Zhang, H., Ganeshan, S., Wang, Y., and Liu, Z. (2010a). First-principles calculations of pure elements: Equations of state and elastic stiffness constants. *Computational Materials Science*, 48(4):813 – 826. (Cited on pages 104 and 287.)

Shang, S.-L., Zhang, H., Wang, Y., and Liu, Z.-K. (2010b). Temperature-dependent elastic stiffness constants of α and θ Al_2O_3 from first-principles calculations. *Journal of Physics: Condensed Matter*, 22(37):375403. (Cited on page 4.)

Shevakin, J. and Tsypin, M. (1997). The curves of plastic flow and deformation strengthening of some solid solution on the basis of copper. *Advanced Performance Materials*, 4(2):233–237. (Cited on page 11.)

Shinoda, T., ichi Masuda-Jindo, K., Mishima, Y., and Suzuki, T. (1987). Extra contribution of transition-metal solutes to the solid-solution hardening of nickel. *Physical Review B*, 35(5):2155–2161. (Cited on page 17.)

Shinoda, T., Choi, G., Mishima, Y., and Suzuki, T. (1990a). Correlation between the solution hardening and the solid solubility in binary fcc dilute alloys. *Iron and Steel Institute of Japan*, 76(10):1720–1727. (Cited on pages 20 and 122.)

Shinoda, T., Masuda-Jindo, K., and Suzuki, T. (1990b). Tight-binding calculation of the solute-dislocation interaction energy in nickel: effect of atomic relaxation. *Philosophical Magazine B*, 62(3):289–309. (Cited on pages 17, 115, 116, 119, and 288.)

Siebke, W. and Friedrich, C. (1980). Untersuchungen zum elastischen Verhalten einer Al-Zn-Legierung bei der Bildung von Guinier-Preston-Zonen. *Zeitschrif für Metallkunde*, 71(12):770–776. (Cited on page 78.)

Slater, J. C. (1964). Atomic radii in crystals. *The Journal of Chemical Physics*, 41(10):3199–3204. (Cited on pages 105, 115, and 118.)

Slotwinski, T. and Trivisonno, J. (1969). Temperature dependence of the elastic constants of single crystal lithium. *Journal of Physics and Chemistry of Solids*, 30(5):1276–1278. (Cited on page 51.)

Slutsky, L. J. and Garland, C. W. (1957). Elastic constants of magnesium from 4.2 K to 300 K. *Physical Review*, 107(4):972–976. (Cited on page 51.)

Smirnova, E., Korzhavyi, P., Vekilov, Y. K., Johansson, B., and Abrikosov, I. (2002). Electronic topological transitions and phase stability in the fcc Al-Zn alloys. *The European Physical Journal B*, 30(1):57–66. (Cited on pages 61 and 62.)

Stacey, F. D., Brennan, B. J., and Irvine, R. D. (1981). Finite strain theories and comparisons with seismological data. *Surveys in Geophysics*, 4(3):189–232. (Cited on page 32.)

Staroverov, V. N., Scuseria, G. E., Tao, J., and Perdew, J. P. (2004). Tests of a ladder of density functionals for bulk solids and surfaces. *Physical Review B*, 69(7):075102. (Cited on page 26.)

Stassis, C., Zaretsky, J., Misemer, D. K., Skriver, H. L., Harmon, B. N., and Nicklow, R. M. (1983). Lattice dynamics of fcc Ca. *Physical Review B*, 27(6):3303–3307. (Cited on page 68.)

Stehle, H. and Seeger, A. (1956). Elektronentheoretische Untersuchungen über Fehlstellen in Metallen. *Zeitschrift für Physik A Hadrons and Nuclei*, 146(2):217–241. (Cited on page 16.)

Steinberg, D. J. (1982). Some observations regarding the pressure dependence of the bulk modulus. *Journal of Physics and Chemistry of Solids*, 43(12):1173–1175. (Cited on pages 50 and 51.)

Sugiyama, A. (1966). Theory of valency effect of impurity atoms on hardening of alloys. *Journal of Physical Society of Japan*, 21(10):1873–1880. (Cited on page 17.)

Suzuki, H. (1952). Chemical interaction of solute atoms with dislocations. *Science reports of the Research Institutes, Tohoku University. Ser. A, Physics, chemistry and metallurgy*, 4:455–463. (Cited on page 16.)

Suzuki, H. (1979). Chapter 15 part 2 solid solution hardening in body-centred cubic alloys. In Nabarro, F. R. N., editor, *Dislocations in solids, volumn IV. Dislocations in metallurgy*, pages 191–217. North-Holland, Amsterdam, Netherlands. (Cited on page 14.)

Suzuki, H. (1983). Solution hardening of fcc alloys by the chemical interaction between solute atoms and a dislocation. In Gifkins, R., editor, *Strength of Metals and Alloys. Proceedings of the 6th International Conference*, pages (I)327–332. Pergamon, Oxford, UK. Strength of Metals and Alloys (ICSMA 6). Proceedings of the 6th International Conference, 16-20 August 1982, Melbourne, Vic., Australia. (Cited on page 16.)

Taga, A., Vitos, L., Johansson, B., and Grimvall, G. (2005). Ab initio calculation of the elastic properties of $Al_{1-x}Li_x$ (x <= 0.20) random alloys. *Physical Review B*, 71(1):014201. (Cited on pages 75, 76, 77, 89, and 90.)

Takeuchi, S. (1968). On the shear modulus parameter in the theory of solid-solution hardening. *Scripta Metallurgica*, 2(9):481–483. (Cited on pages 15 and 16.)

Tang, W., Sanville, E., and Henkelman, G. (2009). A grid-based bader analysis algorithm without lattice bias. *Journal of Physics: Condensed Matter*, 21(8):084204. (Cited on page 41.)

Tardiff, G. E. and Hendrickson, A. A. (1964). Strength of silver-base solutions. *Transactions of the Metallurgical Society of AIME*, 230(3):586–587. (Cited on page 11.)

Tarrat, N., Benoit, M., and Morillo, J. (2009). Core structure of screw dislocations in hcp Ti: an ab initio DFT study. *International Journal of Materials Research*, 100(3):329–332. 11th International Symposium on Physics of Materials (ISPMA) Charles Univ, Fac Math & Phys, Prague, CZECH REPUBLIC, AUG 24-28, 2008. (Cited on page 4.)

Tensi, H. M., Dropmann, P., and Borchers, H. (1970). Plastisches Verhalten von Aluminium-Magnesium-Einkristallen. *Zeitschrif für Metallkunde*, 61(7):518–524. (Cited on pages 96 and 109.)

Torquato, S. (1991). Random heterogeneous media: Microstructure and improved bounds on effective properties. *Applied Mechanics Reviews*, 44(2):37–76. (Cited on page 97.)

Trinkle, D. R. and Woodward, C. (2005). The chemistry of deformation: How solutes soften pure metals. *Science*, 310(5754):1665–1667. (Cited on page 12.)

Urakami, A., Meshii, M., and Fine, M. E. (1970). Effect of li additions on mechanical properties of mg base single crystals in basal and prismatic slip. In *Strength of Metals and Alloys. Proceedings of the 2nd International Conference*, pages (I)272–276. Strength of Metals and Alloys (ICSMA 2). Proceedings of the 2th International Conference, 30 August-4 September 1970, Pacific Grove, California, USA. (Cited on pages 13 and 285.)

Vanderbilt, D. (1990). Soft self-consistent pseudopotentials in a generalized eigenvalue formalism. *Physical Review B*, 41(11):7892–7895. (Cited on page 31.)

Vannarat, S., Sluiter, M. H. F., and Kawazoe, Y. (2001). First-principles study of solute-dislocation interaction in aluminum-rich alloys. *Physical Review B*, 64(22):224203. (Cited on page 14.)

Van der Ven, A., Yu, H.-C., Ceder, G., and Thornton, K. (2010). Vacancy mediated substitutional diffusion in binary crystalline solids. *Progress in Materials Science*, 55(2):61–105. (Cited on page 4.)

Vitek, V. (1968). Intrinsic stacking faults in body-centred cubic crystals. *Philosophical Magazine*, 18(154):773–786. (Cited on page 98.)

Vöhringer, O. and Macherauch, E. (1967). The yield point of α copper-tin alloys. *physica status solidi (b)*, 19(2):793–803. (Cited on page 11.)

Voigt, W. (1910). *Lehrbuch der kristallphysik*. B.G. Teubners Sammlung von Lehrbüchern auf dem Gebiete der mathematischen Wissenschaften mit Einschluss ihrer Anwendungen. B.G. Teubner. (Cited on page 39.)

Waldorf, D. L. (1960). Temperature and composition dependence of the elastic constants of dilute alloys of manganese in copper. *Journal of Physics and Chemistry of Solids*, 16(1-2):90–99. (Cited on pages 50 and 68.)

van de Walle, A. (2008). A complete representation of structure-property relationships in crystals. *Nature Materials*, 7(6):455–458. (Cited on page 4.)

Wang, A., Zhou, L., Kong, Y., Du, Y., Liu, Z.-K., Shang, S.-L., Ouyang, Y., Wang, J., Zhang, L., and Wang, J. (2009). First-principles study of binary special quasirandom structures for the Al-Cu, Al-Si, Cu-Si, and Mg-Si systems. *CALPHAD*, 33(4):769–773. (Cited on pages 61 and 62.)

Wang, H. and Li, M. (2009). Ab initio calculations of second-, third-, and fourth-order elastic constants for single crystals. *Physical Review B*, 79(22):224102. (Cited on pages 237 and 299.)

Wang, Y., Liu, Z. K., and Chen, L. Q. (2004). Thermodynamic properties of Al, Ni, NiAl, and Ni$_3$Al from first-principles calculations. *Acta Materialia*, 52(9):2665–2671. (Cited on page 4.)

Wang, Y.-J. and Wang, C.-Y. (2009). Influence of alloying elements on the elastic properties of ternary and quaternary nickel-base superalloys. *Philosophical Magazine*, 89(32):2935–2947. (Cited on page 6.)

Wendt, H. and Wagner, R. (1982). Mechanical properties of Cu-Fe alloys in the transition from solid solution to precipitation hardening. *Acta Metallurgica*, 30(8):1561–1570. (Cited on page 11.)

Wille, T., Gieseke, W., and Schwink, C. (1987). Quantitative analysis of solution hardening in selected copper alloys. *Acta Metallurgica*, 35(11):2679–2693. (Cited on page 11.)

Wille, T., Wielke, B., and Schwink, C. (1982). On the low temperature anomaly of solution hardened alloys. *Scripta Metallurgica*, 16(5):561–565. (Cited on page 11.)

Wolverton, C. and Ozoliņš, V. (2006). First-principles aluminum database: Energetics of binary al alloys and compounds. *Physical Review B*, 73(14):144104. (Cited on pages 60 and 62.)

Wolverton, C., Yan, X. Y., Vijayaraghavan, R., and Ozoliņš, V. (2002). Incorporating first-principles energetics in computational thermodynamics approaches. *Acta Materialia*, 50(9):2187–2197. (Cited on page 4.)

Woodward, C. (2005). First-principles simulations of dislocation cores. *Materials Science and Engineering A*, 400-401:59–67. Intenational Conference on Fundamentals of Plastic Deformation La Colle sur Loup, France, Sep 13-17, 2004. (Cited on pages 4 and 5.)

Woodward, C., Trinkle, D. R., Hector, L. G., and Olmsted, D. L. (2008). Prediction of dislocation cores in aluminum from density functional theory. *Physical Review Letter*, 100(4):045507. (Cited on page 97.)

Woodward, R. B. and Hoffmann, R. (1969). The conservation of orbital symmetry. *Angewandte Chemie International Edition in English*, 8(11):781–853. (Cited on page 4.)

Yasi, J. A., Hector Jr., L. G., and Trinkle, D. R. (2010). First-principles data for solid-solution strengthening of magnesium: From geometry and chemistry to properties. *Acta Materialia*, 58(17):5704–5713. (Cited on pages 5, 16, 98, 110, 113, 114, 120, 121, 178, 287, and 288.)

Yoo, M. H. (1981). Slip, twinning and fracture in hexagonal close-packed metals. *Metallurgical and Materials Transactions A*, 12(3):409–418. (Cited on page 170.)

Zaiser, M. (2002). Dislocation motion in a random solid solution. *Philosophical Magazine A*, 82(15):2869–2883. (Cited on page 18.)

Zander, J., Sandström, R., and Vitos, L. (2007). Modelling mechanical properties for non-hardenable aluminium alloys. *Computational Materials Science*, 41(1):86–95. (Cited on pages 75, 76, 77, 89, and 90.)

Zhao, J., Winey, J. M., and Gupta, Y. M. (2007). First-principles calculations of second- and third-order elastic constants for single crystals of arbitrary symmetry. *Physical Review B*, 75(9):094105. (Cited on page 4.)

Zhong, Y., Yang, M., and Liu, Z.-K. (2005). Contribution of first-principles energetics to Al-Mg thermodynamic modeling. *CALPHAD*, 29(4):303–311. (Cited on pages 61, 62, and 63.)

Ziesche, P., Kurth, S., and Perdew, J. P. (1998). Density functionals from LDA to GGA. *Computational Materials Science*, 11(2):122–127. (Cited on page 26.)

Zolotorevsky, N., Solonin, A., Churyumov, A., and Zolotorevsky, V. (2009). Study of work hardening of quenched and naturally aged Al-Mg and Al-Cu alloys. *Materials Science and Engineering: A*, 502(1-2):111–117. (Cited on page 96.)

Zubov, L. M. (2001). *Nonlinear Theory of Dislocations and Disclinations in Elastic Bodies , First Edition (Lecture Notes in Physics Monographs)*. Springer. (Cited on page 16.)

Zunger, A., Wei, S.-H., Ferreira, L. G., and Bernard, J. E. (1990). Special quasirandom structures. *Physical Review Letter*, 65(3):353–356. (Cited on page 5.)

List of Figures

List of Tables

Abstract

Any material properties, in principle, can be reproduced or predicted by performing first-principles calculations. Nowadays, however, we are dealing with complex alloy compositions and processes. The complexities cannot be fully described by first-principles, because of the limited computational power.

The primary objective of this study is to investigate an important engineering problem, **solid solution strengthening**, in a simplified manner. The simplified scheme should allow fast and reliable prediction of the solid solution strengthening.

It is simplified by capturing the key features of the solid solution strengthening, namely the **volume and modulus mismatch**. Those two quantities are calculated by **density functional theory (DFT)** and inserted into the linear elasticity models.

Seven Al binary solid solutions were investigated (**Al-X, X=Ca, Sr, Ir, Cu, Mg, Li and Zn**). The calculated strengthening effects of the solute elements by this simplified approach are in very reasonable agreement with what is observed in the experiments and another direct DFT calculation. It is also observed that the decisive parameters of the solid solution strengthening follow a trend on the periodic table, so does the strengthening effect. The volume mismatch parameters are correlated with the solubility enthalpies of the studied Al binary solid solutions. This correlation allows to estimate the optimal strengthening parameter to achieve the maximum strengthening at the solubility limit.

Another objective is to better understand the solid solution strengthening from the electronic origin. This was tentatively investigated by observing the perturbation caused by the solute elements. It is observed that the perturbation can be correlated with the strengthening effect and the supercell size dependence.

All the calculated materials properties in this thesis entered Ashby's materials property and design charts. The performance of the studied Al binary solid solutions indicated by those charts reasonably coincides with their current applications. Although Ca, Sr and Ir cause larger strengthening effect in Al than other studied solute elements, they do not always help Al perform better in some tasks.

Zusammenfassung

Im Prinzip können alle Materialeigenschaften mit Ab-initio-Rechnungen reproduziert oder vorhergesagt werden. Heutzutage liegen uns jedoch hochkomplexe Legierungszusammensetzungen und Prozesse vor. Aufgrund begrenzter Rechenleistung können daher nicht alle der dabei auftretenden komplexen Phänomene vollständig beschrieben werden.

Ziel der vorliegenden Arbeit ist es die in der Anwendung bedeutsame Fragestellung der **Mischkristallverfestigung** auf einfache Weise zu untersuchen. Das effiziente Schema soll eine schnelle und zuverlässige Voraussage der Mischkristallverfestigung ermöglichen.

Die Vereinfachung besteht dabei darin, dass die Hauptparameter der Mischkristallverfestigung, nämlich **die Atomvolumina der beteiligten Elemente und die unterschiedlichen elastischen Moduli**, rechnergestützt vorhergesagt werden. Die Atomvolumina und elastischen Moduli mittels **Dichtefunktionaltheorie (DFT)** berechnet und in ein linear-elastisches Model eingesetzt.

Sieben binäre Aluminium-Mischkristalle wurden untersucht (**Al-X, X=Ca, Sr, Ir, Cu, Mg, Li und Zn**). Die ermittelten Verfestigungspotentiale der gelösten Elemente durch den vereinfachten Ansatz, wiesen eine gute Übereinstimmung mit Ergebnissen aus Experimenten und anderen direkten DFT Rechnungen auf. Es wurde auch beobachtet, dass sowohl die ausschlaggebenden Parameter zur Mischkristallverfestigung als auch die Verfestigung einem Trend im Periodensystem der Elemente folgen. Die Abweichung im Atomvolumen der Legierungselemente korreliert mit den Lösungsenthalpien der behandelten binären Al-Legierungen. Dies erlaubt die Abschätzung des optimalen Atomvolumens, durch das eine größtmögliche Verfestigung an der Löslichkeitsgrenze erreicht wird.

Ein anderes Ziel der Arbeit war die Mischkristallverfestigung im Hinblick auf den elektronischen Hintergrund besser zu verstehen. Zu diesem Zweck wurde die durch die Legierungselemente hervorgerufene Änderung in der elektronischen Struktur eingehend untersucht. Die Abhängigkeit des Verfestigungseffekts von diesen Änderungen, sowie der Einfluss der Superzellgrösse wird in diesem Zusammenhang erörtert.

Alle in dieser Arbeit errechneten Eigenschaften wurden in Materialeigenschafts- und Materialdesign-Diagramme nach Ashby eingetragen. Die Eigenschaften der untersuchten binären Al-Mischkristalle, welche durch die benannten Diagramme abgebildet werden, stimmen mit deren aktuellen Anwendungen überein. Obwohl Ca, Sr und Ir eine größere Verfes-

tigung in Al bewirken als andere untersuchte Legierungselemente, verbessern sie die Eigenschaften von Al nicht in jeder Hinsicht.

Curriculum Vitae

Personal Data

Name: Duancheng Ma
Date of Birth: Sep. 5th, 1980
Place of Birth: China

Education

1999-2003	Bachelor study
	Material Science and Engineering
	University of Science and Technology, Beijing (USTB)
2004-2007	Master study
	Metallurgical Engineering
	Rheinisch-Westfaelische Technische Hochschule Aachen (RWTH Aachen)
	Grade: sehr gut (very good)
2007-2011	Doctorand
	Max-Planck Institut für Eisenforschung, Düsseldorf (MPIE)
	Grade: ausgezeichnet (distinguished)

Selected International Conference Activities

D. Ma, M. Friák, D. Raabe, J. Neugebauer. Theoretical multi-physics approaches to solid-solution strengthening of Al. 15th International Conference on the Strength of Materials (IC-SMA 15), Aug. 16th-21st, 2009, Dresden, Germany.

D. Ma, D. Raabe, F. Roters, R. Maaß, H. Van Swygenhoven. Crystal plasticity finite element study on small scale plasticity of micropillars. 15th International Conference on the Strength of Materials (ICSMA 15), Aug. 16-21, 2009, Dresden, Germany.

D. Ma, M. Friák, W. Counts, F. Roters, D. Raabe, J. Neugebauer. Coupling density functional theory with continuum mechanics for alloy design (Invited). MS&T'08, Oct. 5th-9th, 2008, Pittsburgh, Pennsylvania, USA.

D. Ma, D. Raabe, F. Roters, M. Friák, J. Neugebauer. Modeling rolling textures of β-Ti alloys using constitutive data from ab-initio simulations. 15 th International Conference on the Texture of Materials (ICOTOM 15), Jun. 1st-6th, 2008, Pittsburgh, Pennsylvania, USA

Summer/Winter School

468. Wilhelm und Else Heraeus-Seminar, Ab initio Description of Iron and Steel: Mechanical properties, Oct. 24th-29th, 2010. Ringberg Castle, Tegernsee, Germany.

Summer School on Computational Materials Sciences, 28th Jun.-3rd Jul., 2010, Miramar Palace, San Sebastian, Spain.

Selected Publications

D. Ma, M. Friák, J. von Pezold, D. Raabe, J. Neugebauer. Correlation between solid solution strengthening and solubility: an ab-initio approach (in preparation)

D. Ma, M. Friák, J. von Pezold, D. Raabe, J. Neugebauer. Supercell size dependence in metallic solid solutions: examples of Al binary systems (in preparation)

D. Ma, M. Friák, J. von Pezold, D. Raabe, J. Neugebauer. Trend of solid solution strengthening effect on the periodic table: examples of Al, Ni and Mg (basal slip) binary systems (in preparation).

D. Ma, M. Friák, J. von Pezold, D. Raabe, J. Neugebauer. Solid solution strengthening in Al: a first-principles approach (in preparation).

R. Maaß, S. Van Petegem, D. Ma, J. Zimmermann, D. Grolimund, F. Roters, H. Van Swygenhoven, D. Raabe. Smaller is stronger: The effect of strain hardening, Acta Mater.(2009), vol. 57, p5996.

YP. Cao, D. Ma, D. Raabe. The use of flat punch indentation to determine the viscoelastic properties in the time and frequency domains of a soft layer bonded to a rigid substrate, Acta Biomater.(2009), vol. 5, p240.

D. Ma, M. Friák, J. Neugebauer, D. Raabe, F. Roters. Multiscale simulation of polycrystal mechanics of textured β-Ti alloys using ab initio and crystal-based finite element methods, Phy. Status Solidi (b) (2008), vol. 245, p2642.

D. Raabe, B. Sander, M. Friák, D. Ma, J. Neugebauer. Theory-guided bottom-up design of β-titanium alloys as biomaterials based on first principles calculations: Theory and experiments, Acta Mater.(2007), vol. 55, p4475.

D. Raabe, D. Ma, F. Roters. Effects of initial orientation, sample geometry and friction on anisotropy and crystallographic orientation changes in single crystal microcompression deformation: A crystal plasticity finite element study, Acta Mater.(2007), vol. 55, p4567.

YS. Hu, P. Yang, ZD. Zhao, D. Ma. Investigation of twinning process in magnesium alloy by means of orientation mapping (in Chinese), Chinese J. Nonferr. Metal.(2004), vol. 58, p105.